Characterization of TRIM24 as a centromere-associated protein contributing to mitotic cohesion

Zur Erlangung des akademischen Grades einer

DOKTORIN DER NATURWISSENSCHAFTEN

(Dr. rer. nat.)

von der KIT-Fakultät für Chemie und Biowissenschaften

des Karlsruher Instituts für Technologie (KIT)

genehmigte

DISSERTATION

von

M.Sc. Agnieszka Maria Pancholi

1. Referentin: Prof. Dr. Sylvia Erhardt
2. Referent: Prof. Dr. Lennart Hilbert

Tag der mündlichen Prüfung: 20.04.2026

Abstract

Centromeres are the regions on every chromosome that ensure accurate chromosome segregation during cell division. In humans, centromeres are composed of repetitive α-satellite DNA sequences and are epigenetically defined by the histone H3 variant CENP-A. Although centromeres lack protein-coding genes, they are transcriptionally active, and centromeric chromatin organization is linked to the maintenance of sister chromatid cohesion. However, the molecular mechanisms coordinating centromeric chromatin regulation and cohesion remain poorly defined.

This thesis characterizes TRIM24 as a centromere-associated chromatin factor that contributes to mitotic cohesion. Reanalysis of public ChIP-seq datasets using REDPOINT bioinformatic approach and their alignment to telomere-to-telomere human genome assembly revealed enrichment of TRIM24 at defined subsets of centromeric and pericentromeric repeat classes. Immunofluorescence analyses demonstrated that TRIM24 localizes adjacent to, but largely excluded from, CENP-A domains during interphase and mitosis, indicating an association to CENP-A-depleted core centromeric repeats and proximal pericentromeric regions.

Domain analysis revealed that centromeric association of TRIM24 depends primarily on its PHD and RING domains, while its BRD domain modulates centromeric association. Deletion of the PHD or RING domain reduced centromeric localization and resulted in pronounced cohesion defects. Deletion of the BRD domain altered nuclear distribution, whereas BRD point mutant F979A/N980A caused abnormal centromeric retention and severe cohesion defects. These findings indicate that the regulated chromatin engagement of TRIM24 is required for proper centromeric function.

Functional assays showed that TRIM24 positively contributes to centromeric cohesion. Overexpression suppressed premature sister chromatid separation and decreased intercentromeric distance, whereas depletion increased cohesion defects. Deletion of the HP1-binding domain led to increased cohesion defects without influencing centromeric association, suggesting that TRIM24's interaction with HP1

proteins is important for cohesion maintenance. Co-immunoprecipitation identified an association of TRIM24 with cohesin subunit RAD21, linking TRIM24 to the cohesion network. In addition, TRIM24 levels modestly correlated with transcription of α-satellite repeats, consistent with its role in shaping centromeric chromatin and influencing α-satellite transcription.

Taken together, these findings establish TRIM24 as a chromatin-associated regulator at centromeric and pericentromeric regions. Through domain-dependent chromatin engagement and interaction with cohesion-associated pathways, TRIM24 contributes to a centromeric environment that supports stable sister chromatid cohesion and thereby supports faithful chromosome segregation.

Zusammenfassung

Zentromere sind Regionen auf jedem Chromosom, die eine korrekte Chromosomensegregation während der Zellteilung gewährleisten. Beim Menschen bestehen Zentromere aus repetitiven α-Satelliten-DNA-Sequenzen und sind epigenetisch durch die Histon-H3-Variante CENP-A definiert. Obwohl Zentromere keine proteinkodierenden Gene enthalten, sind sie transkriptionell aktiv, und die Organisation des zentromerischen Chromatins steht in Zusammenhang mit der Aufrechterhaltung der Schwesterchromatidenkohäsion. Die molekularen Mechanismen, die die Regulation des zentromerischen Chromatins und die Kohäsion koordinieren, sind jedoch bisher nicht vollständig verstanden.

In dieser Arbeit wird TRIM24 als ein zentromer-assoziierter Chromatinfaktor charakterisiert, der zur mitotischen Kohäsion beiträgt. Die Reanalyse von öffentlich verfügbaren TRIM24-ChIP-seq-Datensätzen unter Verwendung des bioinformatischen Ansatzes namens REDPOINT und deren Alignment zur Telomer-zu-Telomer-Referenz des humanen Genoms zeigte eine Anreicherung von TRIM24 an definierten Subsets zentromerischer und perizentromerischer Repeats. Immunfluoreszenz-Analysen zeigten, dass TRIM24 während der Interphase und Mitose benachbart zu, aber weitgehend ausgeschlossen von CENP-A-Domänen lokalisiert ist. Dies ist vereinbar mit einer Assoziation zu CENP-A-depletierten Kernbereichen des Zentromers sowie zu proximalen perizentromerischen Regionen.

Domänenanalysen zeigten, dass die zentromerische Assoziation von TRIM24 hauptsächlich von den PHD- und RING-Domänen abhängt, während die BRD-Domäne die zentromerische Bindung moduliert. Die Deletion der PHD- oder RING-Domäne reduzierte die zentromerische Lokalisation und führte zu deutlichen Kohäsionsdefekten. Die Deletion der BRD-Domäne veränderte die nukleäre Verteilung, während die BRD-Punktmutante F979A/N980A eine abnorme Retention am Zentromer und schwere Kohäsionsdefekte verursachte. Diese Ergebnisse zeigen, dass eine regulierte Chromatinbindung von TRIM24 für eine korrekte zentromerische Funktion notwendig ist.

Funktionelle Experimente zeigten außerdem, dass TRIM24 positiv zur zentromerischen Kohäsion beiträgt. Eine Überexpression unterdrückte die vorzeitige Trennung der Schwesterchromatiden und verringerte die interzentromerische Distanz, während eine Depletion zu einer Zunahme von Kohäsionsdefekten führte. Die Deletion der HP1-Bindungsdomäne führte zu erhöhten Kohäsionsdefekten, ohne die zentromerische Assoziation zu beeinflussen. Dies deutet darauf hin, dass die Interaktion von TRIM24 mit HP1-Proteinen für die Aufrechterhaltung der Kohäsion wichtig ist. Co-Immunpräzipitations-Experimente zeigten eine Assoziation von TRIM24 mit der Kohesin-Untereinheit RAD21 und stellen eine Verbindung von TRIM24 zum Kohäsionsnetzwerk her. Zusätzlich korrelierten die TRIM24-Level moderat mit der Transkription von α-Satelliten-Repeats, das mit einer Rolle bei der Gestaltung des zentromerischen Chromatins vereinbar ist.

Zusammenfassend identifizieren diese Ergebnisse TRIM24 als chromatinassoziierten Regulator in zentromerischen und perizentromerischen Regionen. Durch domänenabhängige Chromatinbindung und Interaktion mit kohäsionsassoziierten Signalwegen trägt TRIM24 zu einer zentromerischen Umgebung bei, die eine stabile Schwesterchromatidenkohäsion und damit eine zuverlässige Chromosomensegregation unterstützt.

Contents

1. Introduction **1**

1.1. Chromosome segregation during mitosis 1

1.2. Centromere 2

1.2.1. Centromeric mark CENP-A 2

1.2.2. Centromeric DNA 3

1.3. Mitotic centromeric cohesion 5

1.3.1. Cohesin cycle and centromere protection 6

1.3.2. Spatial organization of cohesion 8

1.4. Centromeric transcription and its function 9

1.4.1. Regulation of centromeric transcription 11

1.5. Identifying centromere-associated proteins 13

1.5.1. Challenges and recent advances in centromere mapping 13

1.5.2. REDPOINT as a tool to systematically investigate public ChIP-seq data 14

1.6. TRIM24: a chromatin reader and E3 ubiquitin ligase 16

1.7. Aim of the thesis 18

2. Results **19**

2.1. TRIM24 localizes to centromeres 19

2.1.1. ChIP-seq shows enrichment of TRIM24 at centromeres in a cell type-specific manner 19

2.1.2. TRIM24 shows cell type-specific enrichment at centromeric and pericentromeric satellites 24

2.1.3. Immunofluorescence supports centromeric localization of TRIM24 in interphase and mitosis 28

2.2. PHD and RING domains contribute to TRIM24 centromere localization 30

2.3. TRIM24 BRD point mutant forms distinct foci in proximity to centromeres . . . 35
2.3.1. TRIM24 BRD point mutant forms centromeric foci in interphase and mitosis . . . 35
2.3.2. TRIM24 BRD point mutant foci are linked to mutant expression levels . . . 40
2.4. TRIM24 contributes to proper sister chromatid cohesion during mitosis 42
2.4.1. TRIM24 contributes to proper intercentromeric distance in mitosis . . . 42
2.4.2. TRIM24 prevents premature sister chromatid separation . . . 44
2.5. TRIM24 associates with cohesin subunit RAD21 . . . 46
2.6. TRIM24 affects transcription of α-satellite higher order repeats . . . 48
2.7. Contributions . . . 50

3. Discussion **51**
3.1. TRIM24 associates with centromeric and pericentromeric chromatin . 52
3.2. TRIM24 centromeric localization depends on PHD and RING domains 55
3.3. Bromodomain mutation causes abnormal TRIM24 foci formation at the centromeres . . . 57
3.4. TRIM24 contributes to mitotic cohesion . . . 59
3.5. TRIM24 associates with cohesin subunit RAD21 . . . 62
3.6. TRIM24 levels correlate with transcription of active α-satellite higher order repeats . . . 63
3.7. TRIM24 as a multifunctional centromeric regulator . . . 64
3.8. Limitations . . . 67
3.9. Conclusions and Perspectives . . . 70

4. Materials and Methods **73**
4.1. Materials . . . 73
4.1.1. Chemicals and reagents . . . 73
4.1.2. Buffers and solutions . . . 75
4.1.3. Antibodies . . . 77
4.1.4. Enzymes . . . 78
4.1.5. Kits . . . 79
4.1.6. Antibiotics . . . 79
4.1.7. Bacterial strains . . . 79

4.1.8. Cell lines . . . 80
4.1.9. Cell culture reagents . . . 80
4.1.10. Primers . . . 80
4.1.11. Plasmids . . . 81
4.1.12. siRNA . . . 82
4.1.13. Equipment and consumables . . . 83
4.1.14. Software . . . 84
4.1.15. Cell culture methods . . . 85
4.1.16. Molecular biology methods . . . 89
4.1.17. Bacterial cell methods . . . 91
4.1.18. Biochemical methods . . . 92
4.1.19. Fluorescence microscopy . . . 94
4.1.20. Flow cytometry-based cell cycle analysis . . . 97
4.2. Bioinformatics . . . 98
4.2.1. Bioinformatic tools . . . 98
4.2.2. ChIP-seq accession numbers . . . 99
4.2.3. Reanalysis of Every Dataset at Positions Of INTerest (REDPOINT) . . . 99
4.2.4. Alignment to T2T-CHM13 genome . . . 100
4.2.5. Extraction of centromeric repeats . . . 102
4.2.6. TRIM24 expression analysis using DepMap . . . 104
4.2.7. AI usage statement . . . 104

5. Supplementary Information **105**

6. Acknowledgments **114**

Bibliography **115**

A. Extended Supplementary Information **140**

List of Figures

1. Human centromeres are composed of highly repetitive DNA. 4
2. Cohesin complex maintains sister chromatid cohesion during mitosis . 7
3. REDPOINT bioinformatics approach identifies centromeric proteins. . 15
4. REDPOINT analysis reveals TRIM24 enrichment at centromeres. . . 20
5. TRIM24 is enriched at the α-satellite higher-order repeats. 22
6. TRIM24 enrichment differs between centromeric repeat classes. 23
7. TRIM24 enrichment at centromeres is cell type-dependent. 26
8. TRIM24 enrichment at centromeric repeat classes varies across cell lines. 27
9. TRIM24 localizes to centromeres during interphase and mitosis. . . . 29
10. Overview of TRIM24 domain mutants. 31
11. TRIM24 domain mutants show altered cellular distribution during interphase. 32
12. TRIM24 domain mutants show altered centromeric localization during mitosis. 33
13. TRIM24 domain mutants differentially affect centromeric localization during mitosis. 34
14. TRIM24 bromodomain point mutant retains centromeric localization during interphase. 37
15. TRIM24 bromodomain point mutant forms large foci near centromeres during mitosis. 38
16. TRIM24 bromodomain point mutant shows enhanced centromeric localization during mitosis, correlated with expression level. 40
17. TRIM24 bromodomain point mutant forms foci near centromeres, and their size depends on mutant expression level. 41
18. TRIM24 influences intercentromeric distance in mitosis. 43
19. TRIM24 prevents premature sister chromatid separation. 45
20. TRIM24 associates with RAD21. 47

21. Alteration in TRIM24 expression changes levels of α-satellite transcription. 49

22. Model summarizing the effects of TRIM24 mutants on centromeric localization and cohesion. 60
23. Proposed model of TRIM24 function at centromeric and pericentromeric chromatin. 66

S1. TRIM24 enrichment across different cell lines, chromosome 9. 106
S2. TRIM24 enrichment across different cell lines, chromosome 6. 107
S3. TRIM24 localizes to the centromere during interphase and mitosis in LNCaP cells. 108
S4. Enrichment of TRIM24 at active α-sat HORs in different cell lines . . 109
S5. Validation of TRIM24 and CENP-A antibodies. 110
S6. TRIM24 colocalization in correlation to TRIM24 intensity in TRIM24 mutants. 111
S7. Cell cycle analysis of TRIM24 mutants using Flow Cytometry. 113

A1. Live-cell imaging of Pol II Ser2P mintbody during mitosis. 141
A2. Nascent RNA detection at mitotic centromeres using EU labelling. . . 142
A3. Mitotic index upon TRIM24 perturbation. 153
A4. Hormone deprivation alters centromeric TRIM24 intensity in LNCaP cells. 155
A5. CENP-A and Pol II Ser2P signal in cells overexpressing TRIM24-GFP or TRIM24 F979A/N980A-GFP. 157
A6. Quantification of CENP-A and Pol II Ser2P signal upon TRIM24 bromodomain perturbation. 158
A7. Immunofluorescence staining of RNA Polymerase II in *Drosophila melanogaster* testis. 159

List of Tables

1. Chemicals used in this thesis. 73
2. Reagents used in this thesis. 74
3. Composition of buffers and solutions used in this thesis. 75
4. Antibodies used in this thesis. 77
5. Enzymes used in this thesis. 78
6. Kits used in this thesis. 79
7. Antibiotics used in this thesis. 79
8. Bacterial strains used in this thesis. 79
9. Cell lines used in this thesis. 80
10. Cell culture reagents used in this thesis. 80
11. Primers used in this thesis. 80
12. Plasmids used in this thesis. 81
13. siRNAs used in this thesis. 82
14. Equipment and consumables used in this thesis. 83
15. Software used in this thesis. 84
16. PCR reaction mixture used for site-directed mutagenesis. 92
17. PCR cycling conditions used for site-directed mutagenesis. 92
18. Bioinformatic tools used in this thesis. 98
19. Accession numbers of the ChIP-seq datasets used in this thesis. . . . 99

S1. Values of TRIM24 centromeric enrichment calculated by REDPOINT analysis, with corresponding accession numbers. 110
S2. TRIM24 enrichment at centromeric repeat classes across datasets. . . 110
S3. Public ChIP-seq datasets used for TRIM24 analysis and their key sequencing parameters. 112

A1. REDPOINT enrichment values for ChIP-seq datasets. 143

A2. Quantification of premature sister chromatid separation in HEK293T cells expressing TRIM24 mutant constructs (C840W, V733D/L735N, K723R, and K741R). 152

1. Introduction

1.1. Chromosome segregation during mitosis

Faithful cell division is one of the most fundamental processes in biology. During mitosis, sister chromatids must be precisely distributed to the daughter cells to preserve genome integrity and ensure cell survival. Errors in this process cause aneuploidy, an abnormal chromosome number, which is associated with developmental disorders and cancer, and often results in cell death [146]. Thus, mitosis must be tightly regulated, both spatially and temporally [3].

The eukaryotic cell cycle is divided into interphase and mitosis. During interphase, DNA replication in S phase produces two identical sister chromatids that remain physically connected until their separation in mitosis. Mitosis itself proceeds through a series of well-defined stages [3, 118]. In prophase, chromosomes condense and kinetochores begin to assemble at centromeres, establishing the attachment sites for the spindle microtubules. During metaphase, chromosomes align at the metaphase plate, achieving proper bi-orientation. At anaphase onset, the centromeric cohesin complex that tethers the sister chromatids is cleaved, enabling their movement toward opposite spindle poles. Finally, in telophase, chromosomes decondense and the cell divides into two genetically identical daughter cells [3].

Proper assembly of the kinetochore, a macromolecular structure responsible for microtubule attachment at the centromere, is essential for faithful chromosome segregation [35]. Failure to form a fully functional kinetochore on each sister chromatid, or defects in kinetochore-microtubule attachment, can lead to chromosome missegregation and lagging chromosomes [131]. To ensure that chromosome segregation occurs only after proper attachments are established, mitotic progression is controlled by the spindle assembly checkpoint (SAC) [127]. The SAC delays anaphase when kinetochores are unattached or incorrectly attached and allows anaphase onset only after stable bi-oriented kinetochore-microtubule attachments are formed. In this way, checkpoint control prevents premature anaphase entry and reduces the risk of

premature cohesion loss and sister chromatid separation [99, 128]. The centromere is a key component of this regulatory system, as it specifies the position of kinetochore assembly and thereby links spindle attachment to accurate chromosome segregation. Therefore, centromeres provide a specialized DNA and chromatin environment that is necessary for faithful chromosome segregation.

1.2. Centromere

Centromeres are specialized chromosomal regions essential for faithful inheritance of genetic material during cell division [20, 43]. In most eukaryotes, each chromosome contains a single centromere, visible as a primary constriction where sister chromatids remain connected [161]. Centromeres act as the foundation for kinetochore assembly and provide attachment sites for spindle microtubules during mitosis and meiosis [6]. Dysregulation of centromere structure or function can cause chromosome missegregation and aneuploidy, and ultimately leads to reduced viability or cell death [180]. At the molecular level, centromere identity is largely defined epigenetically by the presence of the histone H3 variant CENP-A, which forms a specialized chromatin environment required for centromere function [138, 149].

1.2.1. Centromeric mark CENP-A

Centromere identity is defined not by DNA sequence but by an epigenetic signature. In centromeric chromatin, canonical histone H3 is interspersed with the histone H3 variant centromere protein A (CENP-A) [6, 19, 50]. CENP-A is a key determinant of centromere function, and experimentally depositing CENP-A at ectopic sites can promote the formation of a functional kinetochore [165]. Consistent with its central role, both CENP-A overexpression and depletion disrupt centromere function and lead to chromosome instability and mitotic defects [74, 165].

CENP-A homologues are found in nearly all eukaryotes, including Cse4 in *Saccharomyces cerevisiae*, CID in *Drosophila melanogaster*, and CenH3 in *Arabidopsis thaliana* [24, 173, 178]. Compared with histone H3, CENP-A evolves rapidly and shows poor conservation in its N-terminal tail, which varies in length and sequence between species. Despite this variability, CENP-A serves as a functionally conserved mark of centromeres and is essential for faithful chromosome segregation [149].

In human cells, centromere identity is maintained across cell divisions by regulated deposition of new CENP-A nucleosomes [58, 82]. This deposition is mediated by the dedicated chaperone HJURP, which deposits newly synthesized CENP-A at centromeres in a cell cycle-regulated manner, mainly in early G1 after mitotic exit [82, 167, 168]. In this way, centromere identity can be propagated in an epigenetic manner rather than being strictly encoded by a DNA sequence.

Human CENP-A consists of a C-terminal histone fold domain (HFD) with about 62% sequence similarity to histone H3, and a unique N-terminal tail [175]. Within the HFD, the CENP-A targeting domain (CATD) is necessary and sufficient for centromeric localization [21, 22]. The short, intrinsically disordered N-terminal tail promotes partial DNA unwrapping in CENP-A nucleosomes compared to canonical H3 nucleosomes [177]. This altered nucleosome structure, which is conserved across species, contributes to a distinct chromatin architecture that supports centromere function and kinetochore assembly [5, 198].

CENP-A chromatin is also a functional platform that is specifically recognized by the constitutive centromere-associated network (CCAN) proteins [29]. CCAN members such as CENP-C and CENP-N bind CENP-A nucleosomes and help translate the CENP-A mark into a stable centromere scaffold that supports the kinetochore during mitosis [58]. Importantly, this epigenetic CENP-A layer acts on top of a highly repetitive DNA environment, and the organization of centromeric repeats provides an additional structural context that shapes centromere structure and chromatin organization.

1.2.2. Centromeric DNA

Centromeres are essential in all eukaryotes, but their DNA organization varies greatly among species. In humans, centromeres are composed of megabase-sized arrays of highly repetitive DNA [15]. These arrays consist primarily of α-satellite (α-sat) monomers, 171 bp AT-rich repeats arranged in a head-to-tail manner into higher-order repeats (HORs) [122, 176, 194]. The monomers within a given centromere share 50-70% sequence similarity, whereas HORs are highly conserved, with approximately 97-99% similarity [15]. Sequence variation among monomers and HORs generates chromosome-specific repeat patterns that contribute to the structural organization of individual centromeres.

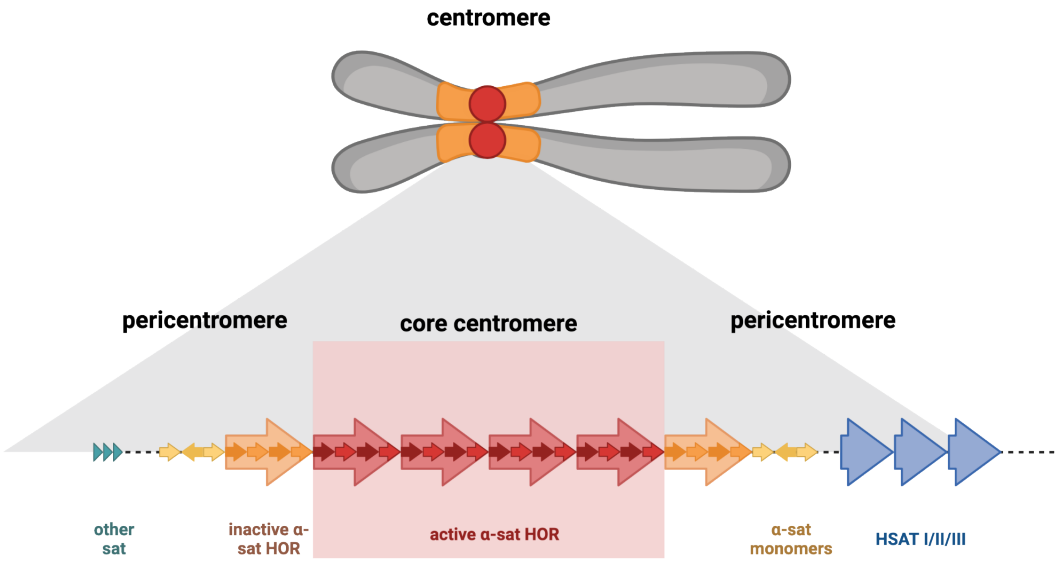


Figure 1.: Human centromeres are composed of highly repetitive DNA. Schematic representation of centromeric DNA organization in humans. α-satellite monomers (α-sat), 171 bp-long repeats, are arranged head-to-tail into higher-order repeats (HORs) extending over megabases. Centromeric histone CENP-A is incorporated at active α-sat HORs, forming the core centromere. Inactive α-sat HORs, together with divergent α-sat monomers and other repeat classes, including HSAT1A/B, HSAT2, HSAT3, β-satellites and γ-satellites, constitute the pericentromere. Adapted from [9]. Created with BioRender.com.

Only a subset of α-sat HORs incorporates CENP-A and forms the active centromeric region that assembles the kinetochore, referred to as the core centromere or active α-sat HORs (Fig. 1) [9, 170]. The remaining inactive α-sat HORs, together with flanking divergent monomeric α-sat sequences and other satellite repeat classes, constitute the pericentromere. Besides α-sat repeats, the pericentromere also includes additional repeat classes such as β- and γ-satellites, HSAT1A/B, HSAT2, and HSAT3 [111]. Unlike α-sat, which is present on all chromosomes, these additional satellite classes are present only on a subset of them [111].

Pericentromeric chromatin is typically heterochromatic, providing rigidity and mechanical resistance during mitosis [151]. Cohesin, which mediates sister chromatid cohesion, is highly enriched in the pericentromere but largely excluded from active α-sat HORs [166]. Recent studies have demonstrated that the pericentromere also contributes to spatial centromere organization, supporting kinetochore assembly and microtubule attachment [154].

Core centromere and pericentromere differ not only in DNA sequence but also in their epigenetic landscapes. The core centromere exhibits chromatin marks characteristic of transcriptionally active regions, including H3K4me2 and H3K36me2,

which promote RNA Polymerase II (Pol II) activity [18, 209]. These marks are essential for CENP-A deposition and kinetochore assembly [18, 176]. Consistent with this open state, Pol II occupancy and α-sat transcription have been detected at core centromeres throughout the cell cycle [32, 139, 142]. Active α-sat HORs also display H3K9me3, a classical repressive mark, highlighting the unique nature of centromeric chromatin [17]. Recent Fiber-seq analysis has confirmed this heterogeneity, revealing interspersed compact nucleosome arrays and accessible intervals [48]. The balance between these states is crucial for centromere stability, because altering this equilibrium can cause centromere loss in human artificial chromosomes [129].

In contrast, pericentromeric chromatin exhibits canonical heterochromatin features, including H3K9me2/3 and HP1 binding, together with DNA methylation [33, 157]. Pericentromeric DNA is heavily methylated, whereas active α-sat HORs display locally reduced CpG methylation, forming a centromere dip region (CDR) that coincides with CENP-A enrichment [9, 158]. These marks compact chromatin and repress transcription. Nonetheless, pericentromeric regions produce low-level transcripts that contribute to heterochromatin maintenance [83].

Together, centromeres exhibit a compartmentalized organization, with the CENP-A-containing core centromere positioned inside the surrounding heterochromatic pericentromere [30]. This separation is important for kinetochore function, but it also creates the chromatin context in which sister chromatid cohesion is established and protected during mitosis. In particular, cohesin enrichment in pericentromeric regions and the specialized organization of centromeric chromatids are important for mitotic centromeric cohesion [154, 166].

1.3. Mitotic centromeric cohesion

Accurate chromosome segregation relies on sister chromatid cohesion, which prevents premature separation of replicated chromatids [179]. Cohesion physically links sister chromatids and counteracts spindle pulling forces, thereby preserving chromosomal integrity until anaphase [130, 144]. Proper cohesion is essential for mitosis, and defects in cohesion establishment, maintenance, or timely release can cause severe developmental abnormalities and embryonic lethality [76]. Notably, cohesion is not uniform along chromosomes but is enriched at centromeres, where it is protected from premature loss by specialized machinery until anaphase [116]. This centromere-specific cohesion allows chromosomes to achieve stable bi-orientation

while withstanding spindle tension [100]. Thus, chromosome architecture, kinetochore function, and sister chromatid cohesion must be tightly coordinated to ensure faithful chromosome segregation.

1.3.1. Cohesin cycle and centromere protection

Sister chromatid cohesion is mediated by the cohesin complex, a multi-subunit ring that can topologically entrap DNA and thereby link sister chromatids from S phase until cohesin is removed or cleaved in mitosis [201]. In humans, cohesin comprises the core subunits SMC1, SMC3, and the α-kleisin subunit RAD21, which together form a ring-like structure (Fig. 2a) [11]. SMC1 and SMC3 are elongated proteins that dimerize through a hinge domain, while their ATPase heads are bridged by RAD21, with the RAD21 N-terminus binding SMC3 and the C-terminus binding SMC1 [69]. RAD21 also interacts with STAG1 or STAG2 and recruits accessory factors, including the loading complex NIPBL-MAU2 and the releasing complex PDS5-WAPL [8, 40].

Cohesin dynamics are tightly regulated across the cell cycle. In human cells, cohesin loading occurs during telophase/early G1 and is mediated by the NIPBL-MAU2 complex, which deposits cohesin onto chromatin [63]. Conversely, RAD21 recruits the PDS5-WAPL complex to promote cohesin release [203]. PDS5-WAPL opens the SMC3-RAD21 interface, resulting in cohesin dissociation [34, 51]. This gives rise to dynamic association of cohesin with chromatin during G1. Stable sister chromatid cohesion is established during S phase, when ESCO1 or ESCO2 acetylates SMC3 [205]. This acetylation inhibits WAPL activity and stabilizes the complex [205]. Sororin provides an additional regulatory layer by binding PDS5 and competing with WAPL, supporting cohesin retention [116, 133].

At mitotic entry, CDK-dependent phosphorylation of Sororin promotes its dissociation from PDS5, allowing WAPL to remove cohesin from chromosome arms [133]. In contrast, centromeric cohesin must be protected from premature WAPL-dependent release to withstand spindle tension until anaphase. This protection is mediated by Shugoshin 1 (SGO1) together with protein phosphatase PP2A [116]. The SGO1-PP2A complex counteracts phosphorylation events that promote cohesin release and helps preserve cohesion-protective factors at centromeres, thereby ensuring correct kinetochore bi-orientation [71, 130]. Recruitment and maintenance of SGO1 at centromeres are controlled by mitotic centromere signaling pathways and histone-based cues that specify the centromeric chromatin [88]. Once all chromosomes are

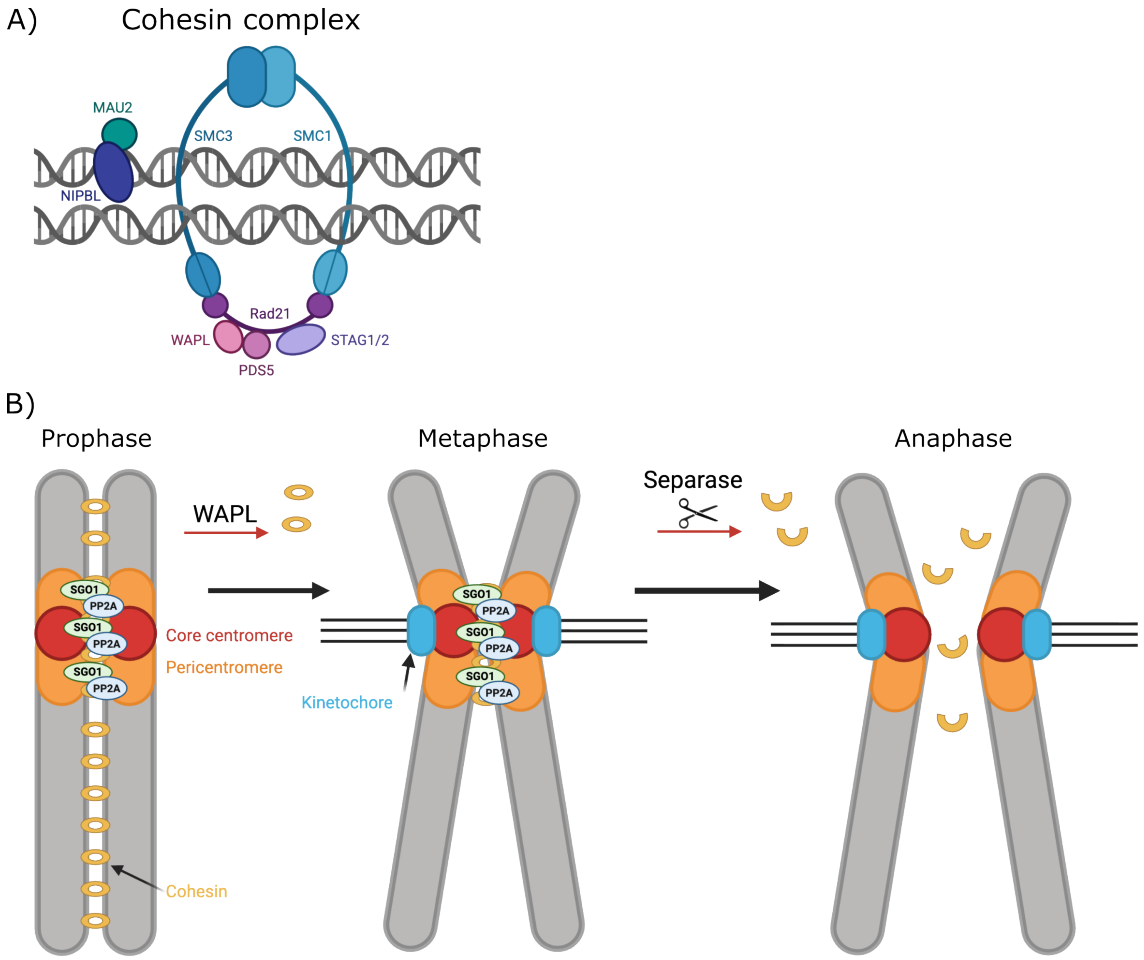


Figure 2.: Cohesin complex maintains sister chromatid cohesion during mitosis. a) Architecture of the cohesin complex. SMC1, SMC3, and RAD21 form a ring-like structure proposed to encircle DNA strands of sister chromatids. STAG1 or STAG2 binds directly to RAD21. Cohesin associates with the loading complex MAU2-NIPBL and the releasing complex PDS5-WAPL. Adapted from [93]. b) Schematic overview of mitosis. Until prophase, cohesin holds sister chromatids together. During prometaphase, WAPL removes cohesin from chromosome arms, whereas centromeric cohesin is protected by Shugoshin 1 (SGO1) and protein phosphatase PP2A. During metaphase, kinetochores assemble and microtubules attach. Once all chromosomes are bi-oriented, Separase cleaves centromeric cohesin, allowing segregation of sister chromatids. Adapted from [68, 170]. Created with BioRender.com.

properly attached and aligned, the anaphase-promoting complex/cyclosome (APC/C) activates Separase, which cleaves RAD21 and triggers sister chromatid separation at anaphase onset [28].

The balance between cohesin loading, establishment, arm removal, and centromere protection is therefore essential for accurate chromosome segregation. Disruption of these processes can cause premature sister chromatid separation, lagging chromosomes, and aneuploidy [28]. Because centromeric cohesion protection depends on

a specialized chromatin environment and its regulatory factors, understanding how centromeres organize and protect cohesin is central to explaining mitotic cohesion control.

1.3.2. Spatial organization of cohesion

Centromeres play a central role in maintaining sister chromatid cohesion during mitosis. In human cells, cohesin localizes predominantly to the pericentromeric region, while it is relatively depleted from the CENP-A-containing core centromere [166]. This spatial separation is thought to allow the core centromere to stretch in response to spindle tension, whereas pericentromeric cohesin provides mechanical resistance and maintains the connection between sister chromatids [63]. A similar arrangement has been described in mouse cells, where pericentromeric chromatin is cohesin-rich, whereas the core centromere contains CENP-A and supports kinetochore function [67].

The heterochromatic nature of pericentromeres, including H3K9me2/3 and HP1 binding, has been implicated in cohesion stabilization and recruitment of cohesion-protective pathways [202]. In yeast, HP1 can directly bind SGO1 and contribute to pericentromeric tethering [6]. In mammals, a direct HP1-SGO1 interaction has not been established, and HP1 depletion does not abolish SGO1 localization in mitosis [86]. Nevertheless, HP1 can still influence centromeric cohesion through additional mechanisms and centromere signaling pathways. It has been linked to factors such as the protein kinase Haspin that contribute to a centromeric environment that supports cohesion retention until anaphase [202].

Although centromeric cohesion clearly depends on pericentromeric heterochromatin, the complete protein landscape linking centromeric chromatin state to cohesion maintenance remains incompletely defined. In addition, recent work in human cells suggests that mitotic transcription can influence centromeric cohesion [39]. Some studies report that ongoing Pol II activity during mitosis contributes to efficient recruitment of SGO1, and that acute inhibition of Pol II specifically during mitosis reduces centromeric cohesion [39, 108]. It has been proposed that transcription may facilitate access of SGO1-PP2A to cohesin at the centromere, thereby supporting its protective function [108]. Conversely, cohesion retention during mitosis appears to support ongoing centromeric transcription [143]. Together, these findings suggest a relationship in which centromeric transcription and cohesion protection influence each other.

1.4. Centromeric transcription and its function

Despite their repetitive nature, centromeres are actively transcribed. Pol II-dependent transcription occurs in diverse organisms, including humans, fruit flies, and yeast, and can be detected in both core and pericentromeric regions [32, 139, 153]. Importantly, centromeric transcription is linked not only to centromere identity and kinetochore function but also to mitotic cohesion, suggesting that transcription contributes to multiple layers of centromere regulation [32, 39, 108, 139]. Transcriptional activity appears to be finely balanced, and both excessive and insufficient transcription can impair CENP-A loading, kinetochore assembly, and overall centromeric function [32].

Low levels of centromeric RNA (cenRNA) and pericentromeric RNA (pericenRNA) are present during interphase and mitosis, although their synthesis fluctuates throughout the cell cycle [32]. In humans, cenRNA production has been reported in mitosis and early G1, coinciding with *de novo* CENP-A assembly [13, 25, 139]. In mice, centromeric repeat transcription is low in G1, peaks in G2/M, and drops again after mitosis [55]. Centromeric transcription has been proposed to serve two main purposes. First, it modulates chromatin accessibility, facilitating CENP-A incorporation and protein binding [209]. Second, it generates (peri)cenRNAs that act directly in centromere regulation by recruiting and stabilizing centromeric proteins [170]. Together, these functions are essential for centromere integrity, faithful chromosome segregation, and cell viability.

Centromere formation and kinetochore assembly

Transcription of core centromeric repeats supports CENP-A nucleosome incorporation across multiple species [32, 36, 37, 103, 135, 153]. Centromeric transcription has been proposed to promote an epigenetic environment that destabilizes H3 nucleosomes and facilitates CENP-A deposition [123]. In *D. melanogaster*, recruitment of CENP-A (CID) by its chaperone CAL1 is reported to be transcription-independent, but Pol II activity enhances nucleosome remodeling that supports efficient CENP-A loading [25]. Moreover, cenRNA knockdown impairs stable CENP-A incorporation, indicating that both transcription and its RNA products can contribute to CENP-A maintenance [153].

A key protein interacting with cenRNA is CENP-C, which contains a DNA-binding domain that has been reported to also bind RNA [47, 196]. In human cells, CENP-C binds single-stranded α-sat transcripts both *in vivo* and *in vitro* [196]. Depletion of

α-sat RNA leads to reduced centromeric CENP-C and loss of additional kinetochore proteins [196]. In *D. melanogaster*, CENP-C binds pericentromeric SATIII RNA, and its depletion reduces SATIII RNA levels [153]. In both species, depletion of centromeric transcripts causes mitotic errors, such as lagging chromosomes and micronuclei formation [32, 153]. Because both CENP-A and CENP-C depend on centromeric transcription or its RNA products, cenRNA has been proposed to act as a molecular scaffold that supports stable protein assembly at centromeres [43].

Another well-characterised RNA-mediated interaction involves the chromosomal passenger complex (CPC), comprising Aurora B, Borealin, Survivin, and INCENP, which regulates chromosome condensation and monitors kinetochore-microtubule attachment [97]. CenRNA can bind the CPC and promote its activation and localization to the centromere [23, 81]. This RNA-dependent CPC recruitment has been reported in humans, mice, and *Xenopus* egg extracts and is required for proper spindle attachment and mitotic progression [23, 55]. Collectively, these findings support the idea that centromeric transcription and cenRNAs contribute to the maintenance of centromere integrity and the promotion of faithful chromosome segregation.

Pericentromeric heterochromatin formation

Although pericentromeric regions are enriched for repressive marks and often described as transcriptionally silent, they generate low levels of RNA that can promote heterochromatin assembly and maintenance [83]. In *S. pombe*, pericenRNA is processed by the RNA interference (RNAi) machinery into small interfering RNAs (siRNAs) that guide the RITS complex to pericentromeric chromatin and initiate transcriptional silencing [84]. Similar RNA-based mechanisms have been proposed in fruit flies, chicken cells, and mouse embryonic stem cells, suggesting that pericentromeric transcription can support heterochromatin formation across species, although the exact mechanisms differ [60, 83, 85, 137, 157]. In mouse cells, the H3K9 methyltransferases SUV39H1 and SUV39H2 were reported to bind pericenRNA, stabilizing their localization, enhancing H3K9 methylation, and promoting heterochromatin formation [84]. These observations link pericentromeric transcription to the establishment and maintenance of repressive chromatin domains that are important for genome stability.

Centromeric transcription misregulation

The multiple functions of centromeric transcription underscore the need for strict control, and misregulation has profound consequences for genome stability. In several cancers, including pancreatic, breast, and prostate cancer, α-sat RNA is overexpressed and correlates with poor patient prognosis [101, 182]. In BRCA1-deficient breast tumors, excessive α-sat RNA induces DNA damage responses and chromosome segregation defects [210]. BRCA1 has been reported to monoubiquitinate histone H2A at centromeres, repressing transcription and maintaining heterochromatin integrity [211]. These findings suggest that loss of repression at satellite repeats can directly contribute to chromosome instability in disease contexts.

In pancreatic cancer, pericenRNAs are strongly upregulated in both humans and mice, likely due to heterochromatin derepression associated with loss of H3K9 methylation and DNA methylation [182]. Proper heterochromatin formation is therefore crucial for limiting aberrant α-sat transcription and maintaining genome stability. Conversely, pericenRNAs can be highly expressed in normal testis tissue but repressed in testicular cancer, indicating that both overexpression and depletion of (peri)cenRNAs can be associated with altered cell states and can disrupt centromere function [54, 70].

Centromeric transcription also responds to cellular stress. Transcription of HSAT3 repeats is strongly induced by heat shock, heavy metals, or ultraviolet radiation [188]. Under these conditions, HSF1 and Pol II form nuclear stress bodies at HSAT3 loci and produce long chromatin-associated RNAs [152, 188]. This stress-induced transcriptional response appears to be conserved across species. In mice, chemical exposure induces short cenRNAs that accumulate at centromeres, and forced accumulation of these transcripts leads to cohesion defects and chromosome missegregation [27]. Similar mechanisms have been reported in insects and *Arabidopsis* [145, 183]. Together, these findings emphasize that centromeric transcription is tightly regulated, responds to developmental and stress signals, and that its misregulation can drive chromosomal instability.

1.4.1. Regulation of centromeric transcription

Despite increasing evidence for the importance of centromeric transcription, the specific transcription regulators that control this process remain incompletely defined and appear to differ between organisms and cell types. In *S. cerevisiae*, Cbf1 and

Ste12 bind core and pericentromeric regions, respectively, and influence transcription; loss of either protein impairs centromeric function [135]. Additionally, protein kinase Rio1 limits cenRNA levels by reducing Pol II accessibility and promoting cenRNA degradation [169]. Its human orthologue RioK1 localizes to kinetochores during mitosis, and RioK1 depletion lowers cenRNA levels and increases chromosome instability, suggesting a conserved link between centromere regulation and genome stability [169].

Chromatin remodelling factors have also been implicated in coupling transcription to centromere maintenance. In *D. melanogaster*, the FACT complex (facilitates chromatin transcription) interacts with the CENP-A chaperone CAL1 and mediates transcription-associated chromatin remodelling that supports CENP-A incorporation [36]. FACT is conserved in chicken and human cells, where it localizes to centromeres and is required for proper CENP-A deposition [32, 136]. This supports the idea that regulated chromatin accessibility is one route to control centromeric transcription and centromere identity.

In mammals, several additional factors have been described, although their mechanisms are not fully resolved. The general transcription elongation factor CTDP1 localizes to centromeres in interphase and mitosis in human and mouse cells [32]. The zinc-finger transcription factor ZFAT binds centromeric regions in human and mouse cells and can modulate (peri)cenRNA levels, with overexpression increasing and depletion reducing (peri)cenRNA transcription [78]. A proposed model suggests that ZFAT recruits the histone acetyltransferase KAT2B, leading to H4K8 acetylation and subsequent recruitment of BRD4 to activate transcription. However, ZFAT induces transcription only at a subset of centromeres, implying additional factors involved in centromere- or chromosome-specific control. ZBTB24 was recently identified as a centromeric transcription factor in mouse embryonic stem cells, where it recruits DNMT3B and contributes to the establishment of DNA methylation at centromeres [65]. Sp1 is another transcription factor reported to localize to centromeres during mitosis [57]. Its degradation causes chromosome missegregation and reduced CPC activity, consistent with a role in maintaining centromere function during mitosis. At the same time, not all factors that accumulate at (peri)centromeres necessarily regulate transcription directly. For example, TEAD1 forms pericentromeric foci in renal carcinoma cells without directly mediating transcription, highlighting that centromere localization alone is not sufficient evidence for transcriptional regulation [59, 106].

Together, these studies suggest that centromeric transcription can be influenced by diverse chromatin- and transcription-related factors, including remodellers, elongation factors, histone acetylation readers and writers, and DNA methylation machinery. However, the overall regulatory network remains poorly studied, and many centromere-associated regulators are likely still missing. This gap can be partly explained by the repetitive nature of centromeric DNA, which has historically limited genome-wide approaches for identifying and mapping centromeric proteins.

1.5. Identifying centromere-associated proteins

1.5.1. Challenges and recent advances in centromere mapping

High-throughput next-generation sequencing (NGS) technologies have revolutionized genomic research by enabling large-scale analysis of animal, plant, and human genomes [181, 195]. Methods such as ChIP-seq or RNA-seq have greatly advanced our understanding of gene regulation, transcription factor binding, and chromatin structure [10, 124, 140]. Despite this progress, centromeres long remained difficult to study by genomic approaches because their DNA consists of megabase-sized arrays of highly repetitive sequences [42, 134]. This repetitive architecture creates a major mapping problem, as many sequencing reads align equally well to multiple locations (multi-mapping), making locus-specific assignment difficult [122, 141].

Widely used short-read platforms such as Illumina generate reads up to 150 bp, which is shorter than a single α-sat monomer and far shorter than an α-sat HOR unit [16]. As a result, reads originating from centromeres often cannot be uniquely aligned, and standard analysis pipelines frequently discard repetitive reads [122]. Early human genome assemblies, such as GRCh37 (hg19), therefore excluded centromeric regions entirely, preventing genome-wide profiling of centromeric chromatin [186].

The GRCh38 (hg38) human genome assembly improved centromeric representation by closing multiple sequence gaps present in earlier assemblies and introducing reference models - simulated centromere arrays [164]. Although these model centromeres did not provide complete base pair-resolved sequence continuity for each centromere, they enabled more informative mapping of repetitive reads and accelerated centromere-focused analyses compared to hg19 [9]. However, even with hg38, genomic

profiling of centromeres remained technically challenging, and centromeric chromatin features often stayed poorly resolved because many pipelines continued to filter out repetitive reads or could not align them confidently [122].

In 2022, the Telomere-to-Telomere (T2T) consortium released the first complete human genome assembly, T2T-CHM13 (hs1), which substantially changed centromere research [9, 134]. The hs1 assembly provided base pair-resolved sequences of all human centromeres, enabling precise read mapping and systematic characterization of centromeric DNA and chromatin. This breakthrough opened new possibilities for identifying previously uncharacterised centromeric proteins and chromatin features, and for integrating centromeres into genome-wide analyses rather than treating them as unmappable regions [44, 59, 166]. At the same time, the increasing volume of public ChIP-seq datasets creates an opportunity to mine existing data for centromeric enrichment patterns at scale.

1.5.2. REDPOINT as a tool to systematically investigate public ChIP-seq data

The widespread availability and reduced costs of NGS have generated an enormous amount of publicly accessible data, archived in large-scale repositories such as the Sequence Read Archive (SRA) and Gene Expression Omnibus (GEO) [14, 87]. By 2024, the SRA contained more than 34.7 million entries of raw high-throughput sequencing data, spanning diverse species and experimental approaches [160]. This created an opportunity to systematically reuse existing sequencing datasets to ask locus-specific questions without generating new data [44].

Building on this resource, Dr. Samuel Corless and colleagues developed a bioinformatics approach termed REDPOINT (Reanalysis of Every Dataset at Position of INTerest) [44]. REDPOINT is designed to systematically reanalyse publicly available human ChIP-seq datasets and identify proteins that are enriched at a locus of interest. In their study, 40,733 ChIP-seq datasets covering more than 1,200 proteins and post-translational modifications were screened for enrichment at centromeric DNA (Fig. 3a). Each dataset was aligned to hg38 and a custom centromeric repeat assembly based on hg38, enabling centromere-focused read assignment. Enrichment was quantified as the ratio of the percentage of centromeric reads in the ChIP sample to that in the matched input control.

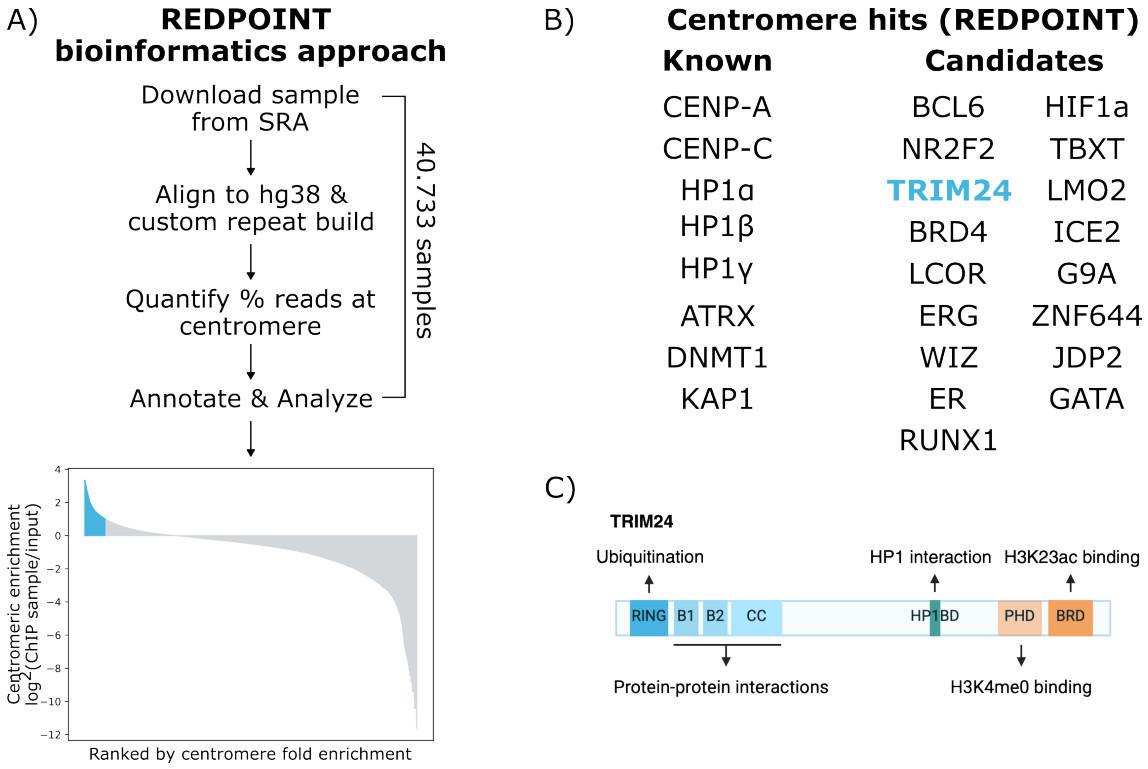


Figure 3.: REDPOINT bioinformatics approach identifies centromeric proteins. a) Summary of the REDPOINT workflow for centromeric loci. A total of 40,733 human ChIP-seq samples were retrieved from the Sequence Read Archive (SRA), aligned to hg38 and a custom centromeric repeat build, and their centromeric enrichment was calculated. Out of all samples analysed, 307 showed significant enrichment (indicated in blue). b) Selected high-confidence centromeric proteins identified with REDPOINT, including known centromeric proteins and newly identified candidates. Among the latter, REDPOINT identified TRIM24 (blue). Adapted from [44]. c) Schematic representation of TRIM24 domain composition, including the N-terminal tripartite motif (RING, B-boxes, coiled-coil), and the C-terminal HP1 binding domain (HP1BD), plant homeodomain (PHD), and bromodomain (BRD). Binding partners and functions of individual domains (RING - ubiquitination; B-boxes and coiled-coil (BBCC) - protein-protein interactions; HP1BD - HP1 binding; PHD - H3K4me0 binding; BRD - H3K23ac binding) are indicated. Adapted from [12]. Created with BioRender.com.

Using this strategy, REDPOINT successfully identified known centromeric proteins and marks, including CENP-A, CENP-C, and HP1 proteins (Fig. 3b) [43]. REDPOINT also identified proteins with strong centromeric enrichment that, at the time of the analysis, had not been characterised as centromere-associated. Recent studies have shown that several of these proteins, including BRD4, G9A, ZNF644, and WIZ, are associated with centromeric or pericentromeric chromatin, indicating that the REDPOINT screen can successfully identify biologically relevant centromeric-associated candidates [44, 78, 193]. Among the proteins with robust centromeric enrichment and largely unexplored centromeric function was TRIM24, a chromatin-associated transcriptional regulator and E3 ubiquitin ligase, which motivated its further investigation in this thesis.

1.6. TRIM24: a chromatin reader and E3 ubiquitin ligase

Tripartite motif-containing protein 24 (TRIM24) belongs to the TRIM family, which is characterised by a conserved N-terminal RING-B-box-coiled-coil (RBCC) motif and a variable C-terminal region [120]. In humans, TRIM proteins form a large protein family and are classified into 11 subgroups based on the variable C-terminal domains [72]. TRIM24 is part of subgroup VI together with TRIM28 (KAP1) and TRIM33, which share a C-terminal PHD-bromodomain tandem [45]. Notably, TRIM28 is a chromatin co-repressor that localizes to centromeric heterochromatin and recruits HP1 to silence repetitive DNA and maintain genomic stability, suggesting that this TRIM subgroup can have functions at centromeric regions [117].

Initially identified as transcriptional intermediary factor 1α (TIF1α), TRIM24 functions as a chromatin-associated transcription regulator and E3 ubiquitin ligase [184]. The C-terminal region contains an HP1-binding sequence (HP1BD), a plant homeodomain (PHD), and a bromodomain (BRD) (Fig. 3c) [150, 184]. The RING domain confers E3 ubiquitin ligase activity and enables TRIM24 to ubiquitinate substrates, including the tumor suppressor p53, and to autoubiquitinate itself [79, 191]. The B-boxes and coiled-coil region mediate homo- and heterodimerization and broader protein-protein interactions [184]. HP1BD facilitates interaction with heterochromatin protein 1 (HP1) [132].

Through its tandem PHD-BRD domains, TRIM24 recognizes two histone modifications on the same histone H3 tail. The PHD domain binds unmodified H3K4 (H3K4me0), whereas the BRD recognizes acetylated H3K23 (H3K23ac) [184]. This dual recognition anchors TRIM24 to chromatin and enables recruitment of additional factors, allowing TRIM24 to act as a transcriptional co-activator or co-repressor depending on the context [184].

Consistent with its molecular properties, TRIM24 has been implicated in diverse cellular processes, including transcriptional regulation, cell identity control, and genome stability pathways [7, 90, 184]. In cancer-related contexts, TRIM24 can act as a transcriptional co-regulator of nuclear hormone receptors. For example, in breast cancer, TRIM24 binds chromatin and the estrogen receptor and co-activates estrogen-dependent genes associated with proliferation [184]. In colorectal cancer, TRIM24 chromatin occupancy correlates with enhanced cell growth [197]. Conversely, TRIM24 can act as a co-repressor of the retinoic acid receptor and has been described

as a liver-specific tumor suppressor, illustrating that TRIM24 can support different transcriptional outcomes depending on cellular state and signaling context [89]. In embryonic stem cells, TRIM24 interacts with pluripotency factors OCT4, SOX2, and NANOG to repress developmental genes and prevent premature differentiation [147]. Together, these studies highlight TRIM24 as a context-dependent transcriptional regulator that couples chromatin binding to functional gene control.

TRIM24 also links chromatin regulation to genome stability mechanisms. Tumor suppressor p53 is a master regulator of genome stability, cell cycle control, and differentiation [26]. TRIM24 functions as an E3 ubiquitin ligase for p53, promoting its proteasomal degradation [7]. In embryonic stem cells, TRIM24 binding to p53 has been reported to prevent differentiation [80]. In addition, p53 can act as a pioneer factor that engages closed chromatin during stress responses, and TRIM24 has been proposed to support this process by simultaneously engaging p53 and H3K4me0-marked nucleosomes in closed chromatin [77]. Beyond p53 regulation, TRIM24 localizes to sites of DNA damage, and its depletion impairs homologous recombination repair [64, 90]. TRIM24 has also been implicated in regulating the termination of DNA damage responses through ubiquitination of p53 [192]. These observations position TRIM24 at the interface of chromatin control, stress responses, and genome maintenance.

In summary, TRIM24 integrates chromatin binding via its PHD-BRD reader domains with E3 ubiquitin ligase activity and its capacity for protein interactions, enabling it to modulate transcriptional programs and genome stability. Despite extensive investigation of TRIM24 in transcription and disease-related pathways, its potential role in mitosis and centromeric regulation remains largely unexplored. TRIM24 was identified as a candidate centromere-associated protein in the REDPOINT reanalysis of public ChIP-seq datasets [44]. Supporting a centromeric association, APEX2 proximity labelling in mouse cells detected TRIM24 near pericentromeric DNA [113]. Moreover, TurboID-based assays in human cells identified TRIM24 close to cohesin complex components RAD21, STAG2, and WAPL, suggesting a potential association with the cohesin machinery [90]. Considering that pericentromeres are key sites of mitotic cohesion protection and that TRIM24 combines chromatin reader function with transcription-regulatory and ubiquitin ligase activities, these observations raise the possibility that TRIM24 contributes to centromere function by influencing chromatin organization and centromeric transcription and, ultimately, by regulating centromeric cohesion.

1.7. Aim of the thesis

Centromeric cohesion must be maintained until anaphase to ensure faithful chromosome segregation. While centromeric transcription has been linked to cohesion protection during mitosis, the proteins and mechanisms involved remain incompletely understood. TRIM24 emerged as a candidate centromere-associated protein in human cells from the REDPOINT reanalysis of public ChIP-seq datasets, and independent proximity labelling studies placed it near cohesin components. Together with its established chromatin-binding and E3 ubiquitin ligase activities, these observations suggested that TRIM24 could contribute to cohesion regulation at centromeres. I therefore hypothesized that TRIM24 contributes to centromeric cohesion, potentially by associating with cohesin or by influencing centromeric chromatin and transcription.

To test this hypothesis, I pursued three specific aims. First, I aimed to determine whether TRIM24 localizes to centromeres in human cells and which domains contribute to this localization. Second, I aimed to examine how TRIM24 perturbations affect centromeric cohesion during mitosis and whether TRIM24 associates with the cohesin subunit RAD21. Finally, I aimed to explore whether TRIM24 influences transcription of centromeric α-satellite repeats as a potential mechanism linking TRIM24 to cohesion maintenance.

2. Results

2.1. TRIM24 localizes to centromeres

2.1.1. ChIP-seq shows enrichment of TRIM24 at centromeres in a cell type-specific manner

TRIM24 was identified as a centromeric protein candidate using the REDPOINT approach [44]. To assess the relative enrichment of TRIM24 at centromeres compared to other novel centromeric candidate proteins reported by Corless et al. [44], I reanalysed the dataset provided in that study. Briefly, I extracted centromeric alignment percentages from each ChIP-seq sample and the corresponding input datasets and subsequently calculated the fold enrichment of each sample over its input. The results were filtered for known and newly identified centromeric proteins, and the enriched novel centromeric candidates were visualized (Fig. 4a).

The REDPOINT analysis in Corless et al. [44] included a single ChIP-seq experiment for TRIM24 in LNCaP prostate cancer cells, consisting of two ChIP-seq samples, either DHT-treated or untreated (accession numbers are provided in Tab. 19). Reanalysis of the first dataset (LNCaP treated with DHT) revealed a centromeric enrichment of 4.16, representing the highest enrichment among all centromeric candidate proteins in the REDPOINT dataset (Fig. 4a). The second dataset (untreated LNCaP) showed a centromeric enrichment of 2.68, placing it among the top 30 REDPOINT datasets for centromere-associated candidate proteins. Collectively, these results suggest that TRIM24 is a promising candidate centromeric protein with previously uncharacterised centromeric localization.

Because the REDPOINT analysis in Corless et al. [44] included only one ChIP-seq experiment in LNCaP prostate cancer cells, I sought to determine whether TRIM24 centromeric enrichment was conserved across multiple cell types or restricted to LNCaP. I identified additional publicly available ChIP-seq datasets and performed REDPOINT analysis on five other cell lines representing distinct tissue origins and

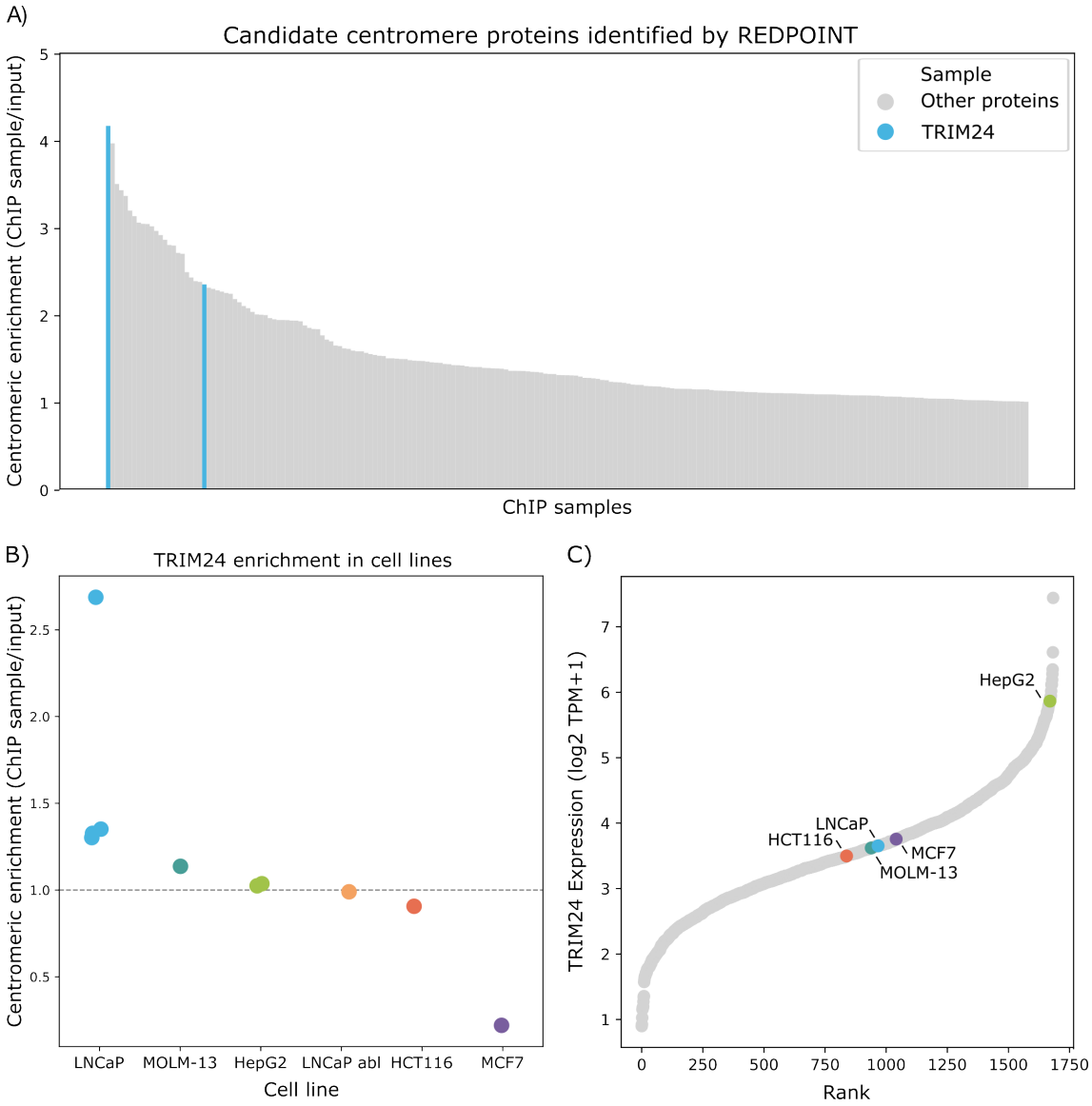


Figure 4.: REDPOINT analysis reveals TRIM24 enrichment at centromeres. a) Centromeric enrichment scores for centromere-associated candidate proteins identified by REDPOINT analysis, based on the dataset from Corless et al. [44]. Proteins were filtered to retain only novel candidates with enrichment > 1. TRIM24 is highlighted in blue, and other candidates in grey. Enrichment scores were calculated by aligning each ChIP-seq dataset to a custom centromeric repeat assembly, dividing by the total number of reads mapped to the hg38 reference genome, and normalizing to the corresponding input control. A total of 212 ChIP-seq samples are shown. b) Centromeric enrichment of TRIM24 across six cell lines (MCF7, MOLM-13, LNCaP, LNCaP abl, HepG2, and HCT116) calculated by REDPOINT using the same approach as in a). Values are presented as sample/input ratios. c) TRIM24 mRNA expression levels in cancer cell lines obtained from the DepMap (Cancer Dependency Map, DepMap Public 25Q2) database. Expression values are shown as $\log_2(\text{TPM}+1)$. Cell lines analysed in b) are highlighted (LNCaP abl not available in DepMap). For accession numbers, see Tab. 19. For details, see Materials and Methods.

cancer types: MCF7 (breast cancer), MOLM-13 (acute myeloid leukemia), HepG2 (hepatocellular carcinoma), HCT116 (colorectal carcinoma), as well as LNCaP abl

(castration-resistant prostate cancer). In addition, a newly published ChIP-seq dataset for the LNCaP cell line (hereafter referred to as "LNCaP 2" to distinguish it from the previous dataset) was included in the analysis.

REDPOINT analysis revealed clear differences in centromeric enrichment across cell types (Fig. 4b). Only three out of six cell lines displayed centromeric enrichment: LNCaP (2.68, 1.3, 1.35, 1.33), HepG2 (1.02, 1.04), and MOLM-13 (1.13), whereas LNCaP abl (0.99), HCT116 (0.91), and MCF7 (0.22) showed centromeric depletion. These findings suggest a degree of cell type specificity of TRIM24 centromeric enrichment. This raises the question of whether centromeric enrichment correlates with TRIM24 expression levels in each cell line. To investigate this, I utilized the DepMap (Cancer Dependency Map, DepMap Public 25Q2 [185]) database to retrieve TRIM24 expression data for cancer cell lines. LNCaP abl is not listed as a separate cell line in DepMap and was therefore not included in expression comparison. Expression values ($\log_2$(TPM+1)) were ranked, and the cell lines used in REDPOINT were highlighted (Fig. 4c). The comparison showed that differences in TRIM24 centromeric enrichment cannot be explained solely by variations in TRIM24 expression between cell lines, suggesting the involvement of additional mechanisms regulating its centromeric localization. Collectively, these results indicate that TRIM24 enrichment at the centromere is cell type specific and not exclusive to LNCaP prostate cancer cells.

REDPOINT analysis revealed enrichment of TRIM24 at centromeric loci in multiple cell lines. However, the REDPOINT approach aligns ChIP-seq samples to a custom build of human centromeric repetitive loci and calculates the number of aligned reads relative to whole-genome alignment, without distinguishing between different repeat families [44]. In addition, this method is based on an outdated human genome build, hg38, which lacks complete annotations of all centromeric repeats [134].

In 2022, the telomere-to-telomere human genome assembly was introduced, providing fully assembled centromeres with comprehensive annotation of centromeric and pericentromeric repeats on all chromosomes [9]. Given this advancement, I sought to determine whether the REDPOINT results could be validated by re-aligning ChIP-seq data to the new genome. To validate TRIM24 enrichment at centromeres, I re-aligned the TRIM24 LNCaP ChIP-seq dataset to T2T-CHM13v2.0 (hs1) using BWA MEM [104]. The resulting BAM files were sorted and indexed with bedtools, and normalized bedgraph files were generated using deeptools by comparing ChIP-seq

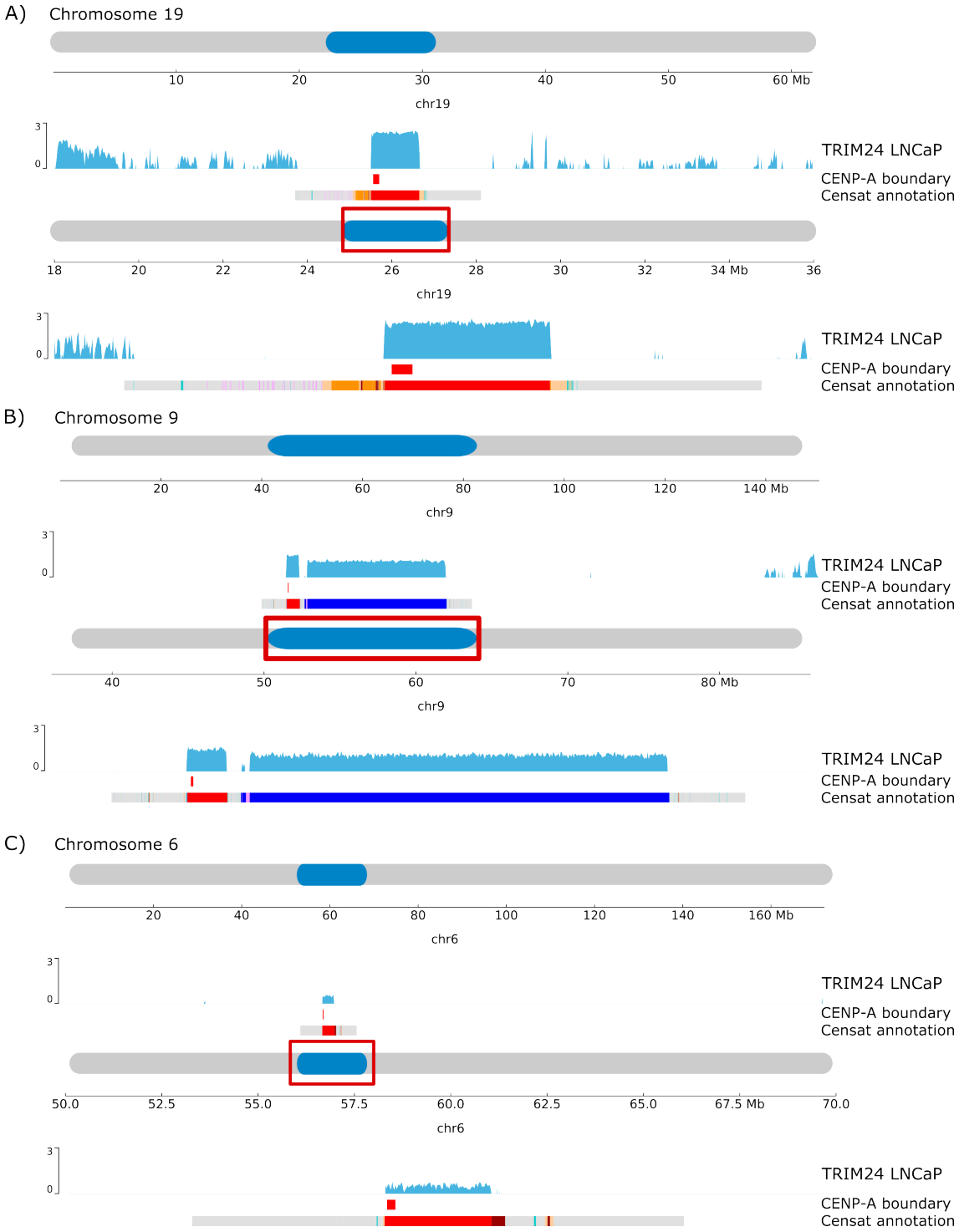


Figure 5.: TRIM24 is enriched at the α-satellite higher-order repeats. Publicly available LNCaP TRIM24 ChIP-seq dataset aligned to the telomere-to-telomere (T2T-CHM13v2.0) genome assembly. Genome tracks are shown for a) chromosome 19, b) chromosome 9, and c) chromosome 6, with a close-up of the centromeric regions. Signal tracks show $\log_2$(ChIP/input) enrichment. CENP-A boundaries are indicated. Centromeric repeat classes are annotated as follows: red - active α-satellite (α-sat) higher-order repeats (HOR), orange - inactive α-sat HOR, dark red - divergent α-sat HOR, yellow - monomeric α-sat, light green - HSAT1A, dark green - HSAT1B, light blue - HSAT2, blue - HSAT3, pink - β-satellite, purple - γ-satellite, teal - other centromeric repeats (censat), grey - centromeric transition regions. For accession numbers, see Tab. 19. For details, see Materials and Methods.

samples to their respective inputs ($\log_2$ ratio), applying a FLAG value of 2308 to remove unmapped, duplicated, and failed QC reads. Bedgraphs were visualized using pyGenomeTracks.

Alignment of the TRIM24 ChIP-seq dataset obtained from LNCaP cells revealed distinct peaks at centromeric regions that exceeded the size of other peaks visible on the chromosomes (Fig. 5). TRIM24 enrichment at telomeric regions was also detected, as expected [90]. Notably, TRIM24 enrichment varied between different chromosomes. For example, chromosome 19 displayed strong enrichment at active α-sat HORs, but not at other centromeric repeat types (Fig. 5a). In contrast, chromosomes with large HSAT repeat arrays, such as chromosome 9, exhibited enrichment at both α-sat HOR and HSAT elements (Fig. 5b). Some chromosomes, such as chromosome 6, showed relatively low centromeric signal (Fig. 5c), although the signal was still clearly higher than on the chromosome arms. These findings confirm the results of the REDPOINT analysis and indicate that TRIM24 is enriched at centromeric repeats.

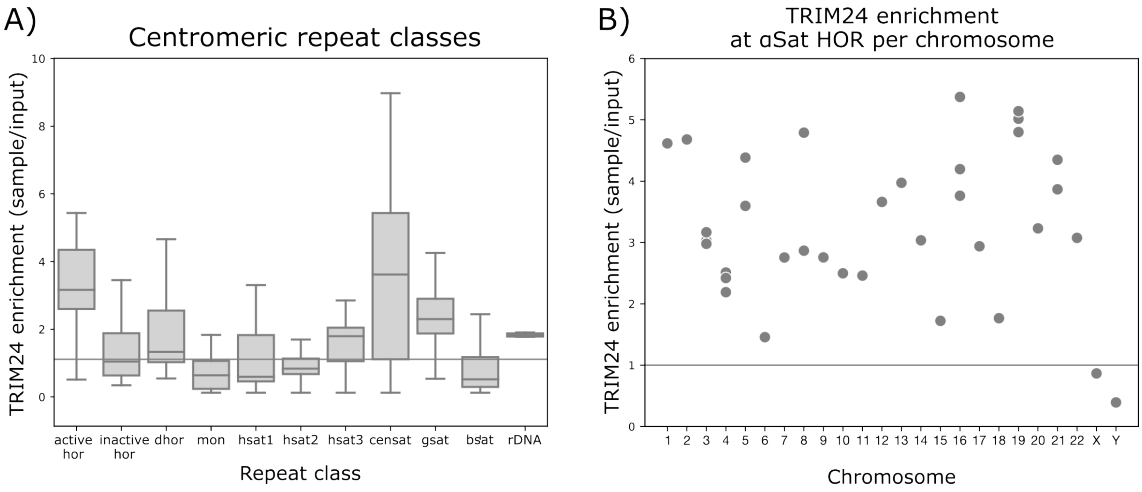


Figure 6.: TRIM24 enrichment differs between centromeric repeat classes. a) TRIM24 enrichment at the centromeric repeat classes in the LNCaP TRIM24 ChIP-seq dataset. For each repeat, the number of reads aligned to that repeat was divided by the total number of reads aligned to the T2T-CHM13v2.0 genome assembly and normalized to the corresponding input control. The boxplot shows the distribution of enrichment values within each repeat class, shown as minimum, first quartile, median, third quartile, and maximum. For accession numbers, see Tab. 19. Centromeric repeat classes are annotated as follows: active hor - active α-satellite (α-sat) higher-order repeats (HOR), inactive hor - inactive α-sat HOR, dhor - divergent α-sat HOR, mon - monomeric α-sat, hsat1 - HSAT1A/B, hsat2 - HSAT2, hsat3 - HSAT3, bsat - β-satellite, gsat - γ-satellite, censat - other centromeric repeats, rDNA - ribosomal DNA. b) TRIM24 enrichment at active α-sat HOR visualized per chromosome. Enrichment values were calculated as in a). For details, see Materials and Methods.

The observed variation in TRIM24 enrichment across centromeric repeats raises the question of whether TRIM24 localizes to a specific class of repeats. To address this, I intersected the aligned ChIP-seq dataset from LNCaP cells with the cen-

sat_hs1.bed file from the T2T genome assembly, which contains all centromeric repeats, using bedtools intersect [134]. For each repeat, the number of reads aligned to the censat_hs1.bed file was divided by the total number of reads aligned to the T2T genome and normalized to the corresponding input. The resulting values were grouped by repeat class and visualized.

While the ChIP-seq track alignments revealed prominent TRIM24 peaks at active α-sat HORs and HSATs, analysis of TRIM24 enrichment across centromeric repeat classes in LNCaP cells revealed a broader association with multiple centromeric satellite classes (Fig. 6a). This preference includes active α-sat HORs, inactive α-sat HORs, divergent HORs, HSAT1, HSAT3, γ-satellites, and other centromeric satellites, with mean fold enrichments of 3.27±1.22, 1.32±1.08, 1.81±1.33, 1.06±1.05, 1.46±0.71, 2.45±1.72, and 3.45±2.64, respectively. Here, active α-sat HORs correspond to core centromeric arrays, whereas inactive α-sat HORs, divergent HORs, HSATs, γ-satellites, and other centromeric satellites are typically associated with flanking pericentromeric arrays. By contrast, monomeric α-sat, HSAT2, and β-satellites showed low enrichment (mean fold enrichments of 0.77±0.70, 0.79±0.48, and 0.90±1.16, respectively), indicating relative depletion of TRIM24 at these repeats and an uneven distribution of TRIM24 across centromeric regions. Notably, TRIM24 was consistently enriched across all rDNA repeats (mean fold enrichment of 1.73±0.06). The difference between the ChIP-seq track alignments and TRIM24 enrichment across centromeric repeat classes can be explained by the different levels of resolution, with peak detection identifying localized enrichment and repeat-class analysis capturing broader centromeric association. Strikingly, TRIM24 showed systematic enrichment at active α-sat HORs across all autosomes (Fig. 6b). Taken together, these results indicate that TRIM24 shows repeat class-specific enrichment within core centromeric and pericentromeric arrays.

2.1.2. TRIM24 shows cell type-specific enrichment at centromeric and pericentromeric satellites

Alignment of the LNCaP ChIP-seq dataset to the T2T genome assembly revealed pronounced TRIM24 enrichment over centromeric repeats, consistent with the observations from REDPOINT analysis. However, TRIM24 enrichment measured by REDPOINT varied across multiple cell lines, raising the question of whether enrichment at these repeats represents a conserved feature. To address this, I aligned

all seven ChIP-seq datasets (MCF7, MOLM-13, LNCaP, LNCaP 2, HCT116, HepG2, and LNCaP abl) to the T2T genome assembly as described in the previous section and visualized the tracks as $\log_2$(ChIP/input) ratios (Fig. 7, Sup. Fig. S1, S2). Detailed inspection of chromosome 19 (Fig. 7) revealed differences in the overall TRIM24 distribution across cell lines.

First, the recently published LNCaP ChIP-seq dataset (LNCaP 2) exhibited lower centromeric enrichment and an altered distribution pattern compared to the previous LNCaP ChIP-seq dataset. Centromeric peaks were approximately threefold lower, with enrichment spanning active α-sat HORs as well as flanking repeats. Nevertheless, centromeric peaks remained higher than other peaks observed on the chromosome arms. MOLM-13 and HepG2, both displaying REDPOINT enrichment values greater than 1, showed clear centromeric peaks with a distribution similar to LNCaP 2. TRIM24 signals covered active α-sat HORs and adjacent HSAT and other centromeric repeats, while also displaying comparatively high peaks on the chromosome arms. HCT116 and MCF7, with REDPOINT enrichment values below 1, showed little to no centromeric signal. Notably, LNCaP abl, with a REDPOINT enrichment value of 0.99, demonstrated detectable centromeric localization, although less pronounced than in LNCaP. This suggests that REDPOINT, which relies on the hg38 genome assembly, may not account for all centromeric repeats.

Overall, these findings confirm that TRIM24 associates with centromeric and pericentromeric satellite repeats in several cell lines, but the strength and shape of this enrichment differ between cell types. Notably, the cell lines showing centromeric enrichment do not share any obvious common features based on simple cell-line metadata, suggesting that the variability in TRIM24 localization is context-dependent.

Alignment of TRIM24 ChIP-seq datasets showed centromeric enrichment of TRIM24 in a subset of cell lines. This raised the question of whether enrichment at specific repeat classes is conserved across cell lines or varies in a cell type-dependent manner. To compare repeat-class enrichment profiles between cell lines, I calculated repeat-level enrichment. For each repeat, the number of reads overlapping the censat_hs1.bed intervals was divided by the total number of reads aligned to the T2T genome and normalized to the corresponding input. For each centromeric repeat class and cell line, the mean TRIM24 fold enrichment was calculated, and all mean enrichments were visualized as a boxplot (Fig. 8).

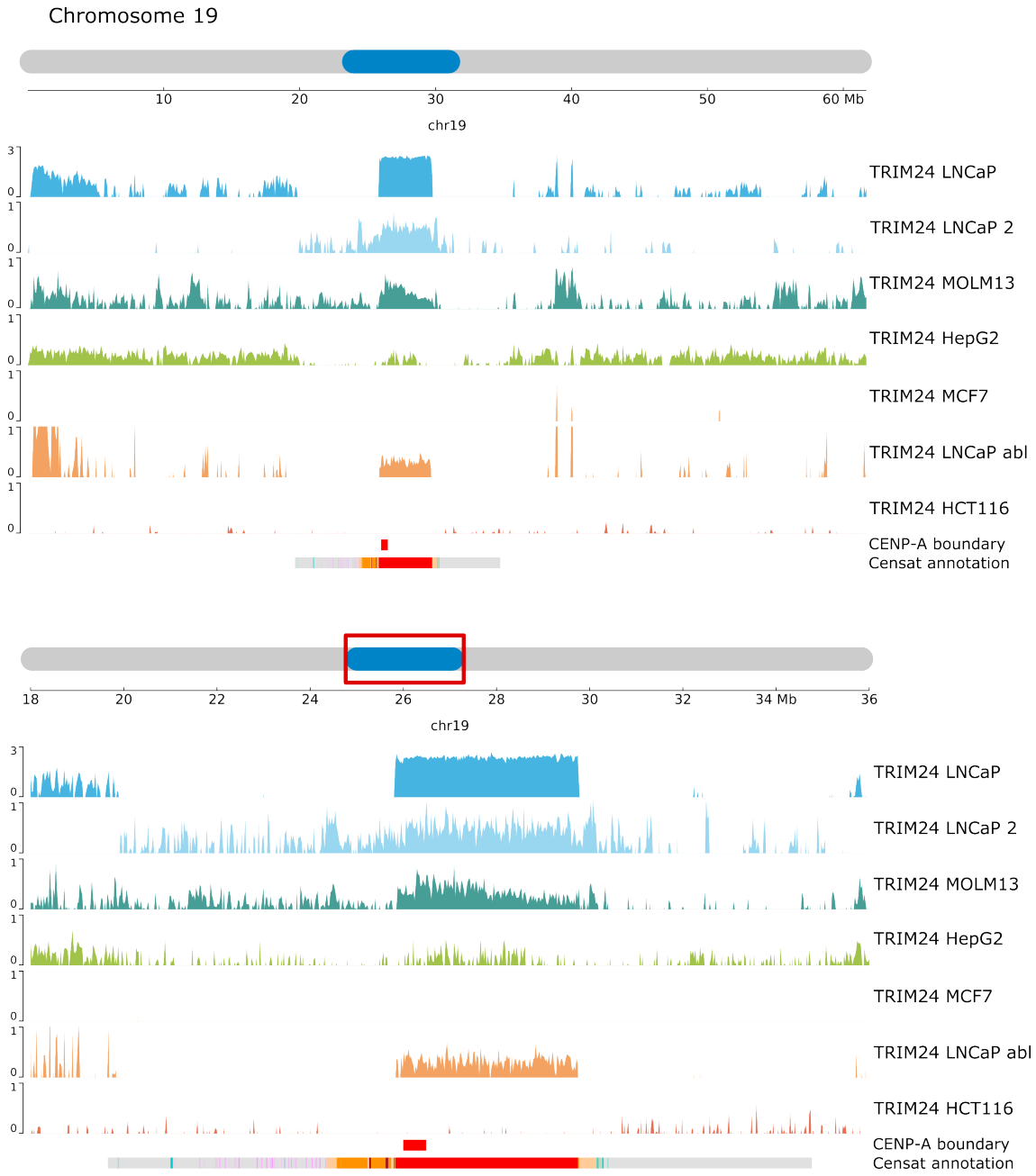


Figure 7.: TRIM24 enrichment at centromeres is cell type-dependent. Publicly available TRIM24 ChIP-seq datasets from six cell lines (LNCaP, MOLM-13, HepG2, MCF7, LNCaP abl, and HCT116) aligned to the telomere-to-telomere (T2T-CHM13v2.0) genome assembly. Genome tracks show TRIM24 signal on chromosome 19 and a close-up of the centromeric region. Signal tracks show $\log_2$(ChIP/input). Note the different y-axis for the first LNCaP track. CENP-A boundaries are indicated. Centromeric repeat classes are annotated as follows: red - active α-satellite (α-sat) higher-order repeats (HOR), orange - inactive α-sat HOR, dark red - divergent α-sat HOR, yellow - monomeric α-sat, light green - HSAT1A, dark green - HSAT1B, light blue - HSAT2, blue - HSAT3, pink - β-satellite, purple - γ-satellite, teal - other centromeric repeats (censat), grey - centromeric transition regions. For accession numbers, see Tab. 19. For details, see Materials and Methods.

Cell lines with positive REDPOINT scores (LNCaP, MOLM-13, HepG2) displayed consistent enrichment (mean fold enrichment > 1) at active and inactive α-sat HORs, divergent HORs, and HSAT3 repeats. In contrast, cell lines with RED-

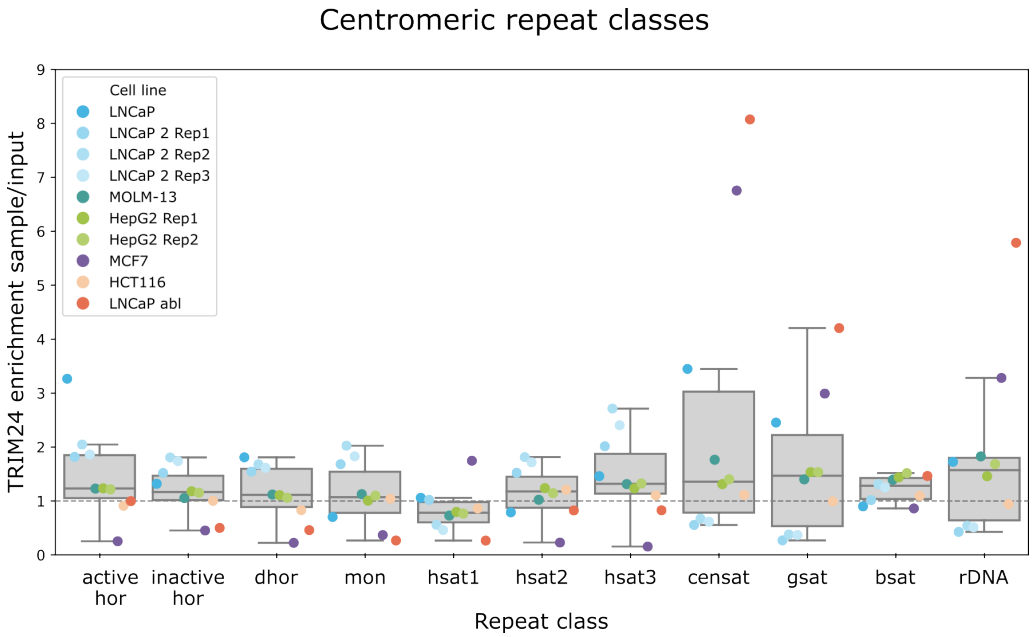


Figure 8.: TRIM24 enrichment at centromeric repeat classes varies across cell lines. Mean enrichment of TRIM24 at centromeric repeat classes for six cell lines (LNCaP, MOLM-13, HepG2, MCF7, HCT116, and LNCaP abl). For each dataset and repeat class, the number of reads aligned to that repeat class was divided by the total number of reads aligned to the T2T-CHM13v2.0 genome assembly and normalized to the corresponding input control. Mean enrichment was then calculated per repeat class for each dataset. The boxplot shows the distribution of these mean enrichment values across cell lines for each repeat class, shown as minimum, first quartile, median, third quartile, and maximum. Centromeric repeat classes are annotated as follows: active hor - active α-satellite (α-sat) higher-order repeats (HOR), inactive hor - inactive α-sat HOR, dhor - divergent α-sat HOR, mon - monomeric α-sat, hsat1 - HSAT1A/B, hsat2 - HSAT2, hsat3 - HSAT3, bsat - β-satellite, gsat - γ-satellite, censat - other centromeric repeats, rDNA - ribosomal DNA. For accession numbers, see Tab. 19. For details, see Materials and Methods.

POINT enrichment values below 1 (MCF7, HCT116, LNCaP abl) showed little or no enrichment at these repeat classes. For other repeat classes, such as monomeric α-sat, HSAT1, HSAT2, and γ-satellites, enrichment in cell lines with positive REDPOINT scores was not uniform, suggesting cell type-specific differences. Additionally, REDPOINT-positive cell lines exhibited enrichment at active α-sat HORs across most chromosomes, whereas REDPOINT-negative datasets were depleted (Sup. Fig. S4).

Interestingly, the LNCaP and LNCaP 2 datasets differed in their TRIM24 enrichment profiles. The earlier LNCaP ChIP-seq dataset showed higher enrichment at active α-sat HORs (mean fold enrichment of 3.27 and 1.91 for LNCaP and LNCaP 2, respectively), divergent HORs (1.81 and 1.61), HSAT1 (1.06 and 0.68), γ-satellites (2.45 and 0.34), rDNA (1.72 and 0.49), and other centromeric repeats (3.45 and 0.62). Conversely, LNCaP showed lower enrichment at other repeats such as inactive α-sat HORs (1.32 and 1.69), monomeric α-sat (0.70 and 1.74), HSAT2 (0.79 and 1.68), HSAT3 (1.46 and 2.38), and β-satellites (0.90 and 1.19). The distribution in LNCaP 2 was more consistent with that observed in the other REDPOINT-positive cell

lines. The two LNCaP TRIM24 ChIP-seq datasets differ in experimental conditions (for example in the antibody used, protocol, and sequencing depth), which may contribute to the observed differences in repeat-class enrichment (Sup. Tab. S3). Taken together, these data indicate that TRIM24 is enriched at centromeric and pericentromeric repeats, with particularly robust signals at α-sat HORs and HSAT3 in several cell types, and that the enrichment pattern differs across cell types.

In summary, analysis of publicly available ChIP-seq datasets reveals a previously uncharacterised localization of TRIM24 to centromeres, detectable in multiple cell lines. Across datasets with positive REDPOINT enrichment, TRIM24 displays a broadly similar repeat-class enrichment signature, with recurring enrichment at α-sat HORs and HSAT3, while the magnitude and distribution of this enrichment vary between cell lines.

2.1.3. Immunofluorescence supports centromeric localization of TRIM24 in interphase and mitosis

REDPOINT analysis and alignment of publicly available ChIP-seq datasets suggested centromeric localization of TRIM24. To investigate whether this enrichment can be observed *in situ*, I performed indirect immunofluorescence staining of HEK293T cells for TRIM24 and the centromeric mark CENP-A. TRIM24 was detected in small nuclear foci distributed throughout the nucleus, excluding the nucleolus (Fig. 9a). Closer inspection of the CENP-A signal revealed that TRIM24 was positioned adjacent to one or both sides of CENP-A foci, indicating centromeric association.

To test this, I performed colocalization analysis using CellProfiler [172]. Briefly, the nucleus was masked, and TRIM24 and CENP-A foci were segmented. Colocalization was scored when TRIM24 overlapped with or directly contacted the CENP-A signal, and the percentages of CENP-A foci and TRIM24 foci that colocalized were calculated per cell. On average, 77% of CENP-A foci overlapped with or directly contacted TRIM24 (Fig. 9c), indicating that TRIM24 is present at most centromeres. In contrast, only 2.6% of TRIM24 foci overlapped with CENP-A (Fig. 9d), consistent with TRIM24 forming many additional non-centromeric foci throughout the nucleus and only a small TRIM24 subpopulation being centromere-associated. Together, these results indicate that TRIM24 is present at most centromeres in interphase, while the majority of TRIM24 foci are non-centromeric.

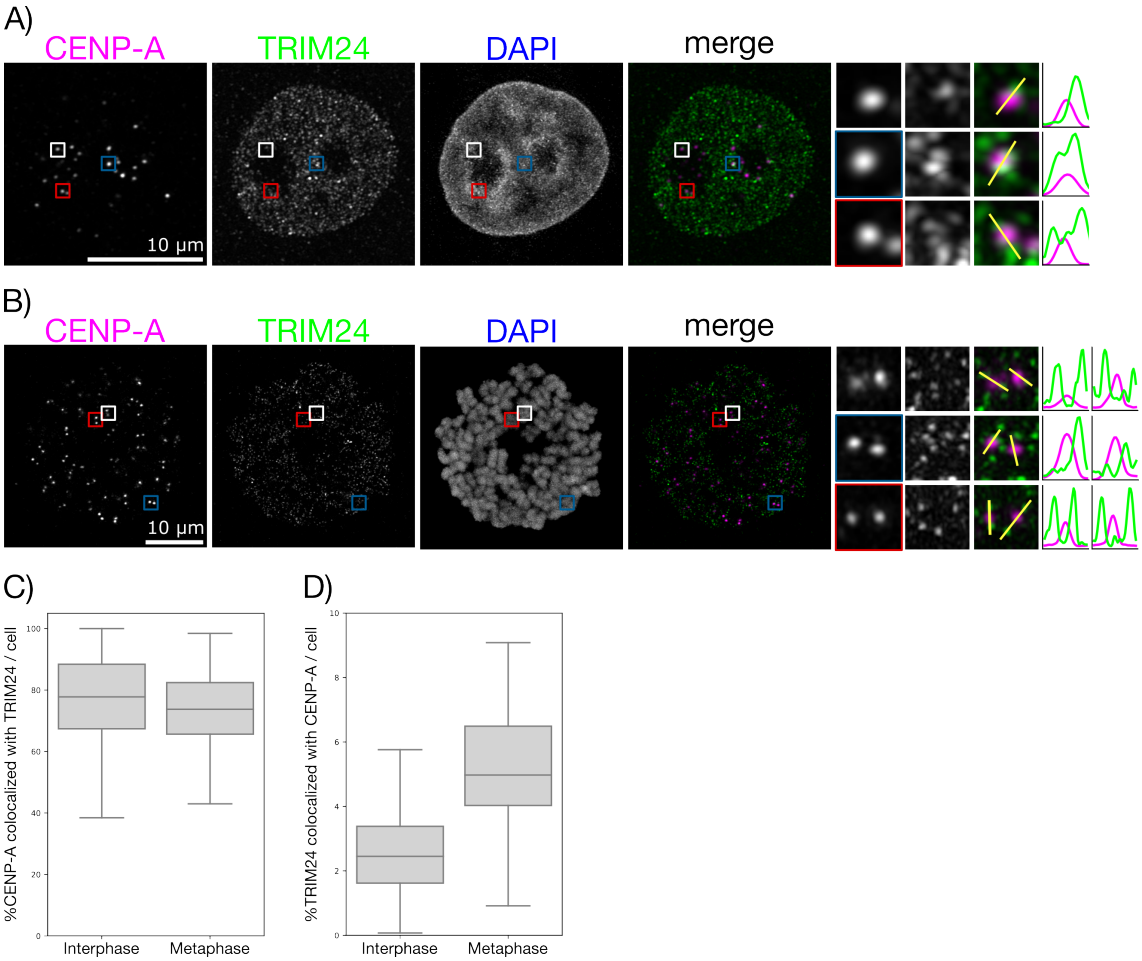


Figure 9.: TRIM24 localizes to centromeres during interphase and mitosis. Representative images of a) an interphase nucleus and b) metaphase chromosome spread from HEK293T cells stained for CENP-A (first column, indirect immunofluorescence) and TRIM24 (second column, indirect immunofluorescence), and DNA (third column, DAPI). Insets show representative CENP-A foci and their corresponding TRIM24 signal, with fluorescence intensity profile plots (magenta: CENP-A, green: TRIM24). Images were recorded by Airyscan super-resolution microscopy. Scale bar: 10 μm. c) Percentage of CENP-A foci colocalizing with TRIM24 per cell, measured in interphase and mitotic HEK293T cells by indirect immunofluorescence. d) Percentage of TRIM24 foci colocalizing with CENP-A per cell, measured in interphase and mitotic HEK293T cells. Boxplots show the minimum, first quartile, median, third quartile, and maximum. Data represent $n = 412$ (interphase), 87 (metaphase) cells from three independent experimental repeats.

To test whether TRIM24 localization at the centromere is retained during mitosis, I performed metaphase spreads of HEK293T cells followed by immunofluorescence staining for TRIM24 and the centromeric mark CENP-A (Fig. 9b). As expected, chromosomes displayed paired CENP-A signals. TRIM24 was detected along chromosome arms, and closer inspection of the CENP-A signal revealed that TRIM24 localized on one or both sides of CENP-A foci. Quantification of metaphase spreads showed that, on average, 74% of CENP-A foci overlapped with or directly contacted TRIM24, indicating that TRIM24 is present at most centromeres during mitosis.

At the same time, only 5.2% of TRIM24 foci overlapped with CENP-A (Fig. 9c,d), consistent with TRIM24 also localizing to additional non-centromeric sites. Together, these results indicate that a subset of TRIM24 associates with centromeres during mitosis.

Importantly, a preliminary staining performed in LNCaP cells also supported centromeric localization of TRIM24, both in interphase and mitosis (Sup. Fig. S3), arguing that the phenotype is not unique to HEK293T cells. All further experiments were conducted in HEK293T due to experimental robustness and sample availability.

In conclusion, both the bioinformatic reanalysis and immunofluorescence data support centromere association of TRIM24. This localization is cell type-dependent but can be robustly detected at centromeres in HEK293T cells during interphase and mitosis. Notably, TRIM24 showed limited overlap with CENP-A foci and was frequently positioned adjacent to the CENP-A signal, consistent with TRIM24 associating with centromeric regions outside the CENP-A-defined core region. Together, these findings identify centromere association as a previously uncharacterized feature of TRIM24.

2.2. PHD and RING domains contribute to TRIM24 centromere localization

Given the centromeric localization of TRIM24, I sought to determine which TRIM24 domains are required for its centromeric localization. TRIM24 contains an N-terminal tripartite motif (RING, B-boxes, and coiled-coil domains) and a C-terminal tail, including the PHD-BRD chromatin reader tandem and the HP1-binding domain (Fig. 10). To test which domains contribute to centromeric localization, I analysed TRIM24 deletion mutants in overexpression assays. Three plasmids containing TRIM24ΔRING-GFP, TRIM24ΔBRD-GFP, or TRIM24ΔPHD-GFP were kindly provided by Prof. Kyle Miller (Emory, USA). In addition, I generated a TRIM24ΔHP1-GFP mutant using site-directed mutagenesis (for construct details, see Materials and Methods, Tab. 12). These four mutants, along with TRIM24-GFP and GFP-only constructs, were overexpressed in HEK293T cells, and expression of all GFP-tagged constructs was confirmed by Western blotting (Fig. 20). Cells were immunofluorescently stained for the centromeric mark CENP-A and for GFP to detect the fusion protein. All images were acquired under identical microscope settings to allow direct comparison.

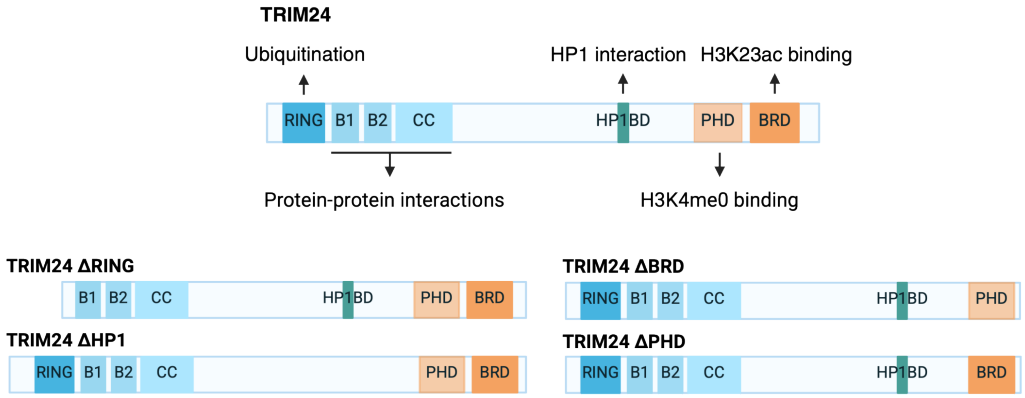


Figure 10.: Overview of TRIM24 domain mutants. Schematic representation of TRIM24 domain composition, including the N-terminal tripartite motif (RING, B-boxes, coiled-coil) and the C-terminal HP1-binding domain (HP1BD), plant homeodomain (PHD), and bromodomain (BRD). Binding partners and functions of individual domains (RING - ubiquitination; B-boxes and coiled-coil (BBCC) - protein-protein interactions; HP1BD - HP1 interaction; PHD - H3K4me0 binding; BRD - H3K23ac binding) are indicated. Deletions in the TRIM24ΔRING, TRIM24ΔHP1, TRIM24ΔBRD, and TRIM24ΔPHD constructs are shown. For construct details, see Materials and Methods (Tab. 12).

Wild-type TRIM24-GFP localized to the nucleus, excluding nucleoli, and resembled endogenous TRIM24 (Fig. 11). TRIM24-GFP concentrated in DAPI-rich regions, and nuclear DNA distribution differed from that of untransfected cells. At centromeres, the TRIM24-GFP signal was detected at CENP-A foci, either overlapping with the CENP-A foci or appearing as flanking foci adjacent to one or both sides of the CENP-A signal. Corresponding intensity profile plots showed GFP peaks flanking or overlapping the CENP-A maximum. By contrast, overexpression of GFP alone did not result in detectable enrichment at CENP-A foci (Fig. 11).

TRIM24ΔRING-GFP formed large cytoplasmic aggregates and showed strongly reduced overall nuclear signal. Despite this altered distribution, centromere-proximal GFP foci were still detectable and typically appeared adjacent to CENP-A signals. The ΔHP1 mutant exhibited nuclear localization comparable to TRIM24-GFP. Clear centromeric foci were detected that overlapped with or flanked CENP-A. Similar to TRIM24ΔRING, TRIM24ΔBRD was largely excluded from the nucleus and formed cytoplasmic aggregates. Nevertheless, the centromere-proximal signal was preserved, with GFP foci at centromeres typically flanking CENP-A. Notably, the BRD deletion also removes one of the nuclear localization signals within the bromodomain, which is likely to contribute to the altered subcellular distribution of TRIM24ΔBRD [191]. By contrast, TRIM24ΔPHD formed nuclear aggregates and

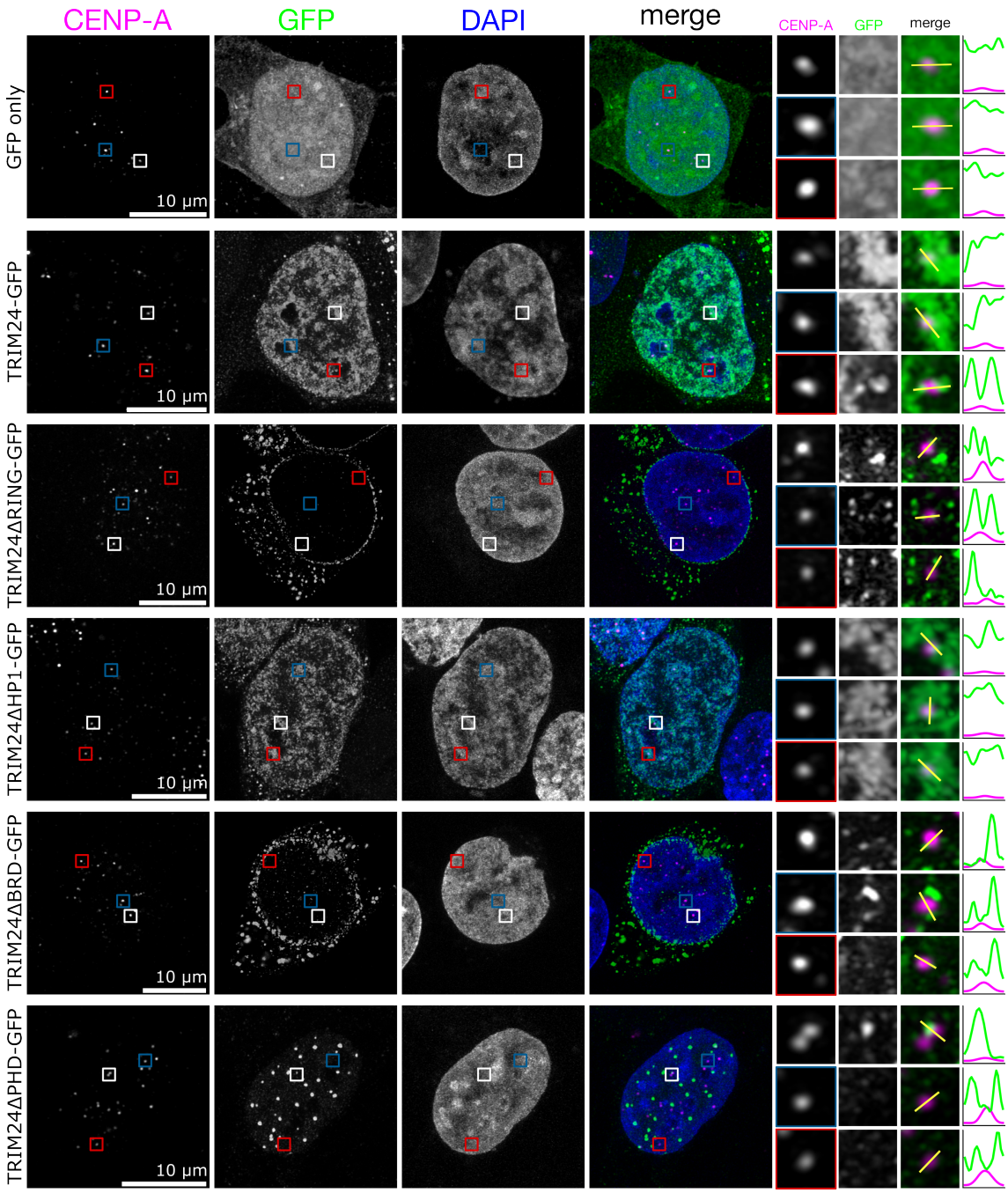


Figure 11.: TRIM24 domain mutants show altered cellular distribution during interphase. Representative images of interphase nuclei of HEK293T cells expressing GFP-only, TRIM24-GFP, or TRIM24 deletion mutants (ΔRING, ΔHP1, ΔBRD, ΔPHD). Cells were stained for CENP-A (indirect immunofluorescence), GFP (indirect immunofluorescence; fusion protein), and DNA (DAPI). Insets show representative CENP-A foci and their corresponding GFP signal, with fluorescence intensity profile plots (magenta: CENP-A, green: GFP). Images were acquired using Airyscan super-resolution microscopy. Scale bar: 10 μm. For details, see Materials and Methods.

showed reduced colocalization with CENP-A. In summary, deletion of individual TRIM24 domains altered overall cellular distribution, while centromeric localization was preserved for ΔRING, ΔHP1, and ΔBRD, but reduced for ΔPHD.

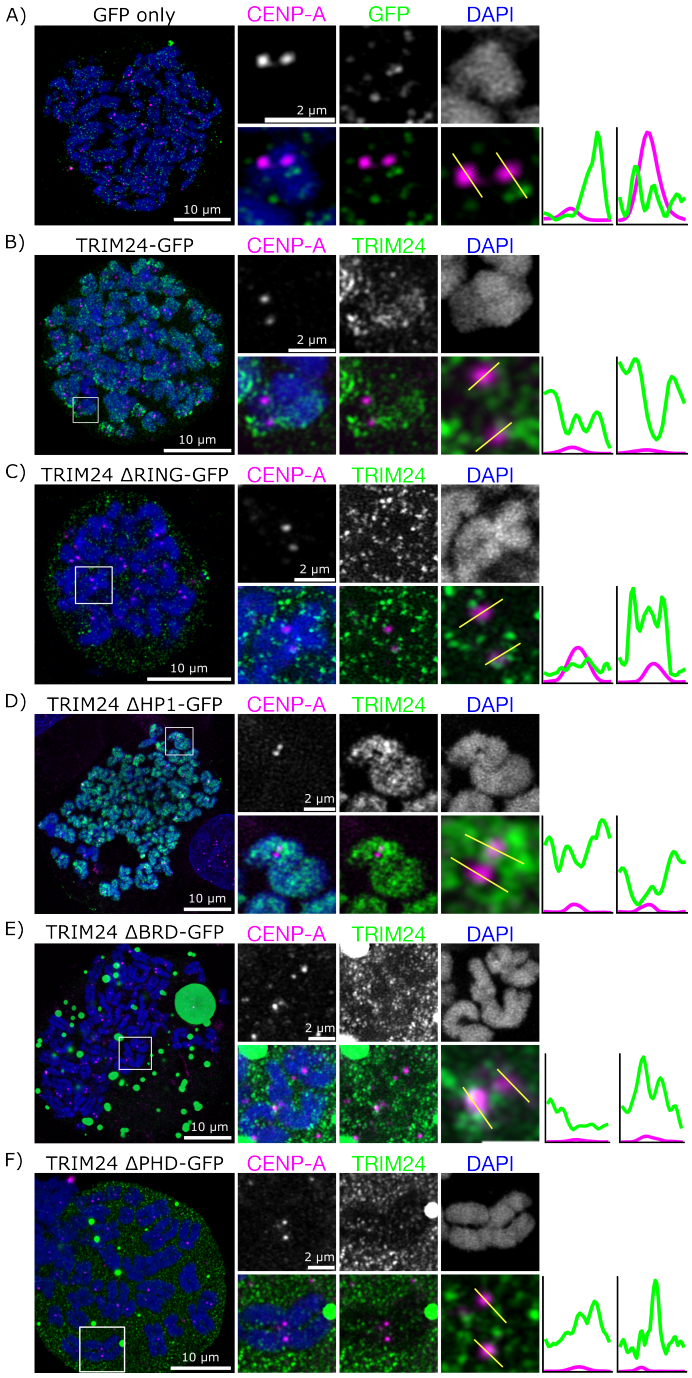


Figure 12.: TRIM24 domain mutants show altered centromeric localization during mitosis. Representative metaphase spreads of HEK293T cells overexpressing a) GFP-only, b) TRIM24-GFP, c) TRIM24ΔRING-GFP, d) TRIM24ΔHP1-GFP, e) TRIM24ΔBRD-GFP, and f) TRIM24ΔPHD-GFP. Cells were stained for CENP-A (indirect immunofluorescence), GFP (indirect immunofluorescence; fusion protein), and DNA (DAPI). Insets show representative chromosomes with their CENP-A, GFP, and DAPI signals, as well as enlarged CENP-A foci with their corresponding GFP signal, with fluorescence intensity profile plots (magenta: CENP-A, green: GFP). Images were acquired using Airyscan super-resolution microscopy. Scale bar: 10 μm (overview), 2 μm (insets). For details, see Materials and Methods.

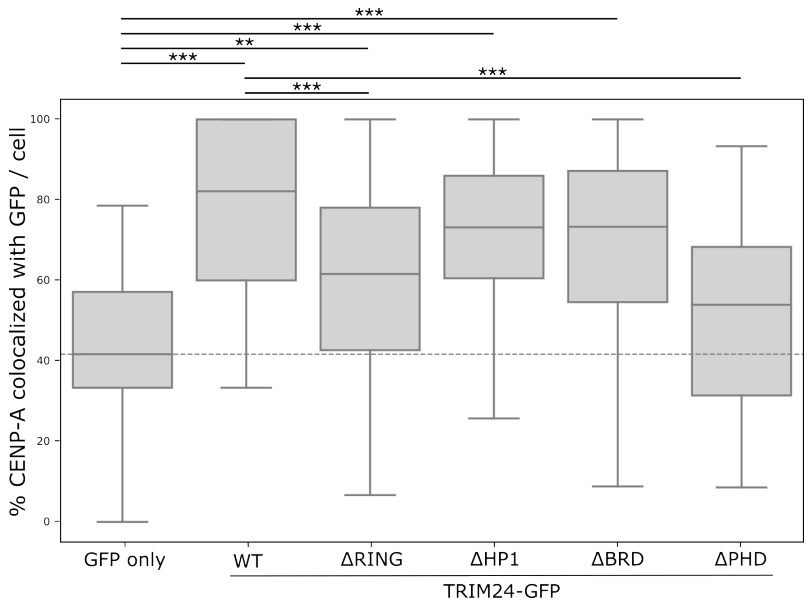


Figure 13.: TRIM24 domain mutants differentially affect centromeric localization during mitosis. Quantification of the percentage of CENP-A foci colocalizing with GFP per metaphase cell in HEK293T cells overexpressing GFP-only, TRIM24-GFP, or TRIM24 deletion mutants (ΔRING, ΔHP1, ΔBRD, ΔPHD). Colocalization was defined as overlap or direct contact between CENP-A and GFP signals. Boxplots show the minimum, first quartile, median, third quartile, and maximum. Data represent $n = 95$, 90, 83, 98, 103, and 89 cells, respectively, across three independent experiments. Statistical analysis was performed using one-way ANOVA with Tukey-Kramer post hoc testing; *: $p < 0.05$, **: $p < 0.01$, ***: $p < 0.001$.

To determine whether deletion of TRIM24 domains influences its localization to centromeres during mitosis, I overexpressed TRIM24 domain mutants in HEK293T cells and prepared metaphase spreads. Spreads were immunofluorescently stained for CENP-A and GFP, and the localization of TRIM24 mutants at centromeres was analysed.

In mitosis, TRIM24-GFP localized broadly along chromosome arms and was detectable at centromeres (Fig. 12b). At CENP-A foci, the TRIM24-GFP signal typically appeared as flanking peaks adjacent to the CENP-A maximum, consistent with the pattern observed for endogenous TRIM24. The TRIM24ΔRING mutant showed little signal on chromosome arms but retained localization to at least a subset of centromeres (Fig. 12c). TRIM24ΔHP1 displayed a chromosome-associated distribution comparable to TRIM24-GFP, with clear centromeric foci flanking CENP-A (Fig. 12d). TRIM24ΔBRD formed large foci that were excluded from mitotic chromosomes (Fig. 12e). Nevertheless, centromeric localization was preserved and typically flanked CENP-A. TRIM24ΔPHD was also excluded from chromosome arms but retained detectable centromeric signal in a subset of centromeres, most

often flanking CENP-A (Fig. 12f). Together, these results suggest that deletion of individual TRIM24 domains alters overall mitotic chromosome association but does not fully abolish centromeric localization.

To quantify centromeric localization of TRIM24 mutants, I manually scored metaphase spreads from HEK293T cells expressing GFP-only, TRIM24-GFP, or TRIM24 deletion mutants (ΔRING, ΔHP1, ΔBRD, ΔPHD). For each cell, the percentage of CENP-A foci colocalizing with GFP was calculated as the number of CENP-A foci overlapping or touching GFP divided by the total number of CENP-A foci (Fig. 13). Because the score counts both overlap and direct contact, and diffused GFP signal can overlap with chromatin, the GFP-only condition provides a baseline level of incidental overlap between GFP and CENP-A.

TRIM24-GFP showed high colocalization with CENP-A (mean 78.2%), in contrast to GFP-only cells (44.7%). TRIM24ΔHP1 (73.1%) and TRIM24ΔBRD (69.1%) were not significantly reduced compared to TRIM24-GFP, whereas TRIM24ΔRING (59.6%) and TRIM24ΔPHD (54.5%) were significantly reduced. Taken together, these results show that centromeric localization of TRIM24 is largely preserved upon deletion of the HP1 or BRD domain and strongly impaired when the RING or PHD domains are deleted.

In conclusion, overexpressed wild-type TRIM24 localized to DNA-rich regions in both interphase and mitosis, with persistent centromere targeting. In mitosis, colocalization scoring on metaphase spreads showed that deletion of either the RING or PHD domain significantly reduced centromeric localization, whereas ΔBRD and ΔHP1 were not significantly reduced. Together, these results indicate that centromeric localization of TRIM24 is differentially affected by domain deletions, with the PHD and RING domains contributing substantially to centromere targeting.

2.3. TRIM24 BRD point mutant forms distinct foci in proximity to centromeres

2.3.1. TRIM24 BRD point mutant forms centromeric foci in interphase and mitosis

Deletion of the TRIM24 bromodomain excluded the protein from chromatin but did not abolish its centromeric association (Fig. 12). Since the PHD and BRD domains function as a single unit for combinatorial recognition of H3K4me0 and

H3K23ac within the same histone tail, the question arises as to whether BRD function fine-tunes PHD-dependent centromeric localization [184]. Domain deletions may cause structural effects beyond loss of binding [1]. Additionally, in the case of TRIM24ΔBRD, the domain deletion removes one of the two nuclear localization signals, which may affect nuclear import [191]. I therefore asked whether a milder perturbation of the bromodomain would change TRIM24 behaviour. To test this, I analysed a point mutant in which phenylalanine 979 (F979) and asparagine 980 (N980) were substituted (F979A/N980A; Fig. 14a), residues essential for binding to H3K23ac [184]. This mutant disrupts H3K23ac binding while keeping the bromodomain and its nuclear localization signal present, and therefore allows testing whether the BRD contributes to centromeric localization in a more subtle way than full deletion.

The plasmid containing TRIM24 F979A/N980A-GFP was kindly provided by Prof. Kyle Miller (Emory, USA). The GFP-only, mutant, and wild-type TRIM24 constructs were overexpressed in HEK293T cells, and expression of the constructs was confirmed by Western blotting (Fig. 20). Cells were immunofluorescently stained for the centromeric mark CENP-A and GFP to detect the fusion protein. All images were acquired under identical microscope settings to allow direct comparison.

Unlike the deletion mutant, the TRIM24 F979A/N980A mutant was not excluded from chromatin. Instead, it formed large, irregular foci that were not observed in cells overexpressing GFP alone (Fig. 14b,c). Intensity profile plots showed CENP-A signals embedded within GFP-rich regions, without the characteristic GFP dip at the CENP-A peak observed for endogenous TRIM24 and wild-type TRIM24-GFP. These results demonstrate that the TRIM24 F979A/N980A mutant retains centromeric localization but alters TRIM24 nuclear organization.

To determine whether the TRIM24 F979A/N980A mutation influences centromeric localization during mitosis, I overexpressed the TRIM24 F979A/N980A mutant in HEK293T cells and prepared metaphase spreads. Spreads were immunofluorescently stained for CENP-A and GFP, and the localization of the TRIM24 F979A/N980A mutant was analysed. Similar to interphase cells, the TRIM24 F979A/N980A mutant localized to chromatin and persisted at the centromeres (Fig. 15). In addition, the mutant formed large foci on chromatin, predominantly positioned near or between sister centromeres, on one or both sides. The intensity profile plot confirmed TRIM24

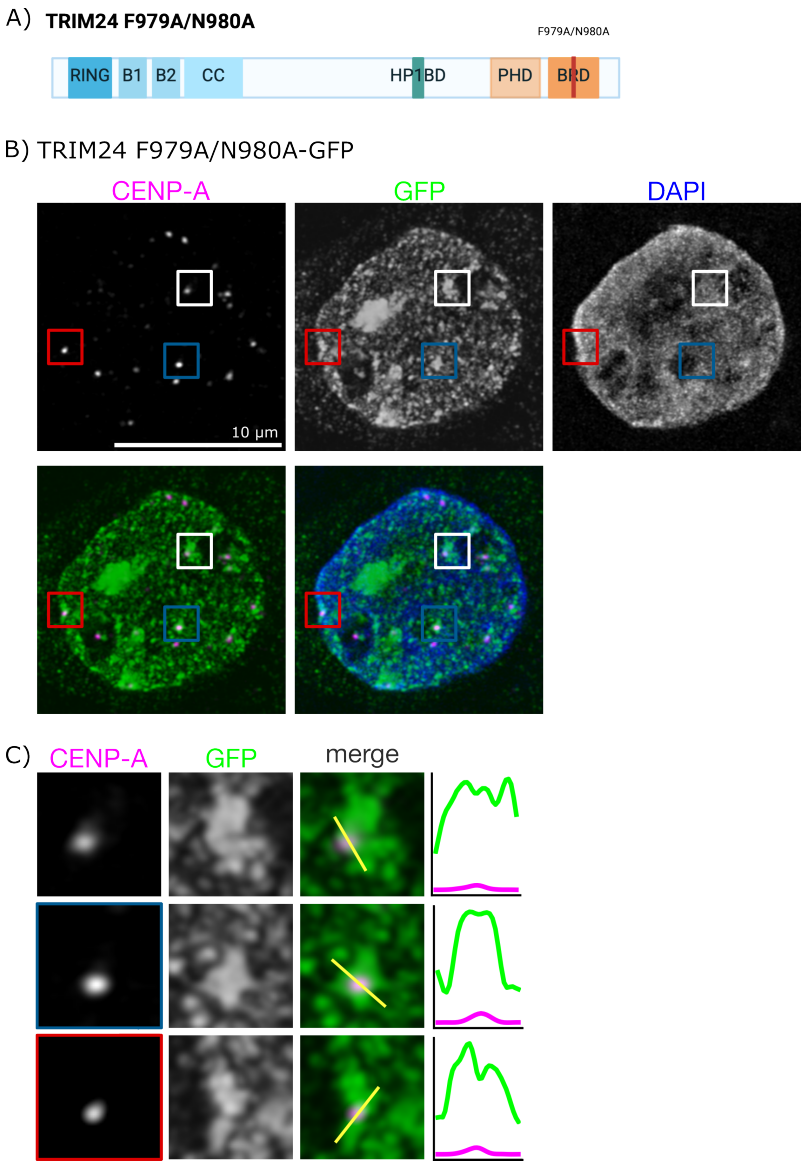


Figure 14.: TRIM24 bromodomain point mutant retains centromeric localization during interphase. a) Schematic representation of the TRIM24 F979A/N980A construct, including the N-terminal tripartite motif (RING, B-boxes, coiled-coil) and the C-terminal HP1-binding domain (HP1BD), plant homeodomain (PHD), and bromodomain (BRD). The point mutations (F979A/N980A) are indicated. b) Representative images of an interphase nucleus of a HEK293T cell expressing TRIM24 F979A/N980A-GFP. Cells were stained for CENP-A (indirect immunofluorescence), GFP (indirect immunofluorescence; fusion protein), and DNA (DAPI). Insets show representative CENP-A foci and their corresponding GFP signal, with fluorescence intensity profile plots (magenta: CENP-A, green: GFP). Images were acquired using Airyscan super-resolution microscopy. Scale bar: 10 μm. For details, see Materials and Methods.

enrichment on or adjacent to CENP-A signals. Taken together, these results show that the TRIM24 F979A/N980A mutant localizes to centromeres during mitosis and forms large foci in close proximity to CENP-A.

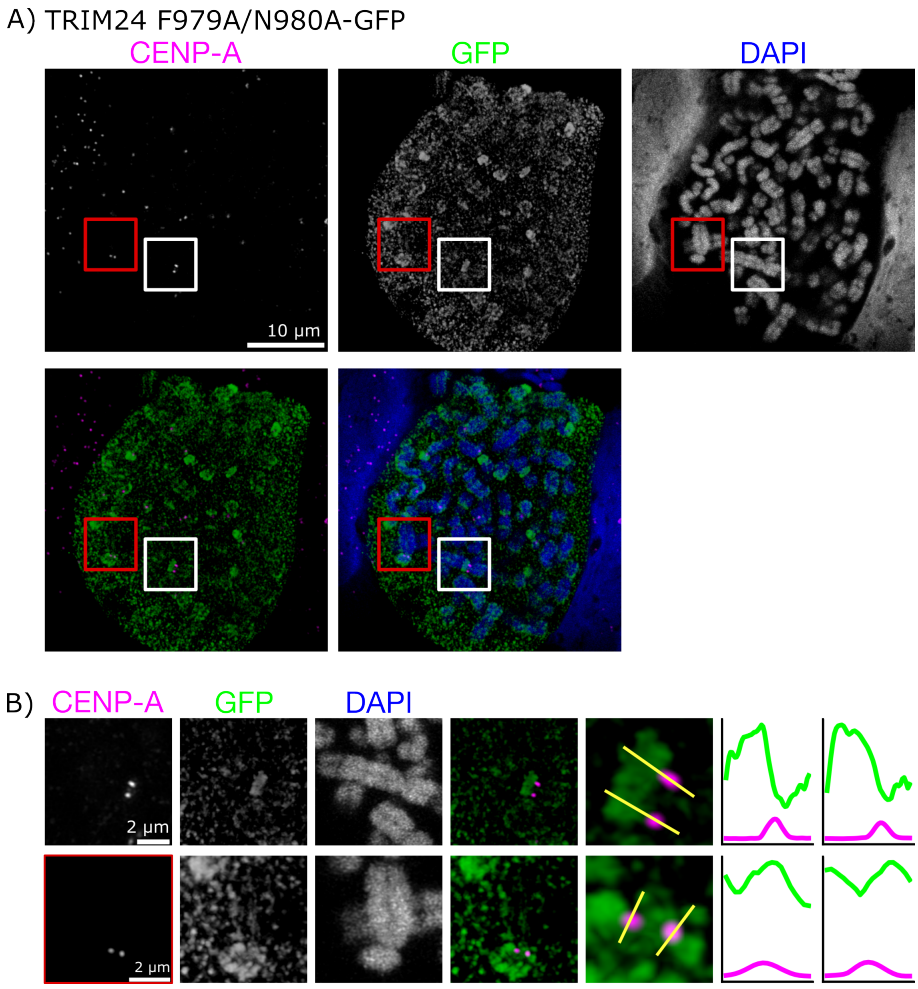


Figure 15.: TRIM24 bromodomain point mutant forms large foci near centromeres during mitosis. Representative metaphase spread of a HEK293T cell overexpressing TRIM24 F979A/N980A-GFP. Cells were stained for CENP-A (indirect immunofluorescence), GFP (indirect immunofluorescence; fusion protein), and DNA (DAPI). Insets show representative chromosomes with their CENP-A, GFP, and DNA signals, as well as enlarged CENP-A foci with the corresponding GFP signal, with fluorescence intensity profile plots (magenta: CENP-A, green: GFP).Images were acquired using Airyscan super-resolution microscopy. Scale bar: 10 μm (overview) and 2 μm (inset). For details, see Materials and Methods.

The TRIM24 F979A/N980A mutant behaved differently compared to the BRD deletion mutant. This raised the question of whether centromeric localization of TRIM24 F979A/N980A is maintained at the same level as in the deletion mutant. To address this, I manually scored metaphase spreads from HEK293T cells expressing GFP-only, TRIM24-GFP, TRIM24ΔBRD-GFP, and TRIM24 F979A/N980A-GFP. For each cell, the percentage of CENP-A foci colocalizing with GFP was calculated as the number of CENP-A foci overlapping or directly touching GFP, divided by

the total number of CENP-A foci (Fig. 16a). The TRIM24 F979A/N980A mutant showed centromeric localization as strong as wild-type TRIM24 (mean 78.4% vs. 78.2%), but significantly stronger than the TRIM24ΔBRD mutant (69.1%).

Because TRIM24 F979A/N980A formed large foci near centromeres, I next asked whether this increased centromeric association compared to TRIM24ΔBRD was connected to construct expression levels. I therefore quantified GFP intensity for the metaphase spreads using CellProfiler [172]. Spreads were masked based on the DNA channel, and the mean GFP intensity inside the mask was measured for each cell. These values were then visualized as a scatterplot of GFP intensity against the percentage of CENP-A foci colocalizing with GFP (Fig. 16b). Indeed, higher GFP intensities correlated with a systematic increase in CENP-A colocalization for the TRIM24 F979A/N980A mutant. This correlation was not visible in GFP-only cells. This suggests that stronger expression of the TRIM24 F979A/N980A mutant enhances its accumulation at centromeres.

Taken together, these results show that the TRIM24 F979A/N980A mutant retains centromeric localization during interphase and mitosis. In contrast to BRD deletion, the point mutation maintained centromeric association at levels comparable to wild-type TRIM24 but higher than TRIM24ΔBRD. This increased association correlated with GFP expression levels, suggesting that the behaviour of the TRIM24 mutant depends on protein concentration in the cell.

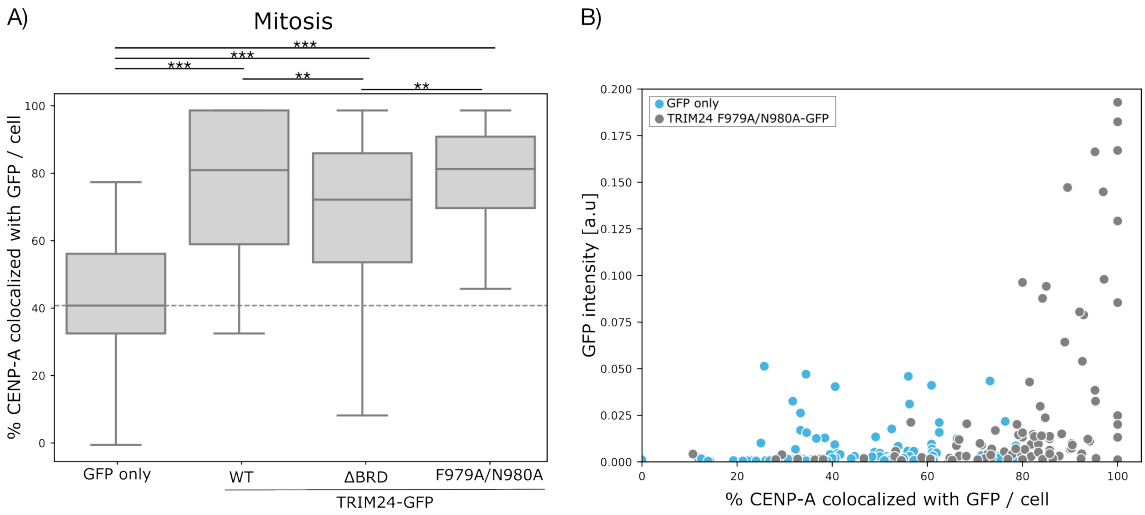


Figure 16.: TRIM24 bromodomain point mutant shows enhanced centromeric localization correlated with expression level. a) Quantification of the percentage of CENP-A foci colocalizing with GFP per metaphase cell in HEK293T cells expressing GFP-only, TRIM24-GFP, TRIM24ΔBRD-GFP, or TRIM24 F979A/N980A-GFP. Colocalization was defined as overlap or direct contact between CENP-A and GFP signals. Boxplots show the minimum, first quartile, median, third quartile, and maximum. Data represent $n = 95, 90, 83, 99$ cells across three independent experiments. Statistical analysis was performed using a t-test; *: $p < 0.05$, **: $p < 0.01$, ***: $p < 0.001$. b) Scatterplot of the percentage of CENP-A foci colocalizing with GFP versus GFP intensity per metaphase cell in HEK293T cells expressing TRIM24 F979A/N980A-GFP (grey) or GFP-only constructs (blue). GFP intensity was quantified in CellProfiler by masking each metaphase spread using the DNA channel and measuring the mean GFP intensity within the mask. Data represent $n = 99, 95$ cells, across three independent experiments. For details, see Materials and Methods.

2.3.2. TRIM24 BRD point mutant foci are linked to mutant expression levels

TRIM24 F979A/N980A caused formation of large foci near or around centromeres on metaphase spreads and in interphase cells. To investigate whether large foci formation is specific to TRIM24 F979A/N980A, I counted the percentage of cells exhibiting large centromeric foci in interphase HEK293T cells expressing GFP-only, TRIM24-GFP, or TRIM24 F979A/N980A-GFP. Per replicate, I counted cells that showed large foci formation near centromeres and divided this value by the total number of cells (Fig. 17a).

Cells expressing GFP-only did not show large centromeric foci formation. In comparison, wild-type TRIM24 displayed a low frequency of large foci-positive cells (mean 23.8%). By contrast, TRIM24 F979A/N980A caused significantly more frequent foci formation than wild-type TRIM24 (41.2%). This suggests that mutation of the BRD promotes TRIM24 centromeric foci formation.

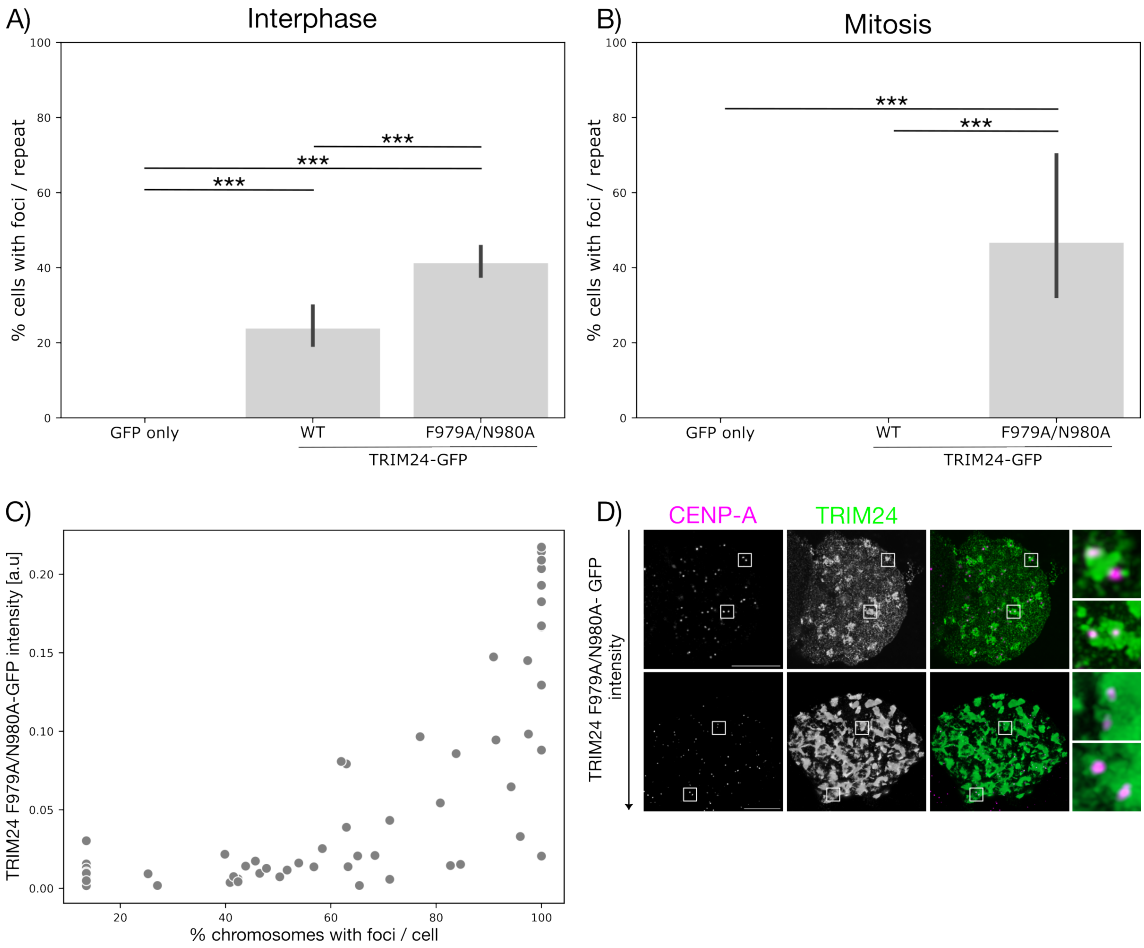


Figure 17.: TRIM24 bromodomain point mutant forms foci near centromeres, and their size depends on mutant expression level. a, b) Quantification of the percentage of GFP foci-positive cells per replicate in a) interphase and b) metaphase spreads of HEK293T cells expressing GFP-only, TRIM24-GFP, or TRIM24 F979A/N980A-GFP. A foci-positive cell was defined as a cell containing at least four large foci overlapping or touching the CENP-A signal. Plots show mean ± SD. c) Scatterplot of the percentage of chromosomes with GFP foci versus GFP intensity per metaphase spread in HEK293T cells expressing TRIM24 F979A/N980A-GFP. GFP intensity was quantified in CellProfiler by masking each metaphase spread using the DNA channel and measuring the mean GFP intensity within the mask. Data represent a) $n = 336, 227, 277$ cells, b) $n = 95, 90, 99$ cells, and c) $n = 81$ cells across three independent experiments. Statistical analysis was performed using a t-test; *: $p < 0.05$, **: $p < 0.01$, ***: $p < 0.001$. d) Representative metaphase spreads of HEK293T cells with low and high expression of TRIM24 F979A/N980A-GFP. Cells were stained for CENP-A (indirect immunofluorescence) and GFP (indirect immunofluorescence; fusion protein). Insets show representative CENP-A foci with the corresponding GFP signal. Images were acquired using Airyscan super-resolution microscopy. The settings and colour maps were kept constant across the samples. Scale bar: 10 μm. For details, see Materials and Methods.

I next analysed metaphase spreads of HEK293T cells expressing GFP-only, TRIM24-GFP, or TRIM24 F979A/N980A-GFP. Neither GFP-only nor wild-type TRIM24 caused foci formation on mitotic centromeres (Fig. 17b). In contrast, TRIM24 F979A/N980A-GFP formed centromeric foci in more than half of the cells (53.8%). These results show that centromeric foci formation during mitosis is specific to the TRIM24 BRD point mutant and does not occur upon wild-type TRIM24 overexpression.

Microscopy images revealed that TRIM24 F979A/N980A centromeric foci varied in intensity and size. To quantify this, I measured the GFP intensity of metaphase spreads and counted the number of chromosomes with centromeric foci per cell. These values were plotted as a scatterplot of GFP intensity versus the percentage of chromosomes with centromeric foci per cell (Fig. 17c). Higher GFP intensity correlated with a higher number of chromosomes carrying TRIM24 centromeric foci. To confirm this observation qualitatively, I compared representative cells with different GFP intensities. Cells with low GFP intensity contained small foci, often localized near centromeres, whereas cells with higher GFP intensity displayed large foci covering entire chromosomes (Fig. 17d). Taken together, these results show that TRIM24 F979A/N980A specifically induces foci formation at centromeres and that foci size and frequency depend on mutant expression level.

In summary, these results reveal that the TRIM24 F979A/N980A bromodomain point mutant localizes to centromeres during interphase and mitosis and forms large foci that preferentially occur at centromeres. Foci formation at mitotic centromeres was specific to the bromodomain point mutant. The size and frequency of these foci depended on mutant expression levels, suggesting that the bromodomain constrains TRIM24 accumulation at centromeres and thereby influences the strength of its centromeric association. In contrast to ΔBRD, the point mutant indicates that the BRD is not strictly required for centromere localization but instead fine-tunes TRIM24 distribution and prevents excessive foci formation.

2.4. TRIM24 contributes to proper sister chromatid cohesion during mitosis

2.4.1. TRIM24 contributes to proper intercentromeric distance in mitosis

TRIM24 localizes to centromeres during both interphase and mitosis. Its PHD and RING domains contribute substantially to centromeric localization, while the BRD fine-tunes the strength and distribution of this association. Notably, the BRD point mutation results in the formation of foci around and between sister centromeres in mitosis, suggesting that TRIM24 with an inactive BRD displays preferential accumulation at centromeres over other chromatin regions. These observations raise the question of what role TRIM24 might play at the centromere.

Based on the centromeric localization of TRIM24 and its predicted interaction with cohesin components, I next asked whether TRIM24 contributes to the regulation of sister chromatid cohesion during mitosis. Reduction of mitotic cohesion typically results in an increased distance between sister centromeres [121]. To test whether TRIM24 influences this distance, I measured the separation between sister centromeres in untreated cells and in cells expressing GFP-only or TRIM24-GFP. The separation was defined as the distance between the centres of paired CENP-A signals, and the mean intercentromeric distance per metaphase spread was calculated. Mean distances from three independent experiments were visualized as boxplots (Fig. 18).

Expression of the GFP-only construct caused a slightly reduced sister centromere distance (mean 0.90 μm) in comparison to untreated cells (0.95 μm). Interestingly, TRIM24-GFP expression further decreased the distance (0.85 μm), suggesting a tighter association between sister chromatids and potentially enhanced cohesion.

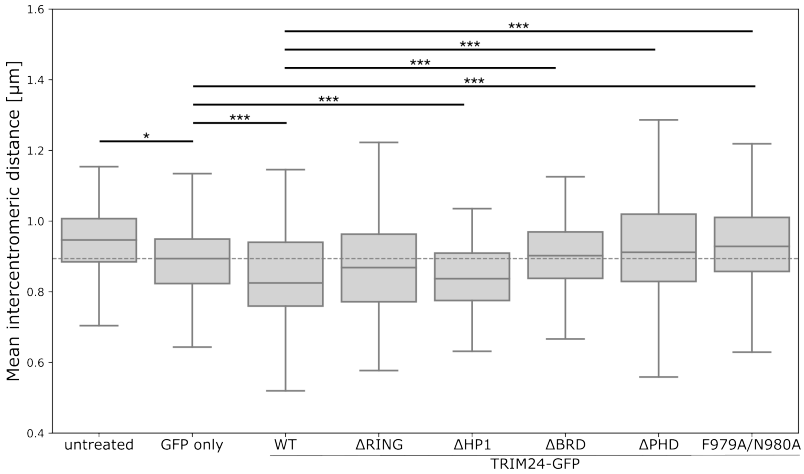


Figure 18.: TRIM24 influences intercentromeric distance in mitosis. Quantification of the mean distance between sister centromeres on metaphase spreads of HEK293T cells expressing GFP-only, TRIM24-GFP, TRIM24 deletion mutants (ΔRING, ΔHP1, ΔBRD, ΔPHD), or the TRIM24 bromodomain point mutant (F979A/N980A). Distance was measured between the centres of paired CENP-A foci, and the mean distance per cell was plotted. Boxplots show the minimum, first quartile, median, third quartile, and maximum. Data represent $n = 88, 93, 86, 82, 131, 102, 90, 109$ cells, across three independent experiments. Statistical analysis was performed using the Kruskal-Wallis test with Benjamini-Hochberg correction; *: $p < 0.05$, **: $p < 0.01$, ***: $p < 0.001$.

To assess whether TRIM24 domains contribute to this phenotype, I analysed TRIM24 mutants (ΔRING, ΔHP1, ΔBRD, ΔPHD, and F979A/N980A) expressed in HEK293T cells and prepared metaphase spreads. The distances between paired CENP-A signals were measured as described above. Mean values were plotted as boxplots (Fig. 18).

Deletion of the RING domain (mean 0.88 μm) or HP1-binding domain (0.85 μm) maintained the reduced centromeric distance, similar to wild-type TRIM24-GFP (0.85 μm). Deletion of the BRD (0.90 μm) abolished the reduction in centromeric distance observed with wild-type TRIM24, resulting in values comparable to GFP-only controls (0.90 μm). Deletion of the PHD domain (0.93 μm) and the BRD point mutant F979A/N980A (0.94 μm) both significantly increased centromeric distance, suggesting reduced cohesion between sister chromatids.

In summary, wild-type TRIM24 overexpression decreases intercentromeric distance, supporting a role in cohesion. The HP1-binding and RING domains are dispensable for this effect under these conditions, whereas deletion of the BRD or PHD domain abolishes the phenotype. Moreover, the BRD point mutation results in increased intercentromeric distance. Together, these results suggest that TRIM24 plays a previously unrecognised role in regulating sister chromatid cohesion, with the PHD and BRD domains being critical for maintaining proper intercentromeric distance.

2.4.2. TRIM24 prevents premature sister chromatid separation

Overexpression of TRIM24 reduced intercentromeric distance (Fig. 18), raising the question of whether TRIM24 modulates sister chromatid cohesion. A hallmark of impaired cohesion is premature sister chromatid separation (PSCS) [75]. If wild-type TRIM24 expression enhances centromeric cohesion, its overexpression should decrease PSCS, whereas loss of TRIM24 would be expected to increase PSCS.

To test this, I quantified PSCS in methanol-fixed metaphase spreads in cells expressing GFP-only or the TRIM24-GFP construct, or in cells depleted of TRIM24 using siRNA (siTRIM24). Metaphase spreads were categorised into four groups of increasing severity of cohesion defects (Fig. 19a). "Normal" spreads displayed chromosomes with aligned sister chromatids connected at centromeres. In the "partial cohesion defect" category, a subset of chromosomes showed loss of centromeric connection. When all chromosomes lost centromeric connection but remained aligned, spreads were scored as "full cohesion defects". Finally, "cohesion failure" indicated complete loss of centromeric connection, with sister chromatids no longer aligned.

Expression of wild-type TRIM24 reduced the overall frequency of cohesion defects (mean 12.5%) compared to the GFP-only control (20.3%) (Fig. 19b). However, TRIM24-GFP cells displayed a small fraction of cohesion failures (0.8%), which were absent in control cells (0%). In contrast, TRIM24 knockdown resulted in a significantly higher frequency of cohesion defects (26.7%) than siCtrl cells (12.7%),

including a low but notable percentage of cohesion failures (2.2% in siTRIM24 and 0% in siCtrl) (Fig. 19c). In summary, TRIM24 overexpression suppresses the formation of PSCS, whereas TRIM24 depletion leads to elevated cohesion defects. These findings support a role for TRIM24 in promoting proper sister chromatid cohesion during mitosis.

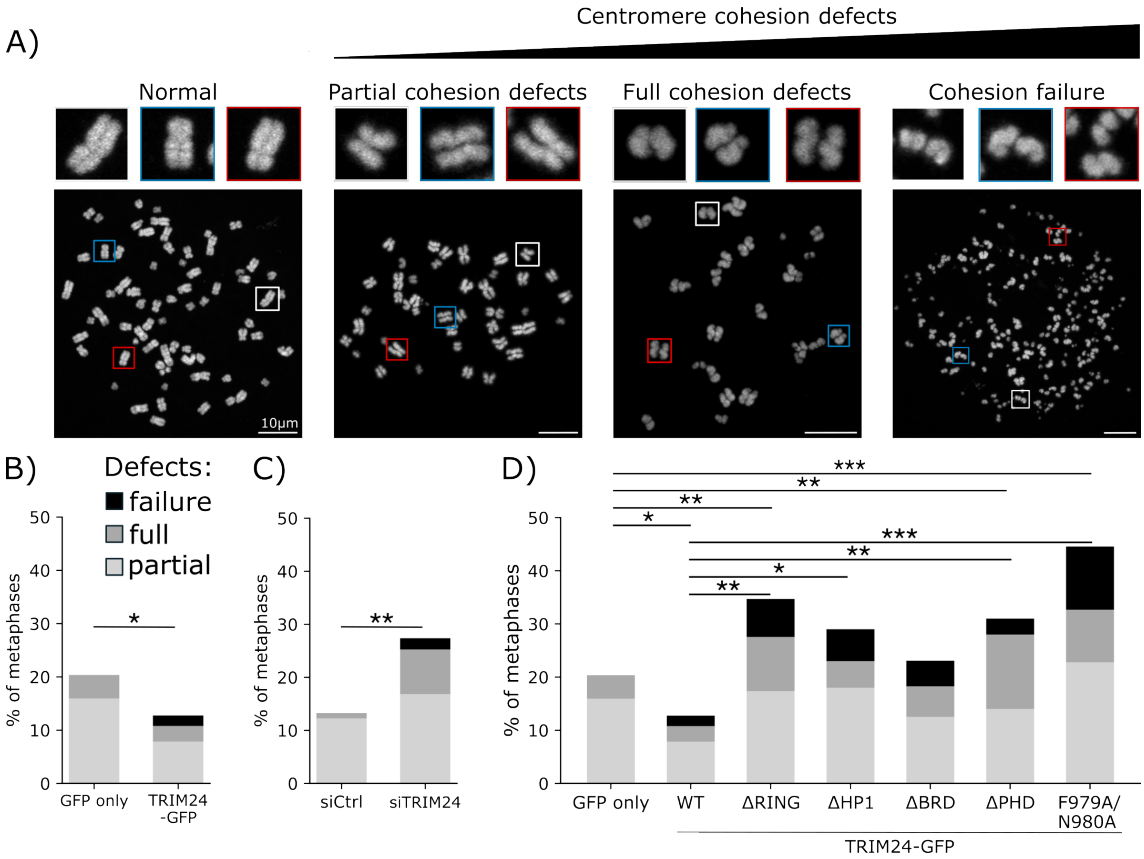


Figure 19.: TRIM24 prevents premature sister chromatid separation. a) Representative methanol-fixed metaphase spreads of HEK293T cells, representing the four categories of centromere cohesion defects: normal, partial cohesion defects, full cohesion defects, and cohesion failure. Insets show exemplary chromosomes for each category. b) Quantification of premature sister chromatid separation in HEK293T cells expressing GFP-only or TRIM24-GFP constructs. c) Quantification of premature sister chromatid separation in HEK293T cells treated with control siRNA (siCtrl) or depleted of TRIM24 using siRNA (siTRIM24). d) Quantification of premature sister chromatid separation in HEK293T cells expressing GFP-only, TRIM24-GFP, or TRIM24 mutant constructs (ΔBRD, ΔPHD, ΔRING, ΔHP1, and F979A/N980A). Stacked bar plots show the percentage of metaphase spreads in each cohesion defect category. Data represent b) $n = 113$ and 102 cells, c) $n = 98$ and 95 cells, and d) $n = 113$, 102, 104, 100, 98, 100, and 101 cells across three independent experiments. Statistical analysis was performed using a t-test; *: $p < 0.05$, **: $p < 0.01$, ***: $p < 0.001$. For details, see Materials and Methods.

To determine whether TRIM24 mutants can maintain reduced PSCS, I analysed methanol-fixed metaphase spreads from cells expressing GFP-only, wild-type TRIM24, or TRIM24 mutants (ΔRING, ΔHP1, ΔBRD, ΔPHD, and F979A/N980A). Spreads were scored as described above (Fig. 19d).

The ΔRING mutant, which maintained reduced centromeric distance similar to wild-type TRIM24, nevertheless caused markedly increased PSCS (36%) compared to wild-type TRIM24 and the GFP-only control. The ΔHP1 mutant also exhibited increased PSCS (28.7%), higher than wild-type TRIM24. The ΔBRD mutant did not significantly influence PSCS frequency (24%), similar to the GFP-only control. The ΔPHD mutant resulted in significantly elevated PSCS (31.2%). Most strikingly, the F979A/N980A mutant induced PSCS in nearly half of metaphase spreads (44.3%) and displayed the highest proportion of cohesion failures (11.9%).

Taken together, TRIM24 contributes to proper sister chromatid cohesion during mitosis. Overexpression of wild-type TRIM24 decreases both intercentromeric distance and PSCS, whereas TRIM24 depletion increases cohesion defects. Domain analysis revealed that the PHD domain contributes substantially to maintaining cohesion, as its loss leads to both increased centromere distance and elevated PSCS. Interestingly, the loss-of-function BRD point mutant causes an increase in centromere distance and a significant increase in PSCS, whereas BRD deletion does not induce cohesion defects. This is consistent with the idea that excessive or abnormal TRIM24 association with centromeres can actively disrupt cohesion. The RING domain, although not required for distance regulation, contributes to suppressing cohesion defects. Similarly, the HP1-binding domain mutant preserves centromeric localization and intercentromeric distance but loses the ability to suppress cohesion defects. In summary, these results establish TRIM24 as a previously uncharacterized factor that influences sister chromatid cohesion during mitosis, with distinct contributions from its individual domains.

2.5. TRIM24 associates with cohesin subunit RAD21

TRIM24 centromere association and its effects on mitotic cohesion raise the question of whether TRIM24 associates with the cohesin complex. In addition, TurboID proximity labelling identified TRIM24 near STAG2, RAD21, and WAPL [199]. To investigate whether TRIM24 physically associates with cohesin complex components, particularly RAD21, I performed GFP co-immunoprecipitation. HEK293T cells were transfected with GFP-only or TRIM24-GFP constructs and lysed 48h after

transfection. GFP fusion proteins and their associated complexes were immunoprecipitated using GFP-binding protein (GBP) beads. GFP expression and RAD21 co-immunoprecipitation were visualised by Western blotting (Fig. 20).

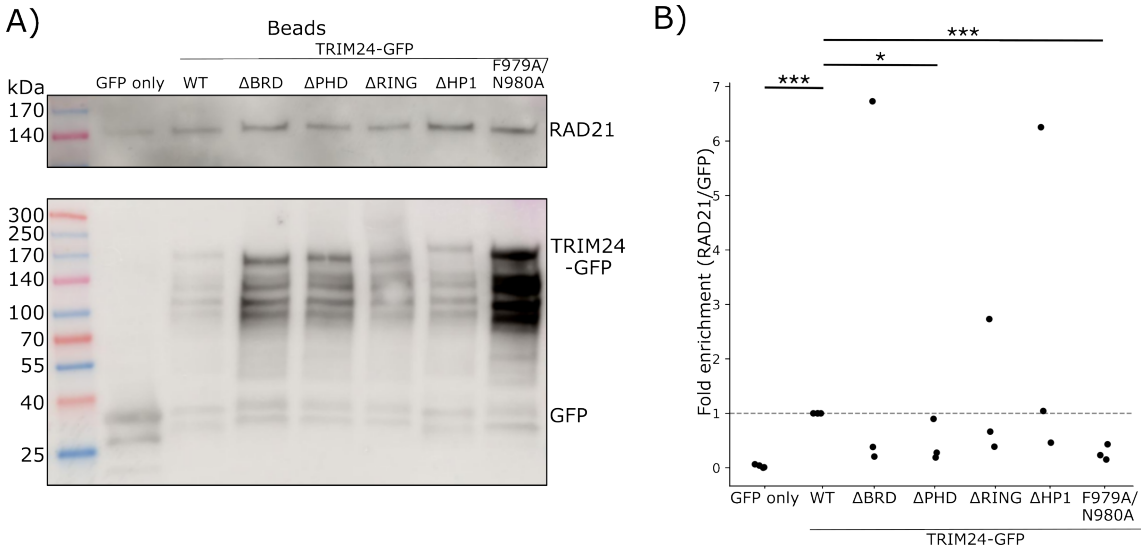


Figure 20.: TRIM24 associates with RAD21. a) Western blot analysis of co-immunoprecipitated material probed for RAD21 and GFP in cells expressing GFP-only, TRIM24-GFP, and the indicated TRIM24 mutants (ΔBRD, ΔPHD, ΔRING, ΔHP1, and F979A/N980A). b) Quantification of RAD21/GFP signal ratios normalised to wild-type TRIM24-GFP. Data represent three independent experiments. Statistical analysis was performed using a t-test; *: $p < 0.05$, **: $p < 0.01$, ***: $p < 0.001$. For details, see Materials and Methods.

Western blotting confirmed expression of TRIM24-GFP, and the characteristic banding pattern of TRIM24 was observed, as previously reported [90]. RAD21 co-immunoprecipitated with TRIM24-GFP, whereas the signal was negligible in the GFP-only control (mean fold enrichment 0.02). These data demonstrate that TRIM24 and RAD21 are present in the same biochemical complex under these conditions, supporting an association between TRIM24 and cohesin that is consistent with the TurboID results.

To investigate whether TRIM24 domains influence this association, I performed co-immunoprecipitation in HEK293T cells expressing GFP-only, TRIM24-GFP, or TRIM24 mutants (ΔBRD, ΔPHD, ΔRING, ΔHP1, and F979A/N980A) (Fig. 20). Three independent replicates were performed as described above. Western blotting confirmed expression of all constructs, and RAD21 co-immunoprecipitated with each TRIM24 variant, although to varying extents. For the ΔBRD, ΔRING, and ΔHP1 mutants, RAD21 pull-down results were variable across replicates, with one replicate in each case deviating strongly, preventing firm conclusions. By contrast, ΔPHD

consistently showed reduced RAD21 enrichment (mean fold enrichment relative to wild-type 0.45), while the F979A/N980A mutant displayed an even lower association (0.27).

Taken together, these results suggest that the PHD domain and an active BRD contribute to TRIM24-RAD21 association. As co-immunoprecipitation reflects complex-level associations and can be influenced by protein expression and chromatin binding, these data should be interpreted as changes in association rather than definitive loss of binding. Combined with the cohesion phenotypes observed for TRIM24 mutants, these data suggest that TRIM24 association with cohesin may correlate with its role in maintaining sister chromatid cohesion.

2.6. TRIM24 affects transcription of α-satellite higher order repeats

TRIM24 regulates intercentromeric distance during mitosis and prevents premature sister chromatid separation. Because TRIM24 is a transcriptional regulator and centromeric transcription has been implicated in cohesion maintenance, I next tested whether TRIM24 affects transcription of centromeric α-sat HORs [39, 184].

To examine whether TRIM24 modulates centromeric transcription, I quantified RNA levels of p82H and D1Z7 α-sat repeats by RT-qPCR. The p82H sequence is a pan-centromeric α-sat sequence present at all human centromeres, whereas D1Z7 is specific to the centromere of chromosome 1 [4, 41]. This combination allows assessment of both global and locus-specific effects of TRIM24 on centromeric transcription [119]. HEK293T cells were transfected with GFP-only or TRIM24-GFP constructs for overexpression, or depleted of TRIM24 using siRNA (siTRIM24) or control siRNA (siCtrl). Total RNA was extracted and α-sat transcript levels were determined by RT-qPCR. For overexpression experiments, RNA extraction and qPCR were performed by Sohyun Kathy Park, and for TRIM24 depletion experiments, qPCR was performed by Mila Riquier.

In TRIM24-GFP-expressing cells, RT-qPCR confirmed strong overexpression of TRIM24 (mean 25,481-fold change), although variability in expression levels between experiments prevented this increase from reaching statistical significance (Fig. 21c). Strikingly, TRIM24 overexpression increased transcript levels of both p82H and D1Z7 α-satellite repeats (Fig. 21a,b). p82H levels ranged between 1.4- and 2.2-fold change relative to the GFP-only control, and D1Z7 levels between 2.3- and 3.2-fold.

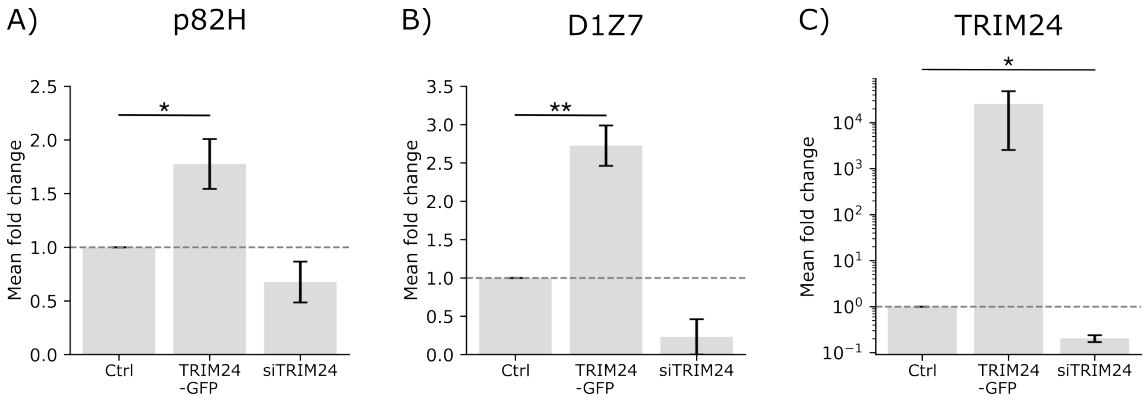


Figure 21.: Alteration in TRIM24 expression changes levels of α-satellite transcription. RT-qPCR quantification of a) p82H, b) D1Z7 α-satellite repeats, and c) TRIM24 transcripts in HEK293T cells expressing GFP-only or the TRIM24-GFP construct, and in cells depleted of TRIM24 using siRNA (siTRIM24) or control siRNA (siCtrl). Fold changes are shown relative to GFP-only or siCtrl conditions. Data represent three independent experiments; for D1Z7 in TRIM24-depleted cells, two independent experiments. Statistical analysis was performed using a t-test; *: $p < 0.05$, **: $p < 0.01$, ***: $p < 0.001$. For details, see Materials and Methods.

TRIM24 depletion (mean 0.20-fold change) was confirmed and was accompanied by a tendency towards reduced p82H and D1Z7 α-satellite repeat transcript levels. p82H expression ranged from 0.29- to 0.87-fold of the siCtrl control, and D1Z7 from 0.001- to 0.46-fold, depending on the efficiency of TRIM24 knockdown. Although these decreases were not statistically significant due to variability in TRIM24 depletion across replicates, both α-satellite repeats displayed a positive relationship between TRIM24 expression level and RNA abundance.

Together, these results indicate that TRIM24 perturbation influences centromeric transcription. Overexpression of TRIM24 enhances transcription of α-satellite repeats, while TRIM24 depletion tends to reduce their expression, although this effect could not be statistically confirmed because of experimental variability.

2.7. Contributions

I want to thank and acknowledge the following scientists for their contribution to this work:
-**Prof. Kyle Miller, Emory, USA** - kindly provided TRIM24 mutant plasmids
-**Dr. Christine Blattner, KIT** - generously provided the LNCaP FGC cell line
-**Dr. Samuel Corless** - established REDPOINT analysis
-**Sohyun Kathy Park** - performed RNA extraction and qPCR from cells overexpressing TRIM24
-**Tamara Fischer** - performed TRIM24 depletion for the PSCS experiments and quantified PSCS in TRIM24-depleted cells.
-**Mila Riquier** - performed qPCR on TRIM24-depleted cells

Bioinformatic analyses were performed using bwForCluster Helix. I acknowledge support by the state of Baden-Württemberg through bwHPC and the German Research Foundation (DFG) through grant INST 35/1597-1 FUGG.

3. Discussion

Centromeres form the chromatin platform required for kinetochore assembly and the maintenance of sister chromatid cohesion, thereby ensuring faithful chromosome segregation. Increasing evidence indicates that both chromatin state and centromeric transcription contribute to cohesion maintenance; however, the molecular link between these processes remains incompletely understood. Previous screening approaches identified the transcriptional regulator TRIM24 as a potential centromeric protein in human cells. Given its chromatin-binding and regulatory functions, TRIM24 represents a plausible candidate linking transcriptional activity and cohesion maintenance, yet its centromeric localization and function had not been investigated.

In this thesis, I identify TRIM24 as a previously uncharacterized centromeric protein that contributes to sister chromatid cohesion and is positively associated with α-sat transcription. I further dissect how individual TRIM24 domains contribute to its centromeric localization and examine how TRIM24 perturbations affect cohesion and transcriptional activity at the centromere. Together with evidence that TRIM24 associates with the cohesin complex, these results support a model in which TRIM24 engages centromeric chromatin through its chromatin reader domains and helps maintain a chromatin landscape compatible with mitotic cohesion. In the following sections, I discuss these findings in the context of centromere biology and outline how TRIM24 may integrate chromatin recognition, transcriptional activity, and cohesion maintenance.

3.1. TRIM24 associates with centromeric and pericentromeric chromatin

TRIM24 was identified as one of the most strongly enriched centromeric protein candidates by REDPOINT analysis, with several cell lines showing clear enrichment above input controls [44]. TRIM24 was enriched in LNCaP, MOLM-13, and HepG2 cells, whereas MCF7, LNCaP abl, and HCT116 showed depletion (Fig. 4b). Importantly, centromeric enrichment did not correlate with TRIM24 expression levels, indicating that centromeric localization is cell type-specific rather than driven by TRIM24 abundance (Fig. 4c). The consistent enrichment of TRIM24 across multiple independent datasets suggests that these differences are not dataset-specific but instead reflect cell type-specific characteristics.

These observations suggest that TRIM24 recruitment to the centromere is governed by local chromatin features rather than by protein abundance alone. First, TRIM24 localization may depend on the histone modification landscape of centromeric chromatin. TRIM24 does not bind DNA directly but is recruited to chromatin via its tandem PHD-BRD domains, where the PHD finger recognizes unmethylated H3K4 and the BRD binds acetylated H3K23 [73, 184]. A similar chromatin-dependent recruitment mechanism has been described for HP1 proteins, which associate with pericentromeric regions via recognition of H3K9me3 [94]. Alternatively, TRIM24 localization might be mediated through protein-protein interactions via its RING-B-box-coiled-coil motif [125]. In this context, TRIM28, which belongs to the same TRIM family, localizes to repetitive chromatin through interaction with KRAB domain-containing zinc finger proteins (KRAB-ZNFs) [117]. Together, these observations suggest that TRIM24 centromeric localization is influenced by chromatin state and centromeric protein networks that differ between cell types. Given that TRIM24 is primarily recruited to bulk chromatin through histone mark recognition, it is plausible that chromatin features constitute the primary determinant of centromeric association, while protein-protein interactions further modulate this association.

To further characterize the nature of TRIM24 centromeric association, TRIM24 ChIP-seq datasets were aligned to the T2T-CHM13v2.0 assembly, enabling analysis at the centromeric repeat class level (Fig. 7). In cell lines with REDPOINT TRIM24 enrichment above 1, TRIM24 showed preferential association with active and inactive α-sat HORs, divergent HORs, and HSAT3, whereas enrichment was less pronounced in other repeat classes, such as monomeric α-sat, HSAT1/2, and β- and γ-satellites

(Fig. 8). This distribution suggests that TRIM24 does not bind uniformly across centromeric and pericentromeric repeats but instead associates with specific subsets of centromeric regions in a cell type-dependent manner.

TRIM24 enrichment on both active and inactive α-sat HORs, as well as divergent HORs and HSAT3, suggests that its localization is not restricted exclusively to either the core centromere or the pericentromere. Instead, TRIM24 associates with repeat classes that contribute to functional centromeric domains as well as to higher-order chromatin organization involved in sister chromatid cohesion [102, 119, 142, 166, 166]. This distribution places TRIM24 within centromeric regions that encompass both CENP-A-associated and CENP-A-depleted active α-sat HOR domains, as well as pericentromeric repeats implicated in higher-order chromatin organization and cohesion. However, repeat-class enrichment alone does not resolve whether TRIM24 directly overlaps with kinetochore-associated chromatin or preferentially occupies adjacent regions. Therefore, spatial resolution of TRIM24 localization requires complementary imaging approaches.

Given the lack of intrinsic DNA-binding ability of TRIM24, its distribution within (peri)centromeric repeats supports a model in which centromeric localization depends on the chromatin landscape and/or associated protein interactions rather than on the underlying satellite DNA sequence itself [184]. While the precise histone modification patterns and protein compositions of individual centromeric repeat classes remain to be fully characterized, the observed repeat-class specificity is consistent with chromatin-mediated regulation of TRIM24 localization.

A chromatin-dependent recruitment model is further supported by the cell type-dependent differences in TRIM24 centromeric association. Although centromeric repeat sequences are broadly conserved between human cell lines, their associated chromatin states and interacting proteins can vary [96, 126]. Such variation provides a plausible explanation for why TRIM24 selectively associates with particular centromeric and pericentromeric repeat classes in different cell types.

To assess TRIM24 localization at the cellular level, immunofluorescence analysis was performed *in vivo*. In HEK293T cells, TRIM24 formed distinct nuclear foci that excluded the nucleoli, and a subset of these foci appeared in close proximity to CENP-A foci (Fig. 9). Rather than directly overlapping the CENP-A signal, TRIM24 foci typically flanked CENP-A on one or both sides. This pattern was observed during both interphase and mitosis, indicating that TRIM24 associates with centromeric regions throughout the cell cycle. Quantification supported this

interpretation: the majority of CENP-A foci colocalized with TRIM24 (around 75% of CENP-A foci), whereas only a small fraction of total TRIM24 foci overlapped with CENP-A (2.5% in interphase and 5.2% in mitosis). This indicates that centromeric TRIM24 represents only a subset of nuclear TRIM24, yet the majority of CENP-A foci are positioned adjacent to TRIM24 signal. Additionally, a similar distribution was observed in preliminary experiments conducted in LNCaP cells, suggesting that TRIM24 association with the centromere is robust across multiple cell lines.

The flanking pattern provides spatial information relative to centromeric subdomains. CENP-A occupies only a subset of active α-sat HORs, whereas the surrounding CENP-A-depleted repeats in the core centromere contribute to proper biorientation and error correction [30]. Pericentromeric repeats, including HSAT2 and HSAT3, also lack CENP-A [166]. Preferential localization of TRIM24 outside the CENP-A domain therefore supports its association with CENP-A-depleted active α-sat HORs or pericentromeric repeats without physically overlapping the CENP-A domain, consistent with the repeat-class enrichment observed in the ChIP-seq reanalysis. However, immunofluorescence provides spatial information only relative to CENP-A and does not resolve the underlying repeat arrays bound by TRIM24.

Structural models of human mitotic centromeres propose a bottlebrush organization, in which active α-sat HORs form extended loops with the CENP-A domain at the loop apex [166]. Within this model, active α-sat HORs that are not associated with CENP-A, as well as pericentromeric repeats, are spatially proximal to but distinct from the kinetochore-forming domain. TRIM24 association with these regions would allow centromeric binding without direct overlap with CENP-A, consistent with both the repeat specificity observed by ChIP-seq and the flanking localization pattern observed by immunofluorescence. In such an arrangement, TRIM24 could contribute to the structural or regulatory properties of centromeric chromatin domains that influence chromosome architecture and cohesion [39].

Taken together, the repeat-class specificity observed by ChIP-seq and the spatial organization revealed by immunofluorescence support a model in which TRIM24 associates with defined centromeric and pericentromeric chromatin regions outside the CENP-A domain. This localization is compatible with recruitment via histone modification binding or protein-protein interactions and positions TRIM24 in regions relevant for higher-order centromeric organization, α-sat transcription, and sister chromatid cohesion [39, 143]. While these observations do not establish a direct

mechanistic role for TRIM24 in these processes, they provide insight into how TRIM24 associates with centromeres and how it may contribute to centromeric chromatin regulation.

3.2. TRIM24 centromeric localization depends on PHD and RING domains

To determine which TRIM24 domains mediate recruitment to the centromere, I examined a series of TRIM24 domain deletion mutants during mitosis. The analysis showed that the PHD and RING domains are important for centromeric localization during mitosis, whereas the BRD domain modulates TRIM24 distribution without being strictly required for targeting.

Deletion of the PHD domain caused the strongest disruption of centromeric localization (Fig. 12-13). TRIM24ΔPHD was largely excluded from chromatin and showed severely reduced colocalization with CENP-A during mitosis, indicating that the PHD domain is a major determinant of stable centromeric recruitment. The PHD domain of TRIM24 recognizes unmethylated H3K4 [184]. Although centromeric chromatin displays substantial levels of H3K4me2, centromeric and pericentromeric regions are likely to contain unmethylated H3K4 [18]. The splice variant C of the speckle protein Sp100 localizes to the centromere via its PHD domain, which recognizes H3K4me0 [206]. Additionally, ATRX recognizes H3K4me0 through its ADD domain and binds to pericentromeric chromatin [53]. This indicates that H3K4me0 is locally available within centromeric and pericentromeric regions. In this context, TRIM24 might use H3K4me0 for centromeric recruitment through its PHD domain.

Deletion of the BRD domain resulted in a distinct phenotype. TRIM24ΔBRD accumulated in the cytoplasm but was still detectable at centromeres during mitosis (Fig. 12-13). This indicates that the BRD domain is not required for centromeric targeting but contributes to overall subcellular distribution. During the preparation of this thesis, a study identified two nuclear localization sequences (NLS-1 and NLS-2) within TRIM24, with NLS-1 localized within the BRD domain [191]. In this study, the C-terminal NLS-2 was shown to function as the primary nuclear localization signal, whereas deletion of NLS-1 alone did not impair nuclear distribution. Importantly, the TRIM24ΔBRD construct used in this work removes the entire BRD domain, including NLS-1, and therefore represents a substantially larger structural perturbation of the

C-terminal region than selective deletion of NLS-1 alone. It is therefore possible that disruption of the BRD domain may indirectly influence nuclear localization, for example by altering protein conformation or the accessibility of NLS-2, rather than through loss of NLS-1 itself [1]. Consistent with this interpretation, TRIM24ΔBRD retained centromeric association once present in the nucleus, indicating that the BRD domain is not strictly required for centromeric targeting.

The RING domain emerged as the second critical determinant of centromeric localization. TRIM24ΔRING was largely excluded from the nucleus and retained only weak centromeric signal during mitosis (Fig. 12-13). Although the RING domain has E3 ubiquitin ligase activity, the observed phenotype could arise from several, not mutually exclusive, mechanisms. RING deletion has been reported to increase TRIM24 stability and disrupt subcellular distribution, but a contribution of the ligase activity itself cannot be excluded [79]. One possibility is that the RING domain contributes to interactions with centromeric proteins. RING domains of many TRIM proteins self-associate into stable dimers to support E3 ligase activity [56]. In contrast, RING domains of class VI TRIM proteins, including TRIM24 and TRIM28, are not capable of self-association and do not show robust E3 ligase activity on their own [171]. It has been proposed that this class requires additional binding partners to assemble an active ligase complex and thereby avoid non-specific ubiquitination of chromatin proteins [171]. TRIM24 can form complexes with TRIM28, which localizes to pericentromeric chromatin, through their RING-B-box-coiled-coil domains [73, 117]. If RING-dependent interactions with TRIM28 or other centromeric proteins contribute to TRIM24 recruitment, ΔRING would be unable to engage these partners and would fail to localize efficiently to centromeres. An alternative possibility is that TRIM24 ubiquitinates substrates in a way that stabilizes its own chromatin association. Ubiquitination targets of TRIM24 remain poorly characterized, but TRIM24-mediated polyubiquitination of ULK1 has been reported to stabilize ULK1 [38]. By analogy, TRIM24-dependent ubiquitination of centromeric chromatin could increase TRIM24 residence time, and loss of the RING domain could reduce centromeric binding stability. Taken together, altered protein stability, impaired RING-dependent complex formation, and loss of RING-dependent enzymatic activity could all contribute to the reduced centromeric localization of ΔRING.

Deletion of the HP1-binding domain did not visibly alter the centromeric or chromosomal distribution of TRIM24 during mitosis, indicating that HP1 interaction is not required for centromeric recruitment (Fig. 12-13). Although centromeric chromatin is enriched in HP1 proteins, the interaction between TRIM24 and HP1 appears to be dispensable for stable centromeric targeting of TRIM24[132, 137].

Taken together, these findings suggest that TRIM24 relies primarily on two features for centromeric localization: chromatin recognition via the PHD domain and structural and/or functional contributions mediated by the RING domain. The BRD domain is not strictly required for initial centromeric targeting but influences nuclear availability and regulates the spatial organization of TRIM24 at centromeres. This domain dependence is consistent with the selective TRIM24 association with centromeric and pericentromeric chromatin and supports the idea that TRIM24 recruitment to centromeric chromatin is mechanistically distinct from recruitment to non-centromeric chromatin, where the BRD domain plays a more prominent role.

3.3. Bromodomain mutation causes abnormal TRIM24 foci formation at the centromeres

The TRIM24 BRD point mutant F979A/N980A caused the formation of large foci localized to centromeric regions in both interphase and mitosis (Fig. 14-17). This phenotype was not observed in the ΔBRD mutant or GFP-only controls. Wild-type TRIM24 occasionally formed foci in interphase, but these did not persist in mitosis. The absence of large centromeric foci in ΔBRD indicates that the presence of the BRD domain is required for this phenotype and that disruption of the BRD binding pocket alters TRIM24 behavior in a way that promotes abnormal retention at centromeres. The F979A/N980A mutation disrupts the H3K23ac binding pocket without removing the overall bromodomain structure, which may allow centromeric recruitment to persist while altering interaction dynamics [184].

Perturbation of chromatin reader domains has been shown to alter protein-chromatin interactions and promote the formation of large nuclear foci [1]. For example, BRD4 forms transcription-associated condensates, and disruption of its bromodomains can change the size and number of these structures [174, 207]. Similarly, HP1 proteins can form heterochromatin-associated condensates, and mutation of

their H3K9me-binding module leads to abnormal foci that no longer localize properly to heterochromatin [162]. These examples illustrate that impaired reader-domain function can shift chromatin regulators into aberrantly clustered states.

In the case of TRIM24, the presence of large centromeric foci suggests that the F979A/N980A mutant remains capable of centromeric recruitment but exhibits altered chromatin engagement or impaired release. PHD-mediated recognition of H3K4me0 may be sufficient to recruit the F979A/N980A mutant protein to centromeres, whereas disruption of the bromodomain may interfere with interaction dynamics that normally limit centromeric retention [184]. In addition, loss of BRD-dependent interactions at non-centromeric chromatin could shift the effective binding distribution of the mutant toward centromeric and pericentromeric regions, where PHD-mediated binding is sufficient. Such redistribution may also reflect altered interaction kinetics, for example reduced dissociation from centromeric chromatin or associated protein complexes, leading to increased local retention. Together, these observations support a model in which the BRD domain fine-tunes TRIM24 chromatin interactions and limits excessive centromeric clustering.

Reduced H3K23 acetylation at centromeric regions has been reported in non-mammalian systems. For example, H3K23ac levels are low at centromeres in rice [112]. If a similar chromatin environment exists at human centromeres, this would be consistent with a limited ability of the BRD domain to engage centromeric chromatin. In such a context, the BRD domain could modulate TRIM24 centromeric retention in response to low H3K23ac levels, thereby restricting excessive accumulation at centromeres.

TRIM24 F979A/N980A foci formation showed a clear dependence on expression level (Fig. 17c,d). Cells expressing low levels of the mutant displayed fewer and smaller centromeric foci, whereas high expression levels resulted in large foci spanning extended chromosomal regions. This dose dependence is consistent with concentration-driven clustering behavior, in which exceeding a critical protein concentration promotes the formation of large assemblies [2]. TRIM24 has recently been reported to form biomolecular condensates upon overexpression [38, 207]. In this context, the F979A/N980A mutation may increase the tendency of TRIM24 to form stable, mitotically persistent clusters.

Notably, F979A/N980A foci were primarily observed at centromeric and pericentromeric regions rather than broadly across chromosome arms, indicating that centromeric chromatin provides a permissive environment for accumulation of the

mutant protein (Fig. 15). The absence of similar foci in ΔBRD further indicates that an intact BRD domain is required for this abnormal accumulation, even though BRD function is not essential for basic centromeric targeting.

Taken together, these findings indicate that the BRD domain is not required for centromeric targeting but contributes to regulating TRIM24 dynamics and preventing abnormal retention at centromeres. The F979A/N980A phenotype highlights a regulatory role of the BRD domain in shaping TRIM24 distribution and centromeric behavior, providing a foundation for understanding how dysregulated TRIM24 accumulation at centromeres could impact centromeric chromatin organization.

3.4. TRIM24 contributes to mitotic cohesion

TRIM24 supports sister chromatid cohesion during mitosis, as reflected by changes in premature sister chromatid separation (PSCS) and intercentromeric distance. Reduced cohesion upon TRIM24 depletion and increased cohesion upon TRIM24 overexpression support the idea that TRIM24 acts as a positive regulator of centromeric cohesion (Fig. 18-19). Given that TRIM24 localizes to centromeric and pericentromeric chromatin domains implicated in cohesion maintenance, this function is likely linked to TRIM24 activity at the centromere rather than representing a purely indirect effect.

Mitotic cohesion is mediated by the cohesin complex, composed of SMC1, SMC3, RAD21, and either STAG1 or STAG2, which form a ring that encompasses sister chromatids [11]. During prophase, cohesion on chromosome arms is removed by the PDS5-WAPL pathway, whereas centromeric cohesion is protected from removal and cleavage by SGO1-PP2A [116, 130]. Loss of centromeric cohesion typically causes PSCS [31]. Intercentromeric distance provides a quantitative readout of centromeric cohesion, although it can also be influenced by spindle tension and changes in centromeric chromatin structure [114]. In this context, TRIM24 emerges as a centromeric protein that may contribute either directly to cohesion maintenance or to the chromatin environment that supports cohesin function at centromeres.

Analysis of TRIM24 domain mutants supports the importance of proper centromeric engagement for TRIM24-mediated cohesion. Deletion of the PHD or RING domains caused cohesion defects comparable to TRIM24 depletion, consistent with a model in which TRIM24 must be correctly associated with centromeric chromatin to support sister chromatid cohesion (Fig. 18-19). Since the PHD and RING domains

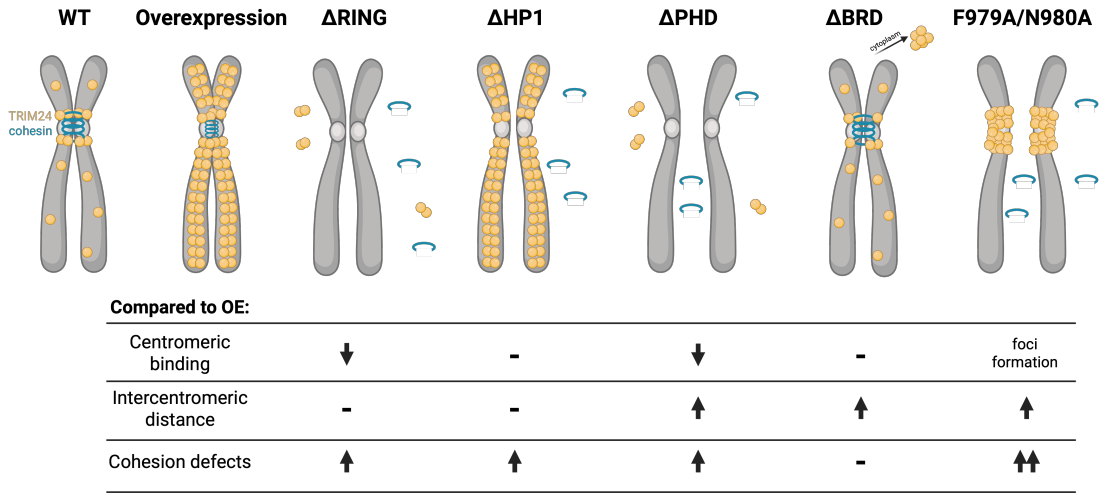


Figure 22.: Balanced centromeric association of TRIM24 contributes to mitotic cohesion. Schematic overview of the centromeric association of TRIM24 and TRIM24 mutants (ΔRING, ΔHP1, ΔBRD, ΔPHD and F979A/N980A) during mitosis. TRIM24 is depicted in yellow and cohesin in blue. The schematic illustrates differences in chromosomal distribution and centromeric localization of TRIM24 mutants and their impact on centromeric cohesion. Below, a summary table compares the effects of TRIM24 mutant overexpression on centromeric localization, intercentromeric distance, and cohesion defects relative to wild-type TRIM24 overexpression. Created with BioRender.com.

contribute to centromeric chromatin engagement and structural and/or functional integrity, respectively, loss of these domains likely reduces centromeric association or impairs centromeric functions of TRIM24.

Additional enzymatic function can be speculated for RING domain. TRIM24-dependent ubiquitination events could modulate the stability or activity of cohesin-associated proteins or chromatin components, thereby influencing cohesin residence time. In yeast, the RING ligase Brl1 monoubiquitinates histone H2B, which is needed for cohesion maintenance and correct chromosome segregation [155]. Similar role has been shown for E3 ligase RNF20 in human [105]. If TRIM24 works in a similar way, it could modify histones or cohesin-associated proteins at (peri)centromeres in a way that alters recruitment or post-translational modification of cohesion factors, influencing cohesion maintenance. This possibility remains to be experimentally tested.

Deletion of the BRD domain resulted in a milder phenotype. Intercentromeric distance was increased, whereas PSCS was not significantly affected (Fig. 18-19). Given that ΔBRD potentially perturbs NLS sequences, this phenotype is likely influenced by reduced nuclear availability rather than by direct loss of bromodomain function at centromeres. Consistent with this interpretation, TRIM24ΔBRD was still

able to localize to centromeres once present in the nucleus. Increased intercentromeric distance without pronounced PSCS is often interpreted as an altered centromeric chromatin state rather than complete loss of cohesion [114].

In contrast, the TRIM24 F979A/N980A mutant, which preserves nuclear localization and overall domain architecture while disrupting H3K23ac recognition, exhibited the strongest cohesion defects, with increased intercentromeric distances and marked PSCS (Fig. 18-19). This severe phenotype is consistent with its aberrant centromeric retention and supports a model in which proper regulation of TRIM24 centromeric association, rather than mere presence, is critical for cohesion.

Deletion of the HP1-binding domain did not alter intercentromeric distance but led to increased PSCS (Fig. 18-19). This indicates that HP1 interaction is not required for basic centromeric targeting or overall centromere structure but contributes to cohesion maintenance once TRIM24 is bound to centromeres. HP1 proteins are known contributors to centromeric cohesion [86]. HP1α and HP1γ bind H3K9me2/3 and have been linked to recruitment of factors that counteract WAPL-mediated cohesin release, including pathways involving Haspin kinase [202]. HP1 also contributes to recruitment of ATRX to centromeres, which has been implicated in limiting cohesin release [204]. If TRIM24 supports cohesion through HP1-dependent interactions, deletion of the HP1-binding domain could weaken these stabilizing mechanisms, providing a plausible explanation for increased PSCS without a strong effect on intercentromeric distance.

Another possibility is that TRIM24 influences cohesion maintenance through pathways involving SGO1. SGO1 is required for faithful chromosome segregation, and SGO1 depletion causes phenotypes that overlap with cohesion defects observed upon TRIM24 depletion [91, 130]. Although a direct role of TRIM24 in regulating SGO1 has not been tested, the centromeric localization of TRIM24 and the observed cohesion phenotypes make this a plausible hypothesis.

Taken together, these findings suggest that TRIM24 positively contributes to centromeric cohesion and that this function depends on correct centromeric engagement and regulated chromatin interactions, including HP1 interaction. The observed cohesion phenotypes are consistent with a model in which TRIM24 acts at centromeric chromatin to support cohesin function, although the direct molecular mechanism remains to be defined.

3.5. TRIM24 associates with cohesin subunit RAD21

TRIM24 associates with the cohesin subunit RAD21, suggesting that TRIM24 can be part of a cohesin-associated protein network. Co-immunoprecipitation experiments in cells overexpressing wild-type TRIM24 showed that RAD21 co-precipitates with TRIM24, whereas the signal in GFP-only controls was negligible (Fig. 20). Under these conditions, TRIM24 and cohesin can therefore be recovered within the same biochemical complex. In addition, TurboID proximity labelling identified multiple cohesin-related proteins, including STAG2, RAD21, and WAPL, in proximity to TRIM24 [90]. Together, these findings place TRIM24 within a cohesion-associated interaction network, although they do not establish whether the association is direct or where in the nucleus it occurs.

Analysis of TRIM24 domain mutants showed domain-dependent differences in RAD21 association (Fig. 20). Deletion of the PHD domain consistently resulted in reduced RAD21 co-precipitation, whereas RAD21 association with ΔBRD, ΔRING, and ΔHP1 mutants was variable across replicates, preventing strong conclusions for these constructs. The BRD point mutant F979A/N980A showed the lowest RAD21 association, consistent with its abnormal centromeric retention and pronounced cohesion defects. Together with the cohesion phenotypes, these observations support a model in which TRIM24 centromeric localization and retention contribute to its association with cohesin-associated factors. In this context, the PHD domain may position TRIM24 on centromeric chromatin, while the BRD domain may limit abnormal retention in a manner that permits normal engagement with cohesin or cohesin-associated proteins.

If the TRIM24-RAD21 association reflects a centromeric interaction, several mechanisms are possible. Centromeric cohesin levels are determined by a balance between retention and release pathways, including SGO1-PP2A-mediated protection and WAPL-mediated removal [61]. TRIM24 could influence this balance by stabilizing centromeric cohesin or by modulating access of release factors such as WAPL to centromeric cohesin. The reduced RAD21 association observed for ΔPHD is consistent with a requirement for chromatin-bound TRIM24 in such a model. However, the present data do not address whether TRIM24 interacts directly with SGO1, WAPL, or other cohesion regulators, and these possibilities remain speculative.

Alternatively, the association between TRIM24 and RAD21 may occur outside centromeres. Cohesin plays a central role in genome folding by forming chromatin loops and topologically associating domains [40, 148]. Given that TRIM24 functions as a transcriptional co-regulator, association with RAD21 could reflect interactions at promoter or enhancer chromatin rather than at centromeric chromatin [148, 184]. Distinguishing between centromeric and non-centromeric interactions will require approaches that localize the interaction spatially within the nucleus and along the genome.

Taken together, these findings indicate that TRIM24 can associate with the cohesin subunit RAD21 and that domains required for chromatin engagement and centromeric localization contribute to this association. This is consistent with a model in which TRIM24 is part of a cohesin-associated protein network and may influence cohesion through chromatin-associated mechanisms, thereby providing a link between chromatin state and cohesion.

3.6. TRIM24 levels correlate with transcription of active α-satellite higher order repeats

Analysis of core centromeric α-sat repeats, including p82H (present on all human centromeres) and D1Z7 (specific to chromosome 1), revealed a positive correlation between TRIM24 levels and transcription of active α-sat repeats (Fig. 21) [41]. Overexpression of TRIM24 led to a significant increase in expression of both p82H and D1Z7, indicating that elevated TRIM24 levels can enhance α-sat transcription. Although TRIM24 depletion did not reach statistical significance due to variability in knockdown efficiency, both p82H and D1Z7 were reduced in all replicates. Together, these data support a positive relationship between TRIM24 abundance and transcription of active centromeric α-sat repeats.

Compared with established centromeric transcription regulators, the magnitude of this effect is modest. For example, ZFAT has been shown to increase α-sat transcription on chromosome 17 by more than 100-fold [78]. ZFAT is a zinc-finger transcription factor that binds centromeric DNA motifs and recruits the histone acetyltransferase KAT2B, leading to H4K8 acetylation and BRD4-dependent transcriptional activation [78]. In contrast, TRIM24 is a chromatin reader that does not bind DNA directly [12]. Thus, the relatively small but reproducible increase in p82H

and D1Z7 transcription upon TRIM24 overexpression is more consistent with a role in modulating the local chromatin environment of α-sat HORs rather than acting as a direct transcriptional activator.

One possible model is that TRIM24 stabilizes a chromatin state that permits low-level centromeric transcription, while sequence-specific DNA-binding factors such as ZFAT provide strong transcriptional activation. TRIM24 could also indirectly support transcription by influencing chromatin accessibility or the recruitment of transcriptional regulators, although this remains speculative.

Notably, transcriptional effects of TRIM24 domain mutants were not assessed. This limits conclusions about how TRIM24 centromeric association, α-sat transcription, and cohesion are mechanistically connected. Based on the localization and cohesion phenotypes, overexpression of mutants that impair centromeric recruitment (ΔPHD and ΔRING) would be expected to reduce α-sat transcription. In contrast, the F979A/N980A mutant, which shows abnormal centromeric accumulation, could either increase transcription through aberrant chromatin opening or reduce transcription if foci formation disrupts required interactions. Systematic profiling of centromeric RNA in cells expressing these mutants would be informative and could test whether transcriptional changes correlate with cohesion defects.

Taken together, these results indicate that TRIM24 levels positively correlate with transcription of active α-sat repeats and that TRIM24 can modestly enhance α-sat transcription when overexpressed. However, the relatively small effect size compared with established centromeric transcription factors suggests that TRIM24 is unlikely to function as a primary transcriptional activator. Instead, TRIM24 likely shapes centromeric chromatin in a manner permissive for low-level transcription and supportive of mitotic cohesion.

3.7. TRIM24 as a multifunctional centromeric regulator

The findings discussed in Sections 3.1-3.6 support a model in which TRIM24 functions as a chromatin-bound regulator at centromeric and pericentromeric regions. TRIM24 localizes to defined subsets of α-sat HORs and pericentromeric repeats flanking the CENP-A core domain, displays domain-dependent centromeric association, modulates sister chromatid cohesion, associates with cohesin-related factors,

and modestly influences α-sat transcription. Together, these findings suggest that TRIM24 contributes to centromeric chromatin regulation in a manner that supports cohesion maintenance.

In this model, TRIM24 shows a specific spatial arrangement rather than uniform centromeric binding across all repeats. TRIM24 preferentially associates with active and inactive α-sat HORs, divergent HORs, and HSAT3, and its nuclear foci preferentially flank CENP-A foci rather than overlap with them. Within the bottlebrush model of human centromeres, this pattern is consistent with TRIM24 localizing to CENP-A-depleted α-sat HORs and pericentromeric repeats that are proximal to the CENP-A domain [166]. In this arrangement, TRIM24 would occupy loop segments flanking the CENP-A-containing core, positioning it to influence cohesin-rich pericentromeric chromatin without directly overlapping the CENP-A core.

Centromeric localization is domain dependent and provides a mechanistic basis for this spatial organization. Recruitment of TRIM24 to centromeric and pericentromeric regions is primarily mediated through its PHD domain. Recognition of H3K4me0 provides a plausible mechanism for anchoring TRIM24 to these regions. Similar H3K4me0-dependent centromere-targeting mechanisms have been described for other chromatin readers such as Sp100 and ATRX, which localize to centromeric or pericentromeric chromatin through recognition of this specific histone mark [53, 206]. Consistent with this interpretation, deletion of the PHD domain strongly reduces centromeric localization and results in pronounced cohesion defects. This indicates that chromatin engagement is central to TRIM24 function.

The RING domain represents a second important determinant of centromeric association. Although it remains unclear whether its contribution depends on enzymatic activity, protein stability, or protein-protein interactions, deletion of the RING domain impairs centromeric localization and results in cohesion defects comparable to PHD deletion. Through the RING-B-box-coiled-coil motif (RBCC), TRIM24 can form complexes with other TRIM family members, including TRIM28, which associates with heterochromatin, including pericentromeres [115]. Thus, it is possible that the RING domain contributes to stabilizing TRIM24 at centromeric regions through interactions with other proteins, such as TRIM28.

In contrast, the BRD domain is not strictly required for centromeric targeting but modulates TRIM24 distribution and retention. The F979A/N980A mutant, which disrupts H3K23ac recognition while preserving overall domain structure, forms enlarged centromeric foci and exhibits severe cohesion defects. This suggests that

the BRD domain contributes to dynamic chromatin engagement and limits excessive accumulation at centromeres. Since the TRIM24 BRD and PHD domains function in tandem, it is plausible that the PHD domain acts as the primary localization determinant, while the BRD domain restricts binding to prevent abnormal retention, possibly due to reduced H3K23ac levels at centromeres [112, 184]. In this context, balanced centromeric association of TRIM24 appears to be required for proper cohesion maintenance.

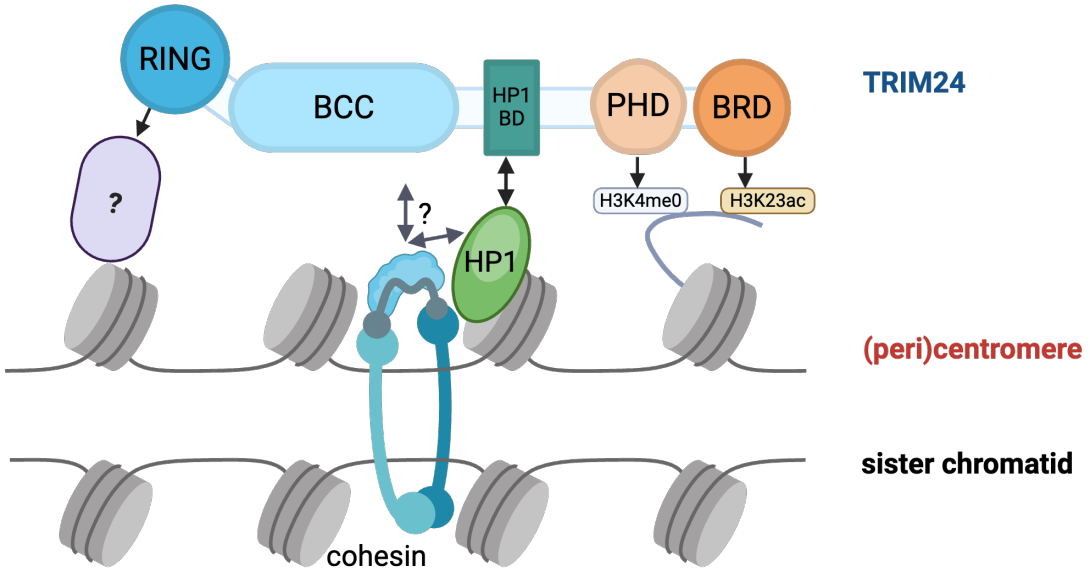


Figure 23.: Proposed model of TRIM24 function at centromeric and pericentromeric chromatin. Schematic representation of TRIM24 domain architecture and its proposed interactions at (peri)centromeres. TRIM24 contains an N-terminal RING domain, a B-box-coiled-coil (BCC) region, an HP1-binding domain (HP1 BD), a plant homeodomain (PHD), and a bromodomain (BRD). The PHD domain recognizes H3K4me0, whereas the BRD domain is proposed to restrict centromeric accumulation, potentially reflecting reduced H3K23ac levels at (peri)centromeres. Through these reader domains, TRIM24 associates with (peri)centromeric nucleosomes, likely in CENP-A depleted regions. The RING domain may contribute to protein-protein interactions and/or ubiquitination of chromatin-associated substrates, thereby stabilizing TRIM24 at these regions. The HP1 BD mediates interaction with HP1 proteins, which may support cohesion maintenance. TRIM24 may associate with the cohesin complex, but it remains unknown whether this interaction is direct or occurs indirectly, for example through HP1. These interactions position TRIM24 as a chromatin-bound regulator that contributes to centromeric chromatin organization and sister chromatid cohesion. Created with BioRender.com.

The cohesion phenotypes position TRIM24 within the centromeric cohesion network. TRIM24 overexpression reduced premature sister chromatid separation, whereas depletion or disruption of key domains increased cohesion defects. Association of TRIM24 with RAD21 and proximity to STAG2 and WAPL further connect TRIM24 to cohesion-associated pathways [90]. Although direct molecular interactions remain to be characterized, the data suggest a model in which chromatin-bound TRIM24 contributes to a centromeric environment that supports cohesin retention.

The HP1-binding domain provides an additional functional link. Deletion of this domain increases PSCS without abolishing centromeric localization, indicating that HP1 interaction contributes to cohesion maintenance after recruitment. Given the established role of HP1 proteins in organizing pericentromeric heterochromatin and supporting cohesion-associated pathways, cooperation between TRIM24 and HP1-rich chromatin domains represents a plausible mechanism [202, 204].

Mechanistically, TRIM24 may influence the balance between cohesin protection and release. By associating with the cohesin complex, TRIM24 could contribute to stabilizing cohesin complexes protected by SGO1-PP2A or modulating WAPL-dependent release [34, 61]. Additionally, RING-dependent ubiquitination of chromatin-associated substrates represents a potential mechanism through which TRIM24 could influence cohesin residence time. These mechanisms are not mutually exclusive and remain to be experimentally defined.

TRIM24 also modestly enhances transcription of active α-sat repeats. The magnitude of this effect is limited compared with sequence-specific factors such as ZFAT, consistent with TRIM24 functioning as a chromatin reader rather than a DNA-binding transcription factor [78]. In this context, TRIM24 likely contributes to a chromatin configuration that permits low-level centromeric transcription. Because centromeric transcription has been implicated in cohesion regulation, this transcriptional modulation may support a cohesion-permissive chromatin state, although this connection remains speculative.

Taken together, the data support a model in which TRIM24 acts as a multifunctional regulator of centromeric chromatin. Through PHD- and BRD-dependent chromatin recognition, RING-supported structural or functional contributions, and interaction with cohesin- and HP1-associated pathways, TRIM24 contributes to maintaining a centromeric environment compatible with stable sister chromatid cohesion. Rather than functioning as a dedicated cohesion factor or primary transcriptional activator, TRIM24 appears to integrate chromatin state, cohesion network interactions, and controlled transcription at CENP-A-depleted centromeric repeats to support faithful chromosome segregation.

3.8. Limitations

Several technical and conceptual limitations should be considered when interpreting the data presented in this thesis.

A first limitation concerns the re-analysis of publicly available TRIM24 ChIP-seq datasets. Alignments were performed using the haploid T2T-CHM13v2.0 reference genome, which does not capture the extensive centromere variation observed across human cell lines, including loss, expansion, or rearrangement of repeat arrays [111, 156]. Alignment to a haploid reference may therefore distort enrichment patterns at individual centromeres. Ideally, future analyses would employ cell line-specific diploid assemblies with resolved centromeres, which are only beginning to become available [190]. Nevertheless, TRIM24 enrichment at α-sat HORs and HSAT3 was observed in multiple independent datasets, and the overall pattern was consistent across enriched cell lines, supporting the conclusion that TRIM24 associates with centromeric chromatin.

A second limitation of the public ChIP-seq analysis relates to technical variability across studies. Published datasets differ in antibodies, library preparation, and sequencing depth, complicating direct quantitative comparisons of TRIM24. REDPOINT evaluates multiple independent ChIP-seq datasets per protein and scores centromeric enrichment relative to the whole genome, but it remains a screening approach and does not replace direct side-by-side profiling under standardized conditions [44].

Short-read ChIP-seq in highly repetitive centromeric regions is further limited by mappability. Multi-mapping reads originating from TRIM24 bound outside the CENP-A domain can be redistributed across the entire HOR array rather than assigned to precise subdomains, generating an apparent signal over the CENP-A peaks even if TRIM24 is depleted from these regions [122, 141]. The flanking immunofluorescence pattern and broad ChIP-seq signal should therefore be interpreted together. Improved resolution will require multi-mapping-aware pipelines combined with ChIP-seq or CUT&RUN approaches applied across multiple cell lines [9, 134].

The immunofluorescence analyses also have limitations. TRIM24 shows broad nuclear chromatin association, and only a subset of foci is centromeric, consistent with its established non-centromeric functions [66, 77, 90, 184]. Moreover, detailed localization and functional experiments were performed in HEK293T cells, which are highly aneuploid and possess a complex karyotype [107]. Although these cells are widely used for centromere and cohesion studies due to their high transfection efficiency and experimental robustness, results obtained in this background may not

fully generalize to near-diploid systems [44, 159, 200]. Preliminary experiments in LNCaP cells indicate a comparable flanking pattern of TRIM24 around CENP-A, but further validation in near-diploid cell lines such as RPE1 will be necessary.

The TRIM24 domain mutant analyses are likewise subject to limitations. All mutants were transiently overexpressed in the presence of endogenous TRIM24, which was not depleted. Overexpression may mask subtle loss-of-function effects, and endogenous TRIM24 may partially compensate. Heterogeneous expression levels complicate quantitative comparisons of localization and cohesion phenotypes. In addition, all constructs were GFP-tagged, which may influence protein conformation or interactions [90]. Definitive assignment of domain-specific functions will require endogenous tagging, stable inducible expression of mutants, and rescue experiments in TRIM24-depleted cells.

The BRD point mutant F979A/N980A introduces an additional caveat. Because this construct was transiently expressed, a wide range of expression levels was observed. Clustering and condensate formation are highly concentration-dependent phenomena, making it difficult to fully separate mutation-specific effects from those driven by local abundance [2]. While the data establish persistent centromeric foci formation, the material properties of these assemblies remain undefined. Live-cell imaging and biophysical assays such as FRAP or *in vitro* reconstitution will be required to determine whether these structures exhibit condensate-like behavior [2, 49].

Interpretation of cohesion phenotypes also requires caution. TRIM24 depletion by siRNA showed variable knockdown efficiency, potentially underestimating the strength of the phenotype. Furthermore, centromeric cohesion is maintained by a cooperative network including cohesin, SGO1, WAPL, HP1 proteins, and additional regulators [71]. The positioning of TRIM24 within this network is currently inferred from phenotypic and proximity data rather than direct pathway analyses. Mechanistic connections to specific cohesion regulators therefore remain to be established.

Similarly, the TRIM24-RAD21 association data do not distinguish between direct and indirect interactions or define the subnuclear location of complex formation. Reciprocal co-IP and endogenous pull-down experiments were not performed, and co-IP of domain mutants was variable. Overexpression of GFP-tagged proteins may exaggerate weak or transient associations, and chromatin binding can influence

co-IP efficiency [208]. Future work will require reciprocal, endogenous, and locus-specific approaches to determine whether TRIM24-RAD21 complexes form directly at centromeres.

Finally, the centromeric transcription analysis has inherent limitations. Centromeric transcription is cell type-dependent and strongly regulated across the cell cycle [170]. qPCR using one generic and one chromosome-specific primer pair provides only a limited view of α-sat RNA levels and does not capture pericentromeric transcripts such as HSAT3. In addition, bulk RNA from asynchronous cells may obscure phase-specific transcriptional effects [170]. More comprehensive approaches, including synchronized analyses and long-read RNA sequencing, will be required to define the full transcriptional impact of TRIM24 perturbation.

Taken together, these limitations indicate that while the data support a role for TRIM24 in centromeric chromatin association, cohesion maintenance, and transcriptional regulation, the precise molecular mechanisms and pathway positioning remain to be resolved.

3.9. Conclusions and Perspectives

In this thesis, I identify TRIM24 as a previously unrecognized centromeric protein that contributes to sister chromatid cohesion. By combining bioinformatic reanalysis of public ChIP-seq datasets with microscopy and functional assays, TRIM24 was shown to associate with defined subsets of centromeric and pericentromeric repeats and to localize adjacent to, but largely excluded from, the CENP-A core domain. This spatial positioning places TRIM24 at the interface between the core centromere and the pericentromere.

Functional analyses demonstrate that TRIM24 positively influences centromeric cohesion. Proper centromeric localization depends on the PHD and RING domains, and perturbation of these domains results in pronounced cohesion defects. TRIM24 associates with cohesin-related factors, including RAD21, and its abundance modestly correlates with α-sat transcription. Together, these findings support a working model in which TRIM24 acts as a chromatin-bound regulator that contributes to a centromeric environment compatible with cohesin maintenance and faithful chromosome segregation.

At the same time, the data raise several mechanistic questions. A central next step will be to directly connect repeat-class occupancy with spatial localization in the same cellular context. Profiling TRIM24 by ChIP-seq or CUT&RUN in the same cell line used for imaging would clarify which centromeric compartments and repeat arrays are occupied and how this relates to the observed flanking pattern. Because many experiments in this thesis relied on transient overexpression, future studies should examine TRIM24 and its mutants at endogenous levels using CRISPR-based tagging, inducible systems, and rescue approaches in TRIM24-depleted cells.

The domain-specific phenotypes raise additional mechanistic questions. For the RING domain, it remains unresolved whether the observed defects reflect loss of enzymatic function, altered protein stability, or disrupted protein-protein interactions. Tethering approaches or separation-of-function mutants could help distinguish these possibilities. For the BRD domain, quantitative binding assays and live-cell imaging will be important to determine whether BRD function primarily regulates TRIM24 chromatin dynamics and retention, and how its disruption leads to abnormal centromeric clustering and severe cohesion defects.

A major open question concerns the positioning of TRIM24 within the established cohesion network. Centromeric cohesin levels are controlled by the balance between SGO1-PP2A-mediated protection and WAPL-dependent release [61]. Given the association of TRIM24 with RAD21 and proximity to STAG2 and WAPL, TRIM24 may influence this balance by stabilizing SGO1-protected cohesin complexes and/or by influencing WAPL-mediated release [90]. Testing whether TRIM24 perturbation alters centromeric localization of SGO1, cohesin residence time, or WAPL recruitment will help clarify whether TRIM24 acts upstream, downstream, or in parallel to known cohesion regulators.

The relationship between TRIM24 and pericentromeric heterochromatin also warrants further investigation. The increased cohesion defects observed upon deletion of the HP1-binding domain suggest a functional interaction with HP1-dependent chromatin organization. Further work should address whether TRIM24 influences HP1 domain structure, chromatin compaction, or recruitment of additional cohesion-supporting factors.

Finally, the modest but consistent effect of TRIM24 on α-sat transcription raises the question of whether transcriptional changes contribute to the cohesion phenotypes or represent a parallel consequence of altered chromatin engagement. Integrating

domain mutants with refined transcriptional profiling and cell-cycle-resolved analyses will help determine whether TRIM24 coordinates transcription and cohesion within a shared chromatin framework.

Overall, this thesis identifies TRIM24 as a centromere-associated chromatin factor that contributes to mitotic fidelity. By defining its spatial positioning relative to the CENP-A core, its domain requirements, and its functional consequences for sister chromatid cohesion, this work expands the set of chromatin readers implicated in centromere regulation.

The findings support a model in which centromeric cohesion is not controlled solely by canonical cohesion factors but can be modulated by chromatin-associated regulators that read histone modifications, interact with cohesion-related proteins, and influence local transcriptional states. In this model, TRIM24 emerges as a chromatin-bound regulator that links centromeric chromatin organization with cohesion maintenance.

Further clarification of how TRIM24 interfaces with cohesin, HP1-dependent chromatin, and centromeric transcription will be necessary to fully define its molecular mechanism. Nevertheless, the data presented here provide a basis for understanding how chromatin readers contribute to the coordination of chromatin architecture and cohesin dynamics to ensure faithful chromosome segregation.

4. Materials and Methods

4.1. Materials

4.1.1. Chemicals and reagents

Table 1.: Chemicals used in this thesis.

Name	**Manufacturer**
2-Propanol	Roth
Aberrior Live 590 DNA dye	Aberrior
Acetic acid	Roth
Acrylamide/Bisacrylamide (37.5:1)	Roth
Ammonium persulfate (APS)	AppliChem
β-Mercaptoethanol	AppliChem
Bromophenol blue	AppliChem
Calcium chloride dihydrate	AppliChem
Chloroform	Roth
Dimethyl sulfoxide (DMSO)	Sigma-Aldrich
DL-Dithiothreitol (DTT)	Sigma-Aldrich
EDTA disodium dihydrate	Roth
EGTA	AppliChem
Ethanol	Roth
Glycerol	Roth
Glycine	Sigma-Aldrich
HEPES	AppliChem
Hydrochloric acid (37%)	Roth
Magnesium chloride	Invitrogen
Methanol	Roth
Nonidet P-40 (NP-40)	AppliChem
Paraformaldehyde (PFA)	AppliChem

Continued on next page

Table 1 – continued from previous page

Name	Manufacturer
Phenol	AppliChem
Phenol/Chloroform/Isoamyl alcohol (25:24:1)	Roth
Phenylmethylsulfonyl fluoride (PMSF)	Sigma-Aldrich
Potassium chloride (KCl)	AppliChem
Potassium hydroxide (KOH)	Roth
SNAP-Cell 647-SiR	NEB
Sodium chloride (NaCl)	AppliChem
Sodium dodecyl sulfate (SDS)	AppliChem
Sodium citrate	Sigma-Aldrich
TEMED	AppliChem
Tergitol solution (NP-40 type)	Sigma-Aldrich
Tris base	AppliChem
Tris-Hydrochloride	AppliChem
Triton X-100	Merck
Tween 20	AppliChem
Vectashield with DAPI	Biozol
Zeiss Immersion Oil 518F	Fisher Scientific

Table 2.: Reagents used in this thesis.

Name	Manufacturer
Agarose	Th. Geyer
Bovine serum albumin (BSA)	AppliChem
cOmplete, EDTA-free protease inhibitor cocktail tablets	Roche
dNTPs	NEB
DAPI	Sigma-Aldrich
DNA Ladder 1 kb Plus	NEB
Ethidium bromide solution (1%)	AppliChem
Fast SYBR Green Master Mix	Fisher Scientific
Gel Loading Dye, Purple (6×)	NEB
GlycoBlue Coprecipitant	Thermo Fisher
LB agar	Roth
Lipofectamine LTX Plus	Thermo Fisher

Continued on next page

Table 2 – continued from previous page

Name	Manufacturer
Lipofectamine RNAiMAX	Thermo Fisher
Nuclease-free water	Thermo Fisher
Poly-L-lysine solution (0.1%)	Sigma-Aldrich
ProSieve QuadColor Protein Marker	Biozym Scientific
Ribonucleotide solution set	NEB
RNaseZAP	Sigma-Aldrich
RNasin Plus RNase Inhibitor	Promega
Skim milk powder	AppliChem
Trans-Blot Turbo 5× Transfer Buffer	Bio-Rad
Trypan Blue	Sigma-Aldrich
TRIzol	Thermo Fisher

4.1.2. Buffers and solutions

Table 3.: Composition of buffers and solutions used in this thesis.

Buffer/Solution	Composition
Immunofluorescence (IF)	
10× Phosphate-buffered saline (PBS)	137 mM NaCl 2.7 mM KCl 10 mM Na_2HPO_4 1.8 mM KH_2PO_4 in ddH_2O
4% Paraformaldehyde (PFA)	40 g/L paraformaldehyde 1.5 mM KOH in 1× PBS
Permeabilization solution	0.1% Triton X-100 in 1× PBS
Blocking solution	4% BSA in 1× PBS
SDS-PAGE and Western blot	
Lysis buffer	0.1% SDS 1× cOmplete protease inhibitor cocktail BaseMuncher (0.5 μL per 10 mL)

Continued on next page

Table 3 – continued from previous page

Buffer/Solution	Composition
	in ddH_2O
4× Laemmli buffer	0.5% β-mercaptoethanol 0.02% bromophenol blue 10% glycerol 2% SDS 50 mM Tris-HCl (pH 6.8) in ddH_2O
Separation gel (10%)	375 mM Tris-HCl (pH 8.8) 10% acrylamide/bisacrylamide (37.5:1) 0.1% SDS 0.05% APS 0.1% TEMED in ddH_2O
Stacking gel (4%)	125 mM Tris-HCl (pH 6.8) 4% acrylamide/bisacrylamide (37.5:1) 0.1% SDS 0.05% APS 0.1% TEMED in ddH_2O
SDS running buffer	25 mM Tris 192 mM glycine 0.1% SDS in ddH_2O
Tris-buffered saline with Tween 20 (TBST)	20 mM Tris-HCl (pH 7.5) 150 mM NaCl 0.1% Tween 20 in ddH_2O
Western blot blocking solution	5% skim milk powder in 1× TBST
Trans-Blot Turbo transfer buffer	1× transfer buffer (Bio-Rad) 20% ethanol in ddH_2O
Stripping solution (low pH)	200 mM glycine 0.1% SDS 1% Tween 20

Continued on next page

Table 3 – continued from previous page

Buffer/Solution	Composition
	HCl to pH 2.2 in ddH_2O
Immunoprecipitation (IP)	
IP lysis buffer	25 mM Tris-HCl (pH 7.5) 150 mM NaCl 1% Triton X-100 2 mM PMSF 1× cOmplete protease inhibitor cocktail in ddH_2O
Metaphase and methanol spreads	
Hypotonic solution	0.5% sodium citrate in ddH_2O
Methanol:acetic acid fixative	Methanol:acetic acid (3:1)
75 mM KOH solution	75 mM KOH in ddH_2O
Gel electrophoresis	
50× Tris-acetate-EDTA (TAE)	2 M Tris base 1 M acetic acid 50 mM EDTA in ddH_2O

4.1.3. Antibodies

Table 4.: Antibodies used in this thesis.

Antigen	Dilution	Host species	Catalog number	Manufacturer
Primary antibodies				
TRIM24	IF: 1:500 WB: 1:1,000	Rabbit	ab256491	Abcam
GFP	IF: 1:500 WB: 1:1,000	Chicken	A10262	Thermo Fisher
CENP-A	IF: 1:500	Mouse	ADI-KAM-CC006-E	Enzo Life Sciences

Continued on next page

Table 4 – continued from previous page

Antigen	Dilution	Host species	Catalog number	Manufacturer
α-Tubulin	WB: 1:5,000	Mouse	T9026	Sigma-Aldrich
RAD21	WB: 1:1,000	Rabbit	ab992	Abcam
H3Ser10P	IF: 1:1,000	Rabbit	06-570	Sigma-Aldrich
RNA Polymerase II Ser2P	IF: 1:200	Rabbit	ab193468	Abcam
Secondary antibodies				
Anti-mouse Alexa Fluor 488	1:500	Goat	A-11001	Thermo Fisher
Anti-rabbit Alexa Fluor 488	1:500	Goat	A-11008	Thermo Fisher
Anti-chicken Alexa Fluor 488	1:500	Goat	A-11039	Thermo Fisher
Anti-rabbit Alexa Fluor 546	1:500	Goat	A-11010	Thermo Fisher
Anti-mouse Alexa Fluor 647	1:500	Goat	A-21235	Thermo Fisher
Anti-mouse HRP-conjugated	1:10,000	Rabbit	A9044	Sigma-Aldrich
Anti-rabbit HRP-conjugated	1:5,000	Goat	A0545	Sigma-Aldrich
Anti-chicken HRP-conjugated	1:5,000	Rabbit	A9046	Sigma-Aldrich

4.1.4. Enzymes

Table 5.: Enzymes used in this thesis.

Name	Manufacturer
BaseMuncher	Abcam
DpnI	NEB
Q5 DNA Polymerase	NEB
RedLoad Taq Master Mix (5×)	Jena Bioscience
RNase A	Qiagen

Continued on next page

Table 5 – continued from previous page

Name	Manufacturer
TURBO DNase	Thermo Fisher

4.1.5. Kits

Table 6.: Kits used in this thesis.

Name	Manufacturer
Click-iT RNA Alexa Fluor 488 Imaging Kit	Thermo Fisher
Mini-PROTEAN TGX gels (4-20%, 10-well)	Bio-Rad
NucleoBond Xtra Midi Kit for plasmid DNA	Macherey-Nagel
NucleoSpin Gel and PCR Clean-up	Macherey-Nagel
NucleoSpin Plasmid	Macherey-Nagel
QuantiTect Reverse Transcription Kit	Qiagen
SuperSignal West Femto Maximum Sensitivity Substrate	Thermo Fisher
SuperSignal West Pico Chemiluminescent Substrate	Thermo Fisher

4.1.6. Antibiotics

Table 7.: Antibiotics used in this thesis.

Name	Manufacturer
Ampicillin sodium salt	Sigma-Aldrich
G-418 disulfate salt solution	Merck
Penicillin-Streptomycin (100×)	Capricorn Scientific

4.1.7. Bacterial strains

Table 8.: Bacterial strains used in this thesis.

Name	Source
Escherichia coli DH5α	Erhardt Lab

4.1.8. Cell lines

Table 9.: Cell lines used in this thesis.

Name	Source
HEK293T	Erhardt Lab
HeLa SNAP-CENP-A	Erhardt Lab
HeLa SNAP-CENP-A Pol II Ser2P-sfGFP mintbody	This study
LNCaP clone FGC	Kindly provided by Dr. Christine Blattner (KIT)

4.1.9. Cell culture reagents

Table 10.: Cell culture reagents used in this thesis.

Name	Manufacturer
Colcemid solution (10 μg/mL) in DPBS	Capricorn Scientific
DMEM, high glucose, GlutaMAX supplement	Gibco
Dulbecco's PBS (1×), without Ca^{2+} and Mg^{2+}, without phenol red	Capricorn Scientific
Fetal bovine serum (FBS)	BioWest
Fetal bovine serum (FBS), charcoal-stripped	Fisher Scientific
Opti-MEM, reduced serum medium	Gibco
RPMI 1640 medium with GlutaMAX supplement	Gibco
Sodium pyruvate (100 mM)	Gibco
Trypsin-EDTA (0.05%) in HBSS (1×) with phenol red	Capricorn Scientific

4.1.10. Primers

Table 11.: Primers used in this thesis.

Primer	Sequence (5'-3')	Target region
Sequencing		
CMV FD sequencing	CGCAAATGGGCGGTAGGCGTG	CMV promoter
seqTRIM24 901 FW1	AATCAAAAGCAGGTGGAACAGG	TRIM24 gene at +901 bp
seqTRIM24 1836 FW2	TCCCTCTCTTCCGGATATTGAC TGT	TRIM24 gene at +1836 bp

Continued on next page

Table 11 – continued from previous page

Primer	Sequence (5'-3')	Target region
seqTRIM24 2514 FW3	CCTCTGCTGTGAAAAGTGCCC CA	TRIM24 gene at +2514 bp
Mutagenesis		
T24 dHP1 mut FW	GAGCCAATTCGAATAAAAC	Deletion of HP1-binding domain in TRIM24
T24 dHP1 mut RV	GACTTTGTGTGTAGAGTC	Deletion of HP1-binding domain in TRIM24
T24 VDLN mut FW	AGTGGATATGAACGAGCC AATTCGAATAAAACAAGAA	Mutagenesis of TRIM24 HP1BD (V733D, L735N)
T24 VDLN mut RV	TCGTTCATATCCACTGGGACTT TGTGTGTAGAGT	Mutagenesis of TRIM24 HP1BD (V733D, L735N)
qPCR		
qTRIM24 FW 2	CGGTCAGCGGCTCGTC	*TRIM24*
qTRIM24 REV 2	TCACAGCTTGTACATACCTG ATTT	*TRIM24*
GAPDHF 018a	CCACTCCTCCACCTTTGAC	*GAPDH*
GAPDHR 018b	ACCCTGTTGCTGTAGCCA	*GAPDH*
D1Z7 002a	GTTCCCTTAGACAGAGCAGA TTT	α-satellite repeat D1Z7
D1Z7 002b	CAACGCAGTTTGTGGGAATG	α-satellite repeat D1Z7
p82HF	ATGTTTGCATTCAACTCACAG AG	α-satellite repeat p82H
p82HR	CAACACAGTCCAAATATCCAG TTG	α-satellite repeat p82H

4.1.11. Plasmids

Table 12.: Plasmids used in this thesis.

Name	Source
pcDNA6.2/N-EmGFP-TRIM24	Addgene #65396
pcDNA3.1-GFP-TRIM24-delBRD	Gift from Prof. Kyle Miller (Emory University, USA)

Continued on next page

Table 12 – continued from previous page

Name	Source
pcDNA3.1-GFP-TRIM24-delPHD	Gift from Prof. Kyle Miller (Emory University, USA)
pcDNA3.1-GFP-TRIM24-delRING	Gift from Prof. Kyle Miller (Emory University, USA)
pcDNA6.2/N-EmGFP-TRIM24-delHP1	This study
pcDNA3.1-GFP-TRIM24-F979A/N980A	Gift from Prof. Kyle Miller (Emory University, USA)
pcDNA3.1-FLAG-MCS-EGFP (GFP-only control)	Erhardt lab
PB533-42B3mutAC2-sfGFP (Pol II Ser2P mintbody)	Gift from Prof. Hiroshi Kimura (Institute of Science Tokyo, Japan)
pcDNA3.1-GFP-TRIM24-C840W	Gift from Prof. Kyle Miller (Emory University, USA)
pcDNA5FRT/TO-GFP-TRIM24-K723R	Gift from Prof. Kyle Miller (Emory University, USA)
pcDNA5FRT/TO-GFP-TRIM24-K741R	Gift from Prof. Kyle Miller (Emory University, USA)
pcDNA6.2/N-EmGFP-TRIM24-V733D/L735N	This study

4.1.12. siRNA

Table 13.: siRNAs used in this thesis.

Name	Sequence (5'-3')	Source
Negative ctrl siRNA	AGGUAGUGUAAUCGCCUUG-dT-dT	Microsynth
TRIM24 siRNA	GAGCUCAUCAGAGGGUAAA-rU-rU	Liu et al. 2014 [109]

4.1.13. Equipment and consumables

Table 14.: Equipment and consumables used in this thesis.

Name	Manufacturer
Agarose gel electrophoresis tank	ZMBH workshop
Agarose gel trays and combs	ZMBH workshop
Amersham ImageQuant 800	Cytiva
Automated cell counter LUNA	Logos Biosystems
Cell counting slides	Logos Biosystems
Cell culture plates (6-, 12-, 24-, 96-well)	Greiner
Cell culture flasks (T25, T75, T175)	Sarstedt
Cell culture incubator	Thermo Fisher
Centrifuge 5424	Eppendorf
Centrifuge 5424R	Eppendorf
Coplin staining jar	Neolab
Coverslips (10 mm, 12 mm, 22 × 50 mm)	Neolab
Cytology funnel	Thermo Fisher
Cytospin 4	Thermo Fisher
Falcon tubes (15 mL)	Sarstedt
Falcon tubes (50 mL)	Sarstedt
Freezer (−20 °C)	Liebherr
Freezer (−80 °C)	Heraeus
Refrigerator (4 °C)	Liebherr
GBP beads	Erhardt Lab
GelDoc gel imaging system	Bio-Rad
Ibidi μ-Dish 4-well glass-bottom plates	ibidi
Innova 44 incubator shaker	New Brunswick
KIMTECH wipes	Roth
MicroAmp Fast 96-well reaction plate (0.1 mL)	Applied Biosystems
Mini plate spinner MPS1000	Labnet
Mini centrifuge	Nippon Genetics
Mr. Frosty freezing container	Thermo Fisher
Multichannel pipette Research Plus (P10, 8-channel)	Eppendorf
NanoDrop One spectrophotometer	Thermo Fisher
Nitrocellulose membrane	Amersham Biosciences

Continued on next page

Table 14 – continued from previous page

Name	Manufacturer
Nunc CryoTubes	Sigma-Aldrich
Optically clear adhesive seal sheets	Thermo Fisher
Parafilm	Bemis
Pipette tips	Sarstedt
Pipettes Research Plus (P2, P10, P20, P200, P1000)	Eppendorf
PowerPac HC	Bio-Rad
QuantStudio 3	Applied Biosystems
Reaction tubes (0.2 mL)	Sarstedt
Reaction tubes (1.5 mL)	Eppendorf
Reaction tubes (2 mL)	Eppendorf
Rotation wheel	Labinco BV
Sapphire filter tips (20, 300, 1250 μL)	VWR
Sonicator Q800R3	Qsonica
Superfrost Plus microscope slides	Thermo Fisher
Thermocycler	Bio-Rad, Nippon Genetics
Thermomixer Compact	Eppendorf
Trans-Blot Turbo transfer system	Bio-Rad
Vortex-Genie 2	Scientific Industries
UV lamp	VWR
Zeiss LSM 900 with Airyscan	Zeiss

4.1.14. Software

Table 15.: Software used in this thesis.

Name	Version	Company
BioRender	Web-based	BioRender
CellProfiler	4.2.6	Broad Institute
Cursor	1.2.4	Anysphere
Cyberduck	9.1.6	Cyberduck
FlowJo	v10.10.1	Ashland
Geneious Prime	2024.2	Biomatters
GraphPad Prism	9.0	GraphPad Software

Continued on next page

Table 15 – continued from previous page

Name	Version	Company
ImageJ2 (Fiji)	2.16.0 / 1.54p	Fiji/ImageJ developers
Inkscape	1.4	Inkscape Project
Overleaf	Web-based	Digital Science
Python	3.7.2	Python Software Foundation
Pyzo	4.7.3	Pyzo Development Team
SnapGene Viewer	7.2.1	Dotmatics

4.1.15. Cell culture methods

Growth and maintenance of cells

Cells were cultured at 37 °C in a humidified atmosphere containing 5% CO_2. HEK293T cells were maintained in DMEM (Gibco) supplemented with 10% fetal bovine serum (FBS, BioWest) and 1% penicillin-streptomycin. LNCaP cells were cultured in RPMI 1640 (Gibco) supplemented with 10% FBS and 1% penicillin-streptomycin. HeLa SNAP-CENP-A and HeLa SNAP-CENP-A Pol II Ser2P-sfGFP mintbody cells were maintained in DMEM (Gibco) supplemented with 10% FBS, 1 mM sodium pyruvate, and 1% penicillin-streptomycin. Cells were maintained in standard tissue culture flasks.

At approximately 80% confluency, the growth medium was removed and cells were washed with pre-warmed 1× Dulbecco's PBS (Capricorn Scientific). Cells were detached using 0.05% trypsin-EDTA (Capricorn Scientific), resuspended in fresh complete growth medium, and passaged at a ratio of 1:10 for HEK293T and HeLa cells or 1:5 for LNCaP cells.

Cryopreservation of human cells

For cryopreservation, cells were grown to approximately 80% confluency at 37 °C in 5% CO_2 in complete growth medium. Cells were washed with pre-warmed 1× Dulbecco's PBS (Capricorn Scientific), detached using 0.05% trypsin-EDTA (Capricorn Scientific), and resuspended in fresh pre-warmed complete growth medium. A total of 1×10^6 cells were pelleted by centrifugation at $800 \times g$ for 4 min.

The supernatant was removed, and the cell pellet was resuspended in 2 mL fetal bovine serum (FBS) containing 5% dimethyl sulfoxide (DMSO). The cell suspension was transferred into cryogenic vials, which were placed into a Mr. Frosty freezing container filled with isopropanol and stored overnight at −80 °C. For long-term storage, cryovials were transferred to liquid nitrogen tank.

Thawing of frozen human cells

Cryovials containing frozen human cells were quickly thawed in a 37 °C water bath and immediately diluted in 5 mL fresh complete growth medium. Cells were pelleted by centrifugation at 800 $\times g$ for 4 min, the supernatant was removed, and cells were resuspended in fresh complete growth medium and transferred into culture flasks. Cells were incubated overnight at 37 °C in 5% CO_2. On the following day, cell viability and morphology were assessed.

Overexpression

Plasmid overexpression was performed using Lipofectamine LTX Plus (Thermo Fisher) according to the manufacturer's protocol for reverse transfection. Briefly, 2.5 μg plasmid DNA was diluted in 500 μL DMEM. Subsequently, 2.5 μL PLUS reagent was added directly to the diluted DNA, mixed gently, and incubated for 5 min at room temperature (RT). Next, 5 μL Lipofectamine LTX was added, mixed, and incubated for 30 min at RT. After incubation, the transfection mixture was transferred into one well of a 6-well tissue culture plate. HEK293T cells were grown to approximately 80% confluency at 37 °C in 5% CO_2 in complete growth medium. Cells were washed with pre-warmed 1× Dulbecco's PBS (Capricorn Scientific), detached using 0.05% trypsin-EDTA (Capricorn Scientific), and resuspended in complete growth medium consisting of DMEM supplemented with 10% fetal bovine serum (FBS) and 1% penicillin-streptomycin. A total of 1×10^6 cells were added to the well containing the transfection mixture, and the final volume was adjusted to 2 mL using complete growth medium. Cells were incubated for 48 h at 37 °C in 5% CO_2. Overexpression efficiency was assessed by fluorescence microscopy and Western blotting. A list of plasmids used in this study is provided in Table 12.

For immunoprecipitation experiments, transfection was performed as described above with the following modifications: 19 μg plasmid DNA, 19 μL PLUS reagent, and 38 μL Lipofectamine LTX were used. The transfection mixture was transferred to a T175 tissue culture flask, and 19 mL of complete growth medium containing cells at a density of 5×10^5 cells/mL was added.

RNA interference (RNAi)

siRNA transfection was performed using Lipofectamine RNAiMAX (Thermo Fisher) according to the manufacturer's protocol for reverse transfection. Briefly, 30 pmol siRNA (concentration 10 μM) and 5 μL Lipofectamine RNAiMAX transfection reagent were diluted in 500 μL Opti-MEM directly in one well of a 6-well tissue culture plate. The solution was gently mixed by pipetting and incubated for 20 min at RT.Cells were grown to approximately 80% confluency at 37 °C in 5% CO_2 in complete growth medium. HEK293T cells were washed with pre-warmed 1× Dulbecco's PBS (Capricorn Scientific), detached using 0.05% trypsin-EDTA (Capricorn Scientific), and resuspended in DMEM supplemented with 10% fetal bovine serum (FBS). Cells were counted, and 2×10^5 cells were added to the transfection mixture. The final volume was adjusted to 2 mL using DMEM supplemented with 10% FBS. Cells were incubated for 48 h at 37 °C in 5% CO_2. The efficiency of siRNA-mediated knockdown was assessed by Western blotting. A list of siRNAs used in this study is provided in Table 13.

Metaphase spreads

Cells were cultured in complete growth medium at 37 °C in 5% CO_2 until approximately 80% confluency. Cells were washed with pre-warmed 1× Dulbecco's PBS (Capricorn Scientific), detached using 0.05% trypsin-EDTA (Capricorn Scientific), and resuspended in complete growth medium. Cells were then seeded at a 1:10 dilution into 12-well plates and incubated overnight under the same conditions. On the following day, cells were arrested in metaphase by treatment with colcemid (Capricorn Scientific) at a final concentration of 1 μg/mL for 1 h. Cells were counted, and 2×10^4 cells were incubated in 500 μL hypotonic solution (0.5% sodium citrate, freshly diluted from a 10% stock; Sigma-Aldrich) for exactly 7 min. The cell suspension was transferred into cytospin funnels (Thermo Fisher) and centrifuged at 1200 rpm for 10 min. Slides were briefly air-dried and subsequently processed for immunostaining or EU-labelling.

Methanol spreads

Cells were cultured in complete growth medium at 37 °C in 5% CO_2 until approximately 80% confluency. Cells were washed with pre-warmed 1× Dulbecco's PBS (Capricorn Scientific), detached using 0.05% trypsin-EDTA (Capricorn Scientific), and resuspended in complete growth medium. Cells were seeded at a 1:10 dilution into 6-well plates and incubated overnight under the same conditions. On the following day, cells were arrested in metaphase by treatment with colcemid (Capricorn Scientific) at a final concentration of 1 µg/mL for 1 h. The culture medium was transferred into a 15 mL tube, and cells were washed with pre-warmed 1× Dulbecco's PBS, detached using 0.05% trypsin-EDTA, and resuspended in complete growth medium. All liquids were combined in the same 15 mL tube, which was centrifuged at 1200 rpm for 4 min to pellet the cells. The supernatant was discarded, and the pellet was gently resuspended in 1 mL 75 mM KCl solution. An additional 4 mL of KCl solution was added, and cells were incubated for 10 min at RT. Cells were then centrifuged at 1200 rpm for 4 min, and the supernatant was removed. The cell pellet was gently resuspended in 1 mL methanol:acetic acid (3:1), added dropwise while vortexing at low speed. Subsequently, 4 mL methanol:acetic acid (3:1) was added, and cells were incubated for 10 min at RT before centrifugation at 1200 rpm for 4 min. The supernatant was discarded, and the fixation step was repeated once more by adding 1 mL methanol:acetic acid (3:1) dropwise under gentle vortexing, followed by addition of 4 mL fixative. Cells were incubated overnight at −20 °C. On the following day, cells were centrifuged at 1200 rpm for 4 min, and the supernatant was removed, leaving approximately 0.5 mL residual volume. Cells were resuspended by gently flicking the tube. Charged microscope slides were briefly humidified by gently breathing onto the surface, and 20 µL of the cell suspension was dropped onto each slide. Slides were air-dried for 30 min and transferred to a Coplin jar containing 1× PBS to rehydrate the chromosomes for at least 5 min. Slides were mounted with 30 µL Vectashield containing DAPI and covered with 22 × 50 mm coverslips. Coverslips were sealed using nail polish.

Generation of stable HeLa SNAP-CENP-A Pol II Ser2P mintbody cell line

HeLa SNAP-CENP-A cells were transfected with the Pol II Ser2P-sfGFP mintbody construct (Tab. 12) using Lipofectamine LTX Plus (Thermo Fisher) according to the manufacturer's protocol for reverse transfection. Briefly, 2.5 µg plasmid DNA was

diluted in 500 µL DMEM. Subsequently, 2.5 µL PLUS reagent was added to the diluted DNA, mixed gently, and incubated for 5 min at RT. Thereafter, 5 µL Lipofectamine LTX was added, mixed, and incubated for 30 min at RT. The transfection mixture was then transferred into one well of a 6-well tissue culture plate.

HeLa SNAP-CENP-A cells were grown to approximately 80% confluency at 37 °C in 5% CO_2 in complete growth medium. Cells were washed with pre-warmed 1× Dulbecco's PBS (Capricorn Scientific), detached using 0.05% trypsin-EDTA (Capricorn Scientific), and resuspended in complete growth medium consisting of DMEM supplemented with 10% fetal bovine serum (FBS), 1 mM sodium pyruvate, and 1% penicillin-streptomycin. A total of 1×10^6 cells were added to the well containing the transfection mixture, and the final volume was adjusted to 2 mL with complete growth medium.

Cells were incubated for 48 h at 37 °C in 5% CO_2. Selection was initiated by adding 300 µg/mL G-418 (Merck). Single-cell clones were obtained by limiting dilution in 96-well plates and expanded under continuous antibiotic selection. Clones were screened by fluorescence microscopy, and one clone exhibiting moderate mintbody expression was selected for further experiments.

4.1.16. Molecular biology methods

Total RNA isolation

Total RNA was isolated from HEK293T cells using TRIzol (Thermo Fisher) according to the manufacturer's protocol with minor modifications. Briefly, cells were washed with PBS, detached using 0.05% trypsin-EDTA, centrifuged at 500 ×g for 5 min, and lysed in 1 mL TRIzol. Following the addition of 200 µL chloroform, samples were vigorously mixed for 1 min, incubated for 5 min at RT, and centrifuged at 12,000 ×g for 15 min at 4 °C. The aqueous phase was transferred to a new tube, and RNA was precipitated by adding 500 µL isopropanol and incubating for 10 min at −20 °C, followed by centrifugation at 12,000 ×g for 15 min. The RNA pellet was washed with 75% ethanol, centrifuged at 7,500 ×g for 5 min, air-dried for 10 min at RT, and dissolved in 20 µL RNase-free water. RNA concentration and purity were determined using a NanoDrop spectrophotometer.

Genomic DNA was removed using TURBO DNase (Invitrogen). For each reaction, 10 µg RNA was incubated with 1 µL TURBO DNase, 3 µL reaction buffer, and 0.5 µL RNasin Plus RNase inhibitor in a total volume of 30 µL for 60 min at 37 °C.

RNA was subsequently re-purified by phenol/chloroform extraction. The reaction was mixed with 170 µL cold RNase-free water, 20 µL sodium acetate (3 M, pH 5.2), and 200 µL phenol/chloroform/isoamyl alcohol (25:24:1), vortexed for 30 s, and centrifuged at 12,000 ×*g* for 20 min at 4 °C. The aqueous phase was re-extracted with one volume of chloroform, vortexed for 15 s, and centrifuged at 12,000 ×*g* for 10 min at 4 °C. RNA was precipitated by adding one volume of cold isopropanol and 1 µL GlycoBlue, followed by incubation for 1 h at −80 °C. The RNA pellet was collected by centrifugation at 15,000 ×*g* for 10 min at 4 °C, washed twice with 75% ethanol, air-dried, and resuspended in 15 µL RNase-free water. RNA concentration was quantified using a NanoDrop spectrophotometer.

Reverse transcription

cDNA synthesis was performed using the QuantiTect Reverse Transcription Kit (Qiagen) according to the manufacturer's protocol. Briefly, 1 µg total RNA was treated with 2 µL gDNA WipeOut buffer in a total volume of 14 µL and incubated at 42 °C for 10 min to remove residual genomic DNA. The reaction was then split into two aliquots for reverse transcription (+RT, with reverse transcriptase) and negative control (-RT, without reverse transcriptase). Each aliquot was supplemented with 0.5 µL RT primer mix, 2 µL 10× RT buffer, and either 0.5 µL reverse transcriptase (+RT) or RNase-free water (-RT). Reverse transcription was carried out at 42 °C for 20 min, followed by enzyme inactivation at 95 °C for 3 min. The resulting cDNA was used directly for qPCR or stored at −20 °C until further use.

Quantitative PCR (qPCR)

Quantitative real-time PCR (qPCR) was performed using Fast SYBR Green Master Mix (Fisher Scientific) according to the manufacturer's instructions. Each reaction (10 µL total volume) contained 1 µL cDNA, 5 µL Fast SYBR Green Master Mix, 0.5 µL forward primer and 0.5 µL reverse primer (10 µM each), and 3 µL nuclease-free water. All reactions were prepared in technical triplicates in 96-well plates. qPCR was performed on a QuantStudio 3 real-time PCR system using the following cycling conditions: 95 °C for 20 s, followed by 40 cycles of 95 °C for 3 s and 60 °C for 30 s. Each experiment included +RT controls (with reverse transcriptase), -RT controls (without reverse transcriptase), and no-template controls to confirm cDNA synthesis

and exclude genomic DNA contamination. Gene expression levels were calculated from mean Ct values and relative fold changes were determined using the ΔΔCt method [110], with *GAPDH* used as a housekeeping gene.

4.1.17. Bacterial cell methods

Transformation of *E. coli*

Chemically competent *E. coli* cells were thawed on ice, and 100 ng plasmid DNA was added to each aliquot. Cells were incubated on ice for 10 min, followed by heat shock at 42 °C for 1 min. Immediately after, cells were returned to ice for 2 min. Subsequently, 300 µL fresh LB medium was added, and cells were incubated at 37 °C for 1 h to allow recovery. Cells were plated on LB agar plates containing the appropriate antibiotic using sterile glass beads and incubated overnight at 37 °C.

Plasmid isolation

Plasmid DNA was isolated from *E. coli* using either the NucleoSpin Plasmid kit (Macherey-Nagel; mini-prep) or the NucleoBond Xtra Midi Kit for plasmid DNA (Macherey-Nagel; midi-prep), according to the manufacturer's instructions. For mini-preparations, 5 mL LB medium containing the appropriate selective antibiotic was inoculated with a single bacterial colony and incubated overnight at 37 °C with shaking at 180 rpm. For midi-preparations, 100 mL LB medium was inoculated in the same manner. On the following day, bacterial cells were harvested, lysed, and plasmid DNA was purified by column-based extraction as described in the respective protocols. DNA was eluted in 50 µL (mini-prep) or 100 µL (midi-prep) nuclease-free water, and DNA concentration was determined using a NanoDrop spectrophotometer. Purified plasmids were subsequently used for site-directed mutagenesis or overexpression experiments.

Site-directed mutagenesis

The plasmids pcDNA6.2/N-EmGFP-TRIM24-delHP1 and pcDNA6.2/N-EmGFP-TRIM24-V733D/L735N were generated by site-directed mutagenesis from the parental vector pcDNA6.2/N-EmGFP-TRIM24 (Addgene #65396) using primers listed in Table 11. Site-directed mutagenesis was performed according to the protocol of the Q5 Site-Directed Mutagenesis Kit (NEB) using individually purchased reagents. PCR amplification was performed using the reaction mixture detailed in Table 16

and cycling conditions summarized in Table 17. Following PCR amplification, template plasmid DNA was digested by incubating 25 µL PCR product with 1 µL DpnI restriction enzyme (NEB) at 37 °C for 1 h to remove methylated template DNA. Subsequently, 10 µL of the reaction mixture was transformed into chemically competent *E. coli* cells as described above. Plasmid DNA was isolated from single colonies and verified by Sanger sequencing (Eurofins Genomics) to confirm the presence of the desired mutation.

Reagent	**Amount**	**Final concentration**
Q5 DNA polymerase	0.25 µL	1×
dNTPs (10 mM)	0.5 µL	-
Q5 reaction buffer (5×)	5 µL	1×
GC enhancer	5 µL	-
Forward primer (10 µM)	1.25 µL	0.5 µM
Reverse primer (10 µM)	1.25 µL	0.5 µM
Template DNA (1-25 ng/µL)	1 µL	1-25 ng
Nuclease-free water	10.75 µL	-
Total	**25 µL**	

Table 16.: PCR reaction mixture used for site-directed mutagenesis.

Step	**Temperature**	**Time**
Initial denaturation	98 °C	30 s
25 cycles	98 °C 54 °C 72 °C	10 s 30 s 4 min
Final extension	72 °C	2 min
Hold	4 °C	-

Table 17.: PCR cycling conditions used for site-directed mutagenesis.

4.1.18. Biochemical methods

Preparation of protein lysates

For plasmid overexpression experiments, cells were treated as described in Section 4.2.1 (Overexpression). For knockdown experiments, cells were treated as described in Section 4.2.2 (RNA interference). Cells were washed with pre-warmed 1× Dulbecco's PBS (Capricorn Scientific), detached using 0.05% trypsin-EDTA (Capricorn Scientific), and centrifuged at 800 ×g for 5 min. Cells were counted and

resuspended in lysis buffer (0.1% SDS, 1× cOmplete protease inhibitor cocktail) to a final concentration of 1×10^7 cells/mL, followed by incubation on ice for 5 min. Subsequently, samples were mixed with 4× Laemmli buffer and denatured at 95 °C for 5 min.

SDS-PAGE and Western blot

Protein samples were separated either on 10% SDS-PAGE gels or on 4-20% Mini-PROTEAN TGX gels at a constant current of 0.02 A for 1 h. Proteins were transferred onto methanol-activated PVDF membranes using the Trans-Blot Turbo system at 1.3 A for 7 min. Membranes were blocked in 5% skim milk in TBST for 1 h and incubated with primary antibodies diluted in 5% skim milk in TBST overnight at 4 °C under rotation. Membranes were washed three times with TBST for 5 min each and incubated with secondary antibodies diluted in 5% skim milk in TBST for 1 h under rotation. Following three additional washes with TBST (5 min each), membranes were rinsed with water and visualized using SuperSignal West Femto Maximum Sensitivity or SuperSignal West Pico chemiluminescent substrates (Thermo Fisher).

For membrane reprobing, membranes were incubated in stripping solution (200 mM glycine, 0.1% SDS, 1% Tween 20, pH 2.2) for 20 min under rotation to remove bound antibodies. Membranes were washed three times with TBST for 5 min, rinsed with water, and incubated with SuperSignal West Femto substrate to confirm removal of secondary antibodies. Membranes were then washed again, blocked in 5% skim milk in TBST for 1 h, and incubated with antibodies as described above.

Immunoprecipitation of GFP-fused proteins

Plasmid overexpression was performed as described in Section 4.2.1 (Overexpression). Cells were harvested 48 h after transfection, collected in 50 mL tubes, and centrifuged at 1200 rpm for 10 min at RT. Cell pellets were resuspended in 1 mL PBS, transferred to 1.5 mL tubes, and centrifuged at 3000 rpm for 5 min. Cell pellets were resuspended in freshly prepared IP lysis buffer (25 mM Tris-HCl, pH 7.5; 150 mM NaCl; 1% Triton X-100; 2 mM PMSF; 1× cOmplete protease inhibitor cocktail; 2.5 U/mL BaseMuncher) at a 1:1 (v/v) ratio and incubated for 15 min under rotation at 4 °C. Chromatin was sheared using a Bioruptor with five cycles of 30 s ON and 30 s OFF at 25% power. Samples were centrifuged at 13,000 rpm for 30 min at 4 °C to remove insoluble debris. An aliquot of 24 μL lysate was immediately mixed with 4× Laemmli buffer, denatured for 5 min at 95 °C, and stored at −20 °C as the input fraction. The

remaining lysate was transferred to a fresh tube containing 100 µL GFP-binding protein (GBP) beads and incubated for 2 h under rotation at 4 °C. An aliquot of 24 µL of the supernatant was collected, mixed with 4× Laemmli buffer, denatured for 5 min at 95 °C, and stored at −20 °C as the flow-through fraction. Beads were pelleted by centrifugation at 2000 rpm for 2 min, and the supernatant was removed. Beads were washed six times with 1 mL fresh IP lysis buffer. Following the final wash, beads were resuspended in 50 µL 2× Laemmli buffer, denatured for 5 min at 95 °C, and stored at −20 °C as the immunoprecipitated (IP) fraction. All fractions were subsequently analyzed by SDS-PAGE and Western blotting.

4.1.19. Fluorescence microscopy

Immunofluorescence of fixed cells on coverslips

Prior to seeding, 12 mm coverslips were washed with ethanol and placed into 24-well plates. Coverslips were coated with poly-L-lysine (Sigma-Aldrich) for 2 min, followed by washes with sterile water and 1× Dulbecco's PBS (Capricorn Scientific). For plasmid overexpression experiments, cells were treated as described in Section 4.2.1 (Overexpression). For wildtype cell staining, cells were cultured in complete growth medium at 37 °C in 5% CO_2 until approximately 80% confluency. Cells were washed with pre-warmed 1× Dulbecco's PBS (Capricorn Scientific), detached using 0.05% trypsin-EDTA (Capricorn Scientific), and resuspended in complete growth medium. A total of 0.5×10^5 cells per well were seeded onto coverslips and incubated overnight under the same conditions. On the following day, the medium was aspirated and cells were fixed with 4% paraformaldehyde (PFA) in PBS for 10 min, followed by three washes with PBS (5 min each). Cells were permeabilized with 0.1% Triton X-100 in PBS for 10 min and washed three times with PBS (5 min each). Coverslips were blocked with 4% bovine serum albumin (BSA) in PBS for 1 h at RT. Primary antibodies (Table 4) diluted in 4% BSA in PBS were applied overnight at 4 °C in a humidified chamber. Coverslips were washed three times with PBS for 5 min each and incubated with secondary antibodies (Table 4) diluted in 4% BSA in PBS for 2 h at RT in a humidified chamber. Following three additional washes with PBS (5 min each), samples were mounted with 20 µL Vectashield containing DAPI (Biozol). Coverslips were briefly air-dried, inverted onto microscope slides with the cells facing downward, and sealed with nail polish.

Immunofluorescence of metaphase spreads

Metaphase spreads were fixed with 4% paraformaldehyde (PFA) in PBS for 10 min, followed by three washes with PBS (5 min each). Cells were permeabilized with 0.1% Triton X-100 in PBS for 10 min and washed three times with PBS (5 min each). Samples were blocked with 4% bovine serum albumin (BSA) in PBS for 1 h at RT. Primary antibodies (Table 4) diluted in 4% BSA in PBS were applied overnight at 4 °C in a humidified chamber. Samples were washed three times with PBS for 5 min each and incubated with secondary antibodies (Table 4) diluted in 4% BSA in PBS for 2 h at RT in a humidified chamber. Following three additional washes with PBS (5 min each), samples were mounted with 20 μL Vectashield containing DAPI (Biozol), covered with coverslips, and sealed with nail polish.

EU-labelling and detection of nascent RNA

Nascent RNA was labeled using 5-ethynyl uridine (EU) as previously described [139]. Following metaphase spread preparation, slides were treated with 0.2% Triton X-100 for 15 min and washed gently with PBS. Slides were incubated with EU diluted 1:1000 in PBS for 20 min. Subsequently, spreads were fixed with 4% paraformaldehyde in PBS for 15 min. Incorporated EU was detected using the Click-iT RNA Alexa Fluor 488 Imaging Kit (Thermo Fisher) according to the manufacturer's instructions. Samples were mounted with 20 μL Vectashield containing DAPI (Biozol), covered with coverslips, and sealed with nail polish.

Live cell imaging of Pol II Ser2P-sfGFP mintbody

For live-cell imaging, HeLa cells stably expressing SNAP-tagged CENP-A and Pol II Ser2P-sfGFP mintbody were seeded onto 4-well glass-bottom ibidi μ-dishes (ibidi) at a density of 3×10^4 cells/mL in complete growth medium and incubated overnight at 37 °C in 5% CO_2.

For SNAP labelling, cells were incubated with SNAP-Cell 647-SiR substrate (NEB) diluted 1.3 μL in 200 μL pre-warmed complete growth medium. A total of 100 μL labelling solution was added per well and incubated for 30 min at 37 °C in 5% CO_2. Cells were subsequently washed three times with fresh complete growth medium to remove excess substrate.

For DNA visualization, cells were incubated with Aberrior Live 590 dye diluted 1:10,000 in complete growth medium for 30 min at 37 °C in 5% CO_2.

Live-cell imaging was performed using an LSM 900 Airyscan super-resolution confocal microscope (Zeiss) equipped with a 63× oil-immersion objective (NA 1.4, Plan-Apochromat 63×/1.4 Oil DIC M27) and an incubation chamber maintained at 37 °C and 5% CO_2. Z-stacks consisting of seven optical sections with a step size of 0.1 μm were acquired at 20-min intervals. Within each experimental replicate, illumination and acquisition settings were kept constant.

Image acquisition

Images were acquired using an LSM 900 Airyscan super-resolution confocal microscope (Zeiss) equipped with a 63× oil-immersion objective (NA 1.4, Plan-Apochromat 63×/1.4 Oil DIC M27). Excitation lasers at 405, 488, 561, and 640 nm were used. For coverslip-based samples, z-stacks consisting of 10 optical sections with a step size of 0.1 μm were acquired. For metaphase spreads, z-stacks consisting of 9 optical sections with a step size of 0.1 μm were acquired. Within each experimental replicate, illumination and acquisition settings were kept constant.

Image analysis

Image analysis was performed using ImageJ [163] and CellProfiler [172]. Airyscan images were processed using Zeiss ZEN Black software with default settings. For all analyses, z-stacks were converted into maximum intensity projections using ImageJ, and a rolling-ball background subtraction (100 px) was applied to all channels.

For colocalization analysis in wildtype cells, maximum intensity projections were used for further analysis in CellProfiler. Nuclei or mitotic chromosomes were segmented using global Otsu thresholding based on the DAPI channel. CENP-A foci were enhanced within the nuclear or chromosomal masks by speckle enhancement of the CENP-A channel and segmented using global Otsu thresholding. TRIM24 foci were segmented within the same masks using minimum cross-entropy thresholding applied to the TRIM24 channel. Colocalization was defined as either a direct overlap or a touching event between TRIM24 and CENP-A foci and was quantified per nucleus or mitotic spread.

For TRIM24 domain mutant analyses, colocalization between TRIM24 and CENP-A was scored manually due to variable protein expression levels. For each cell, CENP-A foci overlapping or touching TRIM24-GFP signal were counted. All scoring was performed in a blinded manner.

For analysis of the TRIM24 F979A/N980A mutant, mean GFP intensity was quantified using CellProfiler. Nuclei or mitotic chromosomes were segmented using global Otsu thresholding, and the mean GFP intensity within each mask was measured.

Foci-positive cells were defined as cells containing at least four large TRIM24 foci overlapping or touching CENP-A foci. Foci were identified visually, and scoring was performed in a blinded manner.

Intercentromeric distance was measured in ImageJ as the distance between the centers of paired CENP-A foci.All scoring was performed in a blinded manner.

Premature sister chromatid separation was scored manually on methanol-fixed metaphase spreads. Each spread was assigned to one of four categories: normal, partial cohesion defects, full cohesion defects, or cohesion failure, as described previously [44]. Scoring was performed in a blinded manner.

For mitotic count, maximum intensity projections were used for further analysis in CellProfiler. Nuclei were segmented using global Otsu thresholding based on the DAPI channel. Nuclei with H3Ser10P signal were defined as mitotic and mitotic and non-mitotic cells were quantified per image.

Data analysis and graph generation were performed in Python [189]. Statistical tests were applied as specified in the corresponding figure legends.

4.1.20. Flow cytometry-based cell cycle analysis

Plasmid overexpression was performed as described in Section 4.2.1 (Overexpression). Cells were cultured in 6-well plates and harvested 48 h after transfection. Cells were washed with pre-warmed 1× Dulbecco's PBS (Capricorn Scientific), detached using 0.05% trypsin-EDTA (Capricorn Scientific), and resuspended in complete growth medium. Cells were centrifuged at 300 ×g for 5 min. Cell pellets were resuspended in 0.5 mL 4% paraformaldehyde (PFA) while vortexing and incubated for 10 min at RT. Cells were centrifuged at 300 ×g for 5 min, washed three times with PBS, and permeabilized in 0.5 mL 0.5% Triton X-100 in PBS for 5 min at RT. Following centrifugation, cells were washed three times with PBS. For DNA staining, cells were resuspended in 0.5 mL PBS containing 0.1 μg/mL DAPI and incubated for 5 min at RT. Cells were washed three times with PBS and stored at 4 °C in the dark until acquisition.

Flow cytometric analysis was performed using a SONY MA900 cell sorter equipped with a 130 μm nozzle. GFP was detected using a 488 nm excitation laser and a 525/50 emission filter. DAPI was detected using a 405 nm excitation laser and a 460/50

emission filter. For each condition, 10,000 events were recorded per biological replicate. Debris was excluded based on forward and side scatter parameters. Doublets were excluded by gating on single-cell populations. GFP-positive cells were defined relative to non-transfected control cells. Cell cycle distribution was analyzed using FlowJo software.

4.2. Bioinformatics

All bioinformatic analyses were performed on the bwForCluster Helix computing cluster.

4.2.1. Bioinformatic tools

Table 18.: Bioinformatic tools used in this thesis.

Tool	Version	Provider
wget	1.21	GNU
Bowtie2	2.4.5	Johns Hopkins University
Samtools	1.15.1	Open source
Bedtools	2.30.0	Quinlan Lab, University of Utah
BWA	0.7.17	Li Lab, UC Berkeley
deepTools	3.5.4.post1	MPI Freiburg
pyGenomeTracks	3.9	MPI Freiburg
Python	3.9	Python Software Foundation
Matplotlib	3.5.1	Open source
Pandas	1.3.5	Open source
Seaborn	0.9.0	Open source
NumPy	1.21.6	Open source

4.2.2. ChIP-seq accession numbers

Table 19.: Accession numbers of the ChIP-seq datasets used in this thesis.

PRNJA	Sample	Cell line	ChIP target	Input ID	Sample ID	Reference
PRJNA285229	LNCaP	LNCaP	TRIM24	SRR2043647	SRR2043644	[66]
PRJNA285229	LNCaP abl	LNCaP abl	TRIM24	SRR2043649	SRR2043646	[66]
PRJNA1199461	LNCaP 2 rep1	LNCaP	TRIM24	SRR31751545	SRR31751544	[52]
PRJNA1199461	LNCaP 2 rep2	LNCaP	TRIM24	SRR31751545	SRR31751543	[52]
PRJNA1199461	LNCaP 2 rep3	LNCaP	TRIM24	SRR31751545	SRR31751542	[52]
PRJNA392161	MOLM-13	MOLM-13	TRIM24	SRR5762042	SRR5762041	[62]
PRJNA130083	MCF7	MCF7	TRIM24	SRR065825	SRR065822	[184]
PRJNA986131	HepG2 rep1	HepG2	TRIM24	SRR16813840	SRR24985370	[125]
PRJNA986131	HepG2 rep2	HepG2	TRIM24	SRR16813840	SRR24985371	[125]
PRJNA638411	HCT116	HCT116	TRIM24	SRR11969101	SRR11969094	[95]

4.2.3. Reanalysis of Every Dataset at Positions Of INTerest (REDPOINT)

For each sample (for accession numbers, see Tab. 19), .fastq files were downloaded using wget (1.21) and unzipped with gunzip:

```
wget -nc {sample1}.fastq.gz
gunzip *fastq.gz
```

Reads were aligned to genome build hg38 using Bowtie2 (2.4.5) [98] using parallel threads. For paired-end datasets, read pairs were provided via -1 and -2, for single-end datasets, read were supplied with -U option. SAM output was converted to BAM using Samtools (1.15.1) [46] samtools view and the coordinates were sorted with samtools sort.

```
bowtie2 -p $THREADS -x HgCh38 \
       -1 "${sample1}_1.fastq" \
       -2 "${sample1}_2.fastq" \
       | samtools view -@ $THREADS -bS - \
       | samtools sort -@ $THREADS - > "${sample1}_redpoint.bam"
or
bowtie2 -p $THREADS -x HgCh38 \
       -U "${sample1}.fastq" \
       | samtools view -@ $THREADS -bS - \
       | samtools sort -@ $THREADS - > "${sample1}_redpoint.bam"
```

BAM files were converted to BED format using `bedtools bamtobed` (Bedtools version 2.30.0). The resulting BED files were intersected with a custom-built annotation of centromeric repeats, generated as described in Corless et al. [44], using `bedtools intersect` with the `-wa`, `-wb`, and `-loj` options to retain all aligned reads together with overlapping feature information. Reads mapping to centromeric regions were extracted using `awk` and saved as separate BED files. The total number of aligned reads and the number of centromeric reads were counted and written to a text file.

```
bedtools bamtobed -i "${sample1}_redpoint.bam" > "${sample1}_redpoint.bed"

echo "$sample1" > "${sample1}_redpoint.txt"

bedtools intersect -a "${sample1}_redpoint.bed" \
       -b Hg38_forIntersectA.bed \
       -wa -wb -loj > "${sample1}_repeat.bed"

awk -F"\t" '$13 == "centr"' "${sample1}_repeat.bed" >
    "${sample1}_repeat_centr.bed"

wc -l "${sample1}_redpoint.bed" >> "${sample1}_redpoint.txt"
wc -l "${sample1}_repeat_centr.bed" >> "${sample1}_redpoint.txt"
```

Centromeric reads were normalized to the total number of aligned reads, and fold enrichment over the corresponding input control was calculated as:

$$\text{Fold enrichment} = \frac{\text{normalized sample reads}}{\text{normalized input reads}}$$

For Figure 4a, datasets provided by Corless et al. [44] were used. Lists of centromeric reads normalized to the total number of aligned reads were downloaded, and fold enrichment over the input control was calculated using Python. The resulting tables were filtered for novel candidate proteins reported in Corless et al. [44], ranked by decreasing fold enrichment, and ChIP-seq samples with fold enrichment > 1 were visualized using Python.

4.2.4. Alignment to T2T-CHM13 genome

For each dataset (for accession numbers, see Tab. 19), .fastq files were downloaded using wget:

```
wget -nc {sample1}.fastq.gz
```

Reads were aligned to the telomere-to-telomere human reference genome (T2T-CHM13v2.0) using BWA-MEM (version 0.7.19) with parallel threads enabled. Aligned reads were sorted and indexed using `samtools sort` and `samtools index`.

```
bwa mem -t "$THREADS" -c 1000000 "$DATA_DIR" \
       "${sample1}_1.fastq.gz" "${sample1}_2.fastq.gz" \
       | samtools sort -@ "$THREADS" -m 4G -o "${sample1}_sorted.bam"
or
bwa mem -t "$THREADS" -c 1000000 "$DATA_DIR" "${sample1}.fastq.gz" \
       | samtools sort -@ "$THREADS" -m 4G -o "${sample1}_sorted.bam"

samtools index -@ "$THREADS" "${sample1}_sorted.bam"
```

Sample and input BAM files were compared using `bamCompare` (deepTools version 3.5.4.post1) with `log2` and `ratio` operations, a pseudocount of 1, a bin size of 1000 bp, and `samFlagExclude 2308` to exclude duplicate reads. Output tracks were generated in both BigWig and BedGraph formats, and BedGraph files were coordinate-sorted.

```
for MODE in log2 ratio; do
       bamCompare \
         -b1 "$CHIP" -b2 "$INPUT" \
         --operation $MODE \
         --pseudocount 1 \
         --scaleFactorsMethod readCount \
         --binSize 1000 \
         --samFlagExclude 2308 \
         --extendReads 200 \
         --centerReads \
         --outFileFormat bigwig \
         -o ${CHIP}_${MODE}.bw

       bamCompare \
         -b1 "$CHIP" -b2 "$INPUT" \
         --operation $MODE \
         --pseudocount 1 \
         --scaleFactorsMethod readCount \
         --binSize 1000 \
         --samFlagExclude 2308 \
```

```
        --extendReads 200 \
        --centerReads \
        --outFileFormat bedgraph \
        -o ${CHIP}_${MODE}.bedgraph

      sort -k1,1 -k2,2n -o "$OUT_BED" "$OUT_BED"
done
```

Genome-wide tracks were visualized using pyGenomeTracks (version 3.9). A configuration file describing the tracks was generated using `make_tracks_file`, and regions of interest were visualized using `pyGenomeTracks`.

```
make_tracks_file --trackFiles <file1.bed> <file2.bw> ... -o tracks.ini

pyGenomeTracks --tracks tracks.ini \
             --region chr19:1-61,707,364 \
             --outFileName tracks_chr19.svg
```

The following genomic coordinates were used for visualization:

```
Chr6:
chr6:1-172,126,628
chr6:50,000,000-70,000,000 (centromeric region)

Chr9:
chr9:1-150,617,247
chr9:36,000,000-86,000,000 (centromeric region)

Chr19:
chr19:1-61,707,364
chr19:18,000,000-36,000,000 (centromeric region)
```

4.2.5. Extraction of centromeric repeats

For extraction of reads aligned to centromeric repeats, datasets aligned as described in Section 4.2.4 were used. Centromeric repeat annotations derived from the T2T-CHM13v2.0 genome assembly [134] (`censat_hs1.bed`) were downloaded from the UCSC Genome Browser. To ensure consistency with the chromosome naming and ordering of the aligned BAM files, one representative BAM file was processed to extract chromosome names and lengths using `samtools view`, generating a genome

size file (`genome.txt`). The centromeric repeat BED file was then sorted according to this genome file using `bedtools sort`. The resulting sorted BED file and `genome.txt` were used for all downstream analyses.

```
samtools view -H ${sample1}_sorted.bam | grep ^@SQ | \
awk -F'\t' '{chr=$2; len=$3; sub("SN:", "", chr); sub("LN:", "", len); \
print chr"\t"len}' > genome.txt

bedtools sort -i censat_hs1.bed -g genome.txt > censat_sorted.bed
```

Aligned reads were intersected with `censat_sorted.bed` using `bedtools coverage`, referencing chromosome sizes from `genome.txt`. Read counts per centromeric repeat were written to `*counts.txt`. The total number of aligned reads in each BAM file was recorded for normalization.

```
bedtools coverage -a censat_sorted.bed -b "${sample1}_sorted.bam" -g genome.txt \
> "${sample1}_counts.txt"

wc -l "${sample1}_sorted.bam" >> "${sample1}_sorted.txt"
```

Centromeric read counts were imported into Python using `pandas`, scaled by one million, and normalized to the total number of aligned reads to calculate reads per million (RPM). Normalized counts were saved as `*normalized.csv`. Fold enrichment of ChIP samples over the corresponding input controls was calculated and used for downstream analyses.

```
df_counts = pd.read_csv("sample_counts.txt", sep="\t", header=None)
total_reads = 12345678 # obtained from sample_sorted.txt
df_counts["RPM"] = df_counts[4] * 1e6 / total_reads
df_counts.to_csv("sample_normalized.csv")
```

```
chip = pd.read_csv("sample_ChIP_normalized.csv")
input = pd.read_csv("sample_Input_normalized.csv")

df = pd.merge(chip, input, on=["Chromosome", "Start", "End", "Repeat"],
    how="outer")
df["ChIP/Input_ratio"] = df["RPM_x"] / df["RPM_y"]

df.to_csv("sample_ratio.csv")
```

Ratio values were visualized in Python.

4.2.6. TRIM24 expression analysis using DepMap

TRIM24 expression data for cancer cell lines were obtained from the DepMap Public 25Q2 dataset [185]. The dataset provides ranked TRIM24 expression values reported as $\log_2$(TPM+1) derived from RNA-seq data. For cell lines included in the REDPOINT analysis, expression values were extracted and visualized using Python.

4.2.7. AI usage statement

During the preparation of this thesis, large language models (ChatGPT-5, Perplexity AI, and the Cursor AI assistant) were used for language polishing, text formatting, and code debugging. All scientific ideas, data analysis, initial text drafts, and data interpretation originate solely from the author. These tools were not used to generate new scientific content, figures, or other original research materials. The final version of this thesis was reviewed and edited by the author, who verified the correctness and accuracy of all content.

5. Supplementary Information

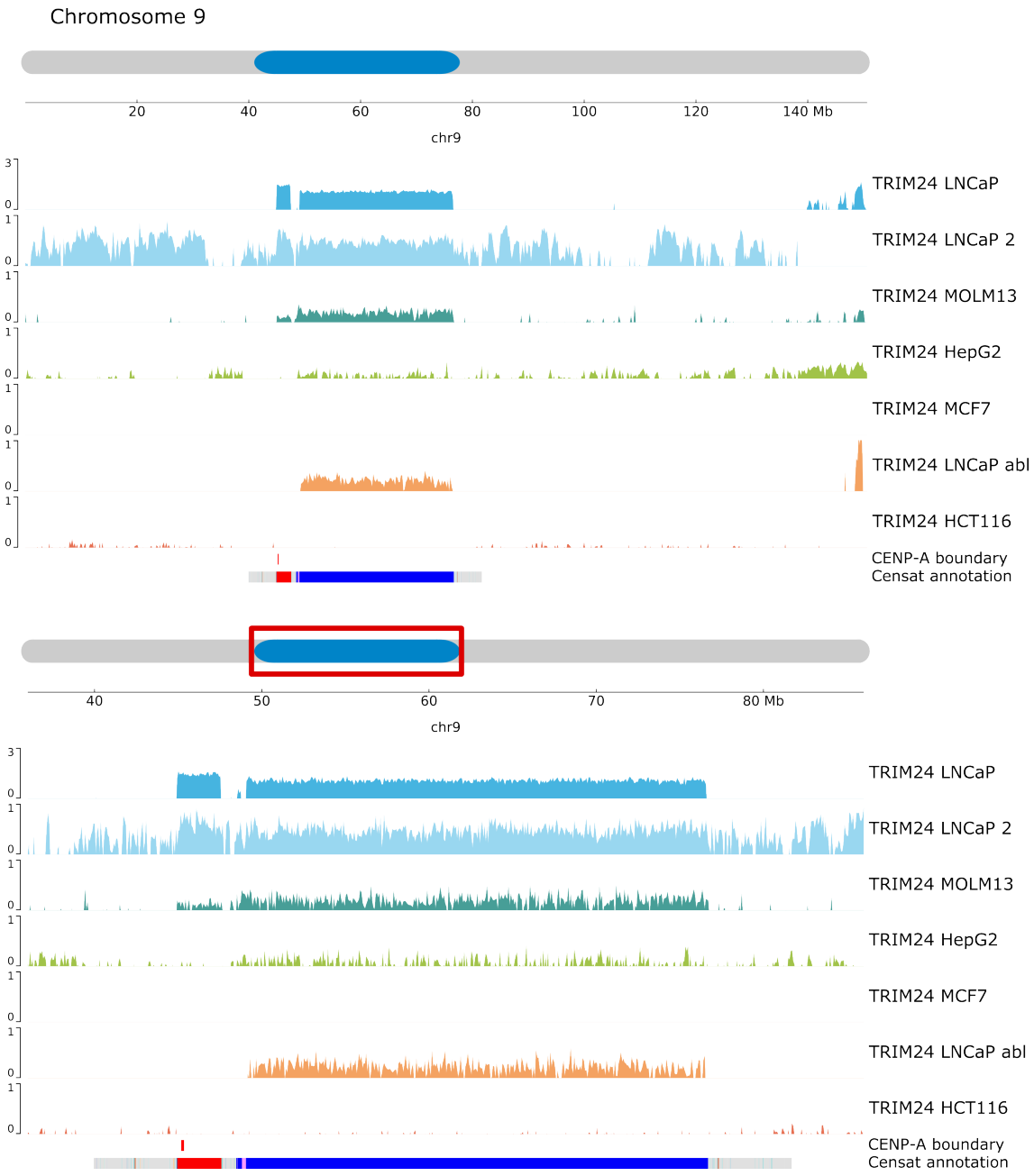
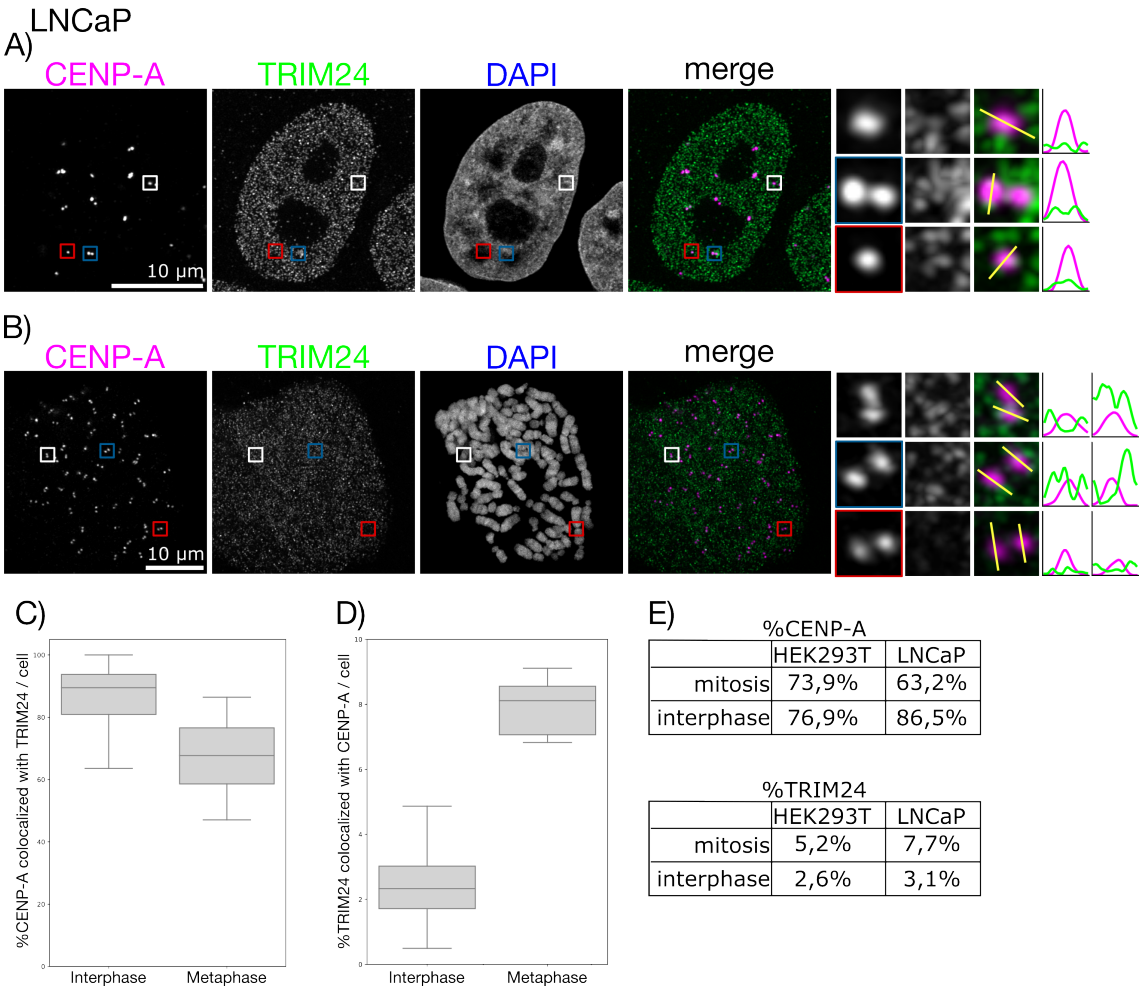


Figure S1.: TRIM24 enrichment at centromeres is cell type-dependent. Publicly available TRIM24 ChIP-seq datasets from six cell lines (LNCaP, MOLM-13, HepG2, MCF7, LNCaP abl, and HCT116) aligned to the telomere 2 telomere (T2T-CHM13v2.0) genome assembly. Genome tracks show TRIM24 alignment at chromosome 9 and close-up of the centromeric region. Signal tracks show $\log_2$(ChIP/input). Note the different y-axis for first LNCaP track. CENP-A boundaries are indicated. Centromeric repeat classes are annotated as follows: red - active α-satellite (α-sat) higher order repeats (HOR), orange - inactive α-sat HOR, dark red - divergent α-sat HOR, yellow - monomeric α-sat, light green - HSAT1A, dark green - HSAT1B, light blue - HSAT2, blue - HSAT3, pink - β-satellite, purple - γ-satellite, teal - other centromeric repeats (censat), grey - centromeric transition regions. For accession numbers, see Tab.19. For details, see Materials and Methods.



Figure S2.: TRIM24 enrichment at centromeres is cell type-dependent. Publicly available TRIM24 ChIP-seq datasets from six cell lines (LNCaP, MOLM-13, HepG2, MCF7, LNCaP abl, and HCT116) aligned to the telomere 2 telomere (T2T-CHM13v2.0) genome assembly. Genome tracks show TRIM24 alignment at chromosome 6 and close-up of the centromeric region. Signal tracks show $\log_2$(ChIP/input). Note the different y-axis for first LNCaP track. CENP-A boundaries are indicated. Centromeric repeat classes are annotated as follows: red - active α-satellite (α-sat) higher order repeats (HOR), orange - inactive α-sat HOR, dark red - divergent α-sat HOR, yellow - monomeric α-sat, light green - HSAT1A, dark green - HSAT1B, light blue - HSAT2, blue - HSAT3, pink - β-satellite, purple - γ-satellite, teal - other centromeric repeats (censat), grey - centromeric transition regions. For accession numbers, see Tab.19. For details, see Materials and Methods.



E)

%CENP-A

	HEK293T	LNCaP
mitosis	73,9%	63,2%
interphase	76,9%	86,5%

%TRIM24

	HEK293T	LNCaP
mitosis	5,2%	7,7%
interphase	2,6%	3,1%

Figure S3.: TRIM24 localizes to the centromere during interphase and mitosis in LNCaP cells. Representative images of a) interphase nucleus and b) metaphase chromosome spreads from LNCaP human cells stained for CENP-A (first column, indirect immunofluorescence) and TRIM24 (second column, indirect immunofluorescence), and against DNA (third column, DAPI). Insets show representative CENP-A foci and their corresponding TRIM24 signal, with fluorescence intensity profile plots (magenta: CENP-A, green: TRIM24). Images were recorded by Airyscan super-resolution microscopy. Scale bar: 10μm. For details, see Materials and Methods. c) Percentage of CENP-A foci colocalizing with TRIM24 per cell, measured in interphase and mitotic human LNCaP cells by indirect immunofluorescence. d) Percentage of TRIM24 foci colocalizing with CENP-A per cell, measured in interphase and mitotic human LNCaP cells. Boxplots show minimum, first quartile, median, third quartile, and maximum. Data represents n=308 interphase cells from three independent repeats, 12 metaphase cells from one experimental repeat. e) Comparison of the percentage of CENP-A foci colocalizing with TRIM24 and TRIM24 colocalizing with CENP-A foci in HEK293T and LNCaP cells.

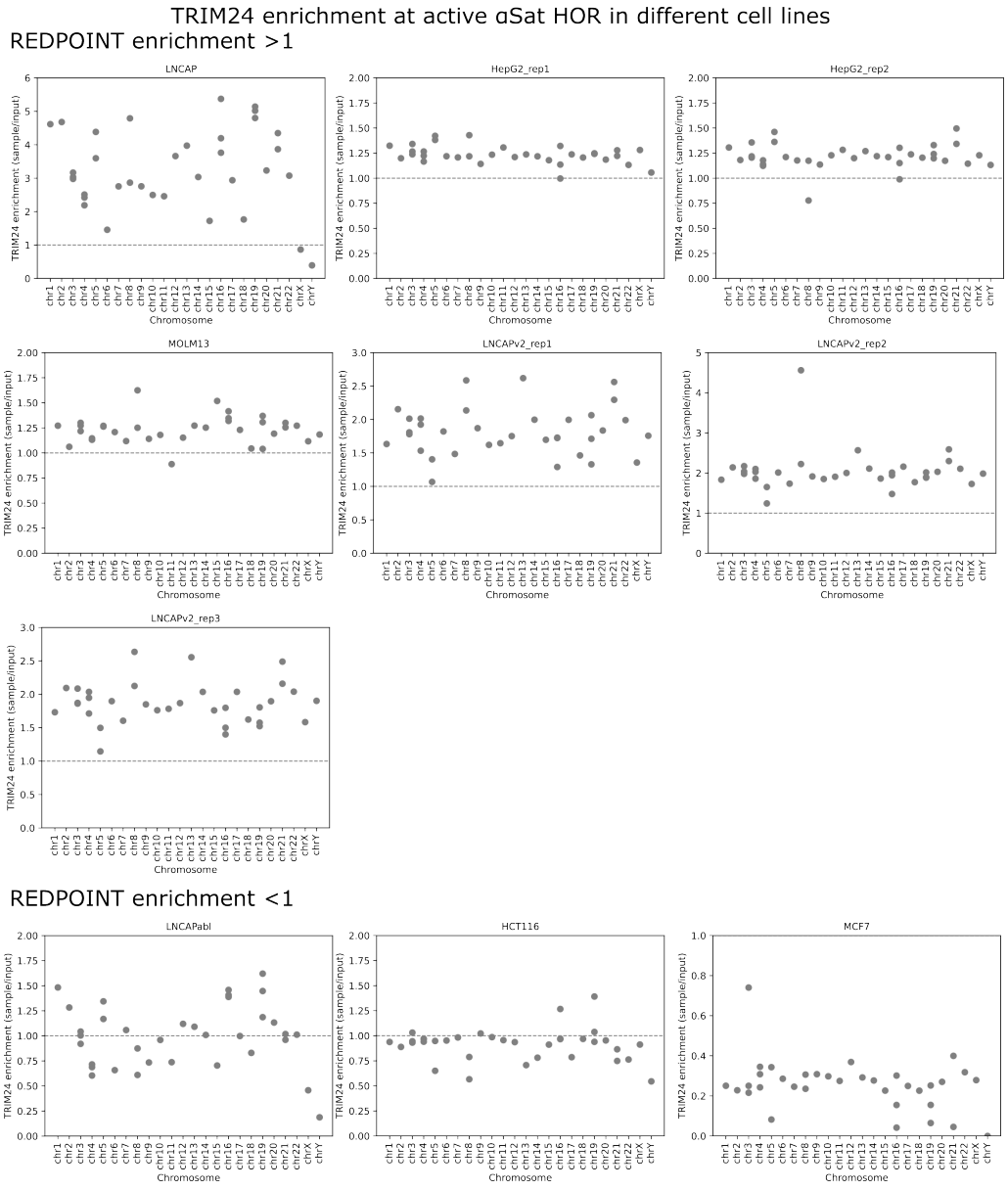


Figure S4.: Enrichment of TRIM24 at active α-sat HORs in different cell lines Enrichment of TRIM24 at active α-satellite higher order repeats (HOR) in different cell lines, per chromosome. Results obtained from publicly available ChIP-seq datasets aligned to T2T genome. For accession numbers, see Tab. 19. For details, see Materials and Methods.

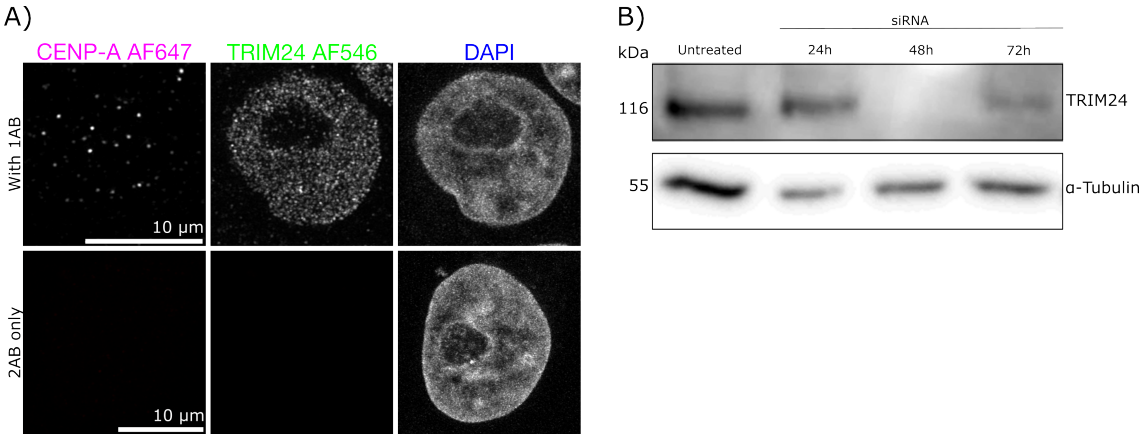


Figure S5.: Validation of TRIM24 and CENP-A antibodies. a) Representative nuclei of HEK293T cells. Cells were either stained for CENP-A with AF647 (indirect immunofluorescence), TRIM24 AF546 (indirect immunofluorescence) and DNA (DAPI) or secondary antibodies only: AF647, AF546, DAPI. Images were acquired using Airyscan super-resolution microscopy. The settings were kept constant across the samples. Scale bar: 10μm. b) Western blot of HEK293T cells, untreated, or treated with siRNA against TRIM24 for 24, 48 or 72h. Top band represents TRIM24, bottom - α-Tubulin. For details, see Materials and Methods.

Table S1.: Values of TRIM24 centromeric enrichment calculated by REDPOINT analysis, with corresponding accession numbers.

Study accession	Experiment accession	Drug	Protein	Cell Line	Sample/Input Ratio
PRJNA392134	SRR5762041	DMSO	TRIM24	MOLM-13	1.13
PRJNA130083	SRR065822	vehicle	TRIM24	MCF7	0.22
PRJNA285229	SRR2043644	vehicle	TRIM24	LNCaP	2.68
PRJNA986131	SRR24985370	vehicle	TRIM24	HepG2	1.02
PRJNA986131	SRR24985371	vehicle	TRIM24	HepG2	1.04
PRJNA638411	SRR11969094	vehicle	TRIM24	HCT116	0.91
PRJNA1199461	SRR31751536	vehicle	TRIM24	LNCaP	1.3
PRJNA1199461	SRR31751537	vehicle	TRIM24	LNCaP	1.35
PRJNA1199461	SRR31751538	vehicle	TRIM24	LNCaP	1.33
PRJNA285229	SRR2043646	DHT	TRIM24	LNCaP-abl	0.99

Table S2.: TRIM24 enrichment at centromeric repeat classes across datasets.

	hor active	hor inactive	dhor	mon	hsat1	hsat2	hsat3	censat	gsat	bsat	rDNA
MOLM13	1.23	1.06	1.12	1.13	0.73	1.02	1.31	1.77	1.4	1.39	1.83
HepG2 Rep1	1.23	1.18	1.11	1.01	0.8	1.24	1.24	1.31	1.54	1.44	1.46
HepG2 Rep2	1.22	1.15	1.06	1.1	0.77	1.14	1.32	1.4	1.54	1.52	1.69
LNCaP	3.27	1.32	1.81	0.7	1.06	0.79	1.46	3.45	2.45	0.9	1.73
LNCaP 2 Rep1	1.82	1.52	1.55	1.68	1.02	1.52	2.02	0.56	0.27	1.02	0.43
LNCaP 2 Rep2	2.05	1.81	1.68	2.03	0.56	1.81	2.71	0.67	0.38	1.31	0.54
LNCaP 2 Rep3	1.86	1.74	1.62	1.83	0.46	1.72	2.41	0.62	0.37	1.25	0.51
LNCaP abl	1	0.5	0.46	0.27	0.27	0.82	0.83	8.08	4.21	1.46	5.79
MCF7	0.25	0.45	0.22	0.37	1.75	0.23	0.16	6.76	2.99	0.86	3.28
HCT116	0.91	1	0.83	1.04	0.86	1.21	1.1	1.11	0.99	1.1	0.94

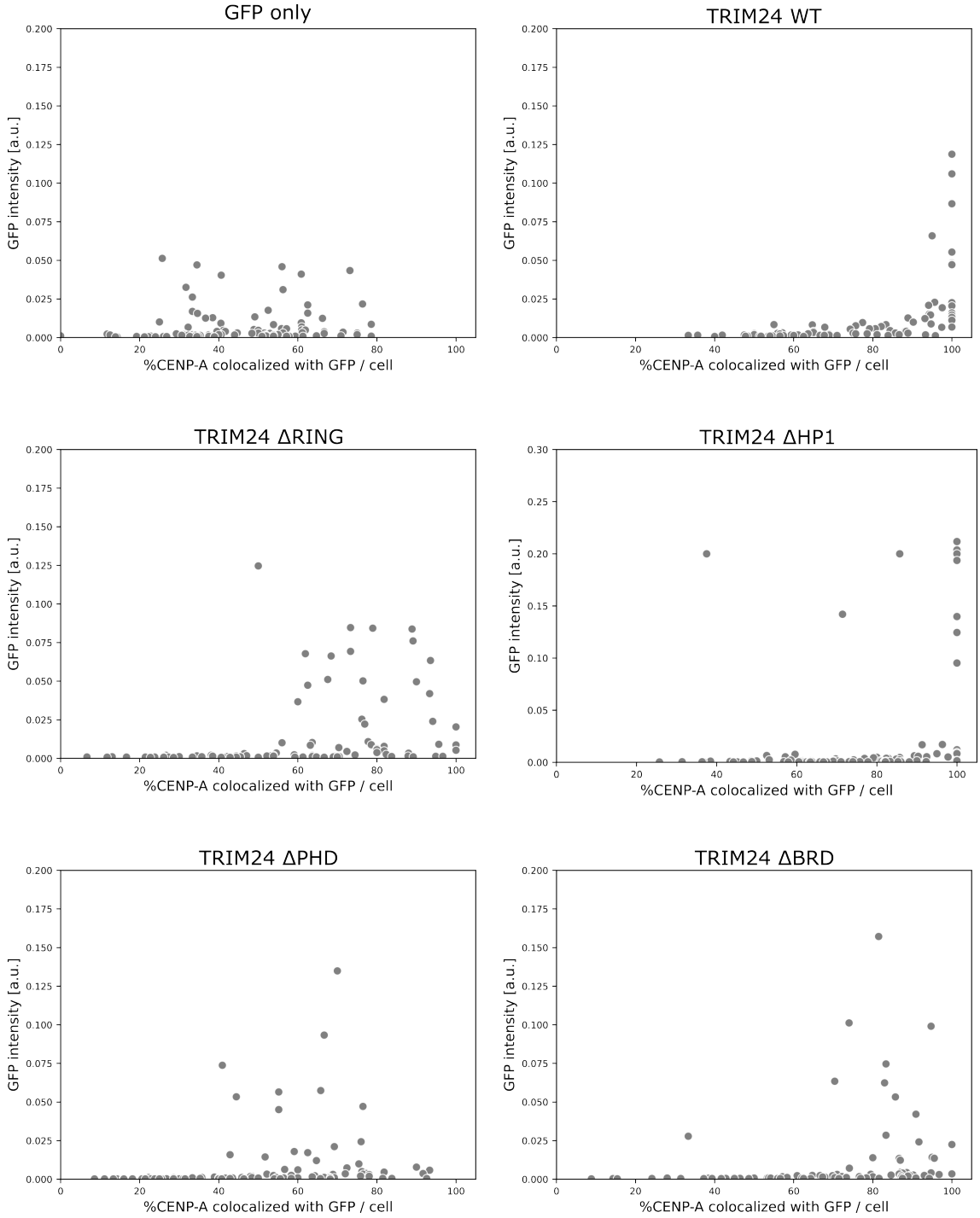


Figure S6.: TRIM24 colocalization in correlation to TRIM24 intensity in TRIM24 mutants. Scatterplot of percentage of CENP-A foci colocalizing with GFP versus GFP intenstiy per metaphase cell in HEK293T cells expressing GFP-only control, wildtype TRIM24 or TRIM24 mutants (ΔRING, ΔHP1, ΔPHD, ΔBRD). Colocalization was defined as overlap or direct contact between CENP-A and GFP signals. GFP intensity was quantified in CellProfiler by masking each metaphase spread using DNA channel and measuring mean GFP intensity within the mask. Data represent n=95, 90, 83, 98, 103, 89 across three independent experiments. For details, see Materials and Methods.

Table S3.: Public ChIP-seq datasets used for TRIM24 analysis and their key sequencing parameters.

PRJNA	Accession ID	Name	Cell Line	Illumina	Antibody	Seq Depth	Library Prep Kit	Library Layout
PRJNA 285229	SRR 2043644	LNCaP	LNCaP	HiSeq 2000	TRIM24 (A300-815A, Bethyl)	31 M	ThruPLEX-FD Prep Kit (Rubicon Genomics, R40048)	single
PRJNA 1199461	SRR 31751542	LNCaP rep1	LNCaP	HiSeq 4000	TRIM24 (NB100-2596, Novus Biologicals)	25.7 M	NovaSeq 6000 Illumina Kit	single
PRJNA 1199461	SRR 31751543	LNCaP rep2	LNCaP	HiSeq 4000	TRIM24 (NB100-2596, Novus Biologicals)	32.2 M	NovaSeq 6000 Illumina Kit	single
PRJNA 1199461	SRR 31751544	LNCaP rep3	LNCaP	HiSeq 4000	TRIM24 (NB100-2596, Novus Biologicals)	19.8 M	NovaSeq 6000 Illumina Kit	single
PRJNA 392161	SRR 5762041	MOLM-13	MOLM-13	NextSeq 500	TRIM24 (A300-851A, Bethyl)	60.5 M	Rubicon ThruPLEX DNA-seq Kit	single
PRJNA 638411	SRR 11969094	HCT116	HCT116	NextSeq 500	TRIM24 (DSHB hybridoma supernatant)	10.5 M	KAPA HTP Library Prep Kit (Roche)	single
PRJNA 130083	SRR 065822	MCF7	MCF7	Genome Analyzer II	TRIM24 (PCRP-TRIM24-1B12, Novus Biologicals)	10.8 M	Illumina IP-102-1001	single
PRJNA 986131	SRR 24985370	HepG2 rep1	HepG2	NovaSeq 6000	Anti-FLAG M2 (Sigma-Aldrich)	42 M	KAPA Library Quantification Kit	single
PRJNA 986131	SRR 24985371	HepG2 rep2	HepG2	NovaSeq 6000	Anti-FLAG M2 (Sigma-Aldrich)	37.8 M	KAPA Library Quantification Kit	single

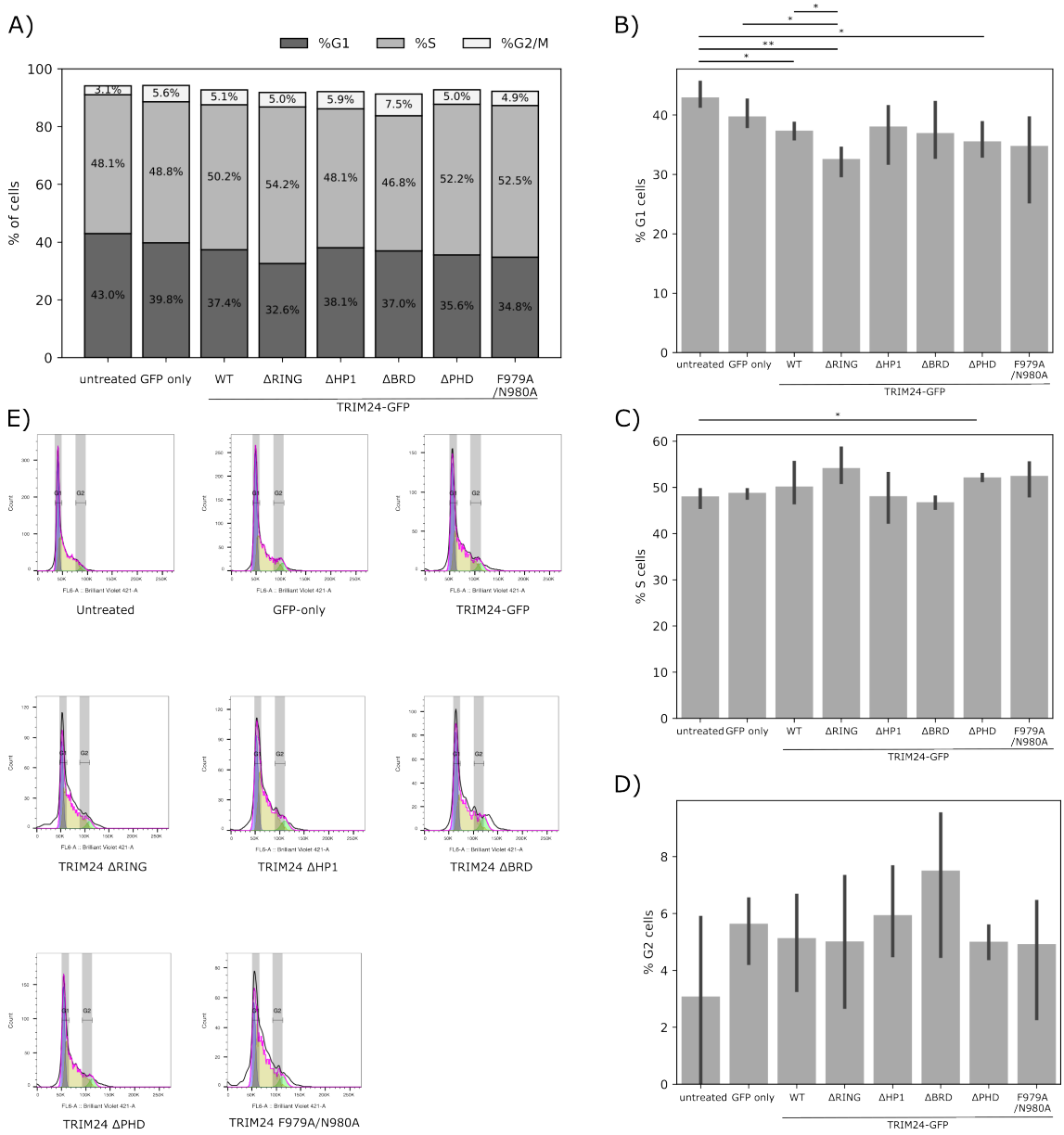


Figure S7.: Cell cycle analysis of TRIM24 mutants using Flow Cytometry. a) The percentage of cell cycle phases G1, S and G2/M in untreated HEK293T cells or cells overexpressing GFP-only, TRIM24-GFP or TRIM24 deletion mutants (ΔRING, ΔHP1, ΔBRD, ΔPHD, F979A/N980A), measured by flow cytometry. b, c, d) Percentage of cells in a) G1 b) S and c) G2/M phases. Data represent three independent experiments. Statistical analysis was performed using t-test; *<0.05, **<0.01. e) Representative cell cycle profiles for untreated cells and cells overexpressing GFP-only, TRIM24-GFP or TRIM24 deletion mutants. For details, see Materials and Methods.

6. Acknowledgments

First and foremost, I would like to express my deepest gratitude to Prof. Dr. Sylvia Erhardt for giving me the opportunity to pursue my doctoral research in her group. Thank you for your supervision and for the scientific freedom that allowed me to grow.

My sincere thanks go to Prof. Dr. Lennart Hilbert for serving as second referee and for valuable scientific discussions. You already guided me during my Master's thesis, and without your support I would not have chosen this path at all.

I thank Prof. Kyle Miller (Emory, USA) for providing the TRIM24 mutant plasmids and for insightful discussions, Dr. Christine Blattner (KIT) for the LNCaP cell line, and Prof. Hiroshi Kimura (Institute of Science Tokyo) for the Pol II Ser2P-sfGFP mintbody plasmid.

I am grateful to all members of the Erhardt lab for their support and discussions. I especially thank Dr. Sam Corless for the project idea and inspiring conversations. My sincere thanks also go to Dr. Anne-Laure Pauleau, whose enormous scientific knowledge and steady support were irreplaceable throughout this PhD.

To Kathy, Jasmin, Angi, Vojta and Alex: thank you for making this journey what it was. I appreciate your support, late-night discussions, and your willingness to listen when experiments (or life) refused to cooperate. It was a privilege to share a lab with you, and I could not have wished for better colleagues.

I would like to thank all the students I had the chance to supervise during their Bachelor's and Master's theses and practical courses - Kathy, Sarah, Marie, Mila, Tamara, Sofia and others. I tried to teach you as much as I could, but in the end I think you taught me even more.

My warmest thanks go to my friends, who have been a constant source of emotional support through every professional and personal challenge of the past years. Thank you for being there, no matter the distance.

Finally, I want to thank my parents and my brother. Your support and encouragement carried me through this journey. Dziękuję Wam z całego serca.

Bibliography

[1] M. R. Ajmal. Protein misfolding and aggregation in proteinopathies: Causes, mechanism and cellular response. *Diseases*, 11(1):30, 2023.

[2] S. Alberti, A. Gladfelter, and T. Mittag. Considerations and challenges in studying liquid-liquid phase separation and biomolecular condensates. *Cell*, 176(3):419–434, 2019.

[3] B. Alberts, A. Johnson, J. Lewis, D. Morgan, M. Raff, K. Roberts, and P. Walter. *Molecular Biology of the Cell*. Garland Science, New York, NY, 5 edition, 2008.

[4] C. Aleixandre, D. A. Miller, A. R. Mitchell, D. A. Warburton, S. L. Gersen, C. Disteche, and O. J. Miller. p82H identifies sequences at every human centromere. *Human Genetics*, 77(1):46–50, 1987.

[5] A. Ali-Ahmad and N. Sekulić. CENP-A nucleosome-a chromatin-embedded pedestal for the centromere: lessons learned from structural biology. *Essays in Biochemistry*, 64(2):205–221, 2020.

[6] R. C. Allshire and G. H. Karpen. Epigenetic regulation of centromeric chromatin: old dogs, new tricks? *Nature Reviews Genetics*, 9(12):923–937, 2008.

[7] K. Allton, A. K. Jain, H. Herz, W. Tsai, S. Y. Jung, J. Qin, A. Bergmann, R. L. Johnson, and M. C. Barton. TRIM24 targets endogenous p53 for degradation. *Proceedings of the National Academy of Sciences of the United States of America*, 106(28):11612–11616, 2009.

[8] D. Alonso-Gil, A. Cuadrado, D. Giménez-Llorente, M. Rodríguez-Corsino, and A. Losada. Different NIPBL requirements of cohesin-STAG1 and cohesin-STAG2. *Nature Communications*, 14(1):1326, 2023.

[9] N. Altemose, G. A. Logsdon, A. V. Bzikadze, P. Sidhwani, S. A. Langley, G. V. Caldas, S. J. Hoyt, L. Uralsky, F. D. Ryabov, C. J. Shew, M. E. G. Sauria, M. Borchers, A. Gershman, A. Mikheenko, V. A. Shepelev, T. Dvorkina, O. Kunyavskaya, M. R. Vollger, A. Rhie, A. M. McCartney, M. Asri, R. Lorig-Roach, K. Shafin, J. K. Lucas, S. Aganezov, D. Olson, L. G. de Lima, T. Potapova, G. A. Hartley, M. Haukness, P. Kerpedjiev, F. Gusev, K. Tigyi, S. Brooks, A. Young, S. Nurk, S. Koren, S. R. Salama, B. Paten, E. I. Rogaev, A. Streets, G. H. Karpen, A. F. Dernburg, B. A. Sullivan, A. F. Straight, T. J. Wheeler, J. L. Gerton, E. E. Eichler, A. M. Phillippy, W. Timp, M. Y. Dennis, R. J. O'Neill, J. M. Zook, M. C. Schatz, P. A. Pevzner, M. Diekhans, C. H. Langley, I. A. Alexandrov, and K. H. Miga. Complete genomic and epigenetic maps of human centromeres. *Science*, 376(6588):eabl4178, 2022.

[10] N. Altemose, A. Maslan, O. K. Smith, K. Sundararajan, R. R. Brown, R. Mishra, A. M. Detweiler, N. Neff, K. H. Miga, A. F. Straight, and A. Streets. DiMeLo-seq: a long-read, single-molecule method for mapping protein–DNA interactions genome wide. *Nature Methods*, 19(6):711–723, 2022.

[11] D. E. Anderson, A. Losada, H. P. Erickson, and T. Hirano. Condensin and cohesin display different arm conformations with characteristic hinge angles. *Journal of Cell Biology*, 156:419–424, 2002.

[12] S. Appikonda, K. N. Thakkar, and M. C. Barton. Regulation of gene expression in human cancers by TRIM24. *Drug Discovery Today: Technologies*, 19:57–63, 2016.

[13] G. Arunkumar and D. P. Melters. Centromeric transcription: a conserved Swiss-army knife. *Genes*, 11(8):911, 2020.

[14] T. Barrett and R. Edgar. Gene Expression Omnibus: microarray data storage, submission, retrieval, and analysis. *Methods in Enzymology*, 411:352–369, 2006.

[15] J. J. Bayes and H. S. Malik. The evolution of centromeric DNA sequences. In *Encyclopedia of Life Sciences (ELS)*. John Wiley & Sons, Ltd, Chichester, 2008.

[16] D. R. Bentley, S. Balasubramanian, H. P. Swerdlow, G. P. Smith, J. Milton, C. G. Brown, K. P. Hall, D. J. Evers, C. L. Barnes, H. R. Bignell, et al. Accurate whole human genome sequencing using reversible terminator chemistry. *Nature*, 456(7218):53–59, 2008.

[17] J. H. Bergmann, J. N. Jakubsche, N. M. Martins, A. Kagansky, M. Nakano, H. Kimura, D. A. Kelly, B. M. Turner, H. Masumoto, V. Larionov, and W. C. Earnshaw. Epigenetic engineering: histone H3K9 acetylation is compatible with kinetochore structure and function. *Journal of Cell Science*, 125(2):411–421, 2012.

[18] J. H. Bergmann, M. G. Rodríguez, N. M. C. Martins, H. Kimura, D. A. Kelly, H. Masumoto, V. Larionov, L. E. T. Jansen, and W. C. Earnshaw. Epigenetic engineering shows H3K4me2 is required for HJURP targeting and CENP-A assembly on a synthetic human kinetochore. *The EMBO Journal*, 30(2):328–340, 2011.

[19] B. E. Black and E. A. Bassett. The histone variant CENP-A and centromere specification. *Current Opinion in Cell Biology*, 20(1):91–100, 2008.

[20] B. E. Black and D. W. Cleveland. Epigenetic centromere propagation and the nature of CENP-A nucleosomes. *Cell*, 144(4):471–479, 2011.

[21] B. E. Black, D. R. Foltz, S. Chakravarthy, K. Luger, J. Woods, V. L., and D. W. Cleveland. Structural determinants for generating centromeric chromatin. *Nature*, 430(6999):578–582, 2004.

[22] B. E. Black, L. E. Jansen, P. S. Maddox, D. R. Foltz, A. B. Desai, J. V. Shah, and D. W. Cleveland. Centromere identity maintained by nucleosomes assembled with histone H3 containing the CENP-A targeting domain. *Molecular Cell*, 25(2):309–322, 2007.

[23] M. D. Blower. Centromeric transcription regulates Aurora-B localization and activation. *Cell Reports*, 15(8):1624–1633, 2016.

[24] M. D. Blower and G. H. Karpen. The role of *Drosophila* CID in kinetochore formation, cell-cycle progression and heterochromatin interactions. *Nature Cell Biology*, 3(8):730–739, 2001.

[25] G. Bobkov, N. Gilbert, and P. Heun. Centromere transcription allows CENP-A to transit from chromatin association to stable incorporation. *The Journal of Cell Biology*, 217(7):1957–1972, 2018.

[26] L. J. H. Borrero and W. S. El-Deiry. Tumor suppressor p53: biology, signaling pathways, and therapeutic targeting. *Biochimica et Biophysica Acta (BBA) - Reviews on Cancer*, 1876(1):188556, 2021.

[27] H. Bouzinba-Segard, A. Guais, and C. Francastel. Accumulation of small murine minor satellite transcripts leads to impaired centromeric architecture and function. *Proceedings of the National Academy of Sciences of the United States of America*, 103(23):8709–8714, 2006.

[28] A. S. Brooker and K. M. Berkowitz. The roles of cohesins in mitosis, meiosis, and human health and disease. *Methods in Molecular Biology*, 1170:229–266, 2014.

[29] C. W. Carroll, M. C. Silva, K. M. Godek, L. E. Jansen, and A. F. Straight. Centromere assembly requires the direct recognition of CENP-A nucleosomes by CENP-N. *Nature Cell Biology*, 11(7):896–902, 2009.

[30] B. L. Carty, D. Dubocanin, M. Murillo-Pineda, M. Dumont, E. Volpe, P. Mikulski, J. Humes, O. Whittingham, D. Fachinetti, S. Giunta, N. Altemose, and L. E. T. Jansen. Heterochromatin boundaries maintain centromere position, size and number. *Nature Structural & Molecular Biology*, 2025.

[31] S. Carvalhal, A. Tavares, M. B. Santos, M. Mirkovic, and R. A. Oliveira. A quantitative analysis of cohesin decay in mitotic fidelity. *Journal of Cell Biology*, 217(10):3343–3353, 2018.

[32] F. L. Chan, O. J. Marshall, R. Saffery, B. W. Kim, E. Earle, K. H. Choo, and L. H. Wong. Active transcription and essential role of RNA polymerase II at the centromere during mitosis. *Proc Natl Acad Sci USA*, 109:1979–1984, 2012.

[33] F. L. Chan and L. H. Wong. Transcription in the maintenance of centromere chromatin identity. *Nucleic Acids Research*, 40(22):11178–11188, 2012.

[34] K. L. Chan, M. B. Roig, B. Hu, F. Beckouët, J. Metson, and K. Nasmyth. Cohesin's DNA exit gate is distinct from its entrance gate and is regulated by acetylation. *Cell*, 150(5):961–974, 2012.

[35] I. M. Cheeseman. The kinetochore. *Cold Spring Harbor Perspectives in Biology*, 6(7):a015826, 2014.

[36] C. C. Chen, S. Bowers, Z. Lipinszki, J. Palladino, S. Trusiak, E. Bettini, L. Rosin, M. R. Przewloka, D. M. Glover, R. J. O'Neill, and B. G. Mellone. Establishment of centromeric chromatin by the CENP-A assembly factor CAL1 requires FACT-mediated transcription. *Developmental Cell*, 34(1):73–84, 2015.

[37] E. S. Chen, S. Saitoh, M. Yanagida, and K. Takahashi. A cell cycle-regulated GATA factor promotes centromeric localization of CENP-A in fission yeast. *Molecular Cell*, 11:175–187, 2003.

[38] Q. Chen and P. Yang. Coiled-coil-domain-mediated TRIM E3 protein condensation modulates enzymatic activity and functional specificity. *Cell Reports*, 44(6):115766, 2025.

[39] Y. Chen, Q. Zhang, Z. Teng, and H. Liu. Centromeric transcription maintains centromeric cohesion in human cells. *Journal of Cell Biology*, 220(7):e202008146, 2021.

[40] H. Cheng, N. Zhang, and D. Pati. Cohesin subunit RAD21: From biology to disease. *Gene*, 758:144966, 2020.

[41] R. Contreras-Galindo, S. Fischer, A. K. Saha, J. D. Lundy, P. W. Cervantes, M. Mourad, C. Wang, B. Qian, M. Dai, F. Meng, A. Chinnaiyan, G. S. Omenn, M. H. Kaplan, and D. M. Markovitz. Rapid molecular assays to study human centromere genomics. *Genome Research*, 27(12):2040–2049, 2017.

[42] L. Corda and S. Giunta. Chromosome-specific centromeric patterns define the centeny map of the human genome. *Science*, 389:eads3484, 2025.

[43] S. Corless, S. Höcker, and S. Erhardt. Centromeric RNA and its function at and beyond centromeric chromatin. *Journal of Molecular Biology*, 432(15):4257–4269, 2020.

[44] S. Corless, N. Pratap-Singh, N. S. Benabdallah, J. Böhm, A. M. Simon, V. Dolejš, S. Anders, A. Banito, and S. Erhardt. The bromodomain inhibitor JQ1 is a molecular glue targeting centromeres. *BioRxiv*, 2023.

[45] F. D'Amico, R. Mukhopadhyay, H. Ovaa, and M. P. C. Mulder. Targeting TRIM proteins: A quest towards drugging an emerging protein class. *ChemBioChem*, 22(12):2011–2031, 2021.

[46] P. Danecek, J. K. Bonfield, J. Liddle, J. Marshall, V. Ohan, M. O. Pollard, A. Whitwham, T. Keane, S. A. McCarthy, R. M. Davies, and H. Li. Twelve years of SAMtools and BCFtools. *GigaScience*, 10(2):giab008, 2021.

[47] Y. Du, C. N. Topp, and R. K. Dawe. DNA binding of centromere protein C (CENP-C) is stabilized by single-stranded RNA. *PLoS Genetics*, 6(2):e1000835, 2010.

[48] D. Dubocanin, G. A. Hartley, A. E. Sedeño Cortés, Y. Mao, S. Hedouin, J. Ranchalis, A. Agarwal, G. A. Logsdon, K. M. Munson, T. Real, B. J. Mallory, E. E. Eichler, S. Biggins, R. J. O'Neill, and A. B. Stergachis. Conservation of dichromatin organization along regional centromeres. *Cell Genomics*, 5(4):100819, 2025.

[49] R. Düster, I. H. Kaltheuner, M. Schmitz, and M. Geyer. 1,6-Hexanediol, commonly used to dissolve liquid-liquid phase separated condensates, directly impairs kinase and phosphatase activities. *Journal of Biological Chemistry*, 296:100260, 2021.

[50] W. C. Earnshaw and B. R. Migeon. Three related centromere proteins are absent from the inactive centromere of a stable isodicentric chromosome. *Chromosoma*, 92:290–296, 1985.

[51] C. S. Eichinger, A. Kurze, R. A. Oliveira, and K. Nasmyth. Disengaging the Smc3/kleisin interface releases cohesin from drosophila chromosomes during interphase and mitosis. *The EMBO Journal*, 32(5):656–665, 2013.

[52] N. Eickhoff, J. Janetzko, N. Padrão, S. Gregoricchio, J. C. Siefert, L. Hoekman, S. Linder, O. Bleijerveld, A. M. Bergman, and W. Zwart. TRIM33 loss reduces androgen receptor transcriptional output and H2BK120 ubiquitination. *Communications Biology*, 8(1):1043, 2025.

[53] S. Eustermann, J. C. Yang, M. J. Law, R. Amos, L. M. Chapman, C. Jelinska, D. Garrick, D. Clynes, R. J. Gibbons, D. Rhodes, D. R. Higgs, and D. Neuhaus. Combinatorial readout of histone H3 modifications specifies localization of atrx to heterochromatin. *Nature Structural & Molecular Biology*, 18(7):777–782, 2011.

[54] A. Eymery, B. Horard, M. El Atifi-Borel, G. Fourel, F. Berger, A. L. Vitte, A. Van den Broeck, E. Brambilla, A. Fournier, M. Callanan, S. Gazzeri, S. Khochbin, S. Rousseaux, E. Gilson, and C. Vourc'h. A transcriptomic analysis of human centromeric and pericentric sequences in normal and tumor cells. *Nucleic Acids Research*, 37(19):6340–6354, 2009.

[55] F. Ferri, H. Bouzinba-Segard, G. Velasco, F. Hube, and C. Francastel. Non-coding murine centromeric transcripts associate with and potentiate Aurora B kinase. *Nucleic Acids Research*, 37(15):5071–5080, 2009.

[56] F. Fiorentini, D. Esposito, and K. Rittinger. Does it take two to tango? RING domain self-association and activity in TRIM E3 ubiquitin ligases. *Biochemical Society Transactions*, 48(6):2615–2624, 2020.

[57] S. Flashner, M. Swift, A. Sowash, A. N. Fahmy, and J. Azizkhan-Clifford. Transcription factor Sp1 regulates mitotic chromosome assembly and segregation. *Chromosoma*, 131(3):175–191, 2022.

[58] D. R. Foltz, L. E. Jansen, B. E. Black, A. O. Bailey, J. R. Yates, and D. W. Cleveland. The human CENP-A centromeric nucleosome-associated complex. *Nature Cell Biology*, 8(5):458–469, 2006.

[59] J. M. Franklin, D. Dubocanin, C. Chittenden, A. Barillas, R. J. Lee, R. P. Ghosh, J. L. Gerton, K.-L. Guan, and N. Altemose. Human Satellite 3 DNA encodes megabase-scale transcription factor binding platforms. *bioRxiv*, 2024.

[60] T. Fukagawa, M. Nogami, M. Yoshikawa, M. Ikeno, T. Okazaki, Y. Takami, T. Nakayama, and M. Oshimura. Dicer is essential for formation of the heterochromatin structure in vertebrate cells. *Nature Cell Biology*, 6:784–791, 2004.

[61] A. García-Nieto, A. Patel, Y. Li, R. Oldenkamp, L. Feletto, J. J. Graham, L. Willems, K. W. Muir, D. Panne, and B. D. Rowland. Structural basis of centromeric cohesion protection. *Nature Structural & Molecular Biology*, 30(6):853–859, 2023.

[62] L. N. Gechijian, D. L. Buckley, M. A. Lawlor, J. M. Reyes, J. Paulk, C. J. Ott, G. E. Winter, M. A. Erb, T. G. Scott, M. Xu, H. S. Seo, S. Dhe-Paganon, N. P. Kwiatkowski, J. A. Perry, J. Qi, N. S. Gray, and J. E. Bradner. Functional TRIM24 degrader via conjugation of ineffectual bromodomain and VHL ligands. *Nature Chemical Biology*, 14(4):405–412, 2018.

[63] D. Gerlich, B. Koch, F. Dupeux, J. M. Peters, and J. Ellenberg. Live-cell imaging reveals a stable cohesin–chromatin interaction after but not before DNA replication. *Current Biology*, 16:1571–1578, 2006.

[64] F. Gong, L. Y. Chiu, B. Cox, F. Aymard, T. Clouaire, J. W. Leung, M. Cammarata, M. Perez, P. Agarwal, J. S. Brodbelt, G. Legube, and K. M. Miller. Screen identifies bromodomain protein ZMYND8 in chromatin recognition of transcription-associated DNA damage that promotes homologous recombination. *Genes & Development*, 29(2):197–211, 2015.

[65] G. Grillo, E. Boyarchuk, S. Mihic, I. Ivkovic, M. Bertrand, A. Jouneau, T. Dahlet, M. Dumas, M. Weber, G. Velasco, and C. Francastel. ZBTB24 is a conserved multifaceted transcription factor at genes and centromeres that governs the DNA methylation state and expression of satellite repeats. *Human Molecular Genetics*, 34(2):161–177, 2025.

[66] A. C. Groner, L. Cato, J. de Tribolet-Hardy, T. Bernasocchi, H. Janouskova, D. Melchers, R. Houtman, A. C. B. Cato, P. Tschopp, L. Gu, A. Corsinotti, Q. Zhong, C. Fankhauser, C. Fritz, C. Poyet, U. Wagner, T. Guo, R. Aebersold, L. A. Garraway, P. J. Wild, J. P. Theurillat, and M. Brown. TRIM24 is an oncogenic transcriptional activator in prostate cancer. *Cancer Cell*, 29(6):846–858, 2016.

[67] M. Guenatri, D. Bailly, C. Maison, and G. Almouzni. Mouse centric and pericentric satellite repeats form distinct functional heterochromatin. *Journal of Cell Biology*, 166:493–505, 2004.

[68] J. H. Haarhuis, A. M. Elbatsh, and B. D. Rowland. Cohesin and its regulation: on the logic of X-shaped chromosomes. *Developmental Cell*, 31(1):7–18, 2014.

[69] C. H. Haering, J. Löwe, A. Hochwagen, and K. Nasmyth. Molecular architecture of SMC proteins and the yeast cohesin complex. *Molecular Cell*, 9:773–788, 2002.

[70] L. E. Hall, S. E. Mitchell, and R. J. O'Neill. Pericentric and centromeric transcription: a perfect balance required. *Chromosome Research*, 20:535–546, 2012.

[71] K. Hara, G. Zheng, Q. Qu, et al. Structure of cohesin subcomplex pinpoints direct Shugoshin–Wapl antagonism in centromeric cohesion. *Nature Structural & Molecular Biology*, 21:864–870, 2014.

[72] S. Hatakeyama. TRIM family proteins: Roles in autophagy, immunity, and carcinogenesis. *Trends in Biochemical Sciences*, 42(4):297–311, 2017.

[73] B. Herquel, K. Ouararhni, K. Khetchoumian, M. Ignat, M. Teletin, M. Mark, G. Béchade, A. Van Dorsselaer, S. Sanglier-Cianférani, A. Hamiche, F. Cammas, I. Davidson, and R. Losson. Transcription cofactors TRIM24, TRIM28, and TRIM33 associate to form regulatory complexes that suppress murine hepatocellular carcinoma. *Proceedings of the National Academy of Sciences of the United States of America*, 108(20):8212–8217, 2011.

[74] P. Heun, S. Erhardt, M. D. Blower, S. Weiss, A. D. Skora, and G. H. Karpen. Mislocalization of the *Drosophila* centromere-specific histone CID promotes formation of functional ectopic kinetochores. *Developmental Cell*, 10(3):303–315, 2006.

[75] M. T. Hoque, F. Ishikawa, K. Shirahige, and T. Hirota. Cohesin defects lead to premature sister chromatid separation, kinetochore dysfunction, and spindle-assembly checkpoint activation. *Journal of Biological Chemistry*, 277(44):42306–42314, 2002.

[76] P. Hunt and T. Hassold. Female meiosis: coming unglued with age. *Current Biology*, 20:R699–R702, 2010.

[77] L. Isbel, M. Iskar, S. Durdu, J. Weiss, R. S. Grand, E. Hietter-Pfeiffer, Z. Kozicka, A. K. Michael, L. Burger, N. H. Thomä, and D. Schübeler. Readout of histone methylation by Trim24 locally restricts chromatin opening by p53. *Nature Structural & Molecular Biology*, 30(7):948–957, 2023.

[78] S. Ishikura, K. Nakabayashi, M. Nagai, T. Tsunoda, and S. Shirasawa. ZFAT binds to centromeres to control noncoding RNA transcription through the KAT2B–H4K8ac–BRD4 axis. *Nucleic Acids Research*, 48(19):10848–10866, 2020.

[79] A. K. Jain, K. Allton, A. D. Duncan, and M. C. Barton. TRIM24 is a p53-induced E3-ubiquitin ligase that undergoes ATM-mediated phosphorylation and autodegradation during DNA damage. *Molecular and Cellular Biology*, 34(14):2695–2709, 2014.

[80] A. K. Jain, K. Allton, M. Iacovino, E. Mahen, R. J. Milczarek, T. P. Zwaka, M. Kyba, and M. C. Barton. p53 regulates cell cycle and microRNAs to promote differentiation of human embryonic stem cells. *PLoS Biology*, 10(2):e1001268, 2012.

[81] A. Jambhekar, A. B. Emerman, C. T. Schweidenback, and M. D. Blower. RNA stimulates Aurora B kinase activity during mitosis. *PLoS ONE*, 9(6):e100748, 2014.

[82] L. E. Jansen, B. E. Black, D. R. Foltz, and D. W. Cleveland. Propagation of centromeric chromatin requires exit from mitosis. *Journal of Cell Biology*, 176(6):795–805, 2007.

[83] A. Janssen, S. U. Colmenares, and G. H. Karpen. Heterochromatin: Guardian of the genome. *Annual Review of Cell and Developmental Biology*, 34(1):265–288, 2018.

[84] W. L. Johnson and A. F. Straight. RNA-mediated regulation of heterochromatin. *Current Opinion in Cell Biology*, 46:102–109, 2017.

[85] C. Kanellopoulou, S. A. Muljo, A. L. Kung, S. Ganesan, R. Drapkin, T. Jenuwein, D. M. Livingston, and K. Rajewsky. Dicer-deficient mouse embryonic stem cells are defective in differentiation and centromeric silencing. *Genes & Development*, 19:489–501, 2005.

[86] J. Kang, J. Chaudhary, H. Dong, S. Kim, C. A. Brautigam, and H. Yu. Mitotic centromeric targeting of HP1 and its binding to Sgo1 are dispensable for sister-chromatid cohesion in human cells. *Molecular Biology of the Cell*, 22:1181–1190, 2011.

[87] K. Katz, O. Shutov, R. Lapoint, M. Kimelman, J. R. Brister, and C. O'Sullivan. The Sequence Read Archive: a decade more of explosive growth. *Nucleic Acids Research*, 50:D387–D390, 2022.

[88] S. A. Kawashima, Y. Yamagishi, T. Honda, K. Ishiguro, and Y. Watanabe. Phosphorylation of H2A by Bub1 prevents chromosomal instability through localizing shugoshin. *Science*, 327(5962):172–177, 2010.

[89] K. Khetchoumian, M. Teletin, J. Tisserand, M. Mark, B. Herquel, M. Ignat, J. Zucman-Rossi, F. Cammas, T. Lerouge, C. Thibault, D. Metzger, P. Chambon, and R. Losson. Loss of TRIM24 (Tif1α) gene function confers oncogenic activity to retinoic acid receptor alpha. *Nature Genetics*, 39:1500–1506, 2007.

[90] D. Kim, R. Bhargava, S.-C. Wang, W.-C. Tseng, D. Lee, R. Patel, S. Oh, I. Bowman, R. W., B. A. Smith, M. Kim, C. H. Na, R. J. O'Sullivan, and K. M. Miller. TRIM24 directs replicative stress responses to maintain ALT telomeres via chromatin signaling. *Molecular Cell*, 85(14):2636–2653.e8, 2025.

[91] T. S. Kitajima, S. Hauf, M. Ohsugi, T. Yamamoto, and Y. Watanabe. Human Bub1 defines the persistent cohesion site along the mitotic chromosome by affecting Shugoshin localization. *Current Biology*, 15(4):353–359, 2005.

[92] T. Klingberg, I. Wachter, A. Pancholi, Y. Gohar, P. Kumar, M. Sobucki, E. Kämmer, S. Eroğlu-Kayıkçı, S. Erhardt, C. Ferrai, V. Zaburdaev, and L. Hilbert. Transcriptional clusters follow a conserved condensation-dispersal sequence during stem cell differentiation. *bioRxiv*, 2023.

[93] M. Kuru-Schors, M. Haemmerle, and T. Gutschner. The cohesin complex and its interplay with non-coding RNAs. *Non-Coding RNA*, 7(4):67, 2021.

[94] M. Lachner, D. O'Carroll, S. Rea, K. Mechtler, and T. Jenuwein. Methylation of histone H3 lysine 9 creates a binding site for HP1 proteins. *Nature*, 410(6824):116–120, 2001.

[95] W. K. M. Lai, L. Mariani, G. Rothschild, E. R. Smith, B. J. Venters, T. R. Blanda, P. K. Kuntala, K. Bocklund, J. Mairose, S. N. Dweikat, K. Mistretta, M. J. Rossi, D. James, J. T. Anderson, S. K. Phanor, W. Zhang, Z. Zhao, A. P. Shah, K. Novitzky, E. McAnarney, M. C. Keogh, A. Shilatifard, U. Basu, M. L. Bulyk, and B. F. Pugh. A ChIP-exo screen of 887 protein capture reagents program transcription factor antibodies in human cells. *Genome Research*, 31(9):1663–1679, 2021.

[96] A. L. Lam, C. D. Boivin, C. F. Bonney, M. K. Rudd, and B. A. Sullivan. Human centromeric chromatin is a dynamic chromosomal domain that can spread over noncentromeric DNA. *Proceedings of the National Academy of Sciences of the United States of America*, 103(11):4186–4191, 2006.

[97] M. A. Lampson and I. M. Cheeseman. Sensing centromere tension: Aurora B and the regulation of kinetochore function. *Trends in Cell Biology*, 21(3):133–140, 2011.

[98] B. Langmead, C. Trapnell, M. Pop, and S. L. Salzberg. Ultrafast and memory-efficient alignment of short DNA sequences to the human genome. *Genome Biology*, 10:R25, 2009.

[99] P. Lara-González, F. G. Westhorpe, and S. S. Taylor. The spindle assembly checkpoint. *Current Biology*, 22(22):R966–R980, 2012.

[100] J. Lawrimore and K. Bloom. Shaping centromeres to resist mitotic spindle forces. *Journal of Cell Science*, 135(4):jcs259532, 2022.

[101] S. Leclerc and K. Kitagawa. The role of human centromeric RNA in chromosome stability. *Frontiers in Molecular Biosciences*, Volume 8 - 2021, 2021.

[102] Y. C. G. Lee, Y. Ogiyama, N. M. C. Martins, B. J. Beliveau, D. Acevedo, C. T. Wu, G. Cavalli, and G. H. Karpen. Pericentromeric heterochromatin is hierarchically organized and spatially contacts H3K9me2 islands in euchromatin. *PLoS Genetics*, 16(3):e1008673, 2020.

[103] I. Lermontova, V. Schubert, J. Fuchs, S. Klatte, J. Macas, and I. Schubert. Loading of *Arabidopsis* centromeric histone CENH3 occurs mainly during G2 and requires the presence of the histone fold domain. *The Plant Cell*, 18:2443–2451, 2006.

[104] H. Li. Aligning sequence reads, clone sequences and assembly contigs with BWA-MEM. *arXiv:1303.3997v2*, 2013.

[105] J. Li, J. Zhao, X. Gan, Y. Wang, D. Jiang, L. Chen, F. Wang, J. Xu, H. Pei, J. Huang, and X. Chen. The RPA-RNF20-SNF2H cascade promotes proper chromosome segregation and homologous recombination repair. *Proceedings of the National Academy of Sciences of the United States of America*, 120(20):e2303479120, 2023.

[106] J. Liang, Y. Wang, J. Demmerle, B. J. He, C. J. Ricketts, W. M. Linehan, C. Zang, and D. Cai. TEAD1 condensates are transcriptionally inactive storage sites on the pericentromeric heterochromatin. *bioRxiv*, 2025.

[107] Y. C. Lin, M. Boone, L. Meuris, I. Lemmens, N. Van Roy, A. Soete, J. Reumers, M. Moisse, S. Plaisance, R. Drmanac, J. Chen, F. Speleman, D. Lambrechts, Y. Van de Peer, J. Tavernier, and N. Callewaert. Genome dynamics of the human embryonic kidney 293 lineage in response to cell biology manipulations. *Nature Communications*, 5:4767, 2014.

[108] H. Liu, Q. Qu, R. Warrington, A. Rice, N. Cheng, and H. Yu. Mitotic transcription installs Sgo1 at centromeres to coordinate chromosome segregation. *Molecular Cell*, 59:426–436, 2015.

[109] X. Liu, Y. Huang, D. Yang, X. Li, J. Liang, L. Lin, M. Zhang, K. Zhong, B. Liang, and J. Li. Overexpression of TRIM24 is associated with the onset and progress of human hepatocellular carcinoma. *PLoS ONE*, 9(1):e85462, 2014.

[110] K. J. Livak and T. D. Schmittgen. Analysis of relative gene expression data using real-time quantitative PCR and the $2^{-\Delta\Delta C_t}$ method. *Methods*, 25(4):402–408, 2001.

[111] G. A. Logsdon and E. E. Eichler. The dynamic structure and rapid evolution of human centromeric satellite DNA. *Genes (Basel)*, 14(1):92, 2022.

[112] L. Lu, X. Chen, D. Sanders, S. Qian, and X. Zhong. High-resolution mapping of H4K16 and H3K23 acetylation reveals conserved and unique distribution patterns in *Arabidopsis* and rice. *Epigenetics*, 10(11):1044–1053, 2015.

[113] R. Ma, Y. Zhang, J. Zhang, P. Zhang, Z. Liu, Y. Fan, H. T. Wang, Z. Zhang, and B. Zhu. Targeting pericentric non-consecutive motifs for heterochromatin initiation. *Nature*, 631(8021):678–685, 2024.

[114] A. L. Manning, M. S. Longworth, and N. J. Dyson. Loss of pRB causes centromere dysfunction and chromosomal instability. *Genes & Development*, 24(13):1364–1376, 2010.

[115] L. Margalit, C. Strauss, A. Tal, and S. Schlesinger. Trim24 and Trim33 play a role in epigenetic silencing of retroviruses in embryonic stem cells. *Viruses*, 12(9):1015, 2020.

[116] A. Marston. Shugoshins: tension-sensitive pericentromeric adaptors safeguarding chromosome segregation. *Molecular and Cellular Biology*, 35, 2014.

[117] E. Matsuda, Y. Agata, M. Sugai, T. Katakai, H. Gonda, and A. Shimizu. Targeting of krüppel-associated box-containing zinc finger proteins to centromeric heterochromatin: Implication for the gene silencing mechanisms. *Journal of Biological Chemistry*, 276(17):14222–14229, 2001.

[118] J. R. McIntosh. Mitosis. *Cold Spring Harbor Perspectives in Biology*, 8(9):a023218, 2016.

[119] S. McNulty, L. Sullivan, and B. Sullivan. Human centromeres produce chromosome-specific and array-specific alpha satellite transcripts that are complexed with CENP-A and CENP-C. *Dev Cell*, 42(3):226–240.e6, 2017.

[120] G. Meroni and G. Diez-Roux. TRIM/RBCC, a novel class of 'single protein RING finger' E3 ubiquitin ligases. *BioEssays*, 27:1147–1157, 2005.

[121] J. A. Merriman, S. I. Lane, J. E. Holt, P. C. Jennings, I. García-Higuera, S. Moreno, E. A. McLaughlin, and K. T. Jones. Reduced chromosome cohesion measured by interkinetochore distance is associated with aneuploidy even in oocytes from young mice. *Biology of Reproduction*, 88(2):31, 1–7, 2013.

[122] K. H. Miga. Completing the human genome: the progress and challenge of satellite DNA assembly. *Chromosome Res*, 23(3):421–6, 2015.

[123] O. Molina, G. Vargiu, M. A. Abad, A. Zhiteneva, A. A. Jeyaprakash, H. Masumoto, N. Kouprina, V. Larionov, and W. C. Earnshaw. Epigenetic engineering reveals a balance between histone modifications and transcription in kinetochore maintenance. *Nature Communications*, 7:13334, 2016.

[124] A. Mortazavi, B. A. Williams, K. McCue, L. Schaeffer, and B. Wold. Mapping and quantifying mammalian transcriptomes by RNA-seq. *Nature Methods*, 5:621–628, 2008.

[125] B. A. Moyers, E. C. Partridge, M. Mackiewicz, M. J. Betti, R. Darji, S. K. Meadows, K. M. Newberry, L. A. Brandsmeier, B. J. Wold, E. M. Mendenhall, and R. M. Myers. Characterization of human transcription factor function and patterns of gene regulation in HepG2 cells. *Genome Research*, 33(11):1879–1892, 2023.

[126] B. Mravinac, L. L. Sullivan, J. W. Reeves, C. M. Yan, K. S. Kopf, C. J. Farr, M. G. Schueler, and B. A. Sullivan. Histone modifications within the human X centromere region. *PLoS One*, 4(8):e6602, 2009.

[127] A. Musacchio. The molecular biology of spindle assembly checkpoint signaling dynamics. *Current Biology*, 25(20):R1002–R1018, 2015.

[128] A. Musacchio and E. D. Salmon. The spindle-assembly checkpoint in space and time. *Nature Reviews Molecular Cell Biology*, 8(5):379–393, 2007.

[129] M. Nakano, S. Cardinale, V. N. Noskov, R. Gassmann, P. Vagnarelli, S. Kandels-Lewis, V. Larionov, W. C. Earnshaw, and H. Masumoto. Inactivation of a human kinetochore by specific targeting of chromatin modifiers. *Developmental Cell*, 14(4):507–522, 2008.

[130] K. Nasmyth. Cohesin: a catenase with separate entry and exit gates? *Nature Cell Biology*, 13:1170–1177, 2011.

[131] A. P. Navarro and I. M. Cheeseman. Kinetochore assembly throughout the cell cycle. *Seminars in Cell & Developmental Biology*, 117:62–74, 2021.

[132] A. L. Nielsen, J. A. Ortiz, J. You, M. Oulad-Abdelghani, R. Khechumian, A. Gansmuller, P. Chambon, and R. Losson. Interaction with members of the heterochromatin protein 1 (HP1) family and histone deacetylation are differentially involved in transcriptional silencing by members of the TIF1 family. *The EMBO Journal*, 18(22):6385–6395, 1999.

[133] T. Nishiyama, R. Ladurner, J. Schmitz, E. Kreidl, A. Schleiffer, V. Bhaskara, M. Bando, K. Shirahige, A. A. Hyman, K. Mechtler, and J.-M. Peters. Sororin mediates sister chromatid cohesion by antagonizing Wapl. *Cell*, 143:737–749, 2010.

[134] S. Nurk, S. Koren, A. Rhie, M. Rautiainen, A. V. Bzikadze, A. Mikheenko, M. R. Vollger, N. Altemose, L. Uralsky, A. Gershman, S. Aganezov, S. J. Hoyt, M. Diekhans, G. A. Logsdon, M. Alonge, S. E. Antonarakis, M. Borchers, G. G. Bouffard, S. Y. Brooks, G. V. Caldas, N.-C. Chen, H. Cheng, C.-S. Chin, W. Chow, L. G. de Lima, P. C. Dishuck, R. Durbin, T. Dvorkina, I. T. Fiddes, G. Formenti, R. S. Fulton, A. Fungtammasan, E. Garrison, P. G. S. Grady, T. A. Graves-Lindsay, I. M. Hall, N. F. Hansen, G. A. Hartley, M. Haukness, K. Howe, M. W. Hunkapiller, C. Jain, M. Jain, E. D. Jarvis, P. Kerpedjiev, M. Kirsche, M. Kolmogorov, J. Korlach, M. Kremitzki, H. Li, V. V. Maduro, T. Marschall, A. M. McCartney, J. McDaniel, D. E. Miller, J. C. Mullikin, E. W. Myers, N. D. Olson, B. Paten, P. Peluso, P. A. Pevzner, D. Porubsky, T. Potapova, E. I. Rogaev, J. A. Rosenfeld, S. L. Salzberg, V. A. Schneider, F. J. Sedlazeck, K. Shafin, C. J. Shew, A. Shumate, Y. Sims, A. F. A. Smit, D. C. Soto, I. Sović, J. M. Storer, A. Streets, B. A. Sullivan, F. Thibaud-Nissen, J. Torrance, J. Wagner, B. P. Walenz, A. Wenger, J. M. D. Wood, C. Xiao, S. M. Yan, A. C. Young, S. Zarate, U. Surti, R. C. McCoy, M. Y. Dennis, I. A. Alexandrov, J. L. Gerton, R. J. O'Neill, W. Timp, J. M. Zook, M. C. Schatz, E. E. Eichler, K. H. Miga, and A. M. Phillippy. The complete sequence of a human genome. *Science*, 376(6588):44–53, 2022.

[135] K. Ohkuni and K. Kitagawa. Role of transcription at centromeres in budding yeast. *Transcription*, 3:193–197, 2012.

[136] M. Okada, K. Okawa, T. Isobe, and T. Fukagawa. CENP-H-containing complex facilitates centromere deposition of CENP-A in cooperation with FACT and CHD1. *Molecular Biology of the Cell*, 20:3986–3995, 2009.

[137] M. Pal-Bhadra, B. A. Leibovitch, S. G. Gandhi, M. Rao, U. Bhadra, J. A. Birchler, and S. C. R. Elgin. Heterochromatic silencing and HP1 localization in *Drosophila* are dependent on the RNAi machinery. *Science*, 303(5658):669–672, 2004.

[138] D. K. Palmer, K. O'Day, M. H. Wener, B. S. Andrews, and R. L. Margolis. A 17-kD centromere protein (CENP-A) copurifies with nucleosome core particles and with histones. *Journal of Cell Biology*, 104(4):805–815, 1987.

[139] K. C. Palozola, G. Donahue, H. Liu, G. R. Grant, J. S. Becker, A. Cote, H. Yu, A. Raj, and K. S. Zaret. Mitotic transcription and waves of gene reactivation during mitotic exit. *Science*, 358:119–122, 2017.

[140] P. J. Park. ChIP–seq: advantages and challenges of a maturing technology. *Nature Reviews Genetics*, 10:669–680, 2009.

[141] S. Pepke, B. Wold, and A. Mortazavi. Computation for ChIP-seq and RNA-seq studies. *Nature Methods*, 6(11 Suppl):S22–S32, 2009.

[142] C. Perea-Resa and M. D. Blower. Centromere biology: Transcription goes on stage. *Molecular and Cellular Biology*, 38(18):e00263–18, 2018.

[143] C. Perea-Resa, L. Bury, I. M. Cheeseman, and M. D. Blower. Cohesin removal reprograms gene expression upon mitotic entry. *Molecular Cell*, 78(1):127–140.e7, 2020.

[144] J. M. Peters and T. Nishiyama. Sister chromatid cohesion. *Cold Spring Harbor Perspectives in Biology*, 4(11):a011130, 2012.

[145] Z. Pezer and D. Ugarkovic. Satellite DNA-associated siRNAs as mediators of heat shock response in insects. *RNA Biology*, 9(5):1–9, 2012.

[146] T. Potapova and G. J. Gorbsky. The consequences of chromosome segregation errors in mitosis and meiosis. *Biology (Basel)*, 6(1):12, 2017.

[147] M. R. Rafiee, C. Girardot, G. Sigismondo, and J. Krijgsveld. Expanding the circuitry of pluripotency by selective isolation of chromatin-associated proteins. *Molecular Cell*, 64(3):624–635, 2016.

[148] S. S. P. Rao, S. C. Huang, B. Glenn St Hilaire, J. M. Engreitz, E. M. Perez, K. R. Kieffer-Kwon, A. L. Sanborn, S. E. Johnstone, G. D. Bascom, I. D. Bochkov, X. Huang, M. S. Shamim, J. Shin, D. Turner, Z. Ye, A. D. Omer, J. T. Robinson, T. Schlick, B. E. Bernstein, R. Casellas, E. S. Lander, and E. L. Aiden. Cohesin loss eliminates all loop domains. *Cell*, 171(2):305–320.e24, 2017.

[149] V. Régnier, P. Vagnarelli, T. Fukagawa, T. Zerjal, E. Burns, D. Trouche, W. Earnshaw, and W. Brown. CENP-A is required for accurate chromosome segregation and sustained kinetochore association of BubR1. *Molecular and Cellular Biology*, 25(10):3967–3981, 2005.

[150] A. Reymond, G. Meroni, A. Fantozzi, G. Merla, S. Cairo, L. Luzi, D. Riganelli, E. Zanaria, S. Messali, S. Cainarca, A. Guffanti, S. Minucci, P. G. Pelicci, and A. Ballabio. The tripartite motif family identifies cell compartments. *The EMBO Journal*, 20(9):2140–2151, 2001.

[151] S. A. Ribeiro, J. C. Gatlin, Y. Dong, A. Joglekar, L. Cameron, D. F. Hudson, C. J. Farr, B. F. McEwen, E. D. Salmon, W. C. Earnshaw, and P. Vagnarelli. Condensin regulates the stiffness of vertebrate centromeres. *Molecular Biology of the Cell*, 20(9):2371–2380, 2009.

[152] N. Rizzi, M. Denegri, I. Chiodi, M. Corioni, R. Valgardsdottir, F. Cobianchi, S. Riva, and G. Biamonti. Transcriptional activation of a constitutive heterochromatic domain of the human genome in response to heat shock. *Molecular Biology of the Cell*, 15(2):543–551, 2004.

[153] S. Rošić, F. Köhler, and S. Erhardt. Repetitive centromeric satellite RNA is essential for kinetochore formation and cell division. *J Cell Biol.*, 207:335–349, 2014.

[154] C. Sacristan, K. Samejima, L. Andrade Ruiz, M. Deb, M. L. A. Lambers, A. Buckle, C. A. Brackley, D. Robertson, T. Hori, S. Webb, R. Kiewisz, T. Bepler, E. van Kwawegen, P. Risteski, K. Vukušić, I. M. Tolić, T. Müller-Reichert, T. Fukagawa, N. Gilbert, D. Marenduzzo, W. C. Earnshaw, and G. J. P. L. Kops. Vertebrate centromeres in mitosis are functionally bipartite structures stabilized by cohesin. *Cell*, 187(12):3006–3023.e26, 2024.

[155] L. Sadeghi, L. Siggens, J. P. Svensson, and K. Ekwall. Centromeric histone H2B monoubiquitination promotes noncoding transcription and chromatin integrity. *Nature Structural & Molecular Biology*, 21(3):236–243, 2014.

[156] A. K. Saha, M. Mourad, M. H. Kaplan, I. Chefetz, S. N. Malek, R. Buckanovich, D. M. Markovitz, and R. Contreras-Galindo. The genomic landscape of centromeres in cancers. *Scientific Reports*, 9(1):11259, 2019.

[157] N. Saksouk, E. Simboeck, and J. Déjardin. Constitutive heterochromatin formation and transcription in mammals. *Epigenetics & Chromatin*, 8:3, 2015.

[158] C. Salinas-Luypaert, D. Dubocanin, R. J. Lee, L. Andrade Ruiz, R. Gamba, M. Grison, L. Velikovsky, A. Angrisani, A. Scelfo, Y. Xu, M. Dumont, V. Barra, T. Wilhelm, G. Velasco, M. Losito, R. Wardenaar, C. Francastel, F. Foijer, G. J. P. L. Kops, K. H. Miga, N. Altemose, and D. Fachinetti. DNA methylation influences human centromere positioning and function. *Nature Genetics*, 57(10):2509–2521, 2025.

[159] H. Sapkota, E. Wasiak, J. R. Daum, and G. J. Gorbsky. Multiple determinants and consequences of cohesion fatigue in mammalian cells. *Molecular Biology of the Cell*, 29(15):1811–1824, 2018.

[160] E. W. Sayers, J. Beck, E. E. Bolton, J. R. Brister, J. Chan, R. Connor, M. Feldgarden, A. M. Fine, K. Funk, J. Hoffman, S. Kannan, C. Kelly, W. Klimke, S. Kim, S. Lathrop, A. Marchler-Bauer, T. D. Murphy, C. O'Sullivan, E. Schmieder, Y. Skripchenko, A. Stine, F. Thibaud-Nissen, J. Wang, J. Ye, E. Zellers, V. A. Schneider, and K. D. Pruitt. Database resources of the National Center for Biotechnology Information in 2025. *Nucleic Acids Research*, 53(D1):D20–D29, 2025.

[161] T. Schalch and F. A. Steiner. Structure of centromere chromatin: from nucleosome to chromosomal architecture. *Chromosoma*, 126(4):443–455, 2017.

[162] L. Schmiedeberg, K. Weisshart, S. Diekmann, G. Meyer Zu Hoerste, and P. Hemmerich. High- and low-mobility populations of HP1 in heterochromatin of mammalian cells. *Molecular Biology of the Cell*, 15(6):2819–2833, 2004.

[163] C. A. Schneider, W. S. Rasband, and K. W. Eliceiri. NIH Image to ImageJ: 25 years of image analysis. *Nature Methods*, 9(7):671–675, 2012.

[164] V. A. Schneider, T. Graves-Lindsay, K. Howe, N. Bouk, H.-C. Chen, P. A. Kitts, T. D. Murphy, K. D. Pruitt, F. Thibaud-Nissen, D. Albracht, R. S. Fulton, M. Kremitzki, V. Magrini, C. Markovic, S. McGrath, K. M. Steinberg, K. Auger, W. Chow, J. Collins, G. Harden, T. Hubbard, S. Pelan, J. T. Simpson, G. Threadgold, J. Torrance, J. M. Wood, L. Clarke, S. Koren, M. Boitano, P. Peluso, H. Li, C.-S. Chin, A. M. Phillippy, R. Durbin, R. K. Wilson, P. Flicek, E. E. Eichler, and D. M. Church. Evaluation of GRCh38 and *de novo* haploid genome assemblies demonstrates the enduring quality of the reference assembly. *Genome Research*, 27:849–864, 2017.

[165] N. Sekulic and B. E. Black. Molecular underpinnings of centromere identity and maintenance. *Trends in Biochemical Sciences*, 37(5):220–229, 2012.

[166] A. Sen Gupta, C. Seidel, D. Tsuchiya, S. McKinney, Z. Yu, S. E. Smith, J. R. Unruh, and J. L. Gerton. Defining a core configuration for human centromeres during mitosis. *Nature Communications*, 14(1):7947, 2023.

[167] R. D. Shelby, K. Monier, and K. F. Sullivan. Chromatin assembly at kinetochores is uncoupled from DNA replication. *Journal of Cell Biology*, 151(5):1113–1118, 2000.

[168] M. Shuaib, K. Ouararhni, S. Dimitrov, and A. Hamiche. HJURP binds CENP-A via a highly conserved N-terminal domain and mediates its deposition at centromeres. *Proceedings of the National Academy of Sciences of the United States of America*, 107(4):1349–1354, 2010.

[169] K. Smurova, M. Damizia, C. Irene, S. Stancari, G. Berto, G. Perticari, M. G. Iacovella, I. D'Ambrosio, M. Giubettini, R. Philippe, C. Baggio, E. Callegaro, A. Casagranda, A. Corsini, V. G. Polese, A. Ricci, E. Dassi, and P. De Wulf. Rio1 downregulates centromeric RNA levels to promote the timely assembly of structurally fit kinetochores. *Nature Communications*, 14(1):3172, 2023.

[170] K. Smurova and P. De Wulf. Centromere and pericentromere transcription: Roles and regulation ... in sickness and in health. *Frontiers in Genetics*, 9:674, 2018.

[171] R. V. Stevens, D. Esposito, and K. Rittinger. Properties of class VI TRIM proteins. *Life Science Alliance*, 2(3):e201900295, 2019.

[172] D. R. Stirling, M. J. Swain-Bowden, A. M. Lucas, A. E. Carpenter, B. A. Cimini, and A. Goodman. CellProfiler 4: improvements in speed, utility and usability. *BMC Bioinformatics*, 22(1):433, 2021.

[173] S. Stoler, K. C. Keith, K. E. Curnick, and M. Fitzgerald-Hayes. A mutation in CSE4, an essential gene encoding a novel chromatin-associated protein in yeast, causes chromosome nondisjunction and cell cycle arrest at mitosis. *Genes & Development*, 9(5):573–586, 1995.

[174] A. R. Strom, J. M. Eeftens, Y. Polyachenko, C. J. Weaver, H. F. Watanabe, D. Bracha, N. D. Orlovsky, C. C. Jumper, W. M. Jacobs, and C. P. Brangwynne. Interplay of condensation and chromatin binding underlies BRD4 targeting. *Molecular Biology of the Cell*, 35(6):ar88, 2024.

[175] K. F. Sullivan, M. Hechenberger, and K. Masri. Human CENP-A contains a histone H3 related histone fold domain that is required for targeting to the centromere. *Journal of Cell Biology*, 127(3):581–592, 1994.

[176] L. L. Sullivan, K. Chew, and B. A. Sullivan. α satellite DNA variation and function of the human centromere. *Nucleus*, 8(4):331–339, 2017.

[177] H. Tachiwana, W. Kagawa, T. Shiga, A. Osakabe, Y. Miya, K. Saito, Y. Hayashi-Takanaka, T. Oda, M. Sato, S. Y. Park, H. Kimura, and H. Kurumizaka. Crystal structure of the human centromeric nucleosome containing CENP-A. *Nature*, 476(7359):232–235, 2011.

[178] P. B. Talbert, R. Masuelli, A. P. Tyagi, L. Comai, and S. Henikoff. Centromeric localization and adaptive evolution of an *Arabidopsis* histone H3 variant. *The Plant Cell*, 14(5):1053–1066, 2002.

[179] T. Tanaka, J. Fuchs, J. Loidl, and K. Nasmyth. Cohesin ensures bipolar attachment of microtubules to sister centromeres and resists their precocious separation. *Nature Cell Biology*, 2:492–499, 2000.

[180] A. M. Taylor, J. Shih, G. Ha, G. F. Gao, X. Zhang, A. C. Berger, S. E. Schumacher, C. Wang, H. Hu, J. Liu, A. J. Lazar, C. G. A. R. Network, A. D. Cherniack, R. Beroukhim, and M. Meyerson. Genomic and functional approaches to understanding cancer aneuploidy. *Cancer Cell*, 33(4):676–689.e3, 2018.

[181] The 1000 Genomes Project Consortium. A map of human genome variation from population-scale sequencing. *Nature*, 467:1061–1073, 2010.

[182] D. T. Ting, D. Lipson, S. Paul, B. W. Brannigan, S. Akhavanfard, E. J. Coffman, G. Contino, V. Deshpande, A. J. Iafrate, S. Letovsky, M. N. Rivera, N. Bardeesy, S. Maheswaran, and D. A. Haber. Aberrant overexpression of satellite repeats in pancreatic and other epithelial cancers. *Science*, 331(6017):593–596, 2011.

[183] M. Tittel-Elmer, E. Bucher, L. Broger, O. Mathieu, J. Paszkowski, and I. Vaillant. Stress-induced activation of heterochromatic transcription. *PLoS Genetics*, 6(10):e1001175, 2010.

[184] W. W. Tsai, Z. Wang, T. T. Yiu, K. C. Akdemir, W. Xia, S. Winter, C. Y. Tsai, X. Shi, D. Schwarzer, W. Plunkett, B. Aronow, O. Gozani, W. Fischle, M. C. Hung, D. J. Patel, and M. C. Barton. TRIM24 links a non-canonical histone signature to breast cancer. *Nature*, 468(7326):927–932, 2010.

[185] A. Tsherniak, F. Vazquez, P. G. Montgomery, B. A. Weir, G. Kryukov, G. S. Cowley, S. Gill, W. F. Harrington, S. Pantel, J. M. Krill-Burger, R. M. Meyers, L. Ali, A. Goodale, Y. Lee, G. Jiang, J. Hsiao, W. F. J. Gerath, S. Howell, E. Merkel, M. Ghandi, L. A. Garraway, D. E. Root, T. R. Golub, J. S. Boehm, and W. C. Hahn. Defining a Cancer Dependency Map. *Cell*, 170(3):564–576.e16, 2017.

[186] O. K. Tørresen, B. Star, P. Mier, M. A. Andrade-Navarro, A. Bateman, P. Jarnot, A. Gruca, M. Grynberg, A. V. Kajava, V. J. Promponas, M. Anisimova, K. S. Jakobsen, and D. Linke. Tandem repeats lead to sequence assembly errors and impose multi-level challenges for genome and protein databases. *Nucleic Acids Research*, 47(21):10994–11006, 2019.

[187] S. Uchino, Y. Ito, Y. Sato, T. Handa, Y. Ohkawa, M. Tokunaga, and H. Kimura. Live imaging of transcription sites using an elongating RNA polymerase II-specific probe. *J Cell Biol*, 221(2):e202104134, 2022.

[188] R. Valgardsdottir, I. Chiodi, M. Giordano, A. Rossi, S. Bazzini, C. Ghigna, S. Riva, and G. Biamonti. Transcription of Satellite III non-coding RNAs is a general stress response in human cells. *Nucleic Acids Research*, 36(2):423–434, 2008.

[189] G. van Rossum and J. de Boer. Interactively testing remote servers using the Python programming language. *CWI Quarterly*, 4(4):283–303, 1991.

[190] E. Volpe, A. Colantoni, L. Corda, E. Di Tommaso, F. Pelliccia, R. Ottalevi, A. Guarracino, D. Licastro, L. Faino, M. Capulli, G. Formenti, E. Tassone, and S. Giunta. The reference genome of the human diploid cell line RPE-1. *Nature Communications*, 16(1):7751, 2025.

[191] Y. Wang, Y. Yao, Z. Liu, S. Long, F. Yi, Q. Fang, D. Wu, Q. Zhu, H. Zai, S. Xiao, F. Wan, and K. Fu. Cytoplasmic TRIM24 promotes colorectal cancer cell proliferation by activating Wnt/β-catenin signaling. *Nature Communications*, 16(1):8598, 2025.

[192] Y. Wang, Y. Yao, Q. Wei, S. Long, Y. Chen, J. Xie, R. Tan, W. Jiang, Q. Zhang, D. Wu, S. Xiao, F. Wan, and K. Fu. TRIM24 is critical for the cellular response to DNA double-strand breaks through regulating the recruitment of MRN complex. *Oncogene*, 42(8):586–600, 2023.

[193] Y. Wang, J. Zhao, Y. Wang, G. Chen, S. Zhao, J. Xu, C. Yin, Y. Xu, Y. Kang, Y. Dong, and X. Chen. G9a-mediated H3K9 di-methylation protects centromere integrity and chromosome stability. *Science Bulletin*, 70(21):3489–3493, 2025.

[194] J. S. Waye and H. F. Willard. Nucleotide sequence heterogeneity of alpha satellite repetitive DNA: a survey of alphoid sequences from different human chromosomes. *Nucleic Acids Research*, 15(18):7549–7569, 1987.

[195] D. Weigel and R. Mott. The 1001 genomes project for *Arabidopsis thaliana*. *Genome Biology*, 10:107, 2009.

[196] L. H. Wong, K. H. Brettingham-Moore, L. Chan, J. M. Quach, M. A. Anderson, E. L. Northrop, R. Hannan, R. Saffery, M. L. Shaw, E. Williams, and K. A. Choo. Centromere RNA is a key component for the assembly of nucleoproteins at the nucleolus and centromere. *Genome Research*, 17(8):1146–1160, 2007.

[197] W. Xie, Y. Zhang, B. Wang, Y. Hu, B. Zhan, F. Wei, J. Tang, and J. Lian. Tripartite motif containing 24 regulates cell proliferation in colorectal cancer through YAP signaling. *Cancer Medicine*, 9(17):6367–6376, 2020.

[198] K. Yan, J. Yang, Z. Zhang, S. H. McLaughlin, L. Chang, D. Fasci, A. E. Ehrenhofer-Murray, A. J. R. Heck, and D. Barford. Structure of the inner kinetochore CCAN complex assembled onto a centromeric nucleosome. *Nature*, 574:278–282, 2019.

[199] L. Yan, X. Yuan, M. Liu, Q. Chen, M. Zhang, J. Xu, L.-H. Zeng, L. Zhang, J. Huang, W. Lu, X. He, H. Yan, and F. Wang. A non-canonical role of the inner kinetochore in regulating sister-chromatid cohesion at centromeres. *The EMBO Journal*, 43(12):2424–2452, 2024.

[200] L. Yang, Q. Zhang, T. Niu, and H. Liu. SET levels contribute to cohesion fatigue. *Molecular Biology of the Cell*, 32(13):1256–1266, 2021.

[201] S. Yatskevich, J. Rhodes, and K. Nasmyth. Organization of chromosomal DNA by SMC complexes. *Annual Review of Genetics*, 53:445–482, 2019.

[202] Q. Yi, Q. Chen, C. Liang, H. Yan, Z. Zhang, X. Xiang, M. Zhang, F. Qi, L. Zhou, and F. Wang. HP1 links centromeric heterochromatin to centromere cohesion in mammals. *EMBO Reports*, 19(4):e45484, 2018.

[203] X. Yuan, L. Yan, Q. Chen, S. Zhu, X. Zhou, L. H. Zeng, M. Liu, X. He, J. Huang, W. Lu, L. Zhang, H. Yan, and F. Wang. Molecular mechanism and functional significance of Wapl interaction with the cohesin complex. *Proceedings of the National Academy of Sciences of the United States of America*, 121(33):e2405177121, 2024.

[204] E. Zhang, L. Peng, K. Yuan, Z. Ding, and Q. Yi. HP1 promotes the centromeric localization of ATRX and protects cohesion by interfering Wapl activity in mitosis. *Frontiers in Bioscience (Landmark Edition)*, 30(1):26426, 2025.

[205] J. Zhang, X. Shi, Y. Li, B. J. Kim, J. Jia, Z. Huang, T. Yang, X. Fu, S. Y. Jung, Y. Wang, P. Zhang, S. T. Kim, X. Pan, and J. Qin. Acetylation of Smc3 by Eco1 is required for S phase sister chromatid cohesion in both human and yeast. *Molecular Cell*, 31:143–151, 2008.

[206] X. Zhang, D. Zhao, X. Xiong, Z. He, and H. Li. Multifaceted histone H3 methylation and phosphorylation readout by the plant homeodomain finger of human nuclear antigen sp100c. *Journal of Biological Chemistry*, 291(24):12786–12798, 2016.

[207] H. Zhao, A. R. Strom, J. M. Eeftens, M. Haataja, A. Košmrlj, and C. P. Brangwynne. Condensate-driven chromatin organization via elastocapillary interactions. *bioRxiv*, 2025.

[208] X. Zheng, C. Q. W. Ho, X. Zheng, K. L. Lee, K. Gradin, T. S. Pereira, P. O. Berggren, and Y. Ali. Co-immunoprecipitation assay using endogenous nuclear proteins from cells cultured under hypoxic conditions. *Journal of Visualized Experiments*, 138:e57836, 2018.

[209] J. Zhu, Q. Guo, M. Choi, Z. Liang, and K. W. Y. Yuen. Centromeric and pericentric transcription and transcripts: their intricate relationships, regulation, and functions. *Chromosoma*, 132(3):211–230, 2023.

[210] Q. Zhu, N. Hoong, A. Aslanian, T. Hara, C. Benner, S. Heinz, K. H. Miga, E. Ke, S. Verma, J. Soroczynski, J. R. r. Yates, T. Hunter, and I. M. Verma. Heterochromatin-encoded satellite RNAs induce breast cancer. *Molecular Cell*, 70(5):842–853.e7, 2018.

[211] Q. Zhu, G. M. Pao, A. M. Huynh, H. Suh, N. Tonnu, P. M. Nederlof, F. H. Gage, and I. M. Verma. BRCA1 tumour suppression occurs via heterochromatin-mediated silencing. *Nature*, 477:179–184, 2011.

A. Extended Supplementary Information

A1. Visualization of centromeric transcription

Live-cell imaging of elongating RNA Polymerase II using Pol II Ser2P mintbody

To assess whether elongating RNA Polymerase II (Pol II Ser2P) localizes to the centromeres in living cells, HeLa SNAP-CENP-A cells were transfected with a Pol II Ser2P mintbody construct and subjected to live-cell imaging [187]. DNA staining was used to define mitotic stages.

The mintbody signal displayed an interphase distribution consistent with previous reports and exhibited increased noise during mitosis [187]. No specific enrichment at condensed chromosomes was observed (Fig. A1). Due to the diffuse and grainy signal and lack of clear mitosis-specific dynamics, this approach was not suitable for visualizing centromere-associated transcription during mitosis.

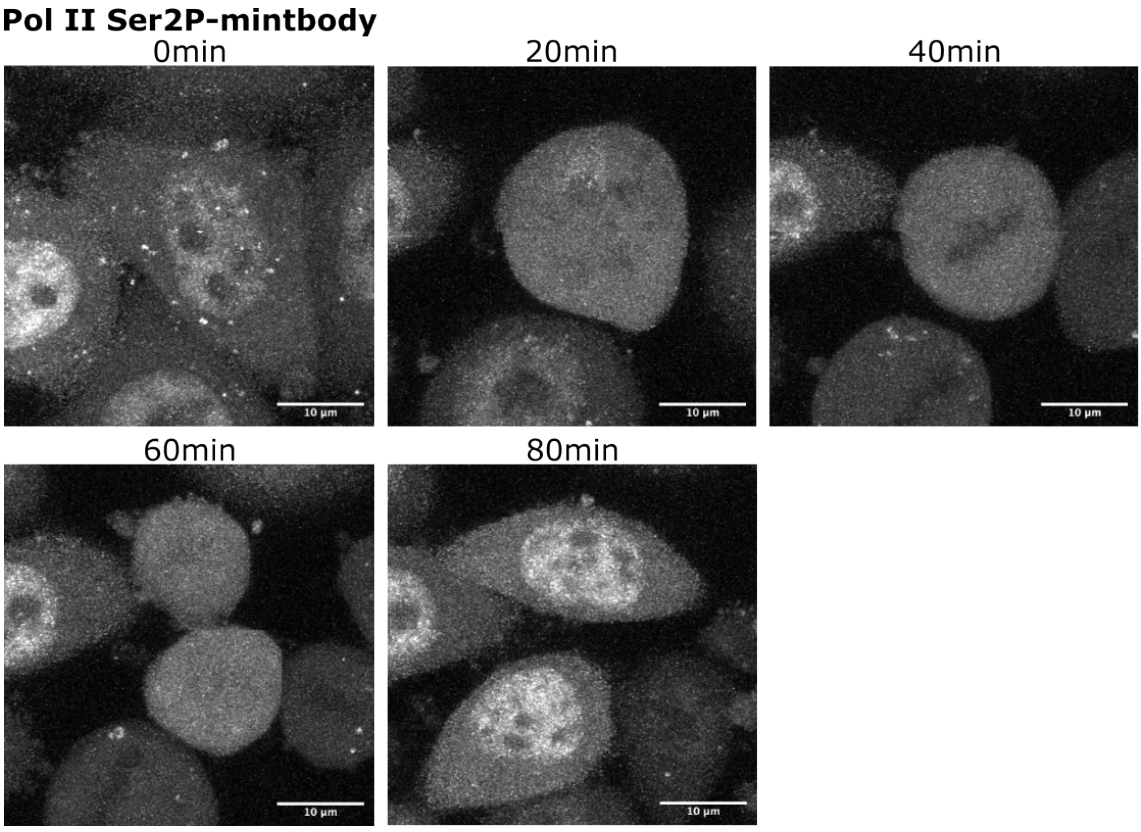


Figure A1.: Live-cell imaging of Pol II Ser2P mintbody during mitosis. Representative time series of HeLa cells expressing Pol II Ser2P-sfGFP mintbody construct. Images show progression from interphase through mitosis in 20min intervals. Scale bar: 10 μm. For details, see Materials and Methods.

Nascent RNA detection at mitotic centromeres using EU labelling

To asses whether centromeric transcription occurs during mitosis, nascent RNA on chromosome spreads from HeLa SNAP-CENP-A cells was labeled using 5-ethynyl uridine (EU) as described previously [139]. EU incorporation was detected by click chemistry.

EU signal was detectable on mitotic chromosomes, however no specific enrichment at constriction sites was observed (Fig. A2). The staining pattern appeared diffused and did not support centromere-specific transcription under these conditions.

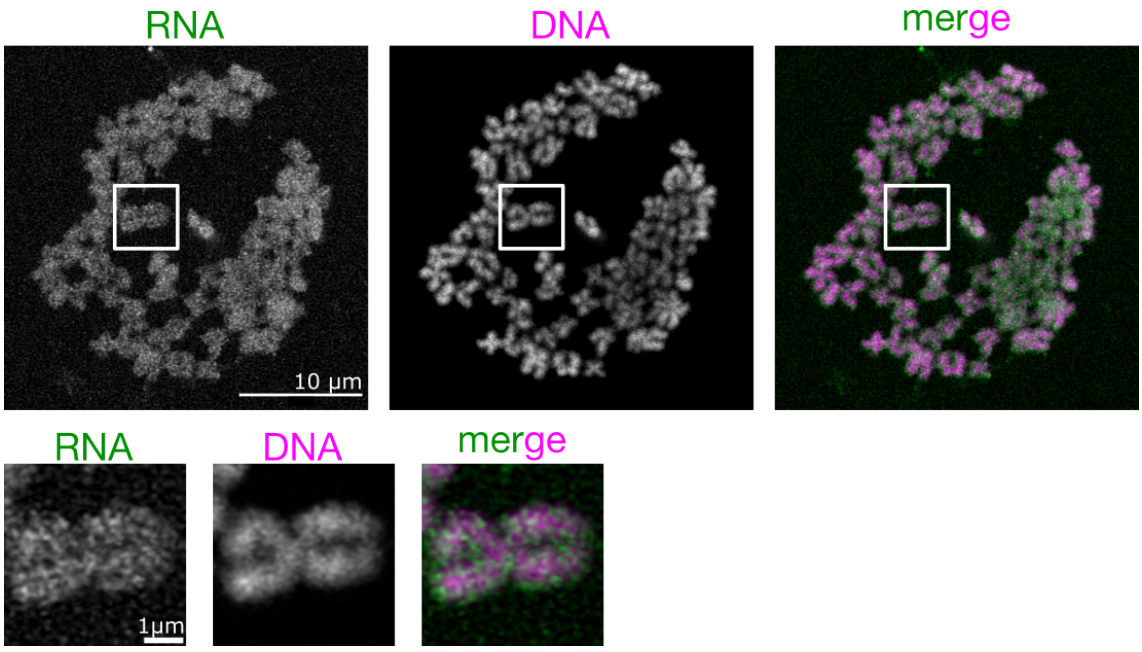


Figure A2.: Nascent RNA detection at mitotic centromeres using EU labelling. Representative chromosome spread of HeLa SNAP-CENP-A cells stained for nascent RNA transcripts using EU-labelling, as previously described in [139]. Cells were stained for DNA (DAPI). Images were acquired using Airyscan super-resolution microscopy Scale bar: 10 μm, inserts 1μm. For details, see Materials and Methods.

A2. REDPOINT reanalysis of additional proteins

REDPOINT enrichment values were additionally calculated for several candidate proteins that were not pursued further in this thesis (Tab. A1).

Table A1.: REDPOINT enrichment values for ChIP-seq datasets.

Study accession	Experiment accession	Whole-genome reads	Centro-meric reads	Centro-meric alignment (%)	ChIP antibody	Cell type	Sample/Input	Drug	Sample/ Input ratio
PRJNA730585	SRR14472223	16768337	572211	3.41	TRIM33	LNCaP	sample	vehicle	1.34
PRJNA730585	SRR14472224	16383990	516211	3.15	TRIM33	LNCaP	sample	100 nM DHT	1.24
PRJNA730585	SRR14472225	77876413	2036497	2.62	AR	LNCaP	sample	vehicle rep1	1.03
PRJNA730585	SRR14472226	10064707	273709	2.72	AR	LNCaP	sample	100 nM DHT rep1	1.07
PRJNA730585	SRR14472227	58894164	1763135	2.99	AR	LNCaP	sample	siTRIM33#1 ETOH	1.18
PRJNA730585	SRR14472228	6966492	214510	3.08	AR	LNCaP	sample	siTRIM33#1 100M DHT	1.21
PRJNA730585	SRR14472229	19738242	569784	2.89	AR	LNCaP	sample	vehicle rep2	1.14
PRJNA730585	SRR14472230	18714470	427067	2.28	AR	LNCaP	sample	100nM DHT rep2	0.90
PRJNA730585	SRR14472231	14492276	503533	3.47	AR	LNCaP	sample	siTRIM33#2 ETOH	1.37
PRJNA730585	SRR14472232	22750237	748916	3.29	AR	LNCaP	sample	siTRIM33#2 100nM DHT	1.29
PRJNA730585	SRR14472233	30578344	777517	2.54	none	LNCaP	input		
PRJNA453537	SRR7063102	49051301	1053487	2.15	TRIM24	MCF7	sample	10nM Estrogen 3h	0.75
PRJNA453537	SRR7063103	41491902	962375	2.32	TRIM24	MCF7	sample	vehicle	0.81
PRJNA453537	SRR7063104	161809503	4612370	2.85	none	MCF7	input	vehicle	
PRJNA422654	SRR6380214	11779726	308382	2.62	HA-TRIM24	LNCaP	sample	vehicle	

Continued on next page

Table A1 – continued from previous page

Study accession	Experiment accession	Whole-genome reads	Centro-meric reads	Centro-meric alignment (%)	ChIP antibody	Cell type	Sample/Input	Drug	Sample/ Input ratio
PRJNA422654	SRR6380215	13064468	308338	2.36	HA-TRIM24	LNCaP	sample	10nM R1881	
PRJNA422654	SRR6380216	25513945	954670	3.74	TRIM28	LNCaP	sample	vehicle	
PRJNA422654	SRR6380217	14452296	559378	3.87	TRIM28	LNCaP	sample	10nM R1881	
PRJNA422654	SRR6380218	12218750	329219	2.69	AR	LNCaP	sample	pLKO	
PRJNA422654	SRR6380219	28298231	750576	2.65	AR	LNCaP	sample	shTRIM24	
PRJNA422654	SRR6380220	11577146	330311	2.85	AR	LNCaP	sample	shTRIM28	
PRJNA392134	SRR5762041	47197690	1019657	2.16	TRIM24	MOLM-13	sample	DMSO	1.14
PRJNA392134	SRR5762042	57426422	1089709	1.90	none	MOLM-13	input	DMSO	
PRJNA392134	SRR5762043	44306172	846838	1.91	TRIM24	MOLM-13	sample	IACS-9571	1.19
PRJNA392134	SRR5762044	49304917	792662	1.61	none	MOLM-13	input	IACS-9571	
PRJNA392134	SRR5762045	44304667	905836	2.04	TRIM24	MOLM-13	sample	dTRIM24	1.25
PRJNA392134	SRR5762046	40800488	665136	1.63	none	MOLM-13	input	dTRIM24	
PRJNA130083	SRR065819	13361881	62015	0.46	ER	MCF7	sample	20 nM Estrogen	0.13
PRJNA130083	SRR065820	16176333	326883	2.02	ER	MCF7	sample	vehicle	0.55
PRJNA130083	SRR065821	13604734	135471	1.00	TRIM24	MCF7	sample	20 nM Estrogen	0.27
PRJNA130083	SRR065822	5799324	47135	0.81	TRIM24	MCF7	sample	vehicle	0.22
PRJNA130083	SRR065823	22663970	556413	2.46	H3K4me2	MCF7	sample	20 nM Estrogen	0.67
PRJNA130083	SRR065824	22243367	236705	1.06	H3K4me2	MCF7	sample	vehicle	0.11
PRJNA130083	SRR065825	22760978	837028	3.68	IgG	MCF7	input	vehicle	
PRJNA285229	SRR2043644	26799140	2712734	10.12	TRIM24	LNCaP	sample	vehicle	2.68
PRJNA285229	SRR2043645	28163015	3725101	13.23	TRIM24	LNCaP	sample	10nM DHT	4.39
PRJNA285229	SRR2043646	45507247	1356300	2.98	TRIM24	LNCaP-abl	sample	10nM DHT	0.99
PRJNA285229	SRR2043647	32940839	1129679	3.43	none	LNCaP	input	vehicle	

Continued on next page

Table A1 – continued from previous page

Study accession	Experiment accession	Whole-genome reads	Centro-meric reads	Centro-meric alignment (%)	ChIP antibody	Cell type	Sample/Input	Drug	Sample/ Input ratio
PRJNA285229	SRR2043648	29762912	895861	3.01	none	LNCaP	input	10nM DHT	
PRJNA285229	SRR2043649	29742037	1219192	4.10	none	LNCaP-abl	input	vehicle	
PRJNA977987	SRR24774453	33888911	273584	0.81	H3K23ac	ZR751	sample	DMSO	0.26
PRJNA977987	SRR24774454	33664679	253434	0.75	H3K23ac	ZR751	sample	DMSO	0.24
PRJNA977987	SRR24774455	20291050	485631	2.39	H3K23ac	ZR751	sample	PF9363	0.75
PRJNA977987	SRR24774456	23207973	569705	2.45	H3K23ac	ZR751	sample	PF9363	0.77
PRJNA977987	SRR24774457	7190362	229718	3.19	IgG	ZR751	input	DMSO	3.13
PRJNA977987	SRR24774458	6305504	205767	3.26	IgG	ZR751	input	PF9363	3.19
PRJNA977987	SRR24774459	9779829	299052	3.06	IgG	ZR751	input	DMSO	
PRJNA977987	SRR24774460	7345744	228618	3.11	IgG	ZR751	input	PF9363	
PRJNA977987	SRR24774461	19428498	104348	0.54	K27me3	ZR751	sample	PF9363	0.17
PRJNA977987	SRR24774462	17909512	97596	0.54	K27me3	ZR751	sample	PF9363	0.17
PRJNA977987	SRR24774463	19500988	107545	0.55	K27me3	ZR751	sample	DMSO	0.18
PRJNA977987	SRR24774464	16940808	92794	0.55	K27me3	ZR751	sample	DMSO	0.18
PRJNA977987	SRR24774465	13012970	84527	0.65	K27ac	ZR751	sample	PF9363	0.20
PRJNA977987	SRR24774466	14098668	73498	0.52	K27ac	ZR751	sample	PF9363	0.16
PRJNA977987	SRR24774467	27200972	180599	0.66	K27ac	ZR751	sample	DMSO	0.21
PRJNA977987	SRR24774468	19989529	143292	0.72	K27ac	ZR751	sample	DMSO	0.23
PRJNA977987	SRR24774469	18672158	33770	0.18	K9ac	ZR751	sample	PF9363	0.06
PRJNA977987	SRR24774470	19699493	31680	0.16	K9ac	ZR751	sample	PF9363	0.05
PRJNA977987	SRR24774471	16666938	26878	0.16	K9ac	ZR751	sample	DMSO	0.05
PRJNA977987	SRR24774472	17274937	25179	0.15	K9ac	ZR751	sample	DMSO	0.05
PRJNA977987	SRR24774473	11396727	41392	0.36	K4me3	ZR751	sample	PF9363	0.11
PRJNA977987	SRR24774474	17022732	72850	0.43	K4me3	ZR751	sample	PF9363	0.13
PRJNA977987	SRR24774475	15511624	61012	0.39	K4me3	ZR751	sample	DMSO	0.12
PRJNA977987	SRR24774476	17133232	66527	0.39	K4me3	ZR751	sample	DMSO	0.12
PRJNA253965	SRR1501980	23304079	272280	1.17	H2AK5ac	HMEL-shGFP	sample		0.45
PRJNA253965	SRR1501981	23949141	329121	1.37	H2BK120ac	HMEL-shGFP	sample		0.53

Continued on next page

Table A1 – continued from previous page

Study accession	Experiment accession	Whole-genome reads	Centro-meric reads	Centro-meric alignment (%)	ChIP antibody	Cell type	Sample/Input	Drug	Sample/ Input ratio
PRJNA253965	SRR1501982	32838999	873353	2.66	H2BK15ac	HMEL-shGFP	sample		1.02
PRJNA253965	SRR1501983	41280705	548372	1.33	H2BK5ac	HMEL-shGFP	sample		0.51
PRJNA253965	SRR1501984	11195033	375866	3.36	H3	HMEL-shGFP	sample		1.29
PRJNA253965	SRR1501985	33928491	552889	1.63	H3K14ac	HMEL-shGFP	sample		0.63
PRJNA253965	SRR1501986	27642763	295366	1.07	H3K18ac	HMEL-shGFP	sample		0.41
PRJNA253965	SRR1501987	28481946	292764	1.03	H3K23ac	HMEL-shGFP	sample		0.39
PRJNA253965	SRR1501988	28870550	311963	1.08	H3K27ac	HMEL-shGFP	sample		0.41
PRJNA253965	SRR1501989	34879957	876807	2.51	H3K27me1	HMEL-shGFP	sample		0.96
PRJNA253965	SRR1501990	27975979	528283	1.89	H3K27me3	HMEL-shGFP	sample		0.72
PRJNA253965	SRR1501991	30400930	609323	2.00	H3K36ac	HMEL-shGFP	sample		0.77
PRJNA253965	SRR1501992	30509338	646742	2.12	H3K36me1	HMEL-shGFP	sample		0.81
PRJNA253965	SRR1501993	23113778	678235	2.93	H3K36me2	HMEL-shGFP	sample		1.13
PRJNA253965	SRR1501994	25283013	474935	1.88	H3K36me3	HMEL-shGFP	sample		0.72
PRJNA253965	SRR1501995	27647143	331440	1.20	H3K4ac	HMEL-shGFP	sample		0.46
PRJNA253965	SRR1501996	34225601	435817	1.27	H3K4me1	HMEL-shGFP	sample		0.49
PRJNA253965	SRR1501997	14302653	262184	1.83	H3K4me2	HMEL-shGFP	sample		0.70
PRJNA253965	SRR1501998	12939561	368028	2.84	H3K4me3	HMEL-shGFP	sample		1.09
PRJNA253965	SRR1501999	14336891	119559	0.83	H3K79me1	HMEL-shGFP	sample		0.32
PRJNA253965	SRR1502000	28851022	313841	1.09	H3K79me2	HMEL-shGFP	sample		0.42
PRJNA253965	SRR1502001	20621480	579899	2.81	H3K79me3	HMEL-shGFP	sample		1.08
PRJNA253965	SRR1502002	26299279	672859	2.56	H3K9ac	HMEL-shGFP	sample		0.98
PRJNA253965	SRR1502003	30666930	430863	1.40	H3K9me1	HMEL-shGFP	sample		0.54
PRJNA253965	SRR1502004	34478399	1690743	4.90	H3K9me3	HMEL-shGFP	sample		1.88
PRJNA253965	SRR1502005	21642078	557120	2.57	H4	HMEL-shGFP	sample		0.99
PRJNA253965	SRR1502006	36959554	687014	1.86	H4K12ac	HMEL-shGFP	sample		0.71
PRJNA253965	SRR1502007	25790758	569994	2.21	H4K16ac	HMEL-shGFP	sample		0.85
PRJNA253965	SRR1502008	31777427	1111586	3.50	H4K20me1	HMEL-shGFP	sample		1.34
PRJNA253965	SRR1502009	14317465	358104	2.50	H4K20me2	HMEL-shGFP	sample		0.96

Continued on next page

Table A1 – continued from previous page

Study accession	Experiment accession	Whole-genome reads	Centro-meric reads	Centro-meric alignment (%)	ChIP antibody	Cell type	Sample/Input	Drug	Sample/ Input ratio
PRJNA253965	SRR1502010	13985999	439107	3.14	H4K20me3	HMEL-shGFP	sample		1.21
PRJNA253965	SRR1502011	39200658	583950	1.49	H4K5ac	HMEL-shGFP	sample		0.57
PRJNA253965	SRR1502012	26043609	348383	1.34	H4K8ac	HMEL-shGFP	sample		0.51
PRJNA253965	SRR1502013	29555727	455136	1.54	H4K91ac	HMEL-shGFP	sample		0.59
PRJNA253965	SRR1502014	34276710	699777	2.04	H4TETRAac	HMEL-shGFP	sample		0.78
PRJNA253965	SRR1502015	35180231	916489	2.61	IgG	HMEL-shGFP	input		
PRJNA253965	SRR1502016	21254774	174530	0.82	H2AK5ac	Hmel-shPTEN	sample		0.30
PRJNA253965	SRR1502017	31225614	505494	1.62	H2BK120ac	Hmel-shPTEN	sample		0.59
PRJNA253965	SRR1502018	31296851	673033	2.15	H2BK15ac	Hmel-shPTEN	sample		0.78
PRJNA253965	SRR1502019	31510380	555450	1.76	H2BK5ac	Hmel-shPTEN	sample		0.64
PRJNA253965	SRR1502020	15805891	416418	2.63	H3	Hmel-shPTEN	sample		0.95
PRJNA253965	SRR1502021	32598340	724035	2.22	H3K14ac	Hmel-shPTEN	sample		0.80
PRJNA253965	SRR1502022	9768034	103011	1.05	H3K18ac	Hmel-shPTEN	sample		0.38
PRJNA253965	SRR1502023	32557509	406512	1.25	H3K23ac	Hmel-shPTEN	sample		0.45
PRJNA253965	SRR1502024	23302950	252764	1.08	H3K27ac	Hmel-shPTEN	sample		0.39
PRJNA253965	SRR1502025	30471845	833087	2.73	H3K27me1	Hmel-shPTEN	sample		0.99
PRJNA253965	SRR1502026	30978741	429558	1.39	H3K27me3	Hmel-shPTEN	sample		0.50
PRJNA253965	SRR1502027	25325009	509537	2.01	H3K36ac	Hmel-shPTEN	sample		0.73
PRJNA253965	SRR1502028	31850806	928222	2.91	H3K36me1	Hmel-shPTEN	sample		1.05
PRJNA253965	SRR1502029	27563092	900649	3.27	H3K36me2	Hmel-shPTEN	sample		1.18
PRJNA253965	SRR1502030	25436738	410167	1.61	H3K36me3	Hmel-shPTEN	sample		0.58
PRJNA253965	SRR1502031	30738281	526217	1.71	H3K4ac	Hmel-shPTEN	sample		0.62
PRJNA253965	SRR1502032	36666928	423982	1.16	H3K4me1	Hmel-shPTEN	sample		0.42
PRJNA253965	SRR1502033	26654599	652249	2.45	H3K4me2	Hmel-shPTEN	sample		0.89
PRJNA253965	SRR1502034	13616125	476620	3.50	H3K4me3	Hmel-shPTEN	sample		1.27
PRJNA253965	SRR1502035	19674588	132845	0.68	H3K79me1	Hmel-shPTEN	sample		0.24
PRJNA253965	SRR1502036	19660177	135671	0.69	H3K79me2	Hmel-shPTEN	sample		0.25
PRJNA253965	SRR1502037	25406502	647825	2.55	H3K79me3	Hmel-shPTEN	sample		0.92

Continued on next page

Table A1 – continued from previous page

Study accession	Experiment accession	Whole-genome reads	Centro-meric reads	Centro-meric alignment (%)	ChIP antibody	Cell type	Sample/Input	Drug	Sample/ Input ratio
PRJNA253965	SRR1502038	24270017	641469	2.64	H3K9ac	Hmel-shPTEN	sample		0.96
PRJNA253965	SRR1502039	30807680	452843	1.47	H3K9me1	Hmel-shPTEN	sample		0.53
PRJNA253965	SRR1502040	31552841	1612627	5.11	H3K9me3	Hmel-shPTEN	sample		1.85
PRJNA253965	SRR1502041	23639185	667019	2.82	H4	Hmel-shPTEN	sample		1.02
PRJNA253965	SRR1502042	28580939	477406	1.67	H4K12ac	Hmel-shPTEN	sample		0.60
PRJNA253965	SRR1502043	20564974	484289	2.35	H4K16ac	Hmel-shPTEN	sample		0.85
PRJNA253965	SRR1502044	26599501	967460	3.64	H4K20me1	Hmel-shPTEN	sample		1.32
PRJNA253965	SRR1502045	8984655	231638	2.58	H4K20me2	Hmel-shPTEN	sample		0.93
PRJNA253965	SRR1502046	17775347	618410	3.48	H4K20me3	Hmel-shPTEN	sample		1.26
PRJNA253965	SRR1502047	29448067	369460	1.25	H4K5ac	Hmel-shPTEN	sample		0.45
PRJNA253965	SRR1502048	31287737	423212	1.35	H4K8ac	Hmel-shPTEN	sample		0.49
PRJNA253965	SRR1502049	19406334	351630	1.81	H4K91ac	Hmel-shPTEN	sample		0.66
PRJNA253965	SRR1502050	35335413	698217	1.98	H4TETRAac	Hmel-shPTEN	sample		0.72
PRJNA253965	SRR1502051	35927364	992680	2.76	IgG	Hmel-shPTEN	input		
PRJNA253965	SRR1502052	33908192	170864	0.50	H2AK5ac	Pmel-shGFP	sample		0.21
PRJNA253965	SRR1502053	24214009	142122	0.59	H2BK120ac	Pmel-shGFP	sample		0.24
PRJNA253965	SRR1502054	10752637	116783	1.09	H2BK15ac	Pmel-shGFP	sample		0.44
PRJNA253965	SRR1502055	31318872	232924	0.74	H2BK5ac	Pmel-shGFP	sample		0.30
PRJNA253965	SRR1502056	13295744	362856	2.73	H3	Pmel-shGFP	sample		1.11
PRJNA253965	SRR1502057	26006630	380991	1.46	H3K14ac	Pmel-shGFP	sample		0.60
PRJNA253965	SRR1502058	15608747	88469	0.57	H3K18ac	Pmel-shGFP	sample		0.23
PRJNA253965	SRR1502059	27545225	310514	1.13	H3K23ac	Pmel-shGFP	sample		0.46
PRJNA253965	SRR1502060	26437653	166528	0.63	H3K27ac	Pmel-shGFP	sample		0.26
PRJNA253965	SRR1502061	16417170	335866	2.05	H3K27me1	Pmel-shGFP	sample		0.83
PRJNA253965	SRR1502062	27101606	330842	1.22	H3K27me3	Pmel-shGFP	sample		0.50
PRJNA253965	SRR1502063	20765140	267408	1.29	H3K36ac	Pmel-shGFP	sample		0.53
PRJNA253965	SRR1502064	28206325	574663	2.04	H3K36me1	Pmel-shGFP	sample		0.83
PRJNA253965	SRR1502065	33860060	1421955	4.20	H3K36me2	Pmel-shGFP	sample		1.71

Continued on next page

Table A1 – continued from previous page

Study accession	Experiment accession	Whole-genome reads	Centro-meric reads	Centro-meric alignment (%)	ChIP antibody	Cell type	Sample/Input	Drug	Sample/ Input ratio
PRJNA253965	SRR1502066	16480395	261928	1.59	H3K36me3	Pmel-shGFP	sample		0.65
PRJNA253965	SRR1502067	63936107	763632	1.19	H3K4ac	Pmel-shGFP	sample		0.49
PRJNA253965	SRR1502068	18066008	173545	0.96	H3K4me1	Pmel-shGFP	sample		0.39
PRJNA253965	SRR1502069	28489003	379572	1.33	H3K4me2	Pmel-shGFP	sample		0.54
PRJNA253965	SRR1502070	20454798	452119	2.21	H3K4me3	Pmel-shGFP	sample		0.90
PRJNA253965	SRR1502071	10955442	61140	0.56	H3K79me1	Pmel-shGFP	sample		0.23
PRJNA253965	SRR1502072	24151894	190857	0.79	H3K79me2	Pmel-shGFP	sample		0.32
PRJNA253965	SRR1502073	28254875	776495	2.75	H3K79me3	Pmel-shGFP	sample		1.12
PRJNA253965	SRR1502074	9349072	179414	1.92	H3K9ac	Pmel-shGFP	sample		0.78
PRJNA253965	SRR1502075	16475554	166492	1.01	H3K9me1	Pmel-shGFP	sample		0.41
PRJNA253965	SRR1502076	19660700	1213109	6.17	H3K9me3	Pmel-shGFP	sample		2.52
PRJNA253965	SRR1502077	18465105	493342	2.67	H4	Pmel-shGFP	sample		1.09
PRJNA253965	SRR1502078	31341333	443406	1.41	H4K12ac	Pmel-shGFP	sample		0.58
PRJNA253965	SRR1502079	31196693	474136	1.52	H4K16ac	Pmel-shGFP	sample		0.62
PRJNA253965	SRR1502080	30917712	1178547	3.81	H4K20me1	Pmel-shGFP	sample		1.56
PRJNA253965	SRR1502081	20675573	683271	3.30	H4K20me2	Pmel-shGFP	sample		1.35
PRJNA253965	SRR1502082	23501416	826775	3.52	H4K20me3	Pmel-shGFP	sample		1.44
PRJNA253965	SRR1502083	31913153	346472	1.09	H4K5ac	Pmel-shGFP	sample		0.44
PRJNA253965	SRR1502084	28515249	375043	1.32	H4K8ac	Pmel-shGFP	sample		0.54
PRJNA253965	SRR1502085	16199407	105862	0.65	H4K91ac	Pmel-shGFP	sample		0.27
PRJNA253965	SRR1502086	21170360	284711	1.34	H4TETRAac	Pmel-shGFP	sample		0.55
PRJNA253965	SRR1502087	10293263	252218	2.45	IgG	Pmel-shGFP	input		
PRJNA253965	SRR1502088	33410836	339782	1.02	H2AK5ac	Pmel-shPTEN	sample		0.40
PRJNA253965	SRR1502089	26648142	400085	1.50	H2BK120ac	Pmel-shPTEN	sample		0.59
PRJNA253965	SRR1502090	40772646	871352	2.14	H2BK15ac	Pmel-shPTEN	sample		0.85
PRJNA253965	SRR1502091	36081721	576255	1.60	H2BK5ac	Pmel-shPTEN	sample		0.63
PRJNA253965	SRR1502092	14056454	387277	2.76	H3	Pmel-shPTEN	sample		1.09
PRJNA253965	SRR1502093	56176781	1181156	2.10	H3K14ac	Pmel-shPTEN	sample		0.83

Continued on next page

Table A1 – continued from previous page

Study accession	Experiment accession	Whole-genome reads	Centro-meric reads	Centro-meric alignment (%)	ChIP antibody	Cell type	Sample/Input	Drug	Sample/ Input ratio
PRJNA253965	SRR1502094	33565809	387349	1.15	H3K18ac	Pmel-shPTEN	sample		0.46
PRJNA253965	SRR1502095	23683181	333088	1.41	H3K23ac	Pmel-shPTEN	sample		0.56
PRJNA253965	SRR1502096	30350556	284397	0.94	H3K27ac	Pmel-shPTEN	sample		0.37
PRJNA253965	SRR1502097	40303887	1014510	2.52	H3K27me1	Pmel-shPTEN	sample		1.00
PRJNA253965	SRR1502098	27221968	375443	1.38	H3K27me3	Pmel-shPTEN	sample		0.55
PRJNA253965	SRR1502099	22842174	485709	2.13	H3K36ac	Pmel-shPTEN	sample		0.84
PRJNA253965	SRR1502100	48809642	1269174	2.60	H3K36me1	Pmel-shPTEN	sample		1.03
PRJNA253965	SRR1502101	15675804	353833	2.26	H3K36me2	Pmel-shPTEN	sample		0.89
PRJNA253965	SRR1502102	28274601	449560	1.59	H3K36me3	Pmel-shPTEN	sample		0.63
PRJNA253965	SRR1502103	25845151	392738	1.52	H3K4ac	Pmel-shPTEN	sample		0.60
PRJNA253965	SRR1502104	23796066	285202	1.20	H3K4me1	Pmel-shPTEN	sample		0.47
PRJNA253965	SRR1502105	27226409	693492	2.55	H3K4me2	Pmel-shPTEN	sample		1.01
PRJNA253965	SRR1502106	18868713	631461	3.35	H3K4me3	Pmel-shPTEN	sample		1.33
PRJNA253965	SRR1502107	14019188	145512	1.04	H3K79me1	Pmel-shPTEN	sample		0.41
PRJNA253965	SRR1502108	21724403	315637	1.45	H3K79me2	Pmel-shPTEN	sample		0.58
PRJNA253965	SRR1502109	23031850	929658	4.04	H3K79me3	Pmel-shPTEN	sample		1.60
PRJNA253965	SRR1502110	27964179	642943	2.30	H3K9ac	Pmel-shPTEN	sample		0.91
PRJNA253965	SRR1502111	28662658	743152	2.59	H3K9me1	Pmel-shPTEN	sample		1.03
PRJNA253965	SRR1502112	38458619	2500834	6.50	H3K9me3	Pmel-shPTEN	sample		2.58
PRJNA253965	SRR1502113	24566681	633646	2.58	H4	Pmel-shPTEN	sample		1.02
PRJNA253965	SRR1502114	24116988	502379	2.08	H4K12ac	Pmel-shPTEN	sample		0.83
PRJNA253965	SRR1502115	32543270	737533	2.27	H4K16ac	Pmel-shPTEN	sample		0.90
PRJNA253965	SRR1502116	31594724	962145	3.05	H4K20me1	Pmel-shPTEN	sample		1.21
PRJNA253965	SRR1502117	9433958	302507	3.21	H4K20me2	Pmel-shPTEN	sample		1.27
PRJNA253965	SRR1502118	14331600	556198	3.88	H4K20me3	Pmel-shPTEN	sample		1.54
PRJNA253965	SRR1502119	25065168	391734	1.56	H4K5ac	Pmel-shPTEN	sample		0.62
PRJNA253965	SRR1502120	33992014	482421	1.42	H4K8ac	Pmel-shPTEN	sample		0.56
PRJNA253965	SRR1502121	21856595	483475	2.21	H4K91ac	Pmel-shPTEN	sample		0.88

Continued on next page

Table A1 – continued from previous page

Study accession	Experiment accession	Whole-genome reads	Centro-meric reads	Centro-meric alignment (%)	ChIP antibody	Cell type	Sample/Input	Drug	Sample/ Input ratio
PRJNA253965	SRR1502122	24786633	536392	2.16	H4TETRAac	Pmel-shPTEN	sample		0.86
PRJNA253965	SRR1502123	29232586	737992	2.52	IgG	Pmel-shPTEN	input		
PRJNA986131	SRR24985370	37269713	627426	1.68	TRIM24	HepG2	sample		1.02
PRJNA986131	SRR24985371	32761749	557933	1.70	TRIM24	HepG2	sample		1.04
PRJNA986131	SRR16813840	25000527	411108	1.64	none	HepG2	input		
PRJNA638411	SRR11968969	42434548	1212991	2.86	CBX5	HCT116	sample		1.35
PRJNA638411	SRR11968970	42012131	983499	2.34	CBX5	HCT116	sample		1.10
PRJNA638411	SRR11968980	28258416	661095	2.34	DNMT3A	HCT116	sample		1.10
PRJNA638411	SRR11968981	29831220	718815	2.41	DNMT3L	HCT116	sample		1.14
PRJNA638411	SRR11969094	10366040	182046	1.76	TRIM24	HCT116	sample		0.65
PRJNA638411	SRR11969100	48165852	852122	1.77	Input	HCT116	input		
PRJNA638411	SRR11969101	30360941	606606	2.00	Input	HCT116	input		
PRJNA638411	SRR11969103	39714821	738983	1.86	Input	HCT116	input		
PRJNA638411	SRR11969104	35829798	760205	2.12	Input	HCT116	input		
PRJNA638411	SRR11969136	33283597	936006	2.81	CBX1	HCT116	sample		1.33
PRJNA638411	SRR11969137	32416405	869829	2.68	CBX3	HCT116	sample		1.26
PRJNA1199461	SRR31751536	32100613	970841	3.02	TRIM24	LNCaP	sample	4h DMSO	1.30
PRJNA1199461	SRR31751537	26749103	839305	3.14	TRIM24	LNCaP	sample	4h DMSO	1.35
PRJNA1199461	SRR31751538	28350473	873588	3.08	TRIM24	LNCaP	sample	4h DMSO	1.33
PRJNA1199461	SRR31751539	25339653	826343	3.26	TRIM24	LNCaP	sample	4h R1881	1.40
PRJNA1199461	SRR31751540	25980460	873375	3.36	TRIM24	LNCaP	sample	4h R1881	1.45
PRJNA1199461	SRR31751541	27721748	852861	3.08	TRIM24	LNCaP	sample	4h R1881	1.32
PRJNA1199461	SRR31751542	22933101	800151	3.49	TRIM24	LNCaP	sample	24h R1881	1.50
PRJNA1199461	SRR31751543	29997818	1058187	3.53	TRIM24	LNCaP	sample	24h R1881	1.52
PRJNA1199461	SRR31751544	18730679	605180	3.23	TRIM24	LNCaP	sample	24h R1881	1.39
PRJNA1199461	SRR31751545	10947495	254198	2.32	Input	LNCaP	input	input	

A3. Additional analyses of TRIM24 localization and regulation

Analysis of additional TRIM24 mutants

In addition to five TRIM24 mutants analyzed in the thesis, four additional variants (C840W, K723R, K741R, V733D/L735N) were tested in preliminary chromosome spread experiments. C840W represent a point mutation in PHD domain that abolished H3K4me0 binding, V733D/L735N is a point mutation in HP1BD that abolishes HP1 interaction, and K723R and K741R mutants remove SUMO-ylation sites [90].

Obtaining sufficient numbers of chromosome spreads for robust quantification was technically challenging, and spread quality was variable across repeats. Preliminary cohesion defect counts are summarized in Tab. A2. Due to limited number of analyzable spreads, no definitive conclusions could be drawn. Therefore, subsequent analyses focused on the five TRIM24 mutants described in the main Results.

Table A2.: Quantification of premature sister chromatid separation in HEK293T cells expressing TRIM24 mutant constructs (C840W, V733D/L735N, K723R, and K741R).

Repeat 1	**normal**	**partial**	**full**	**failure**	**total**
V733D/L735N	0	0	0	0	0
C840W	12	0	0	1	13
K723R	21	2	0	1	24
K741R	14	5	0	3	22
Repeat 2	**normal**	**partial**	**full**	**failure**	**total**
V733D/L735N	33	3	0	1	37
C840W	19	11	1	0	31
K723R	23	6	1	1	31
K741R	0	0	0	0	0
Repeat 3	**normal**	**partial**	**full**	**failure**	**total**
V733D/L735N	21	5	1	2	29
C840W	19	5	4	4	32
K723R	0	0	0	0	0
K741R	0	0	0	0	0

Mitotic index upon TRIM24 perturbation

To assess whether TRIM24 perturbation affects overall mitotic progression, the mitotic index was quantified by immunofluorescence staining for phosphorylated histone H3 (H3Ser10P), a marker of mitotic chromatin, in HEK293T cells expressing TRIM24 constructs or treated with siRNA. Cells displaying strong H3Ser10P signal were classified as mitotic.

Across most cells overexpressing TRIM24 mutants, the fraction of mitotic cells was comparable to GFP-only cells (Fig. A3b). In contrast, TRIM24 depletion (siTRIM24) caused increased proportion of H3Ser10P-positive cells compared to control condition (siCtrl; Fig. A3a). As this analysis was performed once and served primarily as a descriptive assessment, it was not further pursued and cell cycle distribution was subsequently examined by FACS analysis (Fig. S7).

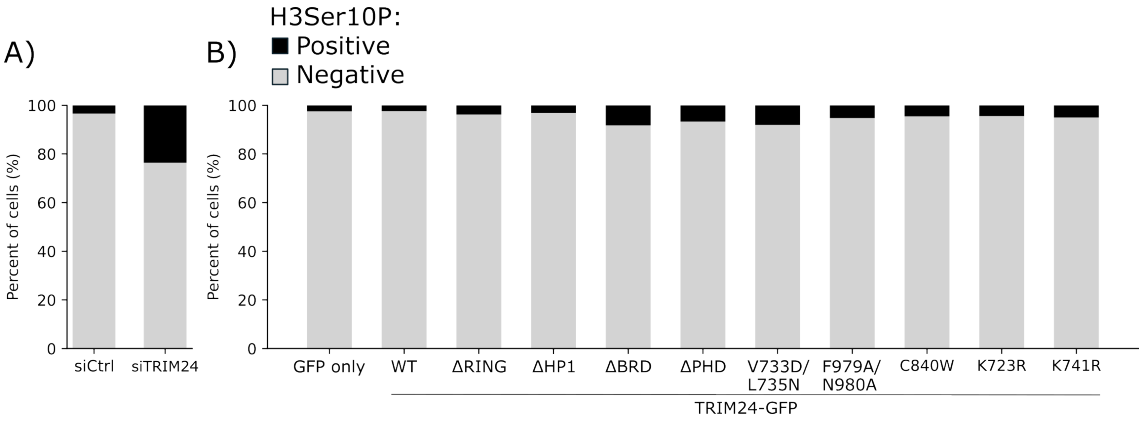


Figure A3.: Mitotic index upon TRIM24 perturbation. Quantification of mitotic index in HEK293T cells a) treated with control siRNA (siCtrl) or siRNA targeting TRIM24 (siTRIM24), or b) expressing GFP-only or TRIM24-GFP constructs, TRIM24 mutant constructs (ΔBRD, ΔPHD, ΔRING, ΔHP1, V733D/L735N, F979A/N980A, C840W, K723R, and K741R). Mitotic cells were identified by immunofluorescence staining for phosphorylated histone H3 (H3Ser10P). Stacked bar plots show the percentage of H3Ser10P-positive and -negative cells for each condition. Data represent a) n= 176 and 144 cells, b) n= 447, 209, 328, 224, 291, 349, 335, 267, 265, 226 and 220 cells from one experiment.

Hormone deprivation alters centromeric TRIM24 levels in LNCaP cells

REDPOINT analysis of LNCaP cells indicated TRIM24 enrichment at the centromeric repeats in androgen-stimulated LNCaP cells compared to hormone-starved conditions. To assess whether hormone availability influences centromeric TRIM24 association, LNCaP cells were cultured either in growth media or in charcoal-stripped media, and

immunofluorescence staining for CENP-A and TRIM24 was performed. Subsequently, the signal intensity and area were quantified at centromeres and across nuclei (Fig. A4a).

Hormone-starved LNCaP cells showed reduced TRIM24 intensity at the centromeres and across nuclei compare to cells grown in standard media (Fig. A4c,e). In contrast, CENP-A intensity at centromeres was increased, while nuclear CENP-A levels remained unchanged (Fig. A4b,d). These findings suggest that androgen signaling influences TRIM24 abundance at the centromere in LNCaP cells, and has an impact on CENP-A level at the centromeres.

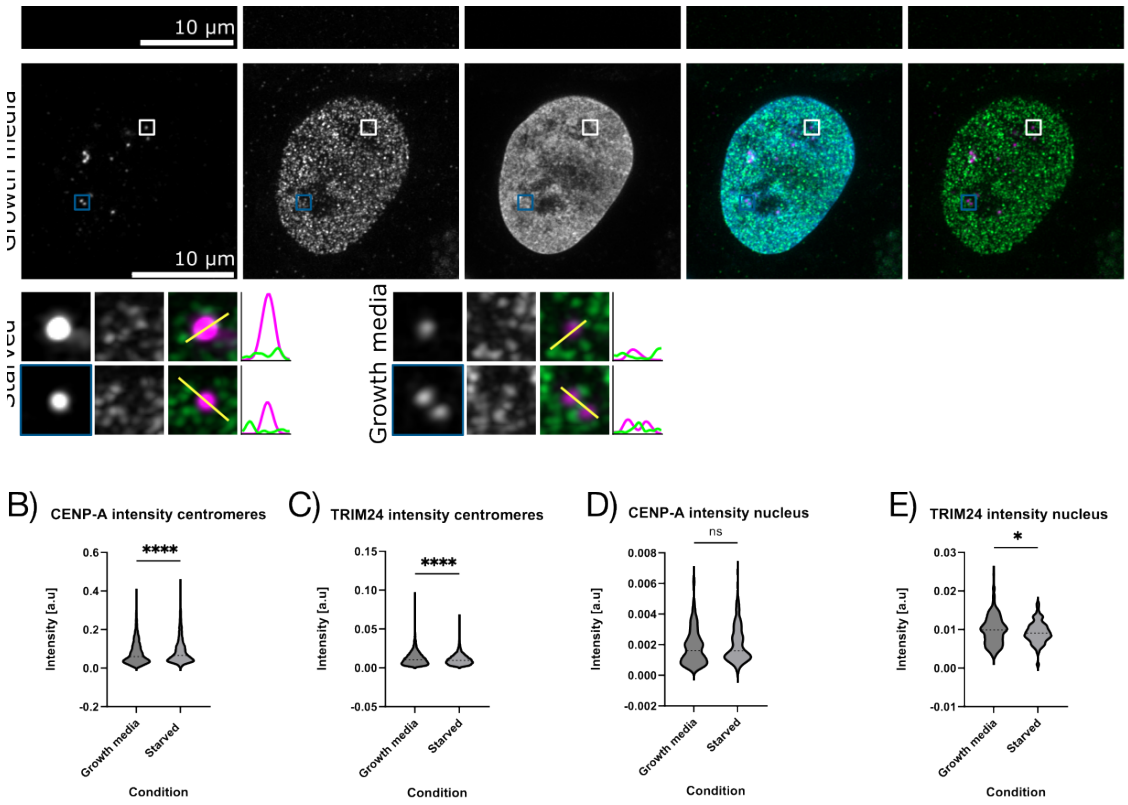


Figure A4.: Hormone deprivation alters centromeric TRIM24 intensity in LNCaP cells. a) Representative interphase nuclei of LNCaP cells cultured in charcoal-stripped media (starved) or standard growth media. Cells were stained for CENP-A (indirect immunofluorescence), TRIM24 (indirect immunofluorescence), and DNA (DAPI). Insets show representative CENP-A foci with the corresponding TRIM24 signal and fluorescence intensity profile plots (magenta: CENP-A; green: TRIM24). Images were acquired using Airyscan super-resolution microscopy. Scale bar: 10 µm. b,c) Quantification of b) CENP-A, c) TRIM24 intensity at centromeres. d,e) Quantification of d) CENP-A, e)TRIM24 across nuclei. Data are shown as violin plots. Statistical analysis was performed using a t-test; * $p < 0.05$, ** $p < 0.01$, *** $p < 0.001$. Data represents b,c) n=3942, 3634 centromeres from d,e) n=256, 267 cells pooled from three independent experiments. For details, see Materials and Methods.

Pol II Ser2P at centromeres upon overexpression of TRIM24 F979A/N980A

To investigate whether disruption of TRIM24 bromodomain function affects active transcription at centromeres, I analyzed the distribution of elongating RNA Polymerase II (Pol II Ser2P). GFP-only, TRIM24-GFP, or TRIM24 F979A/N980A-GFP plasmids were overexpressed in HEK293T cells. Cells were stained for CENP-A, Pol II Ser2P, and GFP. Images were acquired under identical settings.

In GFP-only cells, Pol II Ser2P signal was distributed throughout the nucleus, excluding nucleoli, with detectable signal at CENP-A foci (Fig. A5). Overexpression of wild-type TRIM24-GFP showed reduced overall Pol II Ser2P signal, both across the nucleus and at CENP-A foci. In contrast, overexpression of the bromodomain point mutant did not visibly alter Pol II Ser2P signal intensity.

Quantitative analysis showed that overexpression of wild-type TRIM24-GFP altered both CENP-A and Pol II Ser2P signal intensities at centromeres and across nulei, whereas F979A/N980A mutant failed to reproduce these effects (Fig. A6). Together, this data suggest that an intact TRIM24 bromodomain contributes to modulation of centromere-associated transcriptional features.

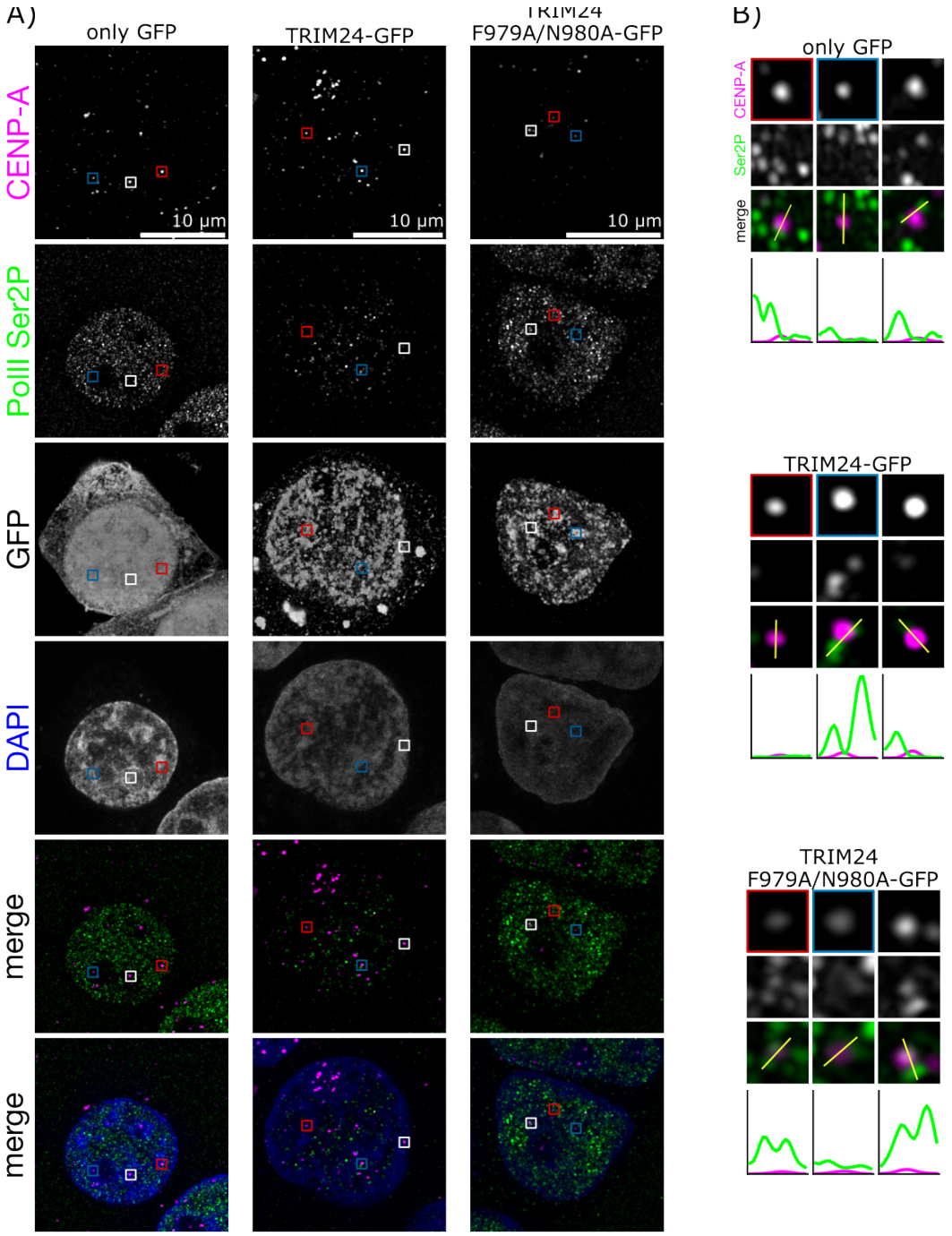


Figure A5.: CENP-A and Pol II Ser2P signal in cells overexpressing TRIM24-GFP or TRIM24 F979A/N980A-GFP. a) Representative interphase nuclei of HEK293T cells expressing GFP-only, TRIM24-GFP, or the TRIM24 bromodomain point mutant F979A/N980A-GFP. Cells were stained for CENP-A (indirect immunofluorescence), elongating RNA Polymerase II phosphorylated at serine 2 of the C-terminal domain (Pol II Ser2P; indirect immunofluorescence), GFP (indirect immunofluorescence; fusion protein), and DNA (DAPI). b) Insets show representative CENP-A foci with the corresponding Pol II Ser2P signal and fluorescence intensity profile plots (magenta: CENP-A; green: Pol II Ser2P). Images were acquired using Airyscan super-resolution microscopy. Scale bar: 10 µm. For details, see Materials and Methods.

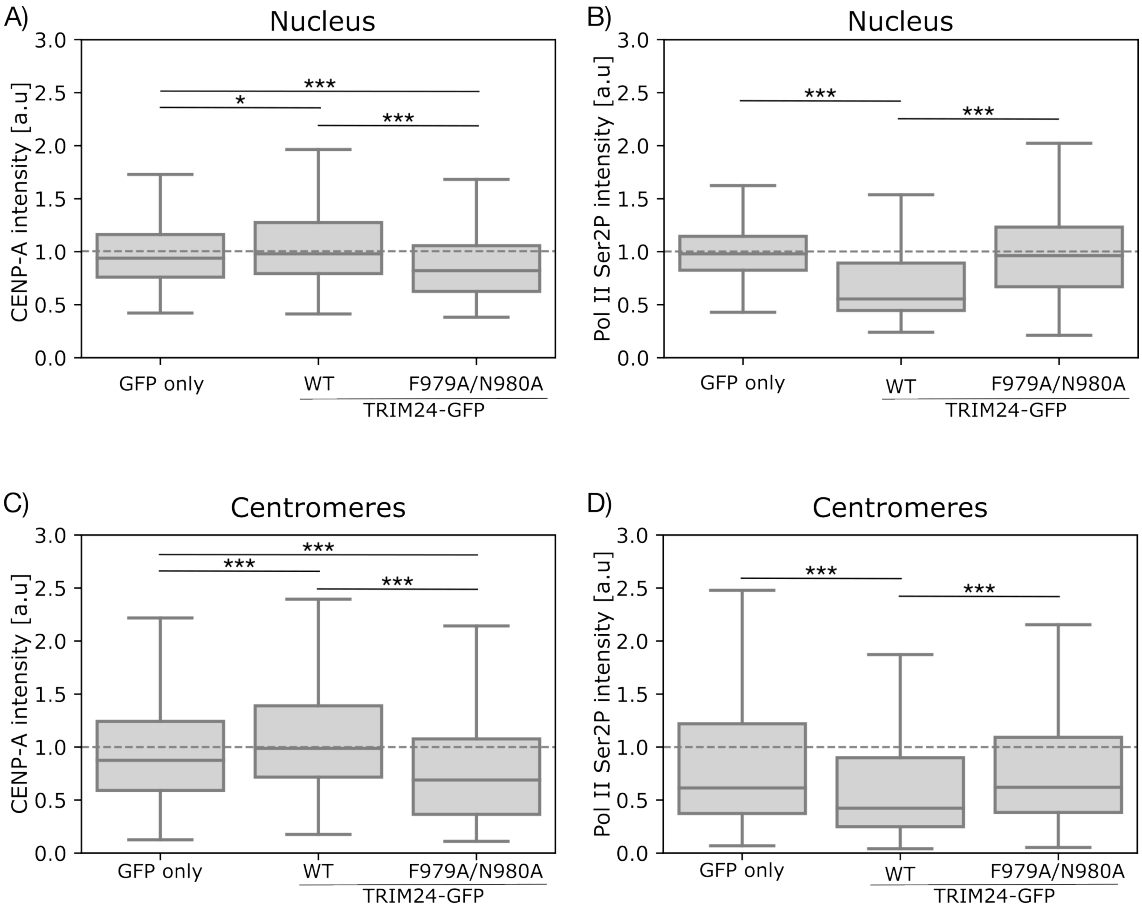


Figure A6.: Quantification of CENP-A and Pol II Ser2P signal upon TRIM24 bromodomain perturbation. Quantitative analysis of CENP-A and RNA Polymerase II Ser2 phosphorylation (Pol II Ser2P) signal in HEK293T cells overexpressing GFP-only, TRIM24-GFP, or TRIM24 F979A/N980A-GFP. a, b) Mean fluorescence intensity of a) CENP-A and b) Pol II Ser2P measured across the entire nuclear area and normalized to the mean value of GFP-only control cells. c, d) Mean fluorescence intensity of c) CENP-A and d) Pol II Ser2P measured at centromeres and normalized to the mean value of GFP-only control cells. CENP-A and Pol II Ser2P intensities were quantified using CellProfiler by masking nuclei based on the DNA channel and centromeres based on the CENP-A channel, followed by measurement of fluorescence intensities within the respective masks. Box plots show the minimum, first quartile, median, third quartile, and maximum. Statistical analysis was performed using a t-test; * $p < 0.05$, ** $p < 0.01$, *** $p < 0.001$. Data represent n = 407, 433, and 473 cells pooled from three independent experiments. For details, see Materials and Methods.

Immunofluorescence staining of RNA Polymerase II in *Drosophila melanogaster* testis

As part of a collaborative project investigating transcriptional cluster dynamics during stem cell differentiation, immunofluorescence staining of *Drosophila melanogaster* testis was performed.

Testes from freshly hatched *Drosophila melanogaster* males were dissected in PBS and fixed in 4% formaldehyde. Samples were permeabilized with 0.1% Triton X-100, washed in PBST, and blocked in 1% BSA in PBST for 45 min, RT. Immunostaining

was performed using rabbit anti-Pol II Ser2P (1:300, Abcam, ab193468) and rat anti-Pol II Ser5P (1:300, Active Motif, 61986), followed by Alexa Fluor-conjugated secondary antibodies (goat anti-rabbit Alexa 647, 1:300, Thermofisher, A21244; goat anti-rat Alexa 488, 1:300, Thermofisher, A11066). Samples were mounted in Vectashield containing Hoechst 33342.

Confocal and super-resolution microscopy were performed using an LSM 900 Airyscan super-resolution confocal microscope (Zeiss) equipped with a 63× oil-immersion objective (NA 1.4, Plan-Apochromat 63×/1.4 Oil DIC M27). Illumination and acquisition settings were kept constant within each experiment.

I carried out tissue preparation, immunofluorescence staining, and image acquisition. Quantitative cluster analysis and data interpretation were performed by members of the collaborating laboratory and are described in a preprint that resulted from this collaboration [92].

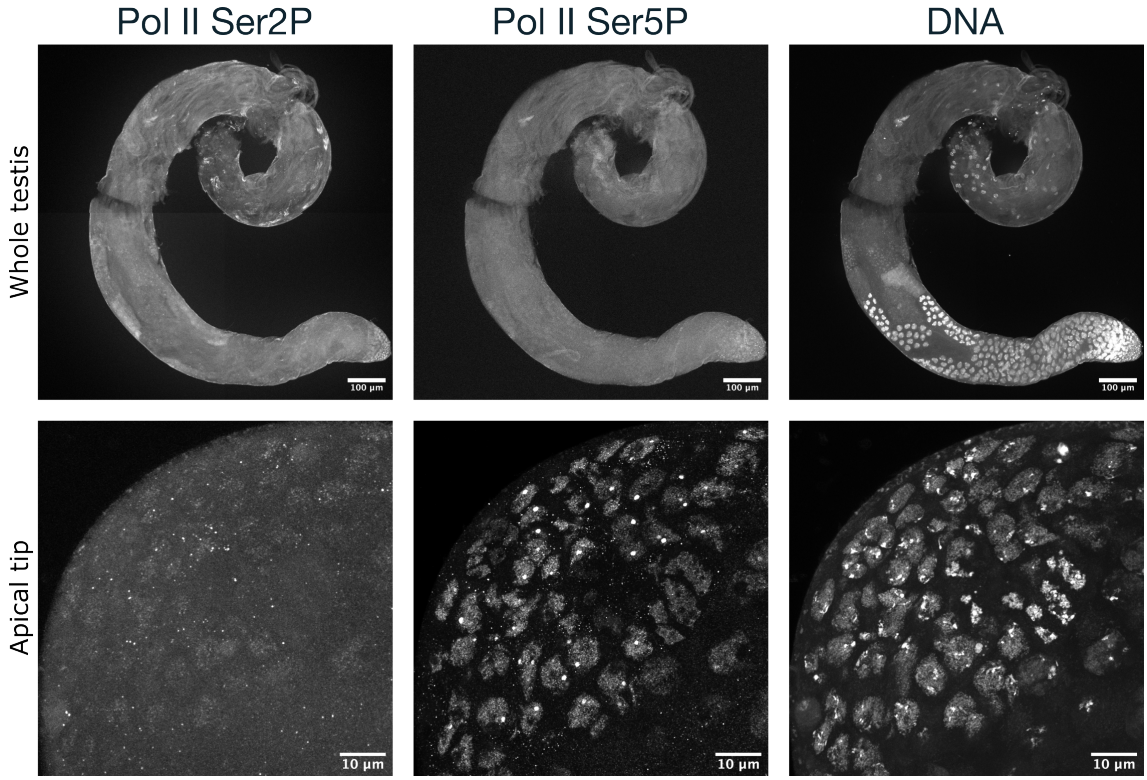


Figure A7.: Immunofluorescence staining of RNA Polymerase II in *Drosophila melanogaster* testis. Representative confocal images of whole testis (top) and apical tip region (bottom). Samples were stained for Pol II Ser2P and Pol II Ser5P (indirect immunofluorescence) and DNA (Hoechst). Scale bars: 100 µm (top), 10 µm (bottom).